Laser-induced plasma as a function of the laser parameters and the ambient gas

Xueshi Bai

Xueshi Bai. Laser-induced plasma as a function of the laser parameters and the ambient gas. Plasma Physics [physics.plasm-ph]. Université Claude Bernard - Lyon I, 2014. English. NNT : 2014LYO10333 . tel-01127499

HAL Id: tel-01127499
https://theses.hal.science/tel-01127499

Submitted on 7 Mar 2015

N° d'ordre : **333 - 2014** Année 2014

THESE DE L'UNIVERSITE DE LYON

Délivrée par

L'UNIVERSITE CLAUDE BERNARD LYON 1

ECOLE DOCTORALE

ED52 PHAST Physique et astrophysique de Lyon

DIPLOME DE DOCTORAT

(arrêté du 7 août 2006)

Soutenue publiquement le 15/12/2014

par

BAI Xueshi

TITRE :

Laser-induced plasma as a function of the laser parameters and the ambient gas

Directeur de thèse : Professeur YU Jin

JURY :

M. Arnaud COUAIRON	Rapporteur
M. Alessandro DE GIACOMO	Rapporteur
Mme. Nicole DELEPINE-GILON	Examinatrice
M. Jean-Marie JOUVARD	Examinateur
M. Vincent MOTTO-ROS	Examinateur
M. Gilles MOUTIERS	Examinateur
Mme. Amanda ROSS	Présidente
M. Jin YU	Directeur
M. Patrick MAUCHIEN	Membre invité
M. Pavel VEIS	Membre invité

UNIVERSITE CLAUDE BERNARD - LYON 1

Président de l'Université	**M. François-Noël GILLY**
Vice-président du Conseil d'Administration	M. le Professeur Hamda BEN HADID
Vice-président du Conseil des Etudes et de la Vie Universitaire	M. le Professeur Philippe LALLE
Vice-président du Conseil Scientifique	M. le Professeur Germain GILLET
Directeur Général des Services	M. Alain HELLEU

COMPOSANTES SANTE

Faculté de Médecine Lyon Est – Claude Bernard	Directeur : M. le Professeur J. ETIENNE
Faculté de Médecine et de Maïeutique Lyon Sud – Charles Mérieux	Directeur : Mme la Professeure C. BURILLON
Faculté d'Odontologie	Directeur : M. le Professeur D. BOURGEOIS
Institut des Sciences Pharmaceutiques et Biologiques	Directeur : Mme la Professeure C. VINCIGUERRA
Institut des Sciences et Techniques de la Réadaptation	Directeur : M. le Professeur Y. MATILLON
Département de formation et Centre de Recherche en Biologie Humaine	Directeur : Mme. la Professeure A-M. SCHOTT

COMPOSANTES ET DEPARTEMENTS DE SCIENCES ET TECHNOLOGIE

Faculté des Sciences et Technologies	Directeur : M. F. DE MARCHI
Département Biologie	Directeur : M. le Professeur F. FLEURY
Département Chimie Biochimie	Directeur : Mme Caroline FELIX
Département GEP	Directeur : M. Hassan HAMMOURI
Département Informatique	Directeur : M. le Professeur S. AKKOUCHE
Département Mathématiques	Directeur : M. Georges TOMANOV
Département Mécanique	Directeur : M. le Professeur H. BEN HADID
Département Physique	Directeur : M. Jean-Claude PLENET
UFR Sciences et Techniques des Activités Physiques et Sportives	Directeur : M. Y.VANPOULLE
Observatoire des Sciences de l'Univers de Lyon	Directeur : M. B. GUIDERDONI
Polytech Lyon	Directeur : M. P. FOURNIER
Ecole Supérieure de Chimie Physique Electronique	Directeur : M. G. PIGNAULT
Institut Universitaire de Technologie de Lyon 1	Directeur : M. C. VITON
Ecole Supérieure du Professorat et de l'Education	Directeur : M. A. MOUGNIOTTE
Institut de Science Financière et d'Assurances	Directeur : M. N. LEBOISNE

Résumé en français

La technique laser-induced breakdown spectroscopy (LIBS), qui consiste à exploiter le spectre du plasma induit par laser sur la surface de l'échantillon pour déterminer sa composition élémentaire, a été inventée il y a plus de 50 ans. Récemment, elle connaît un développement rapide, poussée par des besoins d'application dans différents domaines, citons par exemple, exploration océanique, détection de pollution environnementale, ou contrôle de procédés industriels. Cette technique utilise le plasma généré par ablation laser comme la source spectroscopique. La particularité de LIBS est que le plasma induit par laser présente un comportement transitoire et une distribution spatiale qui ne soit pas uniforme en général. Bien que la détection résolue en temps puisse améliorer considérablement la performance de LIBS, surtout pour le procédé de LIBS auto-calibration avec une meilleure détermination de température, l'évolution temporelle du plasma est souvent corrélée avec sa morphologie et son inhomogénéité spatiale. L'étude de la morphologie ainsi que la structure interne du plasma avec l'évolution pendant l'expansion de celui-ci dans un gaz ambiant, représente donc un point crucial pour l'optimisation du plasma entant qu'une source spectroscopique. Suite à la thèse de Qianli Ma réalisée dans notre équipe et soutenue en décembre 2012, qui a été notamment consacrée à l'étude de l'effet de la longueur d'onde du laser d'ablation sur les propriétés et l'évolution du plasma dans un gaz ambiant d'argon, la présente thèse s'intéresse aux effets des autres paramètres, la fluence du laser d'ablation, la durée de l'impulsion, et les différents gaz ambiants (argon ou air), sur la morphologie et la structure du plasma. Par ailleurs, les mécanismes microscopiques conduisant à l'onde de détonation soutenue par laser dans argon ou dans l'air sont aussi étudiés. Lors du refroidissant du plasma dans l'air, des oxydes métalliques peuvent se former. L'étude de la formation de molécules, au-delà de l'intérêt pratique pour la LIBS, fournit également un aperçu de la cinétique chimique dans le plasma, ce qui est intéressant pour l'étude de la transformation du plasma en phase gazeuse à une phase recondensée de nanoparticules.

Les travaux présentés dans cette thèse sont organisés selon la structure suivante : D'abord les contextes de la recherche et la motivation de ce travail sont présentés dans une introduction générale. Dans le Chapitre 1, la base théorique nécessaire à la compréhension de cette thèse est exposée. Les méthodes de diagnostic du plasma par la spectroscopie d'émission sont présentées dans le Chapitre 2, avec en particulier une discussion sur l'équilibre thermodynamique local. Le Chapitre 3 est consacré à la description des montages expérimentaux, des protocoles de mesure et du traitement de données. Les résultats expérimentaux les plus importants sont présentés dans les Chapitres 4, 5 et 6. En particulier, le Chapitre 4 concerne les propriétés du plasma en fonction des paramètres du laser, la fluence et la durée d'impulsion. Dans le chapitre 5, les caractéristiques et les mécanismes microscopiques de l'onde de détonation soutenue par laser sont étudiés et comparés pour les deux types de gaz ambiant, un gaz monoatomique (Ar) et un gaz moléculaire (l'air atmosphérique). Dans le 6e et dernier chapitre, nous étudions plus spécifiquement le processus de formation d'oxyde métallique (AlO) en termes de l'évolution de la température du plasma. Le manuscrit se termine par une conclusion générale avec des perspectives ouvertes par les avancés réalisées dans ce travail doctoral.

Mots-clés : Plasma induit par laser, laser-induced breakdown spectroscopy (LIBS), gaz choqué, diagnostic du plasma, image spectroscopique rapide, spectroscopie d'émission, onde d'absorption assistée par laser, onde de détonation assistée par laser, breakdown dans le gaz, réaction dans le plasma, recondensation en nanoparticules

Abstract in English

Laser-induced breakdown spectroscopy (LIBS) has been invented for more than 50 years, which analyzes the spectrum of the laser-induced plasma to determine the elemental composition of the ablated sample. Recently, LIBS technique has been well developed and applied in different domains, for example oceanic exploration, pollution monitoring in the environment. LIBS uses the ablation plasma as a light source that contains the elemental composition information of the sample. However, the laser-induced plasma exhibits a transient behavior. Although time-resolved and gated detection can greatly improve the performance of the LIBS technique especially that of calibration-free LIBS (CF-LIBS) with a better determination of plasma temperature, the temporal evolution of the plasma is correlated to its morphology and its spatial inhomogeneity. The determination of the morphology as well as the internal structure of the plasma together with their evolution during plasma expansion into the ambient gas is therefore crucial for the optimization of the use of ablation plasma as a spectroscopic emission source. Evolutions of the morphology and the internal structure of the ablation plasma are considered as the consequence of its hydrodynamic expansion into the ambient gas. Following the thesis of Qianli Ma which has studied the effect of laser wavelength on the behavior of the plasma induced in an ambient gas of argon, the present thesis has used the same diagnostic techniques (time- and space-resolved emission spectroscopy and fast spectroscopic images) together with 1064 nm ns laser pulse ablation of a target of aluminum to investigate the effects of other parameters, such as the fluence and the duration of laser pulse, the effect of different ambient gases (argon and air), on the morphology and internal structure of the plasma. Furthermore, in order to understand the effects of these parameters on the properties of the plasma, the microscopic mechanisms during post ablation and the propagation of the plasma are also studied. While the plasma cools down in air, molecules are formed, AlO for instance. So the thesis also studied the condition for the formation of the molecules in the plasma. Beyond the practical interest of this study for LIBS, it provides also insights to the kinetics of the AlO molecule formation in laser-induced plasma.

The works presented in this thesis manuscript are organized according to the following structure. First, the context and the motivation of this work are presented in a general introduction. In Chapter 1, the theoretical backgrounds needed for the understanding of the results obtained in this thesis work will be discussed in detail. In Chapter 2, plasma diagnostics with emission spectroscopy will be presented together with a discussion about the local thermodynamic equilibrium of the plasma and the laws of statistical distribution. Chapter 3 describes experimental setups and protocols of measurement as well as the data treatment techniques. The main experimental results are present in Chapter 4, 5 and 6. In Chapter 4, plasma properties as a function of the laser fluence and pules duration will be studied. In Chapter 5, the characteristics and the microscopic mechanisms of laser-supported absorption waves will be observed and compared between the plasmas induced in an atomic or molecular ambient gas. In the 6th and the last chapter of this thesis manuscript, the results of the experimental determination of the delay and the temperature for the appearance of the AlO molecule in the plume are presented. Finally, this thesis will end with general conclusion and perspective.

Keywords: Laser-induced plasma, laser-induced breakdown spectroscopy (LIBS), shocked gas, plasma diagnostics, fast spectroscopic imaging, emission spectroscopy, laser supported absorption wave, laser supported detonation wave, breakdown in gas, reaction in plasma, recondensation to nanoparticles

Acknowledgements

Ah... It's done! The time flies by so quickly. It seems like I had started my PhD study yesterday, and now I am finished. Too fast… But these three years have become the sparkling treasure of my life. I want to say thank you to all of the people who made my PhD come true. Without them, today, I would not be as self-confident and strong enough to face the many problems.

First of all, a big THANKS to my thesis supervisor, Jin Yu, for helping and encouraging me to accomplish the work, which almost seemed "impossible". Before the every oral presentation at the conferences, we rehearsed countless times in order to make every word sound perfect. During the presentation, you gave me a big smile to help me to get rid of my fears and to act natural. Without your help, I could have not finished my papers and especially my thesis manuscript. Helping me to learn how to write English scientifically, you gave me the books and techniques of how to write properly and taught me through sentence by sentence in my papers. Correcting my thesis manuscript, I cannot image how many nights you spent. In addition, thank you for your advice in learning the French language too which, helped me to make more friends in Lyon and better communicate to others both professionally and personally. After all, I want to thank you again for your patience, hard-work and profound knowledge.

My co-supervisor, Vincent Motto-Ros, should also be well thanked too. On one hand, you made a lot of programs to control the experimental devices and to treat the experimental data which saved me quite a lot of time for analyzing data. ☺ On the other hand, you taught me an important word to live by, "enjoy." Enjoy the chance that hundreds of people listening to me and enjoy the work.

I want to also thank the reviewers of my thesis, Arnaud Couairon and Alessandro De Giacomo for reading my thesis carefully and sending the reports on time. In addition, I want to thank all of the jury members: Nicole Delepine-Gilon, Jean-Marie Jouvard, Amanda Ross, Patrick Mauchien and Puval Veis, for your attending my thesis defense and for your questions you provide me to have an open mind.

Accomplishing my thesis work, I would also like to thank the CILAS Company to offering their laser and warm reception during our visit at Orléan.

I cherish and treasure the time shared with my dear colleagues in the group: Publi, Qianli Ma, Xiaochun Wang, Junshan Xiu, Lijuan Zheng, Fan cao, Jérôme Menneveux and Ye Tian. Fortunately, you were all here to make the experiments more interesting. Through our discussions, you helped me to understand my work more clearly. All of you are so much fun to work with that I am very happy to have worked with you.

During the three years, the people in the LASIM and after confusion, in ILM institute, helped me to simplify my research and daily life. Also, thank you to Francisco Pinto, Sad Mezzour and Xavier Dagany for their excellent work in maintaining the informatique materials. Thank you to Aurélie Bordas and Claude Lesage for their warm explication to me of all administrative problems.

I would like to give my gratitude's to the China Scholarship Council (CSC) for my three years scholarship, which allowed me to focus on my research work and enjoy my life in Lyon.

At last, I have to say to my close friends in Lyon, thank you all for accompanying me and let me feel that I was around by my family.

In one word, without anyone of you, I could have not finished my thesis. I will remember this precious period forever.

THANK YOU!!!

Contents

General introduction

From laser-induced plasma to laser-induced breakdown spectroscopy (LIBS)

Laser-induced breakdown is a well-known phenomenon which leads to a strongly ionized gas commonly named laser-induced plasma (LIP). When the used laser is a nanosecond pulsed laser with an output pulse energy in the range from several to hundreds mJ (fluence from several to hundreds J/cm^2 and irradiance from several to tens GW/cm^2), as usually used for laser ablation, the generated plasma occupies a particular place in the scales of temperature and density for plasma. Initial temperature in the range from 10^4 to 10^5 K and initial electron density from 10^{17} to 10^{18} cm^{-3} can be typically reached in a LIP. Excitation energy in the orders from several to tens of eV is typically available allowing a large number of processes to occur for particles constituent of the plasma, ions, atoms as well as molecules. Such processes include absorption/emission, ionization/electron capture, dissociation/recombination and formation of molecules, clusters and nanoparticles. In addition to primary interest as a convenient way for easy plasma production with commercially available laser, LIP represents an alternative to simulate what happens in various inaccessible and/or harmful environments such as ionosphere, interstellar space, solar corona, or ionized zone surrounding a nuclear explosion. In presence of laser radiation, such plasma can be characterized by the energy scale, $I_p \gtrsim h\nu \gtrsim kT$. It appears therefore as a hot and ionized gas with optical property sensitively dependent on its thermodynamics state. The last one is in turn determined by its optical emission and absorption properties. Strongly nonlinear processes take place in the plasma, which influence its gas dynamics, hydrodynamic, optical as well as chemical behaviors. Such medium situates therefore between hot plasma and cold gas and its description requires disciplines including atomic and molecular physics, thermodynamics, nonlinear optics, hydrodynamics, gas dynamics and spectroscopy.

Besides fundamental interests, applications of LIP have recently attracted much attention, especially for laser-induced breakdown spectroscopy (LIBS), pulsed laser deposition (PLD) and nanoparticle generation. [2-7] Recent interest in spectrochemical application with LIBS is driven by the unique advantages of the technique. Such advantages include easy or reduced sample preparation, no contact and remote measurement, instantaneous response for multi-elemental analysis and precisely localized (micro) surface analysis. First applications of LIBS were investigated in Los Alamos for detection of hazardous gas and vapors in air. [8] Further development of the technique turned to very practical problems, such as monitoring environmental contaminations, industrial applications for control of material processing, and sorting of materials or wastes. Needs from security and homeland defense trigger investigations in the application of LIBS for detection and analysis of bacteria [9, 10] and explosives [11]. Capability of LIBS to perform remote detection enables its application in nuclear industry. [12] Integration by NASA of a module of LIBS in the Mars exploration rover "Curiosity" for analysis of the soil of Mars highlights application of LIBS for space exploration. [13, 14]

Molecule formation with laser ablation of solid state material, in particular refractory material, and subsequent reaction with background gas have attracted much attention for study of exotic molecules or radicals of instable nature. [14] Ablation plume has been shown to facilitate controlled formation of different molecules and molecular ions which cannot be produced by other means such as in oven or cell. As for material processing, many molecules or radicals have been generated and studied for thin film formation by pulsed-laser deposition (PLD) or nanoparticle manufacturing [15], for example carbon nitride (CN_x) films with a fullerene-like structure.

It is thus clear that laser-induced plasma as a source of atomic and molecular spectroscopy and of particulate matter generation and deposition has its numerous and unique advantages, and provides the basis for a large number of applications.[16-20] Wide range of properties displayed by LIP during its lifetime makes it a source of choice suitable for applications in different domains of atomic and molecular spectroscopy, atmospheric photochemistry, astrophysics, analytical science, materials processing, and new material fabrication.[21-24] Moreover it provides a laboratory model to simulate and study what happens in various inaccessible and/or harmful environments. Experimental results obtained and especially numerical codes developed for a laboratory scale LIP can thus be useful for plasma observed in other circumstances.

More specifically for LIBS, a deeper understanding of the physical and chemical process involved in the evolution of the plasma and the detailed influences of the experimental parameters will be a great help for the improvement of the technique. It is why “back to the fundamental” represents one of the key points which will effectively accelerate the maturation of the LIBS technique. [25]

Temporal and spatial evolutions of the plasma as a key point of LIBS technique

Therefore as a spectroscopic emission source for LIBS application, laser-induced plasma is distinguished from other plasmas (discharge, inductively coupled plasma…) by its violent expansion into the ambient gas. Taking into account the temporal and spatial evolution of the plasma represents indeed a key point for the LIBS technique. Several steps can be distinguished to understand and describe the generation of ablation plasma and its subsequent evolution into the ambient gas. As shown in Figure 2, the process starts at the instant when the leading edge of the laser pulse reaches the target surface. Energy of the incident laser pulse is first absorbed by material touched by the laser pulse, which induces microscopic as well as macroscopic changes in the material. In particular, if the fluence or the irradiance of the laser pulse exceeds the threshold of ablation, phase transitions occur in the irradiated volume leading to the generation of a vapor. Such vapor can be slightly ionized and in the case of ablation with nanosecond or longer duration pulse, it interacts with the incoming laser pulse. Its high density and temperature and initial free electrons inside the vapor permit it to efficiently absorb the laser energy and get highly ionized. A plasma is thus generated above the target surface leaving a crater behind it. The plasma then expands into the ambient gas and interacts strongly with it. Since the laser pulse may still present during the early stage of the plasma expansion, the so-called laser-supported absorption wave (LSAW) dominates the propagation of the plasma into the ambient gas. After the termination of the laser pulse, the resulting system continues to expand into the ambient gas. Relaxation processes, especially radiative decay, take place in the plasma including the spectral emission from the plasma, which is the basis of the LIBS technique. The plasma finally re-condenses itself.

What are the physical and chemical processes involved in the generation and evolution of an ablation plasma?

Before going into detail in Chapter 1, of the description of the physical and chemical processes involved in the generation and evolution of laser-induced plasma, here we first list them for the three phases of evolution.

Ablation

Laser ablation corresponds to material removal and formation of a vapor more or less ionized following the impact of a laser pulse on the surface of a target material. Different mechanisms can lead to laser ablation according to the optical, thermal and mechanical properties of the target, and also according to the characteristics of the incident laser pulse, wavelength, fluence, and pulse duration… The property of the ambient gas can also greatly influence the ablation process. To fix the idea and since the purpose of this PhD thesis is to study the evolution of the laser-induced plasma as a spectroscopic emission source, we have chosen to work with the simplest case: the ablation of a metallic target and especially a pure aluminum or an aluminum alloy. For ablation with ns pulsed laser, since the existence of free electrons and the electron-lattice coupling time constant in the order of several ps, which is much smaller than the laser pulse duration, the ablation process is well described by the photothermal ablation model. In such model, the laser pulse acts as a thermal source which transmits its energy to the target during the pulse duration. The physical processes involved in the photothermal ablation process can be listed as in the following:

- Absorption of laser energy by conduction electrons through intra-band transition. Such free to free transition has not a resonant nature with respective to the wavelength of the used laser. Such choice in our experiment allows us emphasizing the effect of laser wavelength in the expansion of the generated plasma, the effect that we wish to study in our investigation.
- Coupling of the absorbed energy from the electrons to the lattice (electron-phonon coupling).
- Phase transitions, fusion and vaporization.

Post-ablation interaction

The specificity of ablation with nanosecond pulse comes from the fact that the initiation of the ablation plume within an interval of several hundred picoseconds [26] is much shorter than the duration of the ablation pulse. Even with short nanosecond pulse delivered by a Q-switched Nd:YAG laser of about 5 ns pulse duration for example, the laser pulse lasts longtime after the formation of the ablation vapor over the impacted area of the target surface. Post-ablation interaction between the vapor and the tailing part of the laser pulse represents therefore an important process in the early stage of the plasma expansion, which subsequently determines the morphology and the internal structure of the plume after the end of the laser pulse. The processes involved in the post-ablation interaction can be listed as in the following:

- Shockwave propagation, collisional excitation (including ionization and dissociation for molecular gas) of the ambient gas
- Photo-absorption and ionization of the vapor and the shocked gas
- Cascade ionization and breakdown of the vapor and the gas
- Ignition and propagation of the laser-supported absorption waves

Propagation and expansion of the plasma into the ambient gas

After the termination of the ablation laser pulse, the generated plume is left to continue to propagate and to expand into the ambient gas without any further input energy. During this period, the plume cools down through its interaction with the ambient gas. The principal applications based on laser-induced plasma appear in this interval of plasma evolution. The investigation of the behavior of the plasma in this period has thus the most important implication for these applications. The major processes involved are then listed as in the following.

- Gas dynamic expansion of the plasma into the ambient gas
- Impact ionization and electronic capture: Saha equilibrium
- Collisional excitation and radiative decay: local thermodynamic equilibrium (LTE)
- Dissociation and recombination: thermochemical equilibrium
- Re-condensation, cluster and nanoparticle formation

A simplified parametric space to study the influences of the experimental conditions

It is therefore quite clear that laser-induced plasma corresponds to a complex physical and chemical process. The behavior of the induced plasma depends on a quite large number of experimental parameters. The influences of these parameters are often not understood in detail, and their effects correlated each other in a nonlinear and non-trivial way. In order to have a simple representation of the ensemble of influencing parameters in the process of laser-induced plasma, we use a 3-dimansional parametric space which represents the 3 most important groups of experimental parameters: ablation laser wavelength, ablation laser fluence and ambient gas, as shown in Figure 3. Instead of treating continuous variations of the above 3 groups of parameters, which would lead to an infinite number of combinations of parameters to treat in our study, we divide each parametric dimension into two regimes as shown in Figure 3: UV (226 nm) and IR (1064 nm) for the wavelength; low and high levels for the fluence; and atomic gas (argon) and molecular gas (atmospheric air) for the ambient gas. In such representation, the parametric space is divided into 8 distinguished parametric combination volumes, just like an 8-bloc magic cube. A systematic study of effects of the experimental parameters on the properties of the induced plasma can thus be performed for each of these 8 parametric volumes.

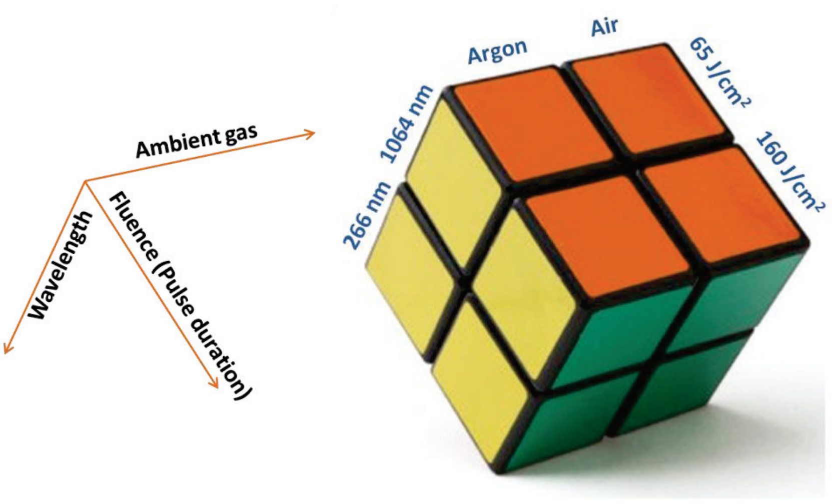

Figure 3 A parametric space with three axes: laser fluence (including pulse duration); laser wavelength and ambient gas.

A global schema of the research projects of our team plans to cover the 8 parametric volumes within two successive PhD theses. A first PhD thesis realized in the period from 2009 to 2012 par Qianli Ma, has essentially covered the 4 parametric volumes with argon as the ambient gas. The study has been performed principally as a function of the wavelength of the ablation laser. The correlated effect with the laser fluence was also studied. The present PhD thesis is thus designed to cover the 4 remaining parametric volumes with the atmospheric air as the ambient gas. The applicative importance of this study is manifest since the majority of LIBS measurements takes place in such ambient gas. By doing this, it is also possible to compare the characteristics of the plasma in a molecular ambient gas, such as the atmospheric air, to that of the plasma in an atomic ambient gas, such as argon.

Objectives of the present PhD thesis and the approach used

The objectives of the present PhD thesis are therefore:

1) Study the effects of ablation laser fluence and pulse duration on the expansion behavior of the plasma induced under the ambient of argon;
2) Compare the expansion behavior of the plasma induced under the atmospheric air to that of the plasma induced under an argon ambient gas. From such comparison, deduce the mechanisms of laser-induced absorption waves in a molecular or an atomic ambient gas;
3) Study the specific features of the evolution of laser-induced plasma under a molecular ambient gas, especially the formation of molecules.

The approach of the present PhD work is essentially experimental. The used experimental investigation methods corresponds to classical plasma diagnostics techniques, including time- and space-resolved emission spectroscopy, fast spectroscopic imaging. The data treatment with spectrum analysis is based on the assumption of the LTE. The specificity of this thesis is a large investigated time interval from several ns to tens of μs. Such long time delay investigated is needed by the observation of molecular (AlO) emissions. It is why atomic as well as molecular emission spectroscopies are used to characterize the ablation plume.

The structure of this thesis manuscript

After this general introduction, the following part of this PhD thesis manuscript will present in detail the works realized in 6 chapters. We will first expose in Chapter 1, the theoretical background necessary for a good understanding of the results presented. Chapter 2 will be devoted to the presentation of the methods of plasma diagnostics by emission spectroscopy of a plasma assumed to be in the local thermodynamic equilibrium. The experimental setup and protocols, and the data treatment methods used will be presented in Chapter 3. The main findings of this PhD work will be described in Chapters 4, 5 and 6 with 3 different aspects: The influences of the laser fluence and the pulse duration on the morphological and physical properties of the plasma will be detailed in

Chapter 4. The influences of the nature of the ambient gas on the expansion behavior of the plasma will be discussed in Chapter 5. We infer especially the microscopic mechanisms which lead to different behaviors of the plasma in an atomic or a molecular ambient gas. The transformation of the plasma into a molecular gas (AlO) will be discussed in Chapter 6. We will especially determine the minimal delay and the maximal temperature necessary for a dominant production of the molecule in the plume through recombination. We then conclude the manuscript and point out the perspectives emerging from the present PhD thesis work.

Chapter 1. Theoretical background

1.1. General description of the laser-induced plasma

A detailed description of the process of laser-induced plasma requires a collection of basic terms being first specified before they will be properly used in this thesis manuscript.

The initial process begins with the ablation laser pulse impacting on the surface of the target. As it is often the case for LIBS, in this thesis we consider that the ablation laser pulse is sent to the target surface along its normal direction. The ambient gas fills the environment where the laser ablation occurs. Usually for LIBS, the ambient gas is the atmospheric air at the room temperature and one atmosphere pressure.

The vapor is the gas-phase material removed from the target, which is composed of electrons, ions, atoms and other forms of the material such as droplets and solid fragments. For example, when aluminum is ablated, an aluminum vapor is produced. The shockwave is a discontinuity (in the thermodynamical point of view) propagating into the ambient gas following the laser pulse impact on the target surface. The shockwave is induced when the removed material (the vapor) is ejected out the target surface with a velocity larger than the speed of the sound in the ambient gas. The shocked gas is the part of the ambient gas left behind the shockwave. The thermodynamic property, as well as the optical property of the shocked gas can be dramatically changed due to the passage of the shockwave. The ensemble vapor and shocked gas is referred to the plume. This definition emphasizes the fact that the plume correspond to a gas with a temperature substantially high than the initial ambient gas, and efficiently emits an optical emission (continuum, atomic, ionic or molecular emission). When the plume is significantly ionized, we call it plasma. It is actually the laser-induced plasma.

When the plume disappears, a crater is definitively left on the surface of the target where the laser pulse was impacted. It is important to remark that a crater does not correspond to the state of the target surface immediately after the rejection of the vapor;

the ablated materials can eventually deposit back on the target surface contributing therefore to the morphology of the final crater.

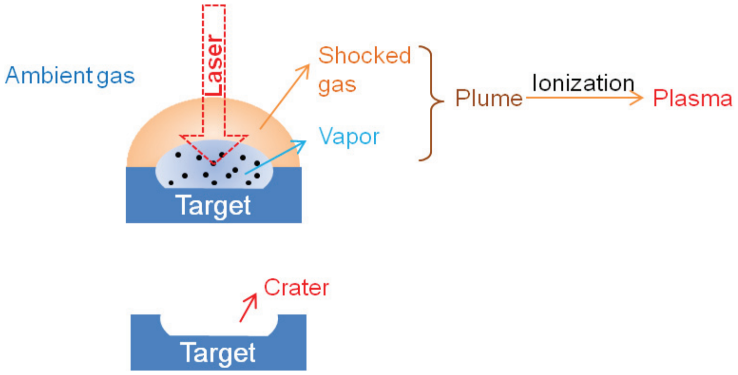

Figure 1.1 Illustration of the process of laser-induced plasma in ambient gas.

With the principal used terms specified, we will now in the following sections, describe more in detail, the generation and the evolution of the laser-induced plasma.

1.2. Laser ablation

Laser ablation is the process of material removed from the surface of a solid or liquid material by irradiating it with a laser pulse. The amount of material removed by a single pulse depends on the optical property of the material and the laser pulse parameters, such as wavelength, pulse energy and pulse duration. The property of the ambient gas influences as well the ablation process. [27]

1.2.1. Mechanisms of laser ablation

In general, laser ablation can be due to one of the following mechanisms: photothermal ablation, photochemical ablation and photophysical ablation [28]. The first two types of ablation are distinguished by the mechanism of laser radiation absorption by the material and the third one corresponds to the case where both the photothermal and the photochemical process play an important role in the ablation. Although LIBS can concern materials in all the phases, solid, liquid and gas, the ablation of solids is most studied and often representative for the majority of involved processes, of the ablation processes of the different phases of material. It is why in the following, we will address more specifically the laser ablation of solid state materials.

In the photothermal ablation, the laser energy is first absorbed by free electron available in the material. Electron-lattice coupling transfers then the absorbed energy to the matrix. In solid state material, such coupling has a time constant in the order of picosecond. Therefore for a nanosecond laser pulse, the pulse duration is much longer than the energy coupling process from the electron to the matrix, in such way that the laser pulse can be considered as a heat source in the ablation process. The temperature rising in the volume touched by the heat transfer can result in the surface material melting and vaporization, which leads to the formation above the target surface of an ablation vapor. The initial temperature of the formed vapor is essentially determined by the vaporization temperature of the ablated material. The thermal ablation is especially suitable to describe the ablation of metals by nanosecond laser pulse, because of the availability of initial free electrons and the long duration of the laser pulse. For other types of materials (dielectrics, polymers…), additional mechanisms are needed to create initial free electrons (multiphoton ionization, ionization from default levels, ionization by cosmic rays…).

Photochemical ablation occurs when the photon energy of the ablation laser is high enough or multiphoton transition is sufficiently efficient (in the case of intense femtosecond laser for example), so that the optical excitation results in direct bond breaking in the volume of the material touched by the laser pulse. Such photochemical dissociation builds up mechanical stress in the touched volume, which leads to material removal through fragmentation. It takes place in principle without any change in the temperature of the target surface. The photochemical ablation is often suitable to describe ablation of dielectric and polymeric materials. UV nanosecond laser pulse or femtosecond laser pulse is often efficient to induce photochemical ablation.

When the both photothermal and photochemical mechanisms contribute to the ablation process, photophysical ablation occurs, which corresponds to ablation with the both thermal and non-thermal processes. In such ablation, the photochemical process creates initial free electrons, which allows the photothermal process further efficiently transferring the absorbed laser energy to the matrix, leading to its fusion and vaporization. Ablation of dielectric or polymeric materials with nanosecond laser can often be described by the photophysical process. The existence of default energy levels in dielectric materials or metallic trace elements with low ionization potential in polymeric materials, facilitates the ablation of these materials even for infrared ns laser pulse with moderate pulse intensity. High temperatures can be reached for the plasma induced from these materials through the photophysical process.

Since the purpose of this thesis is to study the plasma induced from a metallic target, pure or alloy of aluminum for instance, we will in the next section provide a more detailed description of the photothermal ablation process of a metal. We remark also here that such process is up to now the only ablation process that one can numerically simulate in a rather detailed way.

1.2.2. Plasma generation through photothermal ablation of a metal

Absorption and electronic excitation and relaxation in metallic crystalline materials

For metals, the band structure is a general concept to describe the electronic energy level structure in as shown in Figure 1.2 [29-31]. The highest occupied band is only half-filled by the valence electrons. The Femi level (E_F) lies therefore in the middle of the band. Intraband single photon transition is possible for an electron initially under the Fermi level to be excited into an energy level above the Fermi level in the same band. The mechanisms of optical absorption in a metal can be therefore considered as intraband transitions as illustrated in Figure 1.2 (b).

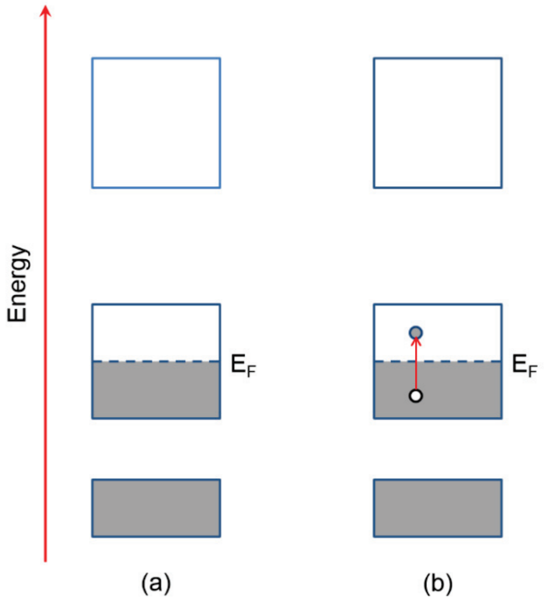

Figure 1.2 (a) Band structure in metal where the bands are filled with electrons up to the Fermi level E_F. Such occupation is indicated by the shading. (b) Optical intraband absorption by metals [29]

In the classical treatment of the optical response of metals with the Drude model [32], the valence electrons are considered as free electrons that interact with electromagnetic field "freely" without restoring force from the ions which form the crystalline lattice. The electrons interact with the lattice through collisions with heavy and relatively immobile positives ions. With such simple model, analytical expression of the absorption coefficient can be obtained for metal. Coupled with the Lorentz dipole oscillator model of atom, the Drude-Lorentz model describe the oscillation of a free electron induced by the AC electric field associated to a laser radiation, $\varepsilon(t)$, with the following equation [29],

$$m^* \frac{d^2x}{dt^2} + m^*\gamma \frac{dx}{dt} = -e\mathcal{E}_0\, e^{-i\omega t}$$

(1-1)

where m^* is the effective mass of the electron, $\mathcal{E}_0$ the amplitude of the laser electric field and ω its pulsation. γ the friction coefficient is considered as equal to $1/\tau$, where τ is considered as the mean time between two successive collisions between an electron and an ion. Compared to the standard Lorentz model of atom, in Eq. (1-1) the term due to the restoring force of the ion on the electron is set to zero ($\omega_0 = 0$). The solution of this equation for the displacement of the electron, x, leads to the relative permittivity of the metal. A characteristic parameter is introduced to describe the optical response of the metal, ω_p, the plasma frequency which is defined by

$$\omega_p = \sqrt{\frac{n_e e^2}{\varepsilon_0 m_0}}$$

(1-2)

where n_e stands for the free electron number density, which is in the order of 10^{22} to 10^{23} cm^{-3} for metals [29]. The plasma frequency is a key parameter for the optical property of a metal. A radiation with $\omega < \omega_p$ is reflected by the surface of the metal with a reflectivity $\mathcal{R}$ close to 1. The absorption coefficient α can be thus expressed as a function of ω_p, τ, and ω,

$$\alpha = \sqrt{\frac{2\omega_p^2\tau\omega}{c^2}}$$

(1-3)

From α, one can define the skin depth, δ, which represents the distance under the target surface where the laser field strength decreases to e^{-1} of the incident strength.

$$\delta = \frac{2}{\alpha} = \sqrt{\frac{2c^2}{\omega_p^2 \tau \omega}} \tag{1-4}$$

The value of α for metals is in the order of 10^6 cm^{-1}, which corresponds to a skin depth in the order of 10 nm. In a real metal, the simple free-electron behavior is modified by a number of secondary effects, such as inter-band transition [33].

An excited electron is in contact with a large number of other particles in the material, the ions forming the lattice, other electrons, or holes created at the same time as the excited electron. The energy stored by the electron can be efficiently relaxed into other forms of excitation. Radiative relaxation corresponds to electron-hole recombination. It is the inverse process of optical absorption. The radiative lifetime of an electron-hole pair is in the nanosecond range, and is longer than the timescales of electron-electron collision and electron-lattice coupling [29]. Collision time between free electrons in a solid can be very short in the range of 10^{-14} s due to the high free carrier density. Coupling with the lattice can be considered as electron-phonon coupling, and electron scattering takes place on a timescale as short as 10^{-12} s [33]. These different timescales determine the principal ways of the relaxation of an excited electron through non-radiative processes, such as electron-electron and electron-phonon couplings. For a nanosecond pulse, these relaxation processes occur instantaneously and transfer the absorbed optical energy into the thermal energy of the free electron and then that of the lattice. The laser pulse acts therefore as a source of heat which induces a rise of temperature in the lattice during its propagation in to a solid target. The consequence can be melting then evaporation of the target material, if the corresponding thresholds in fluences or in irradiance are successively reached. We remark here that the ablation volume does not only concerns that touched by laser radiation. The thermal conduction extends the volume ablated by a laser pulse significantly beyond the depth corresponding to the skin depth defined by Eq. (1-4).

Formation of the ablation vapor

We assume that the laser energy absorbed by the material is totally transformed into heat, so the temperature distribution in the material can be calculated with the heat conduction equation. In the case of aluminum, the absorption coefficient is $\alpha = 1.25 \times 10^6$ cm^{-1}, which corresponds to a penetration depth in target in the order of 8 nm [28]. The penetration depth is thus much smaller than the size of the focused spot of the laser beam (typically 100-500 μm), so the lateral heat flow can be ignored and the temperature distribution in z-direction (laser incident direction perpendicular to the target surface) can be described by a one-dimensional heat equation:

$$c_p \rho \frac{\partial T(z,t)}{\partial t} = \frac{\partial}{\partial z}\left[\kappa \cdot \frac{\partial T(z,t)}{\partial z}\right] + \alpha \cdot I(z,t) + U(z,t)$$

(1-5)

The first term of the right side of Eq. (1-5) corresponds to the heat conduction, whereas the second term indicates the energy coming from the laser energy absorption. T represents the temperature in the target, U describes the additional energy per unit volume and time that is required or provided if phase transition occurs, z is the distance measured from the target surface, t is the time, κ, c_p and ρ denote the thermal conductivity, heat capacity and mass density of the target material respectively. The numerical values of these parameters can be found for various materials in the literature (Ref. 28 for example).

When the surface temperature T_s exceeds the melting point T_m of the sample, the surface starts to melt. Subsequently, T_s increases much slower or not at all, due to the consumption of the absorbed laser energy not only for heating, but also for melting. During the time when the phase change takes place, the local temperature remains constant. If the irradiance of the incident laser is high enough, the surface temperature becomes so high that vaporization becomes significant.

The produced vapor expands into the background. The simplest configuration is a vacuum background. The expansion dynamic of the evaporated material can be described by Euler equations of hydrodynamics. This equation is simplified with the one-dimensional equations of hydrodynamics to express the conservation of mass, momentum and energy, respectively [34]:

$$\frac{\partial \rho}{\partial t} = -\frac{\partial (\rho v)}{\partial z}$$

(1-6)

$$\frac{\partial(\rho v)}{\partial t} = -\frac{\partial}{\partial z}(P + \rho v^2)$$

(1-7)

$$\frac{\partial}{\partial z}\left[\rho\left(E + \frac{P}{\rho} + \frac{v^2}{2}\right)\right] + \varepsilon_{abs} - \varepsilon_{rad}$$

(1-8)

where ρ is the mass density, ρv is the momentum, $\rho v^2/2$ is the kinetic energy density, P is the local pressure, ρE is the internal energy density. The quantity ε_{abs} denotes the locally absorbed laser energy; whereas ε_{rad} is the amount of energy emitted by the vapor per unit volume and time, which corresponds to a loss for the internal energy of the vapor. It should be mentioned that the Eq. (1-6) to Eq. (1-8) describe the expansion of the vapor into the vacuum, where only the evaporated material needs to be considered. Compared to the expansion in the vacuum, the expansion into an ambient gas of the vapor drives a shockwave propagating into the ambient gas. The interaction of vapor with the ambient gas is a more complicated gas-dynamic process which we will discussed in Section 1.3 .

1.2.3. Laser ablation in high fluence regime

Phase explosion

When the fluence of the ablated laser is relative low, the heating process can be quite slow and the liquid has enough time to relax to successive equilibrium states with the rising temperature followed by the evaporation. When the laser pulse becomes very intense, the laser heating generated under the surface can lead to a temperature higher than the normal boiling point, resulting in a metastable state. Phase explosion occurs when the temperature approaches the thermodynamic critical point (T_c), which transforms the melted metal in to a mixture of liquid and vapor. [35]

The phase change induced by pulsed laser heating can be best illustrated using the pressure-temperature diagram shown in Figure 1.3. The normal heat is the representative process when the heated metal becomes liquid but is still below the boiling temperature point. The binode line represents equilibrium between the surface temperature T_s and the vapor saturation pressure P_{vap}.

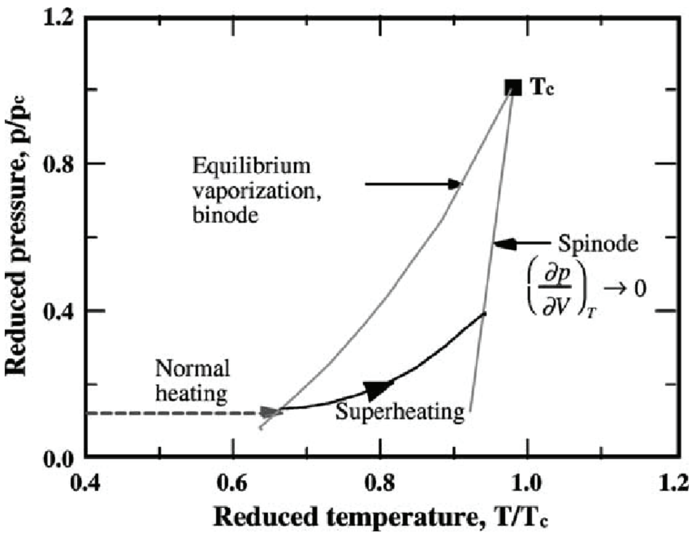

Figure 1.3 The $p-T$ diagram of a liquid metal near the critical point

During pulsed laser heating, the amount of nuclei generated by spontaneous nucleation is negligible at the temperatures lower than $0.9T_c$. At a temperature of about $0.9T_c$, the target material makes an abrupt transformation from superheated liquid into a mixture of liquid droplets and vapor, which are then violently ejected from the target. This process is called phase explosion. Furthermore, for the phase explosion there is a certain time needed for a vapor embryo to grow to a critical nucleus, called the time lag of nucleation [35]. The time lag is important in ablation induction by nanosecond or shorter pulsed lasers. The time lag of metals is estimated between 1 and 10 ns [36].

Plasma shielding

Another phenomenon, plasma shielding, becomes important when the ablation laser energy is relatively high. The tailing part of the laser pulse can be shielded and not arrive on the target surface [37]. Such shielding results in the saturation of the ablation rate with respect to the laser fluence. The effect of plasma shielding on the target surface-temperature is illustrated in Figure 1.4 as example. The calculated time dependences of the surface temperature are given in Figure 1.4 a) for a graphite target irradiated at different laser fluences. Figure 1.4 b) illustrates the effect of plasma shielding on the temporal profile of laser radiation that arrives on the target surface through the plume. At low laser fluencies (curve for 1.75 mJ/cm^2, Figure 1.4 a)) the surface temperature continues to rise after the laser-radiation reaching its maximum. The maximum vaporization rate is thus delayed relative to the laser pulse. This means that no significant plasma shielding effect is observed and that the whole pulse is delivered to the target surface. As the laser fluence increases with a corresponding increase of mass removal, T_S peaks at an earlier time with respect to the incident laser-pulse maximum as the result of plasma absorption (see curves for >= 18 mJ/cm^2 in Figure 1.4 a) and b)).

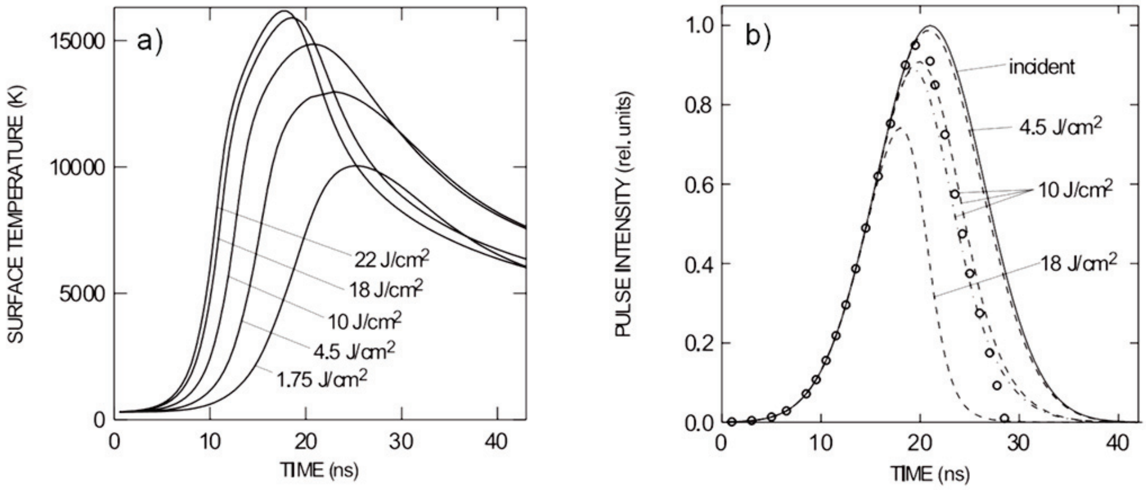

Figure 1.4 a) Calculated time dependences of the surface temperature of a graphite target for ablation with different laser fluences. b) Calculated temporal profiles of laser radiation delivered to the target surface through the laser induced plasma at different laser fluences during graphite (dashed curves) and Nb (dot-dashed curve) ablation. The incident laser pulse, peaked in the calculations at 20.5 ns, is shown by a solid curve. The points represent the experimental data for graphite ablation at 10 J/cm^2 [38].

Splashing ejection

In fluid mechanics, a splash is a sudden disturbance to the otherwise quiescent free surface of a liquid. The disturbance of the liquid can be caused when a solid object or a fluid suddenly hit on the liquid surface. According to the observations reported in the thesis of Qianli Ma [39], for an IR laser pulse ablation, a reflected wave can propagate back toward the surface of the target. Such backward wave can thus initiate an upward velocity component for the melted material, which transforms the melt material into droplets or vapor, leading to a secondary delayed material ejection, as illustrated in Figure 1.5.

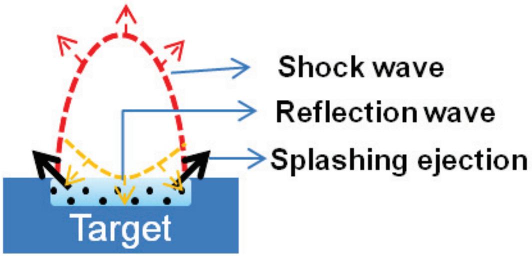

Figure 1.5 Formation of a splashing ejection. The red dashed line is the front of the shockwave with the movement directions indicated by the red arrows. The yellow dashed line is the front of the reflection wave with the movement directions indicated by the yellow arrows. The black arrows indicate the movement of the material due to the splashing ejection.

1.3. Post ablation laser-plasma interaction

1.3.1. General description of post ablation laser-plasma interaction

For nanosecond pulsed laser ablation, the pulse duration is significantly longer than the initiation time of the plasma. The phase of the pulse laser ablation is commonly considered as the interval between the initial impact of the laser pulse on the target and the appearance of evaporated material over its surface. Using picosecond time-resolved shadowgraph imaging, the initiation time is measured in the range of several hundred picoseconds [26].

In the most cases, a LIBS measurement is performed in an ambient gas at the atmospheric pressure, with the ambient air or an introduced gas, such as argon or helium. In the Figure 1.6 (a) the solid material is heated first to be melted, and then it is evaporated (Figure 1.6 b) with further absorption of laser energy. After being evaporated, the vapor begins to expand into the ambient gas, therefore, a shockwave forms and propagates into ambient gas. As a result, the ablated vapor is surrounded by the shocked gas.

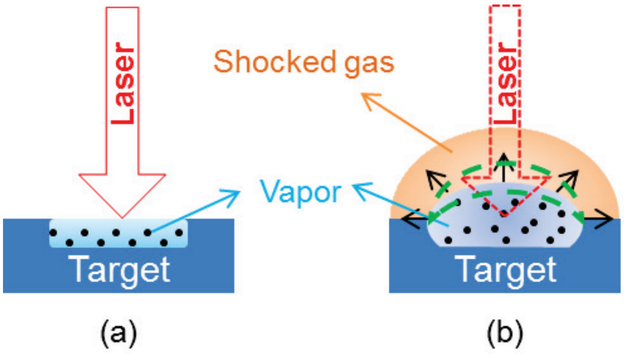

Figure 1.6 Melting (a) and evaporation (b) during laser ablation in an ambient gas (the part in the green dashed line shows the absorption zone of laser energy).

The expanding vapor as well as the shocked gas can absorb energy from the incoming laser pulse, which corresponds to the plasma shielding effect. The shielding is efficient for ablation under an ambient gas at atmospheric pressure, where the vapor is slowed down and confined. Thermal ionization can thus occur in the shocked gas, increasing its absorption rate. The early stage of the plasma expansion is thus driven by laser-supported absorption waves (LSAW) [40]. The absorption of the laser pulse by the interacting system, which can include the vapor and the shocked gas, is the key point that determines the subsequent evolution of the plasma.

In the Figure 1.6 (b) the vapor above the target surface is ejected from the target and is ionized by absorbing laser energy. It can also contain ionized ambient gas which, once ionized, is ingested by the vapor plasma. The shocked gas corresponds to a layer of ambient gas compressed by the out coming plasma. An absorption zone locates in the front part of the plasma which can more or less extend into the shocked ambient gas and back into the vapor. Finally the precursor shock can separate the ensemble of the plume (containing the vapor plasma and the shocked gas) from the ambient gas still in the ambient temperature and pressure. Strong interactions take place between the different parts of the plume with mechanical, thermal or radiative nature. The expansion of the vapor plasma mechanical compresses the surrounding ambient gas, leading to a shocked gas layer behind the precursor shock. Thermal conduction occurs from the hot vapor plasma to the shocked layer. The radiation emitted by the hot vapor plasma can be absorbed by the surrounding ambient gas, leading to its further excitation and ionization. The optical property of the ambient gas can be greatly modified by its interaction with the vapor.

1.3.2. *Absorption of laser radiation by the vapor plume and the shocked gas*

The vapor plume and the shocked ambient gas are therefore considered as a hot and partially ionized gas. For nanosecond laser ablation, the photon energy is smaller than the ionization potential of implicated elements, and the laser irradiance is too small for significant multiphoton absorption to happen. The main mechanisms involved in the absorption of laser radiation by such gas correspond to the inverse bremsstrahlung (IB) (free-free transitions) and the photoionization (PI) (bound-free transition) [40]. The total absorption coefficient (α_{tot}) of the gas is therefore contributed by two processes of single photoionization of excited states (α_{PI}) and inverse bremsstrahlung (α_{IB})

$$\alpha_{tot} = \alpha_{PI} + \alpha_{IB} \tag{1-9}$$

Absorption by inverse bremsstrahlung

The inverse bremsstrahlung corresponds to absorption by a free electron when its trajectory is modified by passing nearby a heavy particle, a neutral atom or an ion. After the three body collision events, a photon (of wavelength λ) is absorbed by the electron which is accelerated. In the classical electrodynamics, the cross section for inverse bremsstrahlung is calculated separately for neutrals, $\sigma_{e,0}^{IB}$, and Z-time ionized ions σ_{eZ}^{IB} due to the different types of interaction force between the two types of particles and the electrons [41]. The absorption coefficient can therefore be written in the following forms [41]:

$$\alpha_{IB} = \alpha_{IB,e0} + \sum_{Z=1} \alpha_{IB,eZ} = n_0 \sigma_{e,0}^{IB} + \sum_{Z=1} n_Z \sigma_{e,Z}^{IB} \tag{1-10}$$

$$\alpha_{IB,e0}(\lambda) = A_1 \lambda^3 n_0 n_e T_e^{1.5} \sigma_{dif} \overline{G_{e0}^{IB}} \tag{1-11}$$

$$\alpha_{IB,ei}(\lambda) = A_2 \lambda^3 \left[1 - \exp\left(-\frac{hc}{\lambda k_B T_e}\right)\right] \sum_{Z=1} \frac{Z^2 n_Z n_e \overline{G_{eZ}^{IB}}}{\sqrt{T_e}} \tag{1-12}$$

Here A_1 and A_2 are two constants, their expression and numerical values in the CGS system of units can be found in the Ref. [42]. The corresponding values in the MKS system are respectively 8.61×10^{-19} and 1.37×10^{-27}. T_e is the electron temperature. n_e, n_0, and n_Z stand for respectively the number densities of electrons, neutral atoms and Z-time ionized ions. σ_{dif} represents the cross section of electron scattering by a neutral atom, which is in the order of 10^{-20} m^2 [43, 44]. $\overline{G_{e0}^{IB}}$ and $\overline{G_{eZ}^{IB}}$ are Gaunt factors and can be expressed in the following forms [45]:

$$\overline{G_{e0}^{IB}} = \left[1 + \left(1 + \frac{hc}{\lambda k_B T_e}\right)^2\right] \exp\left(-\frac{hc}{\lambda k_B T_e}\right) \tag{1-13}$$

$$\overline{G_{eZ}^{IB}} = 1 + 0.1728\left(\frac{hc}{\lambda E_H Z^2}\right)^{1/3}\left(1 + \frac{2k_B T_e \lambda}{hc}\right)$$

(1-14)

These two factors take into account the correction of the quantum effect to the used classical calculation of the cross section. And their value is in general close to 1.

The Eqs. (1-11) and (1-12) can be used to study the behavior of the inverse bremsstrahlung absorption as a function of the electron temperature and the wavelength of the laser radiation. Electron-neutral process, $\alpha_{IB,e0}(\lambda)$, is important only at low temperature for a weekly ionized plasma [46]. The upper limit temperature is in the range of 5 000 K for a metallic plasma such as aluminum vapor, and 10 000 K for a gas such as argon. For higher temperatures, electron-ion process, $\alpha_{IB,ei}(\lambda)$, becomes dominant. Concerning the dependence on laser wavelength, when $k_B T_e \ll h\nu$, α_{IB} varies as λ^3 and when when $k_B T_e \gg h\nu$, α_{IB} varies as λ^2. The transition temperature between these two regimes for typical Nd:YAG laser wavelengths are 13 500 K for 1064 nm, 40 500 for 355 nm and 54 100 K for 266 nm. Inverse bremsstrahlung absorption starts with free electrons initially available in the vapor. It increases the electron temperature and leads to impact excitation or ionization of the atoms in the plasma. Impact ionization can leads to cascade ionization in the vapor and increases significantly its ionization degree.

Single photon ionization from excites states

The condition for single photon ionization of excited states can be given by $h\nu > E_{ion}^k$, where E_{ion}^k represents the energy necessary to ionize an atom in its excited state labeled by the principal quantum number k. This energy is equal to the difference between the ionization potential of the atom, E_{ion}, and the excitation energy of the state k: $E_{ion}^k = E_{ion} - E_k$. The total absorption due to photoionization can be written as

$$\alpha_{PI} = \sum_Z \sum_k^\infty n_Z^k \ \sigma_{k,Z}^{PI}$$

(1-15)

Here n_Z^k is the number density of the population in the excited state k of the Z-times ionized atoms and $\sigma_{k,Z}^{PI}$ is the cross section of single photon ionization of a Z-times ionized atom from its k excited state. The lowest excited state contributing to the total photoionization depends on the structure of the atom and the wavelength of the laser radiation. In the Table 1-1, we provide the quantum number k and the excitation energy of the lowest excited state concerned by single photon ionization with the three wavelengths of a Nd:YAG laser for two elements, aluminum and argon. We can see that for the used wavelengths, only excited atoms can be photoionized [47, 48]. The needed excitation energies are quite high especially for argon. Such excitation is provided in the plasma by collision excitation with electrons and can correspond to very high temperatures. According to this model, the absorption coefficient for single photon ionization can be calculated for hydrogen atoms [49]:

$$\alpha_{PI}(\lambda) = A_2\lambda^3\left[1-\exp\left(-\frac{hc}{\lambda k_B T_e}\right)\right]\left[\exp\left(\frac{hc}{\lambda k_B T_e}\right)-1\right]\sum_{Z=1}\frac{Z^2 n_Z n_e \overline{G_Z^{PI}}}{\sqrt{T_e}} \tag{1-16}$$

with

$$\begin{aligned}\overline{G_Z^{PI}} = 1 - 0.1728\left(\frac{hc}{\lambda E_H Z^2}\right)^{1/3}\left(1-\frac{2k_B T_e\lambda}{hc}\right) \\ - \exp\left(-\frac{hc}{\lambda k_B T_e}\right)\left[1+0.1728\left(\frac{hc}{\lambda E_H Z^2}\right)^{1/3}\left(1+\frac{2k_B T_e\lambda}{hc}\right)\right]\end{aligned} \tag{1-17}$$

Here A_2 is the same factor as in the Eq. (1-12). T_e represents the electron temperature, n_Z and n_e are the number densities of Z-times ionized atoms and electron. $\overline{G_Z^{PI}}$ is the Gaunt factor and E_H stands for the hydrogen ionization potential. The Eq. (1-16) can be generalized to non hydrogenic atoms by replacing the Gaunt factor by the Biberman factor [50, 51].

Table 1-1. The principal quantum number of the lowest excited energy level concerned by single photon ionization and the corresponding excitation energy for two elements of aluminum and argon excited by the three frequently used wavelengths in LIBS of a Nd:YAG laser.

Atom	Aluminum			Argon		
Wavelength (nm)	1064	355	266	1064	355	266
k	8	3	3	19	6	2
E_k (eV)	4.83	3.14	3.14	14.7	12.9	11.5

1.3.3. Relative contributions of IB and PI and the total absorption coefficient

Consider the Gaunt factors are equal to 1 in Eq. (1-12) and Eq. (1-16), the ratio between the PI and IB processes for the case where the electron-ion process dominates the IB absorption:

$$\frac{\alpha_{PI}}{\alpha_{IB}} = \exp\left(\frac{hc}{\lambda k_B T_e}\right) - 1 \tag{1-18}$$

The ratio shows that when $h\nu \gg k_B T_e$, PI is a dominant process, and when $h\nu \ll k_B T_e$, IB is the dominant one.

Combining Eq. (1-11), Eq. (1-12) and Eq. (1-16), the total absorption coefficient is obtained:

$$\alpha_{tot} = A_1 \lambda^3 n_0 n_e T_e^{1.5} \sigma_{dif} \overline{G_{e0}^{IB}} + A_2 \lambda^3 \left[1 - \exp\left(-\frac{hc}{\lambda k_B T_e}\right)\right] \sum_{Z=1} \frac{Z^2 n_Z n_e}{\sqrt{T_e}} \left\{\left[\exp\left(\frac{hc}{\lambda k_B T_e}\right) - 1\right] \overline{G_Z^{PI}} + \overline{G_{eZ}^{IB}}\right\} \tag{1-19}$$

In order to have an insight on the behavior of the total absorption coefficient for typical wavelengths used in LIBS, the ratio between the total absorption coefficients at the two wavelengths of 1064 nm and 355 nm is estimated for a typical configuration of LIBS experiment, in which a shocked argon gas has a pressure of 400 bar and propagates at a velocity of 5 km/s. The result of the estimation is presented in Table 1-2.

Table 1-2 Estimation of the ratio between the total absorption coefficients at the two wavelengths of 1064 nm and 355 nm

T (K or eV)	7 000 K (0.6 eV)	10 500 K (0.9 eV)	46 000 K (4 eV)
$\alpha_{tot}(1046\,nm)/\alpha_{tot}(355\,nm)$	12	3	21

This estimation shows that the absorption in the shocked gas is always more efficient for IR than for UV in the range of temperatures of typical plasmas produced by laser ablation. This behavior is consistent with the calculation reported for carbon plasma expanding in a residual background [52]. For the range of wavelengths considered here and with moderate laser intensity, PI is only efficient from highly excited levels of the atoms through single photon ionization, which can explain this tendency. The PI absorption rate increases with the temperature of the gas and decreases with the laser wavelength. This dependence remains however quite moderate when $k_B T_e \ll h\upsilon$. On the other hand for IB, the absorption is essentially contributed by electron-neutral processes at low gas temperature (below 0.9 eV for argon), and becomes dominated by electron-ion processes as soon as the gas starts to be ionized (larger than 1% of ionization). The latter rapidly increases as λ^3. The total absorption rate of the shocked ambient gas increases therefore sensitively with the laser wavelength. Consequently, in general an IR pulse is much more strongly coupled to plasma than a UV pulse.

1.3.4. Laser-supported absorption waves

Absorption of laser radiation by plasma accelerates its propagation toward the laser incoming direction and leads to an anisotropic expansion. Such propagation corresponds to laser-supported absorption wave (LSAW). There are three major types of LSAW, which can be induced with different laser irradiances for a given laser wavelength and ambient gas. The three LSAW are laser-supported combustion (LSC) wave, laser-supported detonation (LSD) wave, and laser-supported radiation (LSR) wave [40]. The difference between the three modes of laser-supported waves arises from the different roles that the ambient gas plays and the different way it gets ionized and absorbs the laser radiation. For usual laser irradiances used in LIBS, LSC and LSD waves are more often ignited. In the following paragraphs, we will present the principal characteristics of LSC and LSD waves in the simplified one-dimension model as exposed in Ref. 40.

Laser-supported combustion wave (LSC)

At low irradiance, laser-supported combustion waves can be induced. As shown in Figure 1.7 (left), the laser absorption zone is localized in the vapor plasma behind the layer of shocked gas which is comprised between the precursor shock (or shockwave) and the vapor. The shocked gas remains transparent for the laser radiation. The last transmits through the shocked gas and is absorbed by the vapor above the target and behind the shocked gas. Consequently, the vapor is efficiently heated to a high temperature and pressure as shown in Figure 1.7 (c: left) and (d: left). In contrast, the shocked gas remains at a low temperature. The shocked gas is mechanically compressed by the expanding vapor to high pressure and density. The dynamics of the system is maintained by the expansion of the hot vapor. The absorption wave propagates into the cold and high-pressure shocked gas. The main mechanism of propagation is radiative and thermal transfers from the hot plasma to the cold shocked gas. The high pressure of the shocked gas increases the absorption of the extreme ultraviolet radiation emitted from the plasma. The part of the shocked gas in contact with the plasma becomes rapidly heated, ionized and is ingested by the LSC wave. Its expansion maintains the pressure that drives the propagation of the shockwave.

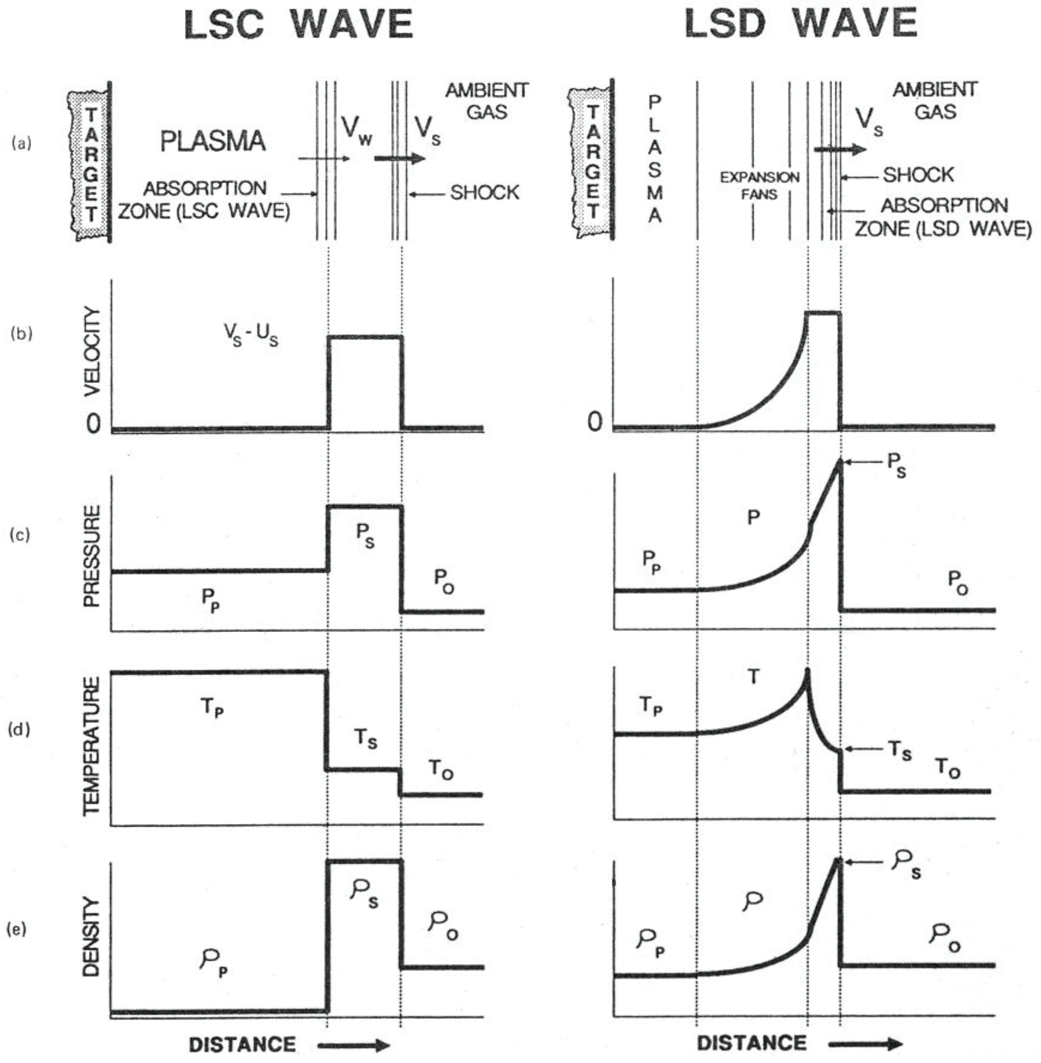

Figure 1.7 Illustration of the structures of one-dimensional LSAWs (a) and qualitative presentation of the profiles of characteristic parameters of the wave, velocity *v* (b), pressure *P* (c), temperature *T* (d) and density *ρ* (e). The subscribe P is used for the vapor plasma, S for shocked gas and 0 for the ambient gas. Reproduced from the Ref. 40

Laser-supported detonation wave (LSD)

As the laser irradiance increases, a threshold value will be reached beyond which the shocked gas will significantly absorb the laser radiation and get significantly ionized. The mode of propagation becomes dominated by the LSD wave. An absorption zone is found just behind the precursor shock inside of the layer of shocked gas (Figure 1.7 a right). No abrupt separation exists between the shocked gas and the vapor plasma. Instead, the pressure, the temperature and the density continuously vary between the vapor and the shocked gas. The propagation of the LSD wave is driven by the absorption of laser energy by the shocked gas. Higher velocity can be found for the shockwave propagation than in the case of the LSC wave as shown in Figure 1.7 b right. This implies that an accelerated propagation along the laser axis of the plasma with LSD. The consequence of laser absorption by the shocked gas is also a layer of gas with higher pressure, temperature and density than in the vapor behind the shocked gas layer. The shielding of laser radiation by the shocked gas leads to a vapor with lower pressure and temperature than in the case of the LSC wave as shown in Figure 1.7 c right and d right.

Transition between different LSAWs: effect of irradiance and wavelength

As mentioned above, transition between the different types of LSAWs is controlled by the role of the shocked gas in the absorption of laser radiation, while the absorption property of a given gas not only depends on the wavelength of the laser pulse as we discussed above, but also on its thermodynamic state determined by its interaction with the shockwave and the vapor. Such interaction critically depends on the initial energy of the vapor which is in turn determined by the laser pulse irradiance. The laser wavelength λ and laser irradiance I appear therefore as two pertinent parameters which provide a practical way to control the regimes of LSAW. In the thesis of Qianli Ma, we have studied the control by the laser wavelength [39]. One of the purposes of the present thesis is to study the effect of laser irradiance (fluence) on the propagation of the plasma. The control of the regime of LSAW by laser irradiance (laser fluence) represents therefore the interest of the present thesis. Figure 1.8 shows the characteristic velocities, pressures and temperatures that can be found in different regimes of LSAW [40]. By measuring these characteristic parameters as a function of laser irradiance, the irradiance ranges corresponding to each type of LSAW can be determined as shown in Figure 1.8 (a). It is important to remark that in Figure 1.8, the irradiance ranges determined for different LSAW regimes are associated to the wavelength of a CO_2 laser at 10.6 μm in the infrared and in the one-atmosphere air ambient. When the wavelength changes, with the absorption coefficient scaling roughly as λ^2 to λ^3, a correction factor has to be applied in order to find the good indication of the irradiance ranges for the different regimes of LSAW.

For typical LIBS applications, a Nd:YAG laser is used for ablation with an irradiance in the range of 10 GW/cm². If the fundamental at 1.064 µm is used, a correction factor can be apply on the irradiance scale of Figure 1.8 for a rough estimation of the irradiance ranges corresponding to the different LSAW regimes. Such estimation indicates that in a typical LIBS experiment, either LSC or LSD wave can be induced according to the detailed experimental parameters concerning the laser irradiance and wavelength as well as the background gas (nature and pressure). In the literature, LSD has been observed for a copper plasma induced by a 1064 nm pulse in an argon ambient gas with laser fluence and irradiance of 15 J/cm² and 7.3 GW/cm² respectively [53], such irradiance corresponds well to the range of irradiance for LSD excitation indicated in Figure 1.8 once the irradiance scale has been multiplied by a factor of between 100 and 1000.

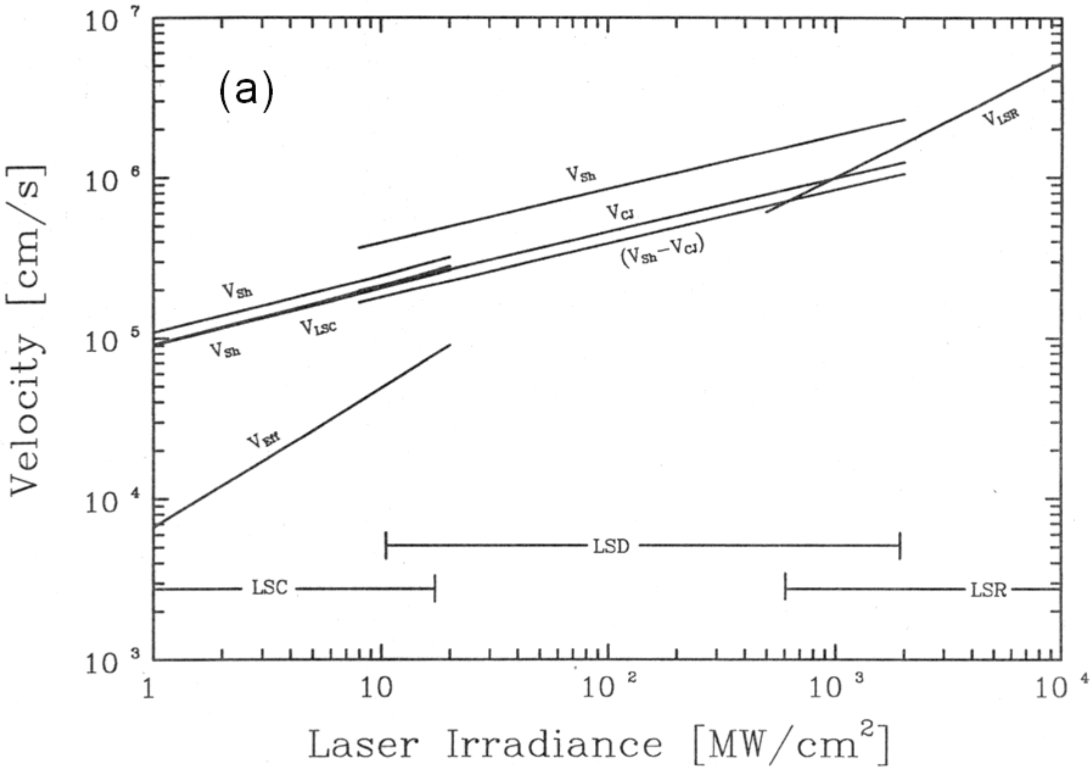

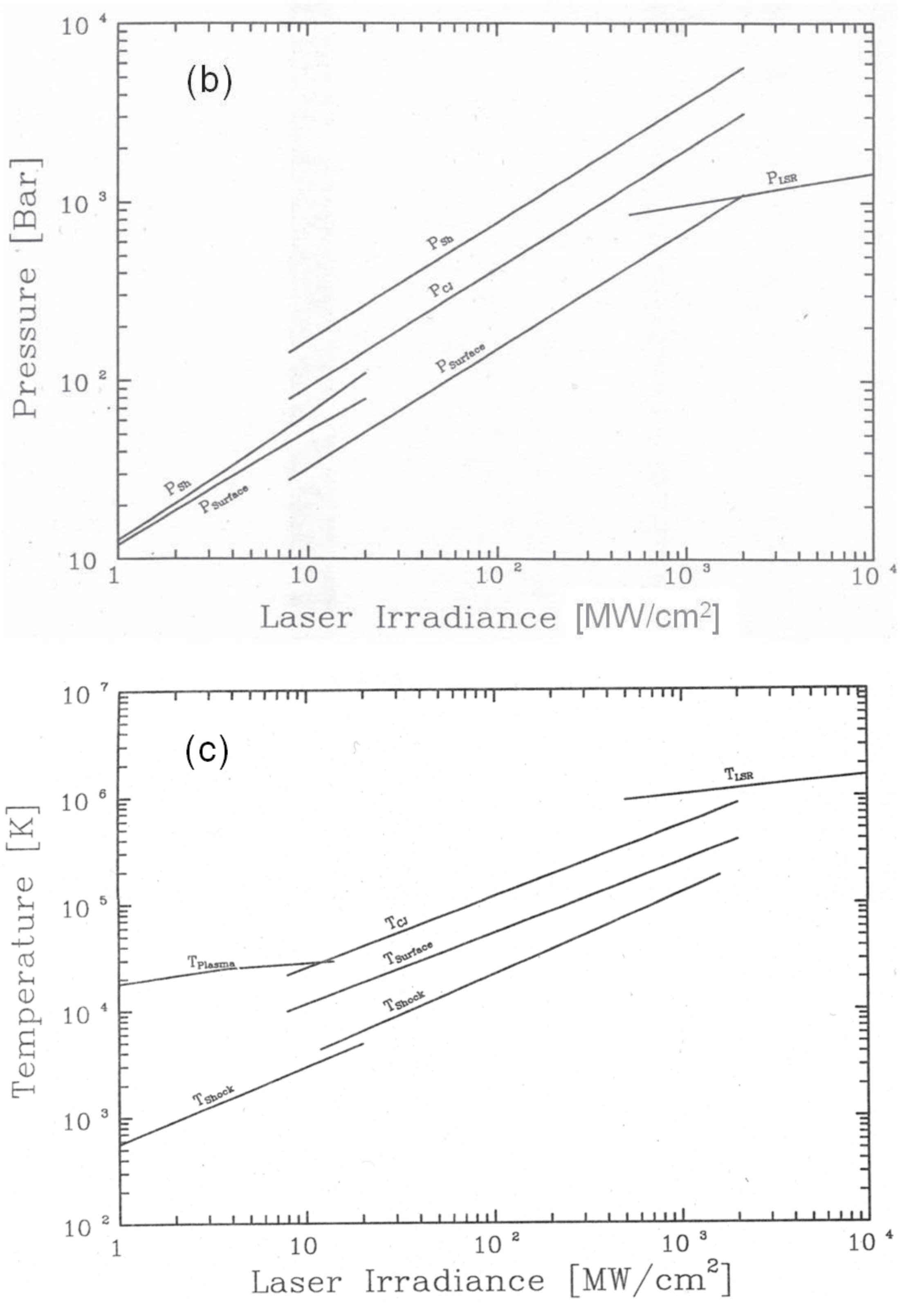

Figure 1.8 Characteristic parameters for plasma expansion into an ambient gas of atmospheric air as a function of the laser irradiance of a CO_2 laser at 10.6 μm. Different irradiance ranges for the three modes of LSAW are also indicated. Reproduced from the Ref. 40

Effect of the LSAW on the propagation of the plasma into the ambient gas

The propagation behavior of the plasma is sensitively influenced by LSAWs. For LIBS measurement which takes place at quite long delay after the post-ablation interaction, the most significant effect is related to the morphology of the plasma left by LSAW. This morphology includes the geometrical form of the plume, the profile of the electron density and the temperature, and the distribution of the different species in the plume. The morphology of the plume in the interval when the LIBS measurement is taken is determined in a large extent, by that just after LSAW, since after this no more energy is provided to the plume. As we can see from the above discussions, during LSAW, laser energy is supplied to the plume. However, in different types of LSAW, laser energy is absorbed in different region of the plume. In LSC, the absorption takes place in the central part of the plume, while in LSD it takes place in the front region of the plume. As consequence, LSC wave is expected to lead to a nearly spherical plume. On the other hand, LSD wave can lead to an elongated form of the plume due to the accelerated propagation of the shocked gas with an efficient absorption of laser energy. Correspondingly, the distributions of electron density, the temperature as well as the various species distribution in the plume can be also significantly changed in the different types of LSAW.

1.4. Elementary processes in a laser-induced plasma in an ambient gas

The two types of ambient gas commonly used for LIBS include atomic rare gas (Ar, He…) and diatomic molecular gas (atmospheric air for example). Different elemental processes can be involved in the interaction of the ambient gas with laser radiation. Atomic gas represents the simplest case where the following elementary processes and its reverse one can occur: excitation/radiative de-excitation, ionization/electronic capture. For molecular gas, the situation becomes more complicated. Besides the above mentioned processes, there can also be dissociation/recombination and reactions among the elements from the ambient gas as well as from the vapor. In this section, we summarize the elementary processes which can occur in a laser-induced plasma induced under an ambient gas.

1.4.1. *Excitation, ionization and their inverse processes*

Excitation corresponds to the transition to a higher energy level from a lower one for a particle (atom, ion or molecule) in the plasma. Excitation can be electronic, and for a molecule, it can be also vibrational or rotational. Ionization is a limiting case of electronic excitation, when a bound electron in an atom or an ion acquires sufficient energy to leave the atom or the ion and pass into the continuum. If sufficient energy is available, each of the elementary processes resulting in the excitation of electron in an atom or an ion can also result in ionization.

Elementary excitation and ionization processes can be divided into two categories: excitation or ionization caused by collision of the particle with other particles on the one hand, and photo processes, in which the role of one of the colliding particle is played by a photon. In the first category, we must distinguish between excitation and ionization by electron impact and excitation and ionization by inelastic collision with heavy particles; this distinction is necessary since the probability of each type of collision is very different. According to this classification, we can denote basic excitation and ionization processes in the following symbolic forms, where A and B denote heavy particles (atoms, ions or molecule), e the electron, and $h\nu$ the photon:

Excitations

$$A + e \rightleftharpoons A^* + e \tag{1-20}$$

$$A + B \rightleftharpoons A^* + B \tag{1-21}$$

$$A + h\nu \rightleftharpoons A^* \tag{1-22}$$

The reverse processes of the two first reactions represent deexcitation of excited atoms by so-called collision of the second type. And the reverse process of the third one represents the spontaneous emission of an excited atom.

And the corresponding ionization processes

$$A + e \rightleftharpoons A^+ + e + e \tag{1-23}$$

$$A + B \rightleftharpoons A^+ + B + e \tag{1-24}$$

$$A + h\nu \rightleftharpoons A^+ + e \tag{1-25}$$

The reverse processes of these three reactions, proceeding from right to left, result in recombination of electrons with ions: the two first correspond to recombination by three-body collision with the participation of an electron or a heavy particle as the third body. And the last reaction is the radiative capture of electron.

In a cascade process, atoms which are ionized may be not only those initially in the ground state. Excited atoms may further be ionized. So that to the list of the reactions (1-23), (1-24) and (1-25) we can add the following ones:

$$A^* + e \rightleftharpoons A^+ + e + e \tag{1-26}$$

$$A^* + B \rightleftharpoons A^+ + B + e \tag{1-27}$$

$$A^* + h\nu \rightleftharpoons A^+ + e \tag{1-28}$$

In a gas and especially a hot gas as laser-induced plasma irradiated by laser, the processes of all the three types mentioned above occur simultaneously. Usually the velocities of the heavy particles with comparable energies are approximately a hundred times smaller than the electron velocities (as the square root of the ratio of their masses). Therefore, processes of the type (1-24) and (1-27) in a high-temperature gas are important only if free electrons are practically absent. If the gas is “instantaneously” heated, as sometimes occuring, for example, during the passage of a strong shockwave, ionization by atomic or molecular collisions is of importance only for the formation of a small number of initial “priming” free electrons.

1.4.2. Dissociation and recombination

The dissociation of molecules and the recombination of atoms into molecules can be considered as two types of chemical reactions. Dissociation of diatomic molecules as a result of collisions of sufficiently energetic particles usually corresponds to the reaction

$$A_2 + M \rightleftharpoons A + A + M \tag{1-29}$$

or

$$AB + M \rightleftharpoons A + B + M$$

(1-30)

where M is any particle. In a homogeneous diatomic gas the particle M can be either the molecule A_2 (AB) or the atom A (B). The reverse process is the recombination of atoms as a result of three-body collision, where the third body M absorbs a portion of the binding energy released in the process.

There is a very small probability that a sufficiently strongly excited molecule will decompose directly into atoms:

$$A_2 \rightleftharpoons A + A$$

(1-31)

and these atoms will recombine into a molecule without the participation of a third body which could absorb a portion of the energy liberated during the reaction. The probabilities of photodissociation and of recombination with the emission of a photon are also very small. [54] Normally, the dissociation of molecule is an endothermic reaction requiring a definite amount of energy; and the recombination of atoms is exothermic reaction accompanied by the liberation of heat.

1.5. Decay, recombination and re-condensation of the plasma in an ambient gas

The quenching of a laser-induced plasma is at same time a very quick and quite long process. It is a very quick process, because the total lifetime of a plume does not exceed the millisecond scale. It is at same time a quite long process, because during the lifetime of the plume, its temperature drops from 10^4 K to the ambient one. Several stages can be distinguished during to the cooling of the plasma, which exhibits very different behaviors in the different stages of it damping. In this section, we summarize the different stages of decay of the plume by emphasizing the characteristic processes in each of the plume damping stages.

1.5.1. Decay of the radiative emission

Evolution of the emission spectrum

In short and intermediary delays after the impact of the laser pulse on the sample surface, typically from several nanoseconds to several microseconds, the plume is significantly ionized with a temperature in the range from 5×10^3 to 10^4 K. The plume is characterized by its optical emission. The spectrum of the emission evolves as the temperature of the plume decreases. Figure 1.9 shows the kinetic series of the spectrum emitted by a plasma induced by a 50 mJ laser pulse on the surface of an Al alloy sample placed in the atmospheric air. At short delay, there is a strong continuum emission. As the delay increases, the intensity of the continuum emission drops significantly as a result of the decay of the plasma. After a delay of 300 ns (Figure 1.9), the spectrum is dominated by spectral emission lines associated to the optical transitions between discrete states of different species, such as atoms and ions in the plasma. Spectrum narrowing was also observed with the increasing delay.

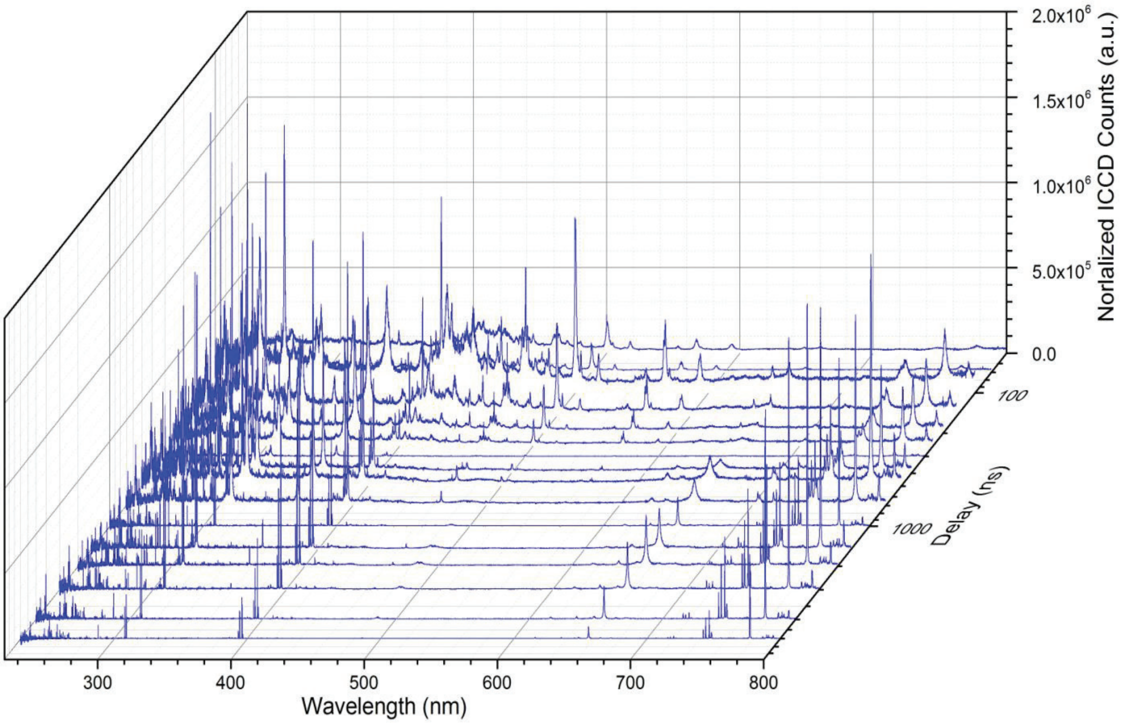

Figure 1.9 Kinetic series of spectrum emitted by plasma induced with a 50-mJ laser pulse on an aluminum target placed in the air.

LIBS operation

A LIBS measurement consists in recording the characteristic line emission from the plasma. In order to avoid the continuum emission which does not carry analytical information and can significantly increase the noise, a gated detection synchronized on the laser pulse is preferred as shown in Figure 1.10. Different delays can be chosen to optimize the detection of the different species in the plasma, ions at very short delay (up to 500 ns), atoms at intermediary delay (500 ns to several μs), and molecules at quite long delay (several to tens of μs).

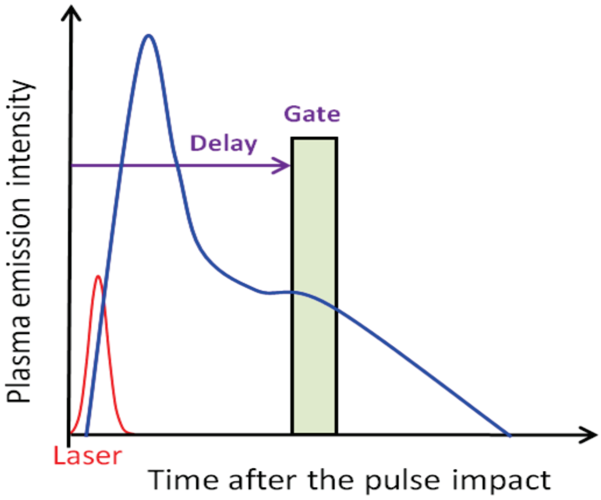

Figure 1.10 Schematic presentation of the time evolution of the plasma emission. The red curve corresponds to the profile of laser pulse. The blue curve represents the plasma emission intensity after the ablation as a function of time.

1.5.2. Recombination in the plume: molecule formation

Starting from an intermediary delay of several μs with the decrease of the temperature, recombination occurs in the plasma, leading to the formation of molecules and/or radicals. The recombination can occur between the elemental species evaporated from the target or with the contribution of the elements from the ambient gas. For the ablation of a metallic target in the atmospheric air, oxidation of metallic elements is a dominant process. Taking the example of ablation of an aluminum target, aluminum vapor, $Al(g)$, can react with either atomic or molecular oxygen to form aluminum monoxide AlO. The main path ways of oxidation have been identified as in Ref. 55.

$$Al(g) + O_2 \rightarrow AlO + O \tag{1-32}$$

$$Al(g) + O + M \rightarrow AlO + M \tag{1-33}$$

1.5.3. Re-condensation: deposition and crater formation

Beyond hundreds of microseconds, the temperature of the plume in general decreases below thousands of Kelvins and further recombination in the plume leads to the formation of clusters and nanoparticles of different nature. Taking again the example of ablation of an aluminum target under the atmospheric air, aluminum or aluminum oxide nanoparticles can be formed in the plume with various stoichiometries. Optical emission from the plume ceases and diagnostics with optical emission becomes inefficient. Other types of diagnostics, X-ray scattering for example, can be used to characterize the plume.

Re-condensed matter is finally transported far away from the target surface, if the initial departure velocity of the material is high enough, or is re-deposited over the area touched by the laser pulse or around this area if the departure velocity is small. The area of the target surface touched by laser pulse and the nearby region is modified by the impact of the laser pulse with material removing. This area is call laser crater. Notice however the re-condensation material can be found to be deposited either in the crater or in the region around the crater.

1.6. Resume

To sum up, in this chapter we have reviewed the main physical and chemical processes involved in laser ablation and evolution of the generated plasma. The overall process can be divided into several stages of laser ablation and generation of the plume, post ablation plasma-laser interaction, decay of the plasma, recombination in the plume and re-condensation of the ablated materials. In the different stages of plasma evolution, it exhibits different properties. For the LIBS technique, the plasma is interested in the interval of time when it efficiently emits optical emission. This period situates just after the post ablation interaction. It is the reason for which not only the ablation but also the propagation of the ablation vapor into the ambient gas is crucial for determining the property of the resulting plasma and sensitively influences the property of the plasma as a spectral emission source. The post ablation interaction between the plasma and the laser pulse depends obviously on the laser parameters, such as the wavelength and the fluence, and on the ambient gas. It is why in the present thesis we have performed a detailed investigation on the influence of these parameters on the property of the resulting plume. And the obtained results will be reported and discussed in the rest of the thesis.

Chapter 2. Plasma diagnostics with emission spectroscopy

Plasma diagnostic is considered as the basis of LIBS, because of most of the LIBS information comes from the emission lines of the plasma. In this chapter, we consider optical diagnostics of the plasma at local thermodynamic equilibrium (LTE). [56] The methods of determination of the electron density and the electron as well as molecule temperatures are presented in detail.

2.1. Temperature equilibrium in the plasma

2.1.1. Overview of the equilibrium relations in the plasma

When a plasma is in thermodynamic equilibrium (TE), the whole system composed by electrons, atoms, ions and radiation, can be fully described by statistical mechanics, where the equilibrium distributions are characterized by a same temperature [56], denoted as T. Such property is the consequence of the fact that each process is balanced by its reverse one, which is known as the principle of detailed balancing [57]. In this case, the electron velocity distribution has a Maxwellian form (Maxwell–Boltzmann distribution shown as Eq.(2-1)) characterized by the temperature of the system.

$$f(v) = \sqrt{\left(\frac{m}{2\pi k_B T}\right)^3} 4\pi v^2 e^{-\frac{mv^2}{2k_B T}}$$

(2-1)

where v is the particle speed, m is the particle mass, k_B is the Boltzmann constant and T is thermodynamic temperature.

Relative population of the excited level in an atom/ion, is described by the Boltzmann distribution [58, 59]

$$N_n = N \frac{g_n \exp\left(-E_n/k_B T\right)}{Z(T)}$$

(2-2)

where N_n , E_n and g_n are the population, the energy and the degeneracy of the quantum level n, N is the number density of the species involved, k_B is the Boltzmann constant, T and $Z(T)$ are the temperature and the partition function of the atomic system at such temperature.

The populations of the different ionization stages of a species, for example, neutral (N_{I}) and singly ionized ion (N_{II}) usually considered under the typical LIBS condition, are described by Saha-Eggert equation [59]

$$\frac{n_e N_{\mathrm{II}}}{N_{\mathrm{I}}} = 2\frac{Z_{\mathrm{II}}(T)}{Z_{\mathrm{I}}(T)}\left(\frac{m_e kT}{2\pi\hbar^2}\right)^{3/2} exp\left(-\frac{E_\infty - \Delta E}{k_B T}\right) \tag{2-3}$$

where n_e is the electron number density, m_e is the mass of the electron, E_∞ and ΔE are the first ionization energy for an isolated system and the correction of this quantity for interactions in the plasma, and $\hbar = h/2\pi$. h is the Planck constant.

Finally, the photon energy is described by the Planck function at temperature T, where the spectral energy density in the vacuum for a given polarization, is given by [59]

$$\varepsilon(\nu) = \frac{8\pi h\nu^3}{c^3(e^{h\nu/k_B T} - 1)} \tag{2-4}$$

or

$$\varepsilon(\lambda) = \frac{2hc^2}{\lambda^5(e^{hc/\lambda k_B T} - 1)} \tag{2-5}$$

where c is the speed of light.

2.1.2. Local thermodynamic equilibrium (LTE)

For most laboratory type laser-induced plasmas, the radiative energy is converted from other forms of energy, such as the kinetic and thermal energies of electrons or atoms. When photons escape from the plasma, their energy distribution deviates from the Planck law [60]. However, if the energy lost by radiation is much smaller than those involved in the other processes involving material species, the Saha–Boltzmann and Maxwell distributions are still a valid description of the system and a new state of equilibrium, namely LTE, is settled. In this case,

$$T_{\mathrm{exc}} = T_{\mathrm{e}} = T_{\mathrm{H}} \neq T_{\nu}$$

(2-6)

where T_{exc} is the excitation temperature, T_{e} and T_{H} are the temperatures of electrons and heavy particles, such as atoms and ions, and T_{ν} is the temperature describing the photon distribution. For a plasma with spatial gradient and transient behavior, the spatial and temporal variations are needed to be furthermore enough small for the LTE to be established. In this case, the plasma is called quasi-stationary and characterized by local values of temperature and electron density [59, 61].

2.1.3. Criteria for evaluating the validity of LTE

McWhirter Criterion

For homogenous and stationary plasma, the most used criterion for LTE is the McWhirter LTE condition:

$$n_e(cm^{-3}) > 1.6 \times 10^{12} T_e^{0.5} \Delta E_{ki}^3$$

(2-7)

where ΔE_{ki} is the gap of adjacent levels. For validation of LTE, the electron density has to fulfill the Eq. (2-7) for the largest ΔE_{ki} involved in the system. It usually corresponds to the energy differences between the ground state and the first excited state of an atom (or an ion). However, the McWhirter criterion is a necessary but not sufficient condition for LTE, even in the approximation of stationary and homogenous plasma.

Additional requirement for evaluating the validity of the LTE

Because laser-induced plasma is transient and inhomogeneous, even if the McWhirter criterion is fulfilled, it must also fulfill other conditions to ensure the LTE.

A first additional requirement is that the relaxation time τ_{rel} of a plasma for the establishment of the thermodynamic equilibrium must be shorter than the time of variation of thermodynamic parameters of the plasma, such as the temperature or the electron density: [56]

$$\frac{T(t+\tau_{rel})-T(t)}{T(t)} \ll 1 \quad \text{and} \quad \frac{n_e(t+\tau_{rel})-n_e(t)}{n_e(t)} \ll 1$$

(2-8)

In order to check the criterion expressed in Eq. (2-8), the thermodynamic relaxation time τ_{rel} has to be estimated. If the Eq. (2-8) is always valid during the evolution of the plasma, it can pass through different thermodynamic states in LTE with different temperatures. Within these different equilibrium states, the τ_{rel} between the fundamental and the first excited level is in general longest and can be estimated [58, 62] by Eq.(2-9):

$$\tau_{rel} \approx \frac{1}{n_e\langle\sigma_{12}v\rangle} = \frac{6{,}3\times10^4}{n_e f_{12}\langle\bar{G}\rangle}\Delta E_{21}T_e^{0,5}\exp\left(\frac{\Delta E_{21}}{T_e}\right)$$

(2-9)

where $\langle\bar{G}\rangle$ is the Gaunt factor and f_{12} is the spectroscopic oscillator length.

The second additional requirement is, in space domain, that the variation length of temperature and electron density should be larger than the distance traveled by a particle due to diffusion during relaxation time τ_{rel}.[56] The diffusion length can be estimated by Eq.(2-10) [62]:

$$L_{dif} \approx \sqrt{D_{dif}\times\tau_{rel}} = 1{,}4\times10^{12}\frac{T_e^{0,75}}{n_e}\left(\frac{\Delta E_{21}}{\mathrm{M_{mol}}f_{12}\langle\bar{G}\rangle}\right)^{0,5}\exp\left(\frac{\Delta E_{21}}{2T_e}\right)$$

(2-10)

To make the LTE conditions valid, the relationships for temperature and the electron density should be established:

$$\frac{T(x+L_{dif})-T(x)}{T(x)} \ll 1 \text{ and } \frac{n_e(x+L_{dif})-n_e(x)}{n_e(x)} \ll 1$$

(2-11)

For the estimation of time and spatial relaxation, Eq. (2-9) and Eq. (2-10) are deduced for completely ionized plasma. Because LIBS plasma is usually partially ionized, there is a multiplying factor to be applied.

$$\tau_{rel}^{partial\ ionezed} = \frac{n_{II}}{n_I+n_{II}}\tau_{rel} \quad \text{and} \quad L_{dif}^{partial\ ionezed} = \sqrt{\frac{n_{II}}{n_I+n_{II}}}L_{dif}$$

(2-12)

where n_I and n_{II} are the number density of atoms and ions respectively.

In general, for Eq. (2-11), the variation length of the temperature and the electron density should be at least 10 times larger than the distance traveled by a particle with the diffusion length of L_{dif}:

$$\frac{T(x)}{\mathrm{d}T(x)/\mathrm{d}x} > 10L_{dif}$$

(2-13)

Using the McWhirter criterion and the two above discussed additional requirements, we can check the existence of the LTE in laser-induced plasma.

Application of the LTE criteria in our experimental conditions

With the three above criteria, we can check the LTE condition for the experimental conditions encountered this work. Table 2-1 shows the results of the check of the validation of the LTE condition with the experimental parameters used in this thesis. The results confirm in detail the validation of the LTE for the plasmas generated in this work.

Table 2-1 Plasma parameters typically found in our experiments and check of the validity of the LTE for an Al plasma induced in Ar with different ablation energies used in this thesis. (Delay: Experimental delay; T: Electron temperature determined by experimental spectrum; V: validity, the letter O means the criterion condition is satisfied); NO mead nearly satisfied.

Criterion	Ablation laser energy (mJ)	Delay (ns)	T (K)					V
McWhirter				Electron density				
				Experimental value (cm^{-2})	McWhirter value for Al II (cm^{-2})	McWhirter value for Ar I (cm^{-2})		
	20	350	13000	1.20×10^{18}	7.39×10^{16}	2.81×10^{17}		O
		1500	11000	2.0×10^{17}	6.80×10^{16}	2.58×10^{17}		NO
	50	500	13000	1.2×10^{18}	7.39×10^{16}	2.81×10^{17}		O
		2000	12000	3.0×10^{17}	7.10×10^{16}	2.70×10^{17}		O
Time variation				Relaxation time(s)		Requirement (s)		
				Al I	Ar I	For N_e	For T_e	
	20	350	13000	6.18×10^{-11}	3.96×10^{-14}	1.00×10^{-7}	1.30×10^{-6}	O
		1500	11000	5.67×10^{-10}	3.64×10^{-13}	1.64×10^{-8}	1.10×10^{-6}	O
	50	500	13000	6.18×10^{-11}	3.96×10^{-14}	1.00×10^{-7}	1.30×10^{-6}	O
		2000	12000	3.00×10^{-10}	1.92×10^{-13}	2.50×10^{-8}	1.20×10^{-6}	O

				Diffusion length (mm)		Requirement (mm)		
				Al I	Ar I	For N_e	For T_e	
Space inhomogeneity	20	350	13000	1.16×10^{-4}	6.25×10^{-4}	0.08	0.52	O
		1500	11000	4.70×10^{-4}	1.22×10^{-3}	1.33	0.44	O
	50	500	13000	1.16×10^{-4}	6.25×10^{-4}	0.08	0.52	O
		2000	12000	3.83×10^{-4}	1.43×10^{-3}	0.02	0.48	O

2.2. Determination of the electron density

The different spectral line broadening mechanisms need to be understood in order to correctly extract the electronic density from spectral broadening. Each of them has a particular influence on the spectral line. Some are represented by the Gaussian profile and others the Lorentzian one. This will be explained in more detail below followed by a presentation of the electron density determination method.

2.2.1. Broadening mechanisms of an emission line in plasma

Natural line broadening

The uncertainty principle relates the lifetime of an excited state (due to the spontaneous radiative decay) and the uncertainty of its energy. A short lifetime corresponds to a large energy uncertainty and a broad emission. This broadening effect results in a Lorentzian profile without shift with a line width of $\Delta\lambda_N$ [63]:

$$\Delta\lambda_N = 2\pi c/(\frac{1}{\Delta t_k} - \frac{1}{\Delta t_i}) \tag{2-14}$$

where Δt_k and Δt_i corresponds respectively to the lifetimes of the up and the lower states of a transition.

This value of $\Delta\lambda_N$ in the spectral range around 300 nm is of the order of 5×10^{-5} nm. Such broadening can be neglected for an emission spectrum from laser-induced plasma.

Doppler broadening

Doppler broadening is due to the Doppler effect caused by a distribution of velocity of atoms, ions or molecules. Different velocities of the emitting particles result in different

Doppler shifts, the cumulative effect of which is the associated line broadening. [64] For a gas in thermal equilibrium, a particle in motion is considered to have Maxwellian velocity distribution, which results in a Gaussian spectral profile. In this case, the broadening depends only on the frequency of the spectral line, the mass of the emitting particles, and their temperature. The FWHM of the profile is given by

$$\Delta\lambda_D = 7.16 \times 10^{-14}\lambda\sqrt{(T/M)} \tag{2-15}$$

Where T and M are the emitters kinetic temperature (in Kelvin) and mass (in a.m.u.), and λ is the central wavelength of the line.

For the spectral range frequently used in LIBS, Doppler broadening is not the main line broadening mechanism. If an extremely high plasma temperature is considered (10^5 K), the corresponding Doppler broadening for the visible range is only 0.01 nm. This is negligible compared to actual spectral line widths.

Van der Waals broadening

Van der Waals broadening occurs when the emitting particle is being perturbed by van der Waals force. The energy shift as a function of distance is given by the Lennard-Jones potential ($\Delta E \sim 1/r^6$). For a collision between Ar atoms, in a temperature about 7000 K and N_a (atom density)$= 10^{18}$ cm^{-3}, the broadening width (FWHM) is about 0.00356 nm for a central wavelength of 810 nm. It could also be negligible in LIBS.

Stark broadening

The Stark broadening is due to the perturbation of the two levels of a heavy particle (ion or atom) involved in a radiative transition, during its collision with a charged particle. Therefore, it depends on both the atomic structure and its environment. Inside a plasma, there are two types of charge particles: ions, whose effects can be considered with the quasi-static approximation, and electrons, whose effects can be considered with the approximation of collision impact [65]. In typical LIBS conditions, the broadening due to ions can be negligible with respect to that of due to electrons [66]. We consider then the Stark broadening of an emission line (atomic or ionic) can be determined if the electron density in a plasma is known.

According to the electronic configuration of an atom or an ion, two cases can be distinguished to establish simple relationship between Stark broadening $\Delta\lambda_{Stark}$ and electron density n_e. The first case corresponds to a hydrogen or hydrogen-like ion where the excited level, E_n ($n \geq 2$), is degenerated with respect to the angular quantum number *l*. The Starke effect exhibits in this case a linear dependence on the electric field strength. [67].

Considering the effects of the all surrounding perturbers, the line broadening profile $\Delta\lambda_{Stark}$ (Stark broadening) of the hydrogen Balmer α line at 656,3 nm (H_α) is given by [63, 68]:

$$\Delta\lambda_{Stark} = w_{Stark,H}\left(\frac{n_e}{n_{ref,H}}\right)^{\frac{2}{3}}$$

(2-16)

Where $w_{Stark,H}$ is the electron impact parameter of the H_α [63], $n_{ref,H}$ is a reference density which is set to 10^{17} cm^{-3} in the database of Griem [63] and n_e is the electron density of plasma in cm^{-3}. For example for the H_α line at the electron density of 2×10^{17} cm^{-3}, the $\Delta\lambda_{Stark}$ is about 0.878 nm.

The second case is more general and applies to all other types of atoms and ions. The Stark broadening is proportional to F^2 (F is the perturbing electric field) and thus it is called the quadratic Stark effect. [68] In general, it is much weaker (often an order of magnitude smaller) than the linear Stark effect discussed above. In this case, the emission line is disturbed not only by the effect of Stark broadening but also by the effect of Stark shift D_{Stark} (the shift of the center wavelength). The normalized spectral profile $L_n(v)$ of a transition can be represented by the Lorentz profile with an FWHM $\Delta\lambda_{Stark}$ and a center at $\lambda_0 + D_{Stark}$:

$$L_n(v) = \frac{\Delta\lambda_{Stark}}{2\pi}\frac{1}{(\lambda-\lambda_0-D_{Stark})^2+(\Delta\lambda_{Stark}/2)^2}$$

(2-17)

$$\Delta\lambda_{Stark} = 2w_e\left[1+1{,}75A\left(1-B\times N_D^{-\frac{1}{3}}\right)\right]\left(\frac{n_e}{n_{ref}}\right)$$

(2-18)

$$D_{Stark} = w_e\left[\frac{d_e}{w_e}\pm 2A\left(1-B\times N_D^{-\frac{1}{3}}\right)\right]\left(\frac{n_e}{n_{ref}}\right)$$

(2-19)

where λ_0 is the central wavelength at vacuum, n_{ref} is the reference electron density, with a value of 10^{16} cm^{-3} for an atomic line and 10^{17} cm^{-3} for an ion line[63]. w_e and $d_e$are the parameters of electronic impact broadening and shift for a given temperature. Their numerical values can be found in Ref. 63 for most usually used emission lines. B is equal to 0.75 for a neutral line and 1.2 for an ionized one. N_D is the number of particles in the Debye sphere [65] and A is ionized broadening parameter which can be negligible because of its small value within LIBS experimental conditions. For example, for Ar I 696.5 nm line, A is equal to 0.0844 [69]. For an ionic line, it is equal to 0. Therefore, in typical LIBS conditions, the contribution due to ions can be neglected for most atomic lines.

Instrumental broadening

Observed spectral line shape and line width are also affected by instrumental factors. The observed line shape is a convolution of the intrinsic line shape with the instrument transfer function.[70] The standard procedure to determine the apparatus profile of a spectrometer is to scan over a line with intrinsic width very small compared to that of the apparatus. The instrumental line shape of a spectrometer is often approximately Gaussian profiles. We have used two spectrometers in this work. We have used a lamp with narrow lines to obtain the instrumental broadening in our experiments. The results indicated that the Mechelle 5000 Echelle spectrometer (Andor Technology) has a resolution power of 4005 ($\lambda/\Delta\lambda$ FWHM) [39]. The other spectrometer is a Czerny-Tuner spectrometer with an instrumental line broadening of $\Delta\lambda = 0.27$ nm (FWHM).

Self-absorption

Self-absorption can lead to distorting and especially broadening of emission lines and therefore it can produce an apparently larger line width. If the self-absorption originates mostly from the cooler boundary layer with lower electron density and if the spectral resolution of the used spectrometer is high enough, the line center exhibits self-reversal. But more often, self-absorption only slightly distorts the shape of a line profile [71]. Thus, it is very difficult to judge the amount of self-absorption from the observed shape of a line.

Electron density determination with Stark broadening

In typical LIBS conditions ($T \sim 1$ eV et $n_e \sim 10^{17}$ cm^{-3}), the above mentioned three first types of broadenings are negligible compared to the Stark broadening. Self-absorption can often be avoided by using lines from minor or trace elements or from the ambient gas. In such case, the line broadening is mainly due to Stark broadening and instrumental broadening. Such consideration can lead to the determination of the electron density in the plasma.

In order to determine the electron density, we can choose a proper line profile to fit experimental spectrum with the consideration of Lorentzian profile ($L(\lambda)$) for Stark broadening and Gaussian profile ($G(\lambda)$) for instrumental broadening. The last becomes especially important at long delay when the electron density becomes low. Accordingly, we used a Voigt profile ($V(\lambda)$) with the convolution of a Lorentzian and a Guassian profiles:

$$V(\lambda) = G(\lambda, \Delta\lambda_{ins}) \otimes L(\lambda, \Delta\lambda_{Stark}) \tag{2-20}$$

to fit experimental spectral lines and to extract the corresponding Stark broadening. The electron density is then determined with the help of needed spectral broadening parameters.

2.3. Determination of the temperatures in the plasma

The temperature, which can be considered as one of the most important parameters characterizing the plasma, can be determined by emission spectroscopy. A high electron density plasma allows generally assuming LTE to be realized and to valid the use of Boltzmann and Saha equations [72]. However, as we have discussed in Chapter 1, as the delay increases, the plasma cools down in the plasma, the LTE will not be satisfied. In addition, chemical reactions can happen in the plasma with the contribution of the species from the ambient gas, leading to change of the stoichiometry of the plasma. Therefore, in an intermediary delay interval, when the plasma is hot enough and the LTE condition is satisfied, the electron temperature can be deduced using Boltzmann equation, Saha equation or the combination of the both. For longer delay, when the emission from molecules becomes dominant in the emission spectrum, we can determine the molecular temperature by fitting experimental spectrum with a theoretical one.

2.3.1. Electron temperature

Boltzmann plot

For plasma in LTE, the population in different energy levels of an atom or an ion is given by the Boltzmann distribution law [72]

$$\frac{n_j^Z}{n^Z} = \frac{g_j^Z}{U^Z(T)} \exp\left(-\frac{E_j^Z}{k_B T}\right)$$

(2-21)

where Z corresponds the ionization stage of the species (Z=0 and 1 refer to the neutral and singly ionized atoms respectively), n_j^Z , E_j^Z and g_j^Z are the population, energy and degeneracy of the upper energy level j respectively, n^Z is the number density of the atom or the ion and $U^Z(T)$ is the partition function of the species in ionization stage Z at temperature T,

$$U^Z(T) = \sum_j g_j \, e^{-E_j/k_B T}$$

(2-22)

k_B is the Boltzmann constant and T is the plasma temperature. The intensity I^Z of an emission line due to the transition between the upper energy level j and the lower energy level i of a species in the ionization stage Z is given by

$$I^Z = \frac{hc}{4\pi\lambda_{ij}^Z} A_{ij}^Z n_j^Z L$$

(2-23)

where h is the Planck constant, c is the speed of light, L is the length of the integrated path, $A_{ij,Z}$ is the transition probability and λ_{ij}^Z is the transition line wavelength. Using Eq. (2-21) and Eq. (2-22)we can get

$$I^Z = \frac{hc}{4\pi\lambda_{ij}^Z} A_{ij}^Z L \frac{n^Z}{U^Z(T)} g_j^Z \exp\left(-\frac{E_j^Z}{k_B T}\right)$$

(2-24)

By taking the natural logarithm of Eq. (2-24), we get

$$\ln\left(\frac{I^Z\lambda_{ij}^Z}{g_j^Z A_{ij}^Z}\right) = -\frac{1}{k_B T}E_j^Z + \ln\left[\frac{hcLn^Z}{4\pi U^Z(T)}\right]$$

(2-25)

This equation can lead to the so called Boltzmann plot, when, for several emission lines, the quantity in the left side of the equation is plotted as a function of the energy of the upper level of the transition. The value of electron temperature T is deduced from the slope of the plot.

Saha-Boltzmann plot

For plasma in LTE, the excitation temperature is the same as the ionization temperature. The former determines the populations in the atomic (and ionic) energy levels (Boltzmann equation) and the latter determines the population distribution of the same element in the different ionization stages (Saha equation). In the case of the neutral and singly ionized species of the same element, the Saha equation can be written as

$$n_e \frac{n^{\mathrm{II}}}{n^{\mathrm{I}}} = \frac{2\pi m_e k_B T^{3/2}}{h^3}\frac{2U^{\mathrm{II}}}{U^{\mathrm{I}}} e^{-\frac{E_{ion}}{k_B T}}$$

(2-26)

where n_e is the plasma electron density, n^{I} and n^{II} are the number densities of the neutral atomic species and the singly ionized species, respectively, E_{ion} is the ionization potential of the neutral species in its ground state and m_e is the electron mass.

By considering two lines λ_{ij} and λ_{mn} of the same species, characterized by different values of the upper level energy ($E_j \neq E_n$), because emission lines from different ionization stages are usually present in a laser-induced plasma, a combination of the Saha ionization and Boltzmann excitation distributions can be used to measure the electron temperature. The most common form of the coupled Saha-Boltzmann equation takes the form of the ratio between ionic and atomic emission intensities [73]

$$\frac{I_{ij}^{\mathrm{II}}}{I_{mn}^{\mathrm{I}}} = \left(\frac{A_{ij}^{\mathrm{II}} g_j^{\mathrm{II}} \lambda_{mn}^{\mathrm{I}}}{A_{mn}^{\mathrm{I}} g_n^{\mathrm{I}} \lambda_{ij}^{\mathrm{II}}}\right)\left(\frac{2(2\pi m_e k_B T)^{3/2}}{n_e h^3}\right) e^{-\frac{\left(E_{ion}-\Delta E_{ion}+E_j^{\mathrm{II}}-E_n^{\mathrm{I}}\right)}{k_B T}}$$

(2-27)

In the above equation, the superscripts I and II indicate atomic and ionic species respectively. E_{ion} is the first ionization potential and ΔE_{ion} is a correction parameter due to the fact that in a plasma the presence of charged particles lowers the ionization potential.

By inserting the Boltzmann equation in to Eq. (2-27) and taking the natural logarithm, we get:

$$\ln\left(\frac{I_{ij}^{\mathrm{II}}\lambda_{ij}^{\mathrm{II}}A_{mn}^{\mathrm{I}}g_{n}^{\mathrm{I}}}{I_{mn}^{\mathrm{I}}\lambda_{mn}^{\mathrm{I}}A_{ij}^{\mathrm{II}}g_{j}^{\mathrm{II}}}\right)=\ln\left(\frac{2(2\pi m_e k_B T)^{3/2}}{n_e h^3}\right)-\frac{\left(E_{ion}-\Delta E_{ion}+E_j^{\mathrm{II}}-E_n^{\mathrm{I}}\right)}{k_B T} \tag{2-28}$$

It has to be noted that, unlike the Boltzmann plot, it is required the electron density to be measured independently for determining the temperature with Saha-Boltzmann plot.

Multi Saha-Boltzmann plot

In order to precisely determine the electron temperature in the plasma, J. A. Aguilera et al. [74] have proposed the multi-Saha-Boltzmann plot to deduce the electron temperature with the use of lines (neutrals and ions) of different elements with known concentrations present in the target, under the assumption of the conservation of the stoichiometry between the ablated vapor and the target. In this work, we take the most of spectra from a target of certificated aluminum with known elemental concentrations, the multi-Saha-Boltzmann plot was therefore used to determine the electron temperature. This method increases the accuracy of the temperature determination because the use of lines of different atomic and ionic species increases the energy gap between the used levels [74].

Theoretical description of the multi-Saha-Boltzmann plot

For a plasma in LTE with the optically thin condition, the spatially path-integrated line intensity I^z for an element with an ionization degree of z can be expressed as [63]

$$\ln\left(\frac{I^Z\lambda_{ij}}{A_{ij}g_j}\right)^{*}=-\frac{1}{k_B T}E_j^{Z^*}+\ln\left(\frac{hcN^0}{U^0(T)}\right) \tag{2-29}$$

where N^0 is the number density of the neutral atoms and $Q^0(T)$ the partition function for neutral atoms. The superscript $*$ indicates that the expression for the emissivity of ionic lines must be modified according to

$$\ln\left(\frac{I^{Z}\lambda_{ij}}{A_{ij}g_{j}}\right)^{*} = \ln\left(\frac{I^{Z}\lambda_{ij}}{A_{ij}g_{j}}\right) - B^{Z}(T,N_{e})$$

(2-30)

where

$$B^{Z}(T,N_{e}) = Z\ln\left[2\left(\frac{m_{e}k_{B}}{2\pi\hbar^{2}}\right)^{3/2}\right]\frac{T^{3/2}}{n_{e}}$$

(2-31)

and

$$E_{j}^{Z^{*}} = E_{j}^{Z} + \sum_{k=0}^{Z-1}\left(E_{\infty}^{k} - \Delta E_{\infty}^{k}\right)$$

(2-32)

In these expressions, m_e is the electron mass, n_e is the electron number density and E_{∞}^{k} is the ionization potential of ionic species z, which is corrected by the corresponding plasma reduction of ionization energy $\Delta E_{\infty}^{k}(j)$.

In the usual LIBS condition, the population of ionic species with ionization degree larger than 1 can be neglect, therefore, for an element, the total number density N_α can be approximately expressed as the sum of the concentrations of the neutrals and the singly ionized species:

$$N_{\alpha} = N_{\alpha}^{0} + N_{\alpha}^{1}$$

(2-33)

The neutral atom number density can be related to the total number density for a given element by

$$N_{\alpha}^{0} = \frac{N_{\alpha}}{1 + S_{\alpha}^{10}}$$

(2-34)

where S_{α}^{10} is the number density ratio of the ionic species to the corresponding neutral one. Such ratio can be determined using the Saha equation

$$S_{\alpha}^{10} = \frac{N_{\alpha}^{1}}{N_{\alpha}^{0}} = \frac{2Q_{\alpha}^{1}(T)}{N_{e}Q_{\alpha}^{0}(T)}\left(\frac{m_{e}k_{B}T}{2\pi\hbar^{2}}\right)^{3/2}\exp\left(-\frac{E_{\infty,\alpha}^{k} - \Delta E_{\infty}^{k}}{k_{B}T}\right)$$

(2-35)

which as mentioned before, depends on the partition functions $Q_\alpha^z(T)$ of the element for its ionization degrees $z = 0$ and $z = 1$, and on the ionization potential $E_{\infty,\alpha}^0$ of the element. If stoichiometry of the plasma is conserved, the elemental concentrations in the sample, C_α (%) are assumed to be maintained for the elemental number densities in the plasma, and then

$$N_\alpha = C_\alpha N \tag{2-36}$$

where N is the total number density of the plasma including the number densities of neutral atoms and first ions of all the elements in the plasma.

By using the Eqs. (2-34) and (2-36), the Saha-Boltzmann Eq. (2-29) can be rewritten to a similar shape for the line intensities from different elements as

$$\ln\left(\frac{I_\alpha^Z \lambda_{ij}}{A_{ij} g_j}\right)^* = -\frac{1}{k_B T} E_{j,\alpha}^{Z^*} + \ln(hcN) \tag{2-37}$$

where

$$\ln\left(\frac{I_\alpha^Z \lambda_{ij}}{A_{ij} g_j}\right)^* = \ln\left(\frac{I_\alpha^Z \lambda_{ij}}{A_{ij} g_j}\right) - B^z(T, N_e) - D_\alpha(T, N_e) \tag{2-38}$$

$$D_\alpha(T, N_e) = \ln\left(\frac{C_\alpha}{100} \frac{1}{Q_\alpha^0(T)(1 + S_\alpha^{10})}\right) \tag{2-39}$$

where $D_\alpha(T, N_e)$ depends on elements and has the same form for the two ionization degrees considered in this work. Also, the energy of the upper level of the transition for ionic lines must be corrected by adding the ionization energy of the corresponding element according to

$$E_{j,\alpha}^{Z^*} = E_{j,\alpha}^Z + Z E_{\infty,\alpha}^0 \tag{2-40}$$

Therefore, we can construct the Saha-Boltzmann plot in which the data of all the elements contained in the target may be fitted by a single straight line called multi-Saha-Boltzmann plot. The larger number of experimental intensities included in such plot allows a more precise determination of the temperature.

2.3.2. Determination of the molecular temperature by fitting molecular emission spectrum

In most of the cases in LIBS molecular emission is expected from a plasma with long delay of detection, since molecules and radicals are generated through recombination when the temperature decreases in the plasma. For ablation of an Al target in air for example, molecular emission bands from AlO can be easily observed in the visible spectral range. These bands can often be used for the determination of the molecular temperatures. Figure 2.1 shows the details of the rovibrational energy levels involved in emission of a diatomic molecule.

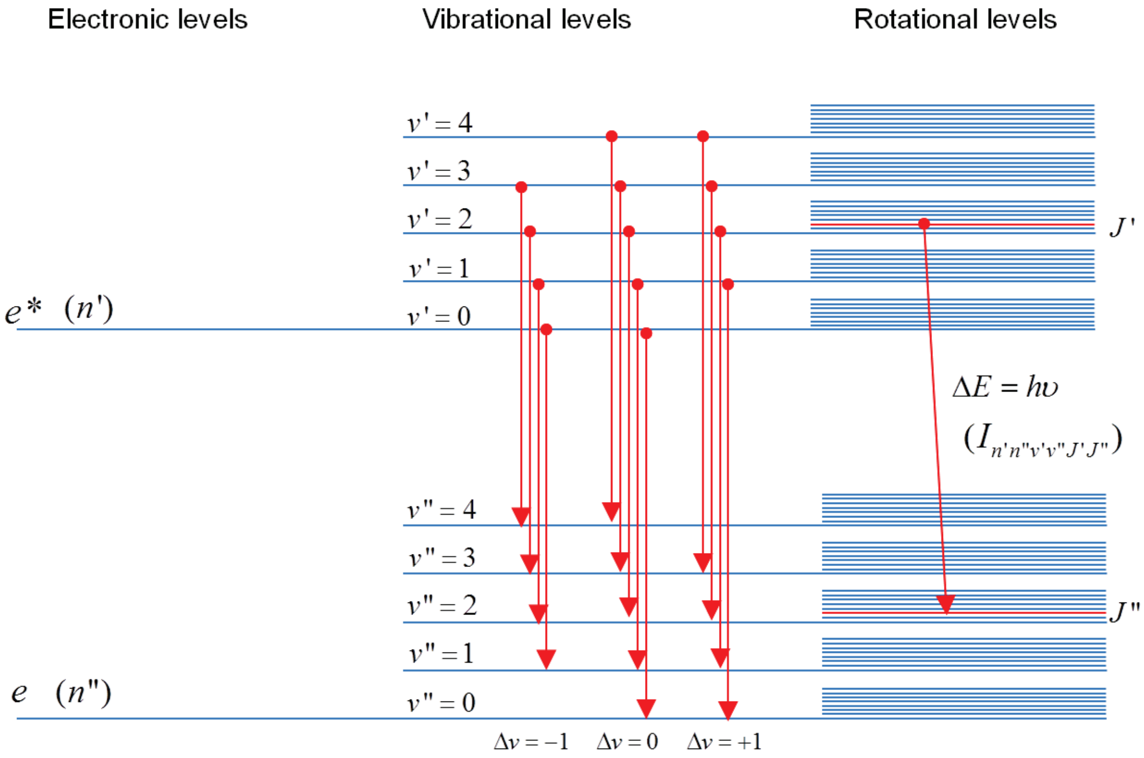

Figure 2.1 Rovibrational energy levels involved in a molecular emission.

In our experiments, to determine the temperature of the plume at long delays beyond several µs, the AlO molecular $B^2\Sigma^+ - X^2\Sigma^+$emission bands were simulated with a synthetic spectrum. We consider that the emission intensity associated to a rovibrational transition of a diatomic molecule, $I_{n'n''v'v''J'J''}$, can be expressed in the following form [75]:

$$I_{n'n''v'v''J'J''} = C_{em} \frac{S_{v'v''} S_{J'J''}}{Q_{rot} v'} \nu^4_{J'J''} \times e^{-F'(J')hc/k_B T_{rot}} \times e^{-G_0(v')hc/k_B T_{vib}} \tag{2-41}$$

where n', n'' are the principal quantum numbers of the up and low states respectively, v', v'' the vibrational quantum numbers, J', J'' the rotational quantum numbers. C_{em} refers to the emission constant. The vibrational band strength, $S_{v'v''}$, is given by [77]:

$$S_{v'v''} = R_e(\bar{r}_{v'v''})q_{v',v''}$$

(2-42)

where $R_e(\bar{r}_{v'v''})$ is the magnitude of the electronic transition moment function and $q_{v'v''}$ is the Frank-Condon factor. $S_{J'J''}$ is the rotational line strength, also known as Hönl-London factor [78]. Q_{rot} is the rotational partition function. $\nu_{J'J''}$ is the transition wavenumber with the corresponding R,P,Q expression [75]. In the two exponentials, the rotational term, $F_v(J)$, is given by [75]

$$F_v(J) = B_v J(J+1) - D_v J^2(J+1)^2$$

(2-43)

where the rotational constants B_v and the centrifugal distortion constant D_v can be found in the literature [79]. The vibrational term,G_0, can be expressed as [75]

$$G_0(\nu) = G(\nu) - G_0(0)$$

(2-44)

with

$$G(\nu) = \omega_e\left(\nu + \frac{1}{2}\right) - \omega_e x_e(\nu + \frac{1}{2})^2 + \cdots$$

(2-45)

Eq. (2-41) involves also a number of constants such as h the Planck constant, c the speed of light in the vacuum and k_B the Boltzmann constant.

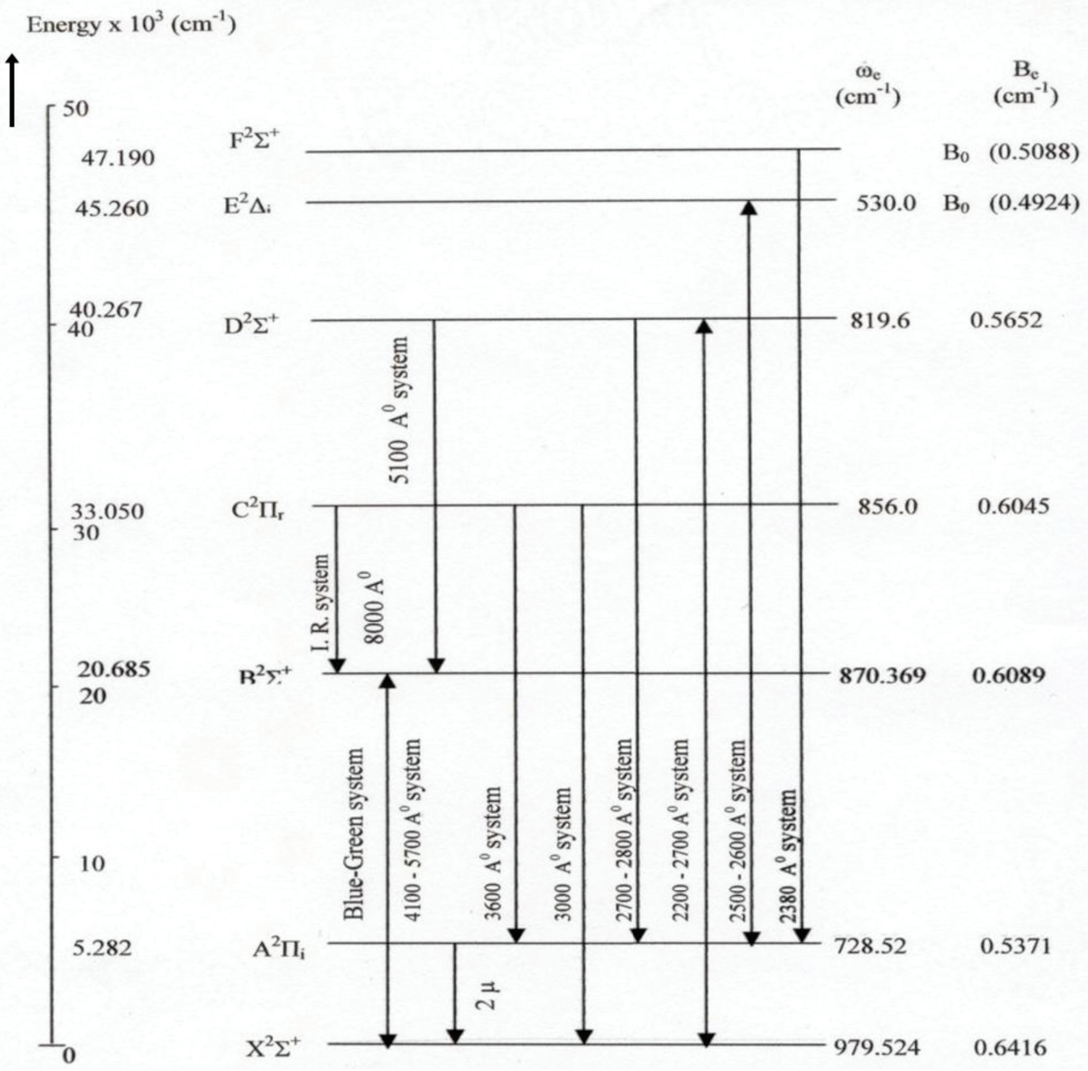

Figure 2.2 **Energy level diagram of AlO molecule [76]**

When the needed spectroscopic constants are known for a given molecular band system, a synthetic spectrum can be calculated as a function of T_{rot} and T_{vib}, which are respectively the rotational and vibrational temperatures. The fitting of the synthetic spectrum to the experimental one can thus allow extracting the two temperatures.

In a laser-induced plasma, and especially for the $B^2\Sigma^+$ state of the AlO molecule however, a number of authors observed internal equilibrium between the vibrational and the rotational modes [80-83]. The temperature $T_{vib} = T_{rot}$ is thus taken as the molecular temperature, T_{mol}, in the plasma, even though the LTE condition is no longer fulfilled at such long delays [84]. The fitting of the synthetic spectrum to the experimental one leads therefore to an unique temperature, which is defined as the molecule temperature, T_{mol} in our work. Another approximation that we have taken is due to the relative high temperature in the plume. This allows expressing the rotational partition function in the form of [75]

$$Q_{rot} \approx k_B T_{rot}/hcB'$$

(2-46)

In order to reduce the eventual effect of self-absorption, in this work the experimentally recorded $\Delta\nu = -1$ branch of rovibrational band was chosen to be fitted with a synthetic spectrum. The necessary spectroscopic parameters for computing the synthetic spectrum are shown in the two following tables. Table 2-2 shows the electronic structure parameters for the AlO blue-green band system $B^2\Sigma^+ - X^2\Sigma^+$ [79]. The Table 2-3 provides the rotational and vibrational structure parameters for the $\Delta\nu = -1$ sequence [79, 85]. Another important factor to be taken into account is the instrumental broadening of the recorded spectrum. Such broadening was measured using a spectral lamp (Hg/Ar) to be $\Delta\lambda = 0.274$ nm for the full width at half maximum (FWHM). Such broadening is taken into account by assuming a Gaussian profile of the apparatus function when fitting the synthetic spectrum to the experimental one. The optimization procedure used to reach the best fit of the experimental spectrum was the Levenberg–Marquardt algorithm which corresponds to a nonlinear least square curve-fitting method [74].

Table 2-2 Electronic structure constants of the AlO blue-green band system $B^2\Sigma^+ - X^2\Sigma^+$.

State	T_e (cm^{-1})	ω_e (cm^{-1})	$\omega_e x_e$ (cm^{-1})
$X^2\Sigma^+$	0	979.52(7)	7.030(8)
$B^2\Sigma^+$	20689.06	870.44(4)	3.668(3)

Table 2-3 Rotational and vibrational structure parameters for the $\Delta\nu = -1$ sequence of the AlO $B^2\Sigma^+ - X^2\Sigma^+$band.

(v', v'')		(0,1)	(1,2)	(2,3)
Band origin (cm^{-1})		19669.962(01)	19581.622(01)	19500.182(01)
Franck-Condon Factor		0.243	0.353	0.385
$R_e(\bar{r}_{v',v''})$ (a.u.)		1.00	0.925	0.867
B_v (cm^{-1})	v'	0.601724(16)	0.597242(17)	0.592742(16)

	v''	0.632618(17)	0.626860(17)	0.620954(17)
D_v ×10^6 (cm^{-1})	v'	1.143(02)	1.142(02)	1.133(03)
	v''	1.107(02)	1.135(03)	1.132(02)

2.4. Resume

In this chapter, we have discussed the principle of the diagnostics by emission spectroscopy of a plasma in LTE. In such equilibrium state, statistics laws can be applied allowing the description of by a unique temperature of the motion of the elections and the populations in the different atomic and ionic levels. Different types of spectral broadening mechanism have been then discussed. This discussion concludes on the fact that the Stark broadening is the major spectral line broadening mechanism in the plasma. The determination of the Stark broadening by fitting the experimental line profile with a convolution profile between the Stark broadening and the instrument broadening, represents an efficient way to determine the electron density in the plasma. The method to determine the temperature in the plasma has been then presented. Especially the multi Saha-Boltzmann plot method can be used to precisely extract the temperature from the emission spectrum over a delay interval from several hundred nanoseconds to several μs. Beyond these delays, molecular emission bands are fitted by a synthetic spectrum in order to extract vibrational and rotational temperatures. However for the plasmas that we study in this work, we consider the thermal equilibrium between vibrational and rotational degrees of freedoms, and set $T_{vib} = T_{rot}$ for the synthetic spectrum.

Chapter 3. Experimental setups and protocols of measurement and data treatment

The experimental setups used can be described into two parts: plasma generation and emission detection. Furthermore for the detection, we have used two types of systems: “spectroscopy” type and “image” type. In the first part of this chapter, we describe in detail the used experimental setups. In the second part of this chapter, the measurement and data treatment protocols are presented.

3.1. Plasma generation

3.1.1. Targets used in the experiments

Aluminum targets used in the experiment were of two different qualities. A certified reference aluminum alloy (Al 89.5%, Si 8.39%, Fe 0.999% and some traces, shown in Figure 3.1 a) which was used for measurements of “spectroscopy” type, while a pure aluminum (Al 99.99%, Cu 0.005%, Si 0.002%, Fe 0.001%) target, shown in Figure 3.1 (b), was used for those of “image” type.

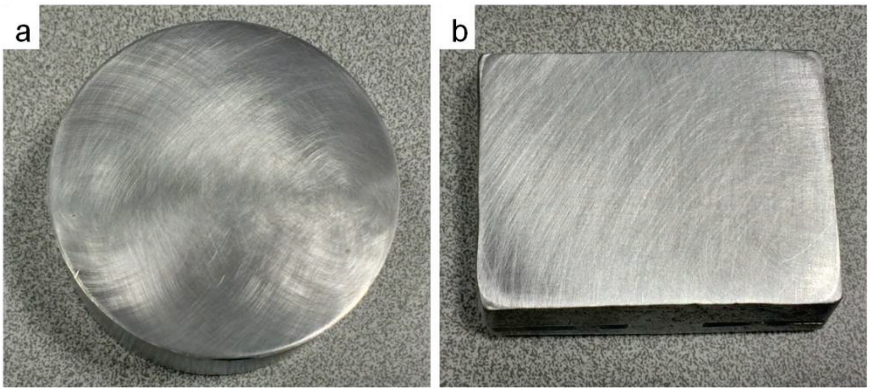

Figure 3.1Photos of the two types of taget: a) the certified reference aluminum alloy; b) the pure aluminum .

3.1.2. Experimental arrangement for plasma generation

The part of the experiment setup for plasma generation is shown in Figure 3.2. For the experimental results presented in Chapter 4, two Nd:YAG lasers were used. One of them was provided by the Quantel Laser Company (Brilliant) and the other by the CILAS Laser Company. In this thesis, we respectively named them laser "B" for Brilliant and laser "C" for CILAS. In the experiment presented in Chapters 5 and 6, only the Brilliant laser was used. These two lasers were operated at a repetition rate of 10 Hz and at the fundamental wavelength of 1064 nm. The nominal pulse duration of laser B was 4 ns (FWHM). The pulse duration of the laser C was significantly longer of several tens of ns dependent on the output energy. In our experiments, ablations were performed with different pulse energies delivered onto the surface of the target as shown in Table 3-1. The pulse duration of laser C at these two output energies was respectively 25 and 45 ns (FWHM).

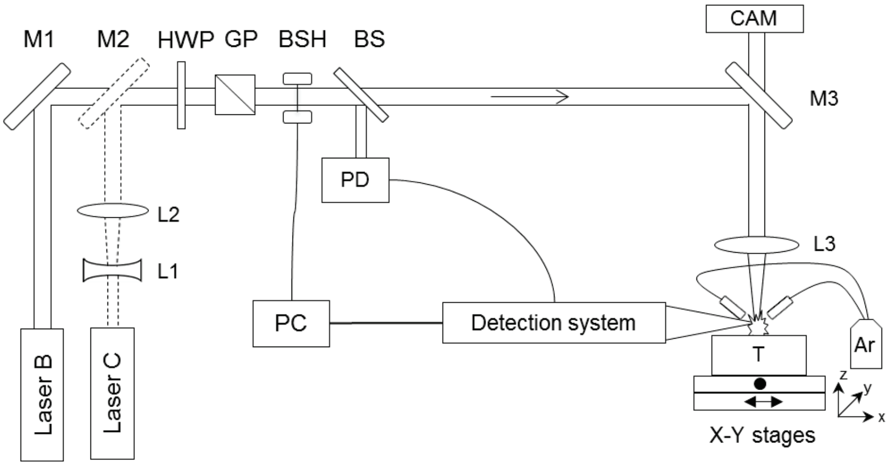

Figure 3.2 Experimental setup for plasma generation. M1- M3: Mirrors, L1 – L3: lenses, HWP: half wave plate, GP: Glan prism, BSH: Beam shutter, BS: Beam splitter, T: Target, CAM: Camera, PD: Photodiode, PC: Computer.

Table 3-1 Laser parameters used in the work

Laser	Brilliant (B)					CILAS (C)	
Pulse duration (ns)	4					25	45
Pulse energy (mJ)	5	10	20	30	50	20	50
Fluence (J/cm^2)	16	32	65	96	160	65	160
Irradiance (GW/cm^2)	4	8	16	24	40	1.5	6

As shown in Figure 3.2, for the experiments presented in Chapter 4, since the beam diameters were different between the two lasers, a telescope including two lenses (L1 divergent and L2 convergent) was used to magnify the beam diameter of the laser C (4 mm) to match that of the laser B of 6 mm. The paths of the two lasers were then superimposed by using two high reflection mirrors M1 and M2. The M2 was removable, which allowed the passage of the beam of the laser B. The laser beams passed through an ensemble of a half-wave plate (HWP) and a Glan prism (GP). This ensemble allowed a fine adjustment of the laser energy delivered to the target. A mechanical beam shutter (BSH) controlled the delivery of the laser pulse onto the target. A beam splitter (BS) sampled a pulse by sending 4% of it to a photodiode (PD). A synchronization signal was thus generated and was used to trigger the detection system. Laser pulses were focused onto the target by a lens (L3) with a focal length of 50 mm. A computer (PC) was used to ensure the synchronization of the different events in the experiment and to control the measurement procedure.

The surface of the target was polished and cleaned prior to ablation. During a series of measurements, the target was translated using a motorized X-Y stage in order to provide a fresh surface for each burst of laser shots. The distance between the focusing lens (L3) and the target surface was kept constant during a measurement by using a monitoring system which consisted of a combination of a laser pointer with its beam in oblique incidence onto the target surface and a video camera (CAM) installed above the mirror M3. A pair of tubes installed above the target and surrounding the laser ablation zone was used to deliver a stream of argon gas of a fixed flow of 8 ℓ/min, which ensured the plasma to expand into pure argon ambient gas at atmospheric pressure. For experiments under air, these tubes were removed.

3.1.3. Protocol of plasma generation

In order to avoid direct breakdown in the ambient gas, laser pulses were focused slightly under the target surface. Figure 3.2 shows time-resolved plasma image with its emission in a spectral band around 400 nm (with a narrow band filter of 400 nm ± 5 nm) for different distances between the focal point and the sample surface from 0.8 to -3.0 mm, a negative sign indicates a laser focalization under the target. The bottom line in Figure 3.3 indicates the position of the target surface. Each image is normalized by its own maximum value. From these images, we can see that when the focal point is above or very close to the surface, as in Figure 3.3 (a)-(d), the plasma is clearly separated into two parts:

one corresponds to the ionized air and the other the ablated materials. As shown in Figure 3.3 (e) and (f) the plasma becomes more spherical when the focal point goes under the surface by a distance of 1.0 to 1.5 mm. And a real time observation showed a more stable plasma. With further increasing the penetration of the focal point into the target (Figure 3.2 g and h), the emission from the plasma becomes weaker, because the reduction of the laser fluence as the laser spot on the target surface grows. We used finally in this work a depth of 1.5 mm for the focal point under the target surface.

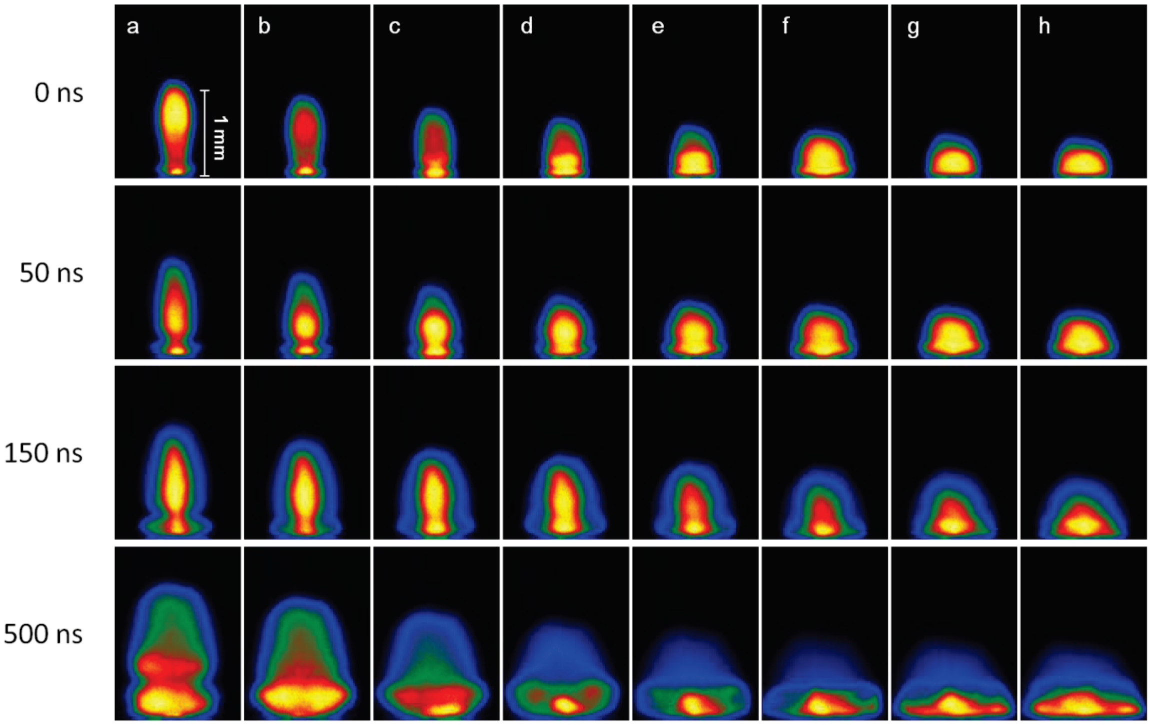

Figure 3.3 Images of plasma around 400 nm (400 nm ± 5 nm) with different focalization conditions for 50 mJ ablation energy on a pure aluminum target obtained with a narrowband filter centered at 400 nm. The distance between the focal point for laser pulse and the surface of the target are: a) 0.8 mm, b) 0.4 mm, c) 0 mm, d) -0.5 mm, e) -1.0 mm, f) -1.5 mm, g) -2.5 mm and h) -3.0 mm. A negative value indicates a focalization of the laser beam under the target surface.

The resulting craters had thus a diameter larger than the waist of the laser beam. The crater diameter was measured in our work using a microscope to be about 200±20 μm for all laser pulse energies used (see Table 3-1). The measured crater size was used in our experiment to estimate the diameter of the laser spot on the surface of the target. The microscopic images of the craters were also used to ensure that the laser beams were perfectly perpendicular to the surface of the target with the symmetrical aspect of the crater. The estimated fluence and irradiance delivered to the target (theoretically reachable if not absorbed) are shown also in Table 3-1.

For a good signal-to-noise ratio of the spectra, each of them was accumulated over 200 laser shots. They were distributed over 20 craters with each of them ablated by 10 successive laser pulses. The shift of the target between two neighboring craters was about 900 μm, much larger than the crater size.

3.2. Dual-wavelength differential spectroscopic imaging

3.2.1. Experimental setup for "image" type measurement

In the "image" type measurement, the produced plasma was imaged by using a two-lens system in a 4-f configuration (L4 and L5 in Figure 3.4) replacing the detection system in Figure 3.2. Two achromatic lenses L4 and L5 of focal length of respectively 6 cm and 20 cm formed a magnified image of the plasma. The resulting image was direct recorded by an intensified charge coupled device (ICCD) camera. In our experiment, monochromatic images were recorded corresponding to the emission from the species to be studied in the plasma. Such spectroscopic imaging was realized with the help of narrowband filters (F).

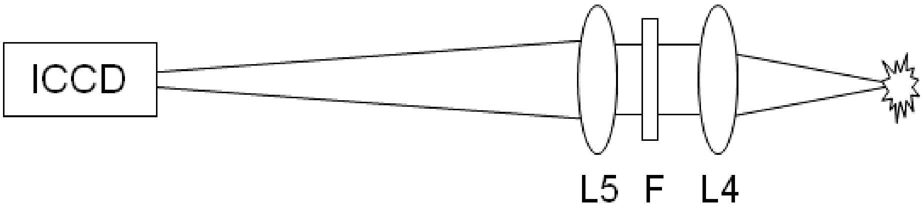

Figure 3.4 Experimental setup for "image" type measurement. L4, L5: lenses, F: filter.

Principle of dual wavelength differential spectroscopic imaging

The radiation emitted from the plasma is not monochromatic. It is however possible to perform monochromatic imaging with the help of an interference filter with a certain spectral bandwidth, $\Delta\lambda_B$. As explained in Section 1.5, the emission spectrum of a plasma is a superposition of lines and a continuous background. With a detector placed behind a filter of a center wavelength λ_0 and a bandwidth $\Delta\lambda_B$, the intensity recorded is the integrated intensity in the passing bandwidth of the filter. Such intensity can include spectral lines and the continuum. A pair of two filters were therefore used with one of them centered on the spectral line (λ_0, $\Delta\lambda_B$) and the another shifter outside the line (λ_0', $\Delta\lambda_B'$). The first is called "filter-on" and the second filter-off. Assuming that the intensity of the continuum remains almost constant in the vicinity of a considered line, it is possible to subtract the continuum in the spectral range of the corresponding filter-on from the total intensity with the intensity recorded using the corresponding filter-off.

Intensities measured with filter-on (I_{l+c}) and the corresponding filter-off (I_c'), can be written as follows:

$$I_{l+c} = \int_{-\frac{\Delta\lambda_B}{2}+\lambda_0}^{\frac{\Delta\lambda_B}{2}+\lambda_0} \{T_{tran}(\lambda) \times [I_l(\lambda) + I_c(\lambda)]\} d\lambda \tag{3-1}$$

$$I_c' = \int_{-\frac{\Delta\lambda_B'}{2}+\lambda_0'}^{\frac{\Delta\lambda_B'}{2}+\lambda_0'} [T_{tran}'(\lambda) \times I_c'(\lambda)] d\lambda \tag{3-2}$$

where $T_{tran}(\lambda)$ is the transmission curve of the filter which is chosen for the wavelength considered. Primed symbols are used for quantities concerning the filter-off. $I_l(\lambda)$ and $I_c(\lambda)$ respectively represent the intensity of the line and the continuum in the spectral range $\Delta\lambda_B$. $I_c'(\lambda)$ represents the intensity of the continuum in the band width of the filter-off. As we assume $I_c'(\lambda) \approx I_c(\lambda)$, Eq.(3-1) can be written as:

$$I_l = \int_{-\frac{\Delta\lambda_B}{2}+\lambda_0}^{\frac{\Delta\lambda_B}{2}+\lambda_0} [T_{trans}(\lambda) \times I_l(\lambda)] d\lambda = I_{l+c} - R_r \times I_c' \tag{3-3}$$

with

$$R_r = \left(\int_{-\frac{\Delta\lambda_B}{2}+\lambda_0}^{\frac{\Delta\lambda_B}{2}+\lambda_0} T_{tran}(\lambda) d\lambda \right) \Big/ \left(\int_{-\frac{\Delta\lambda_{B'}}{2}+\lambda_0'}^{\frac{\Delta\lambda_{B'}}{2}+\lambda_0'} T_{tran}'(\lambda) d\lambda \right) \tag{3-4}$$

the ratio between the total transmissions of the two filters. An example is shown in Figure 3.5 to illustrate this method.

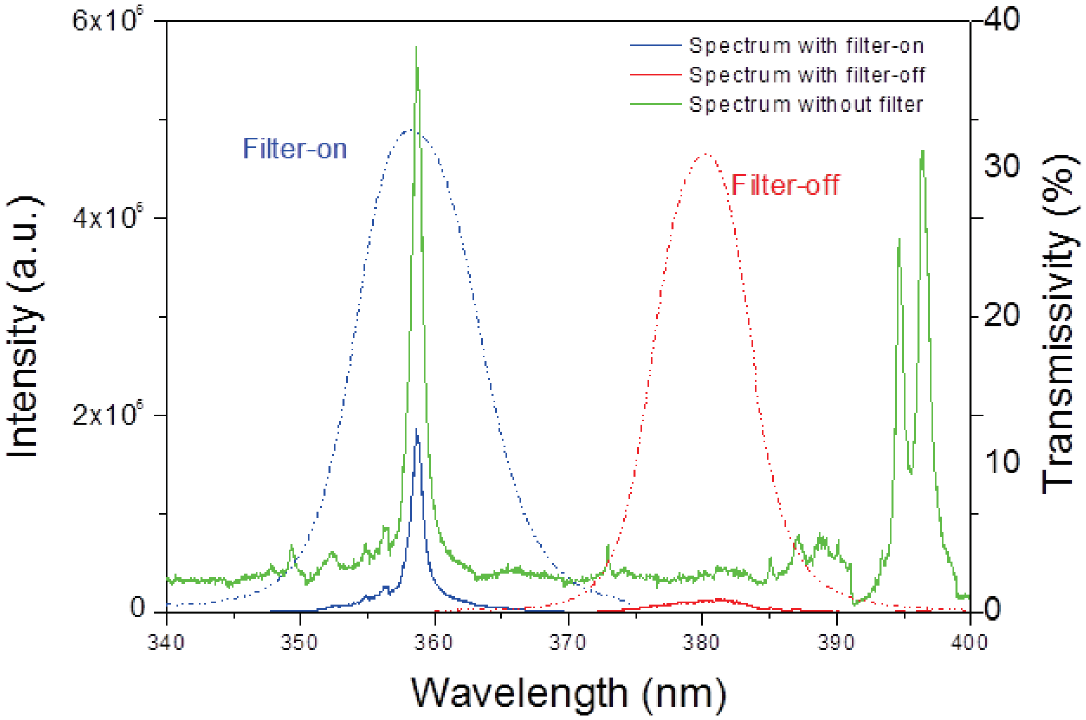

Figure 3.5 Spectra around 370 nm including the Al II 358.6 nm line, without filter, with a filter-on and with a filter-off.

The unfiltered spectrum (green curve) obtained in our experiment is the result of superposition of the continuum and the emission line of Al II at 358.6 nm. The images recorded with the two filters (filter-on: blue curve, filter-off: red curve) were first corrected by the transmission curves of the filters according to Eq. (3-4). The image with filter-off was then subtracted from the image with the filter-on. After subtracting, the emission image corresponding to the emission line is obtained.

Calibration of the pixel of the ICCD camera

It is necessary to calibrate the inter-pixel interval of used the ICCD camera for a given focusing optics in order to determine the real size of the plasma. A resolution test target (Thorlabs, R3L3S1N, shown in Figure 3.6) was used as a ruler. It is put at the point where the plasma is formed and is perpendicular to the optical axe of the collection system and the target is lightened by a white light source. A part of the target (indicated by a yellow circle in Figure 3.6 is recorded with the ICCD camera (Figure 3.7 (left)) as a calibration image with the interval of the lines of 0.1 mm. Then the horizontal and vertical profiles of the image were extracted in the Figure 3.7 (a) and (b) respectively.

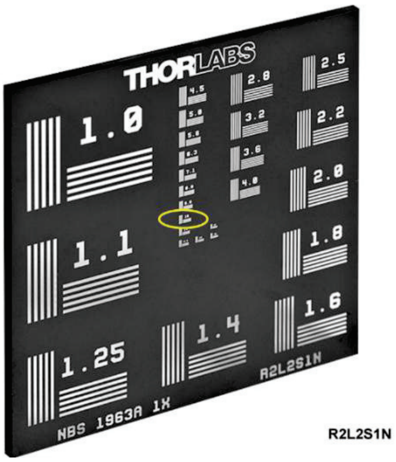

Figure 3.6 Resolution test target (Tholabs, R3L3S1N), the part in the yellow circle is recorded on the ICCD camera.

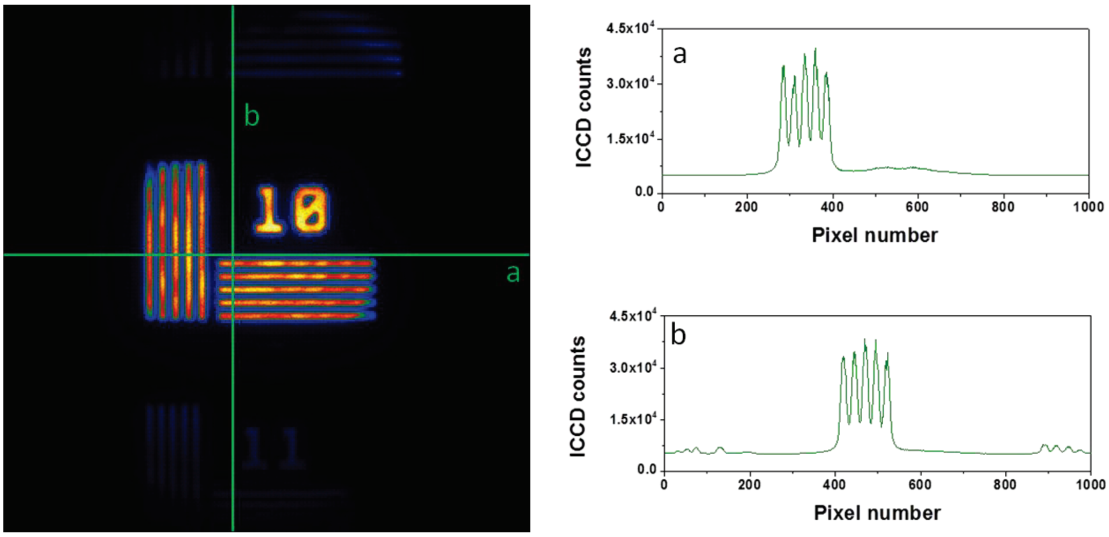

Figure 3.7 The calibration image on ICCD camera with the interval of the lines of 0.1 mm (left) and the horizontal (a) and vertical (b) profiles of the image.

In order to reduce measurement error, we counted the number of pixels of the total five lines together as shown in Figure 3.8. For both two directions, the five lines occupy 100 pixels on the ICCD camera, that is to say, each pixel represents 4 μm on the target surface.

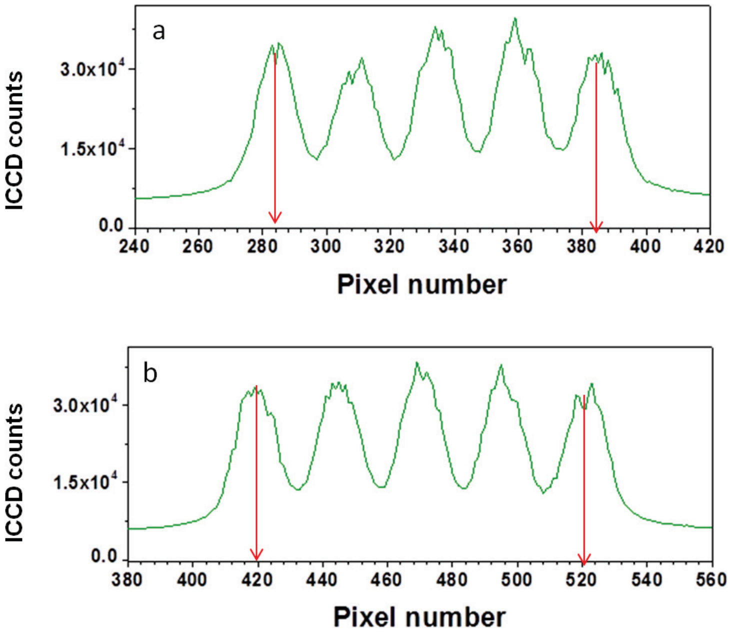

Figure 3.8 Profiles of the image of the resolution test target.

Check on the Chromatic aberration

Although we used the achromatic lenses to image the plasma, it is still necessary to check the chromatic aberration of the imaging system. For this purpose, 4 types of lamps were used to illuminate the target: white light, LEDs with wavelengths of 365, 400 and 600 nm. The obtained images are shown in Figure 3.9. The horizontal intensity profiles of the images were extracted. The results are shown in Figure 3.10. The resolution for these wavelengths remains the same and the contrast is good enough for all of them. That ensures that the collection system is suitable to image the plasma with different wavelengths without chromatic aberration.

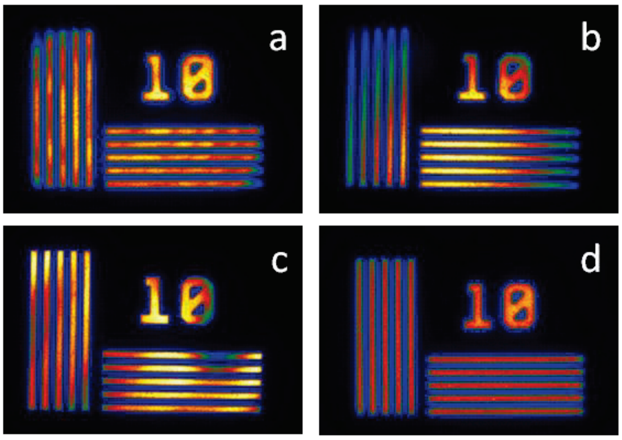

Figure 3.9 Image with different light sources: a: white light, b: 365 nm, c: 400 nm and d: 600 nm.

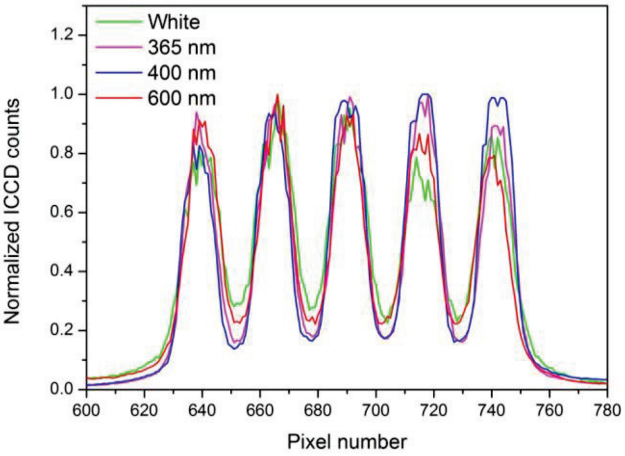

Figure 3.10 The horizontal profiles of the images extracted and aligned to the same starting point from the images of Figure 3.8.

Position of the surface of the target on an ICCD camera image

The position of the target surface was first recorded with the ICCD camera without plasma. During the experiment, each time the target was replaced, we made sure that the surface remains at the same position. The image of the illuminated flank of the target is shown in Figure 3.11 (a). The pixel binned vertical intensity profile of the image is shown in Figure 3.11 (b) together with the derivative of the intensity profile (Figure 3.11 (c)). The position of maximal derivative corresponds to the position of the surface because the light intensity changes abruptly at the surface.

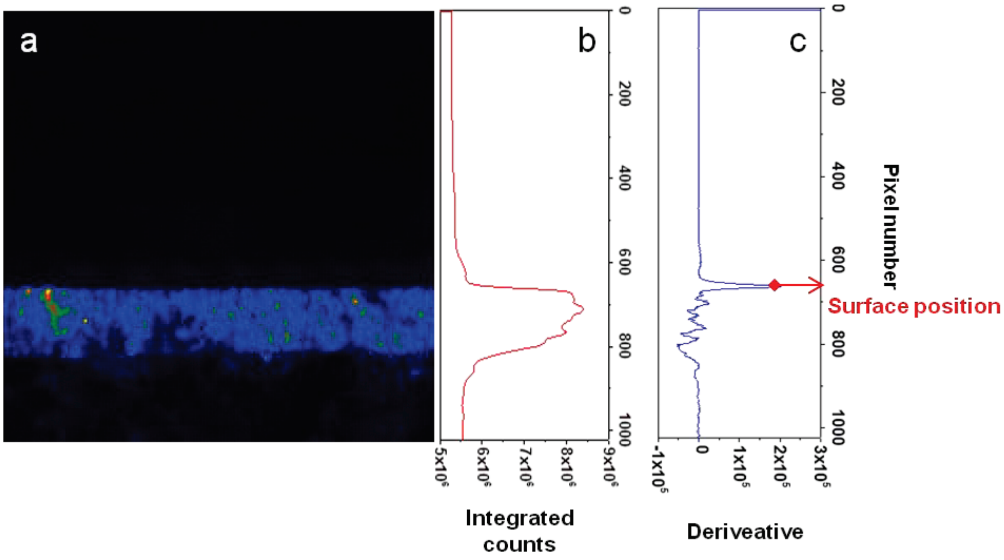

Figure 3.11 Position of the surface of the target. a: the image of the flank of the target recorded by the ICCD camera ; b: pixel binned vertical intensity profile ; c: the derivative of the intensity profile.

3.2.2. Measurement protocol of "image" type measurement

Emission lines chosen to represent the different species in the plume

In order to choose emission lines representative of studied species in the plasma, a spectrum was recorded (c.f. the section 3.3) with a delay of 500 ns and a gate of 50 ns from a plasma induced with 50 mJ ablation in argon ambient. The recorded spectrum is shown in Figure 3.12. We can see in the figure a relatively simple spectrum in which emission lines from the four studied species, Al I, Al II, Ar I and Ar II, can be identified. One or two lines were then chosen to represent each species of interest. Several criteria were used for the line selection. First, the lines were relatively intense and free of interference with emissions from other species. And they were chosen close to the visible spectral range to reduce the chromatic variation of the magnification of the optical imaging system. Finally resonant lines involving the ground state as the lower level of the transition were avoided if possible to reduce self-absorption. These conditions were fulfilled for the lines representing singly ionized aluminum and neutral and singly ionized argon. The lines selected for representing these species are indicated in Figure 3.12 by letter "a" for Al II, "d" for Ar II and "g" for Ar I. Their wavelengths are shown in the Table 3-2. It was however impossible to find a line of neutral aluminum at the same time close to the visible range and without involving the ground state. The two Al I lines around 395 nm (Table 3-2) were then chosen to represent neutral aluminum as indicated in Figure 3.12 by the letter "c". Since the major concern of this work is the morphology and the structure of the plasma, the possible self-absorption of the chosen lines still allows a good representation of the distribution of neutral aluminum in the plasma with the images obtained with these lines.

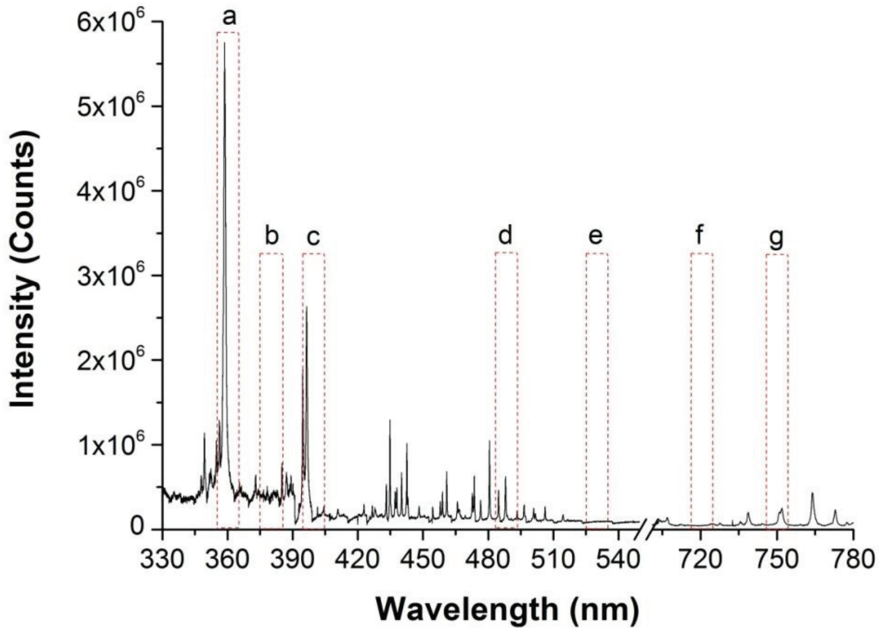

Figure 3.12 Typical emission spectrum from a plasma induced on a pure aluminum target in argon ambient by a 50 mJ pulse from the laser B detected at a delay of 500 ns with a gate of 50 ns. The letters from "a" to "g" indicate the different spectral lines used for spectroscopic imaging observation of Al II (a), Al I (c), Ar II (d) and Ar I (g) together with spectral bands for imaging with the continuum emission (b, e, f).

The choice of the simple configuration for ablation of a pure aluminum target in argon atmosphere allowed the characterization of the plasma in terms of these 4 species. For each couple of filters, the gain of the ICCD camera was chosen to fit the intensities of the resulting images. Different gains were thus chosen for different species, which means that the emission intensities of different species cannot be compared. However the structure of the plasma is clearly revealed with the images corresponding to each species normalized to their own maximum. The normalized images can then be superimposed in a same picture to show the structure of the plasma with emission images of different species in the plume. Table 3-2 also shows the emission lines chosen to represent the different species in the plume produced in air and the corresponding pairs of filters used to perform dual wavelength differential spectroscopic images. An image was the result of an accumulation of 100 laser shots distributed over 10 craters.

Table 3-2 Emission lines chosen to represent the different species in the plasma induced on the surface of an aluminum target under argon or air ambient and the corresponding pairs of filters used to get differential spectroscopic images of the species. The energies of the upper levels of the transitions corresponding to the selected lines are also indicated. Data are extracted from the NIST database [86]

Element	Species	Emission line (nm)	Upper level energy (eV)	Central wavelength of the filters (nm)
Al	Ion (Al II)	358.7	15.3	on : 360
				off : 380
	Neutral (Al I)	394.4, 396.2	3.1	on : 400
				off : 380
Ar	Ion (Ar II)	484.8, 488.0	19.3, 19.7	on : 488
				off : 530
	Neutral (Ar I)	750.4, 751.5	13.5, 13.3	on : 750
				off : 720
Air (N)	Ion (N II)	500.1, 500.7	23.1, 23.4	on : 488
				off : 530
	Neutral (N I)	746.8	12.0	on : 750
				off : 720

3.2.3. Data treatment protocol for spectroscopic imaging

Procedure for the subtraction of the images

Figure 3.13 (a) and (b) show the images for the Ar I emission with the filter-on and the filter-off respectively. The bottom line of the images represents the target surface. The two images were taken at the same conditions, concerning the parameters for the detection with ICCD (delay 280 ns and gate width 10 ns), the ablation laser energy (20 mJ) and in the Ar ambient. Before the subtraction, the intensities of the images corresponding to the pair of two filters were corrected by the transmission curves of the filters. Figure 3.13 (c) shows the result of the subtraction, which represents the emission intensity distribution of neutral Ar in the plasma.

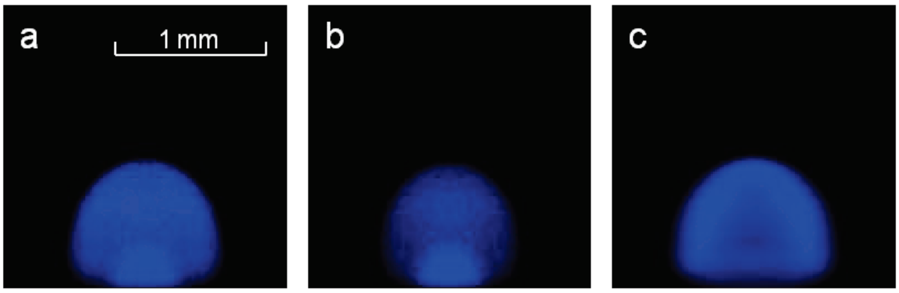

Figure 3.13 Illustration of the background subtraction: Emission images of laser induced plasma from an Al target under Ar ambient with 20 mJ ablation laser energy and a detection delay of 280 ns for Ar I emission image. a) raw image of Ar I line with the filter-on, b) image of the background with the filter-off, c) emission image of the Ar I line after the background subtraction.

Abel inversion for emissivity distribution

In LIBS, spatially integrated emission is usually observed. After the above discussed subtraction, the Abel inversion [74, 87] can be applied to the resulting image in order to obtain the two-dimensional distribution of the corresponding emitters inside the plume. As schematized in Figure 3.14, the laterally recorded intensities correspond to the integrated values for different transversal sections (Figure 3.14 a) of the plasma. The radial distribution of emissivity $\varepsilon(r)$ (Figure 3.14 b) cannot be measured directly, but can be computed using the experimentally measured integrated intensity $I(x)$ (Figure 3.14 c). This procedure of calculating the radial emissivity profile from the experimentally recorded laterally integrated distribution is known as Abel inversion. [58, 88, 89] The condition to apply this procedure is however the plasma to be symmetric with respect to the rotation about its axis (laser pulse propagating axis). The procedure is a commonly used numerical method for the spatial diagnostics of rotationally symmetric plasma [90-93].

As shown in Figure 3.14, x_0 and y_0 are the values of x- and y- coordinates at the plasma edge. And R_0 is the radius beyond which $\varepsilon(r)$ is negligible. The relationship between the measured lateral intensity distribution $I(x)$ and the radial emissivity function $\varepsilon(r)$ is given by [90]

$$I(x) = \int_{-y_0}^{y_0} \varepsilon(r)\, dy \tag{3-5}$$

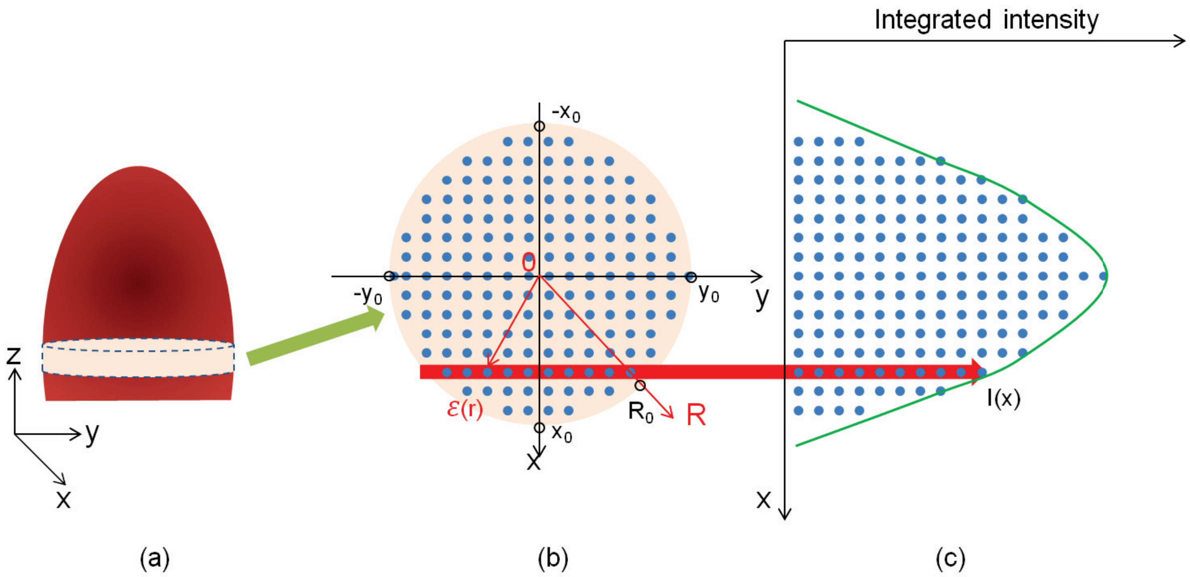

Figure 3.14 Illustration of the Abel inversion (a) a transversal segment of the plasma; (b) the transversal section of the plasma with a radial distribution emissivity $\varepsilon(r)$; (c) Path-integrated intensity profile as a function of the lateral dimension x.

In this expression, the integral is taken along the line of sight at constant coordinate of x. Assuming a rotational symmetry of the plasma about its axis, and with $\mathrm{r}^2 = x^2 + y^2$, Eq. (3-5) can also be written

$$I(x) = 2\int_{x}^{R_0} \varepsilon(r)\frac{r}{\sqrt{r^2 - x^2}}dr \tag{3-6}$$

Eq. (3-6) is one form of Abel's integral equation. The reconstruction of the unknown function $\varepsilon(r)$ from the measured intensity $I(x)$ can be done analytically by means of the inversion of the Abel's integral equation

$$\varepsilon(r) = -\frac{1}{\pi}\int_{r}^{R_0} \frac{dI(x)}{dx}\frac{dx}{\sqrt{r^2 - x^2}} \tag{3-7}$$

However the experimental measurement of $I(x)$ provides a discrete set of data points. Thus, both the derivative and integral in Eq. (3-7) cannot be performed directly. Several methods have been developed to overcome these difficulty and obtain the radial emissivity distribution $\varepsilon(r)$.

Abel inversion algorithms: Nestor–Olsen Method

The three main issues that an Abel inversion algorithm has to fix [87] are: (1) the divergence of Eq. (3-7) at $x = r$; (2) its dependence on the first derivative of $I(x)$, which amplifies noise in the measured data; and (3) the limited available number of experimental data of $I(x)$. Methods developed to perform the Abel inversion can be classified into two types: fitting method and numerical method. In practice, the experimental data of $I(y)$ exhibit a variety of distribution profiles that cannot be fitted with the same type of function, so the task of fitting can be hard. Instead, the numerical methods can be an alternative for providing a good evaluation of $\varepsilon(r)$. Therefore, one of the three widely used numerical methods, the Nestor–Olsen method [90], has been employed in our work because it is fast enough to compute the inversion function of an experimental observed $I(x)$ profile with more than 200 discrete values.

The Nestor-Olsen method assumes that $I(x)$ is constant over a small interval of $\varDelta x$. Then the subsequent series of integrals can be evaluated. After some rearrangement, the emissivity at a radius of $(k-1)\varDelta x$ is given by [90]

$$\varepsilon_k(r) = -\frac{2}{\varDelta x\pi}\sum_{n=k}^{N-1} I_n(x)B_{k,n}$$

(3-8)

where k and n are the integer position indexes for the radial and lateral intensity, and Δx is the interval between the two adjacent discrete experimental data points. The coefficients $B_{k,n}$ can be evaluated by using the expressions

$$B_{k,n} = -A_{k,n} \text{ for } n = k$$

(3-9)

and

$$B_{k,n} = A_{k,n-1} - A_{k,n} \text{ for } n \geq k+1$$

(3-10)

where

$$A_{k,n} = \frac{[n^2-(k-1)^2]^{1/2} - [(n-1)^2-(k-1)^2]^{1/2}}{2n-1}$$

(3-11)

In order to show the result of the inversion algorithm and to evaluate the effect of possible self-absorption, affecting the invese images, we present in Figure 3.15 two examples of emission images of Ar I lines around 751 nm and Al I lines around 395 nm before and after Abel inversion. The images have been taken at a delay of 280 ns after the plasma generation with a laser pulse of 20 mJ. In this figure, we can see that the inverted image of Ar I, Figure 3.15 (b), clearly indicates the absence of the gas in the central part of the plasma. In the case of Al I line, self-absorption is possible because of the implication of the ground state in the transition. However the inverted image in Figure 3.15 (d) shows clearly the concentration of the population of neutral aluminum in the central part of the plasma near the target surface, as expected (for detailed discussion see Chapter 4). We are thus quite confident with the used Abel inversion algorithm. Finally we mention that the inverted emissivity images represent only the space distribution of the corresponding emitters, i.e. the population of the associated species in the upper level of the transition. Using emissivity images to represent spatial distribution of the species needs taking into account the corrections due to temperature and the pressure gradients in the plasma and applies only if the plasma is in a local thermodynamic equilibrium (LTE). In this work we limit ourselves in the use of such representations to observe qualitatively the morphology and the internal structure of the plasma.

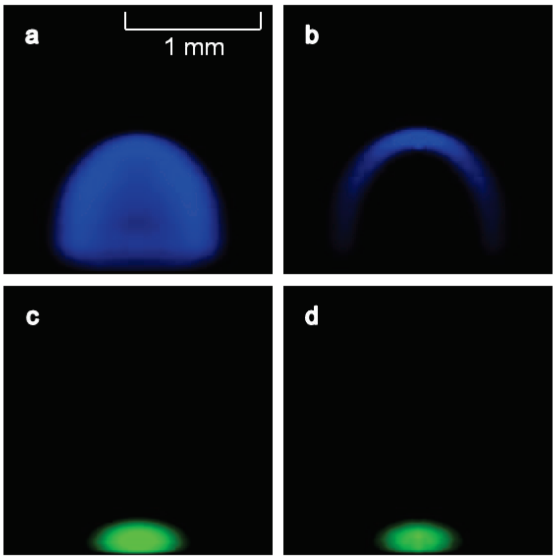

Figure 3.15 Top: emission images of Ar I lines around 751 nm at a delay of 280 ns, a) background-subtracted image, b) Abel-inverted image. Bottom: emission images of Al I lines around 395 nm at the same delay, c) background-subtracted image, d) Abel-inverted image. All the images are normalized to their own maximal value.

3.3. Time- and space-resolved emission spectroscopy

3.3.1. Experimental setup for "spectroscopy" type measurement

In the "spectroscopy" type measurement, the produced plasma was imaged by using a two-lens system in a 4-f configuration (L6 and L7 in Figure 3.16). The combination of the two lenses L6 and L7 of focal length of respectively 7.5 cm and 5.0 cm formed a reduced image of the plasma,. An optical fiber of 50-µm core diameter was positioned in the image plane in order to capture a part of emission from the plasma with spatial resolution. In the following Chapters, axial profiles of the emission intensity from the plasma will be presented, which were obtained by translating the fiber step by step along the laser incidence axis (z axis) at the middle transversal position of the image of the plasma. Such detection system allowed a space resolution of 75 µm for the local detection of the plasma emission. The output of the fiber was connected to the entrance of an echelle spectrometer, which was in turn connected to an intensified charge-coupled device (ICCD) camera (Mechelle and iStar from Andor Technology). A spectral range from 220 nm to 850 nm is covered with a resolution power ($\lambda/\Delta\lambda$) of 4005. The time resolution of the camera was about 5 ns.

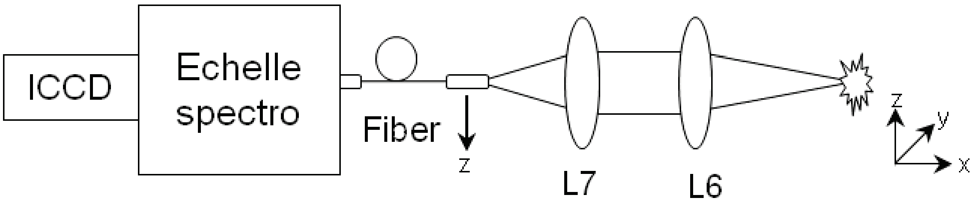

Figure 3.16 Experimental setup for "spectroscopy" type measurement. L6, L7: lenses

3.3.2. "Spectroscopy" type measurement protocols

The blue curve in Figure 3.17 represents schematically the emission intensity after laser ablation. Due to the strong continuum emission in the early stage of the plasma expansion, the "spectroscopy" type measurement could be performed only after a certain delay of several hundred ns in our ablation conditions. The longer the delay, the slower the properties of the plasma change and this allows a larger detection window (the ICCD gate opening time). In this detection window, the emission from the plasma is accumulated. Table 3-3 provides the definition of the detection windows used for plasma induced by 50 mJ ablation laser pulse. For the presentation of the experimental results in the following chapters, we will use the notation "DXXXX" to indicate the delay in ns for brevity. The evolution of the plasma has been recorded over the delay interval between several hundred ns and several µs. In order to compare the emission intensities measured at different delays, the signal was divided by the gate width. This leads to an averaged value of the signal for the concerned delay interval independent on the chosen gate width. Once an emission spectrum was recorded, the intensities of a certain number of emission lines were measured to extract the intensity profiles of the species in the plasma.

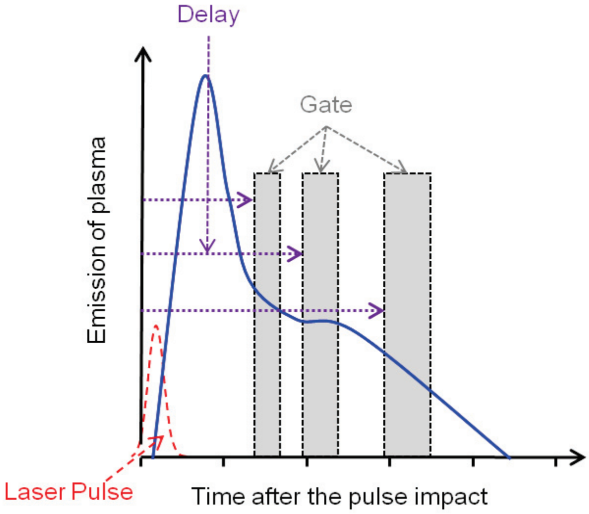

Figure 3.17 Schema for time-resolved detection. The blue line represents the total emission intensity from the plasma. The detection window (Gate) becomes larger as the delay increases.

Table 3-3 An example of the used detection windows

Ablation pulse energy		Delay (ns)	Gate width (ns)	Notation
Energy (mJ)	Fluence (J/cm^2)			
50	160	500	200	D500
		1000	300	D1000
		2000	400	D2000

After a delay of several hundred nanoseconds when the spectrum is recorded, the axial size of the plasma is about one millimeter. With the help of the optical fiber connected onto the echelle spectrometer, the space-resolved detection could be realized by moving the fiber step by step along the axial direction of the plasma on the image plane of the plasma, as shown in Figure 3.18. In this way the time-and space- resolved spectra can be recorded.

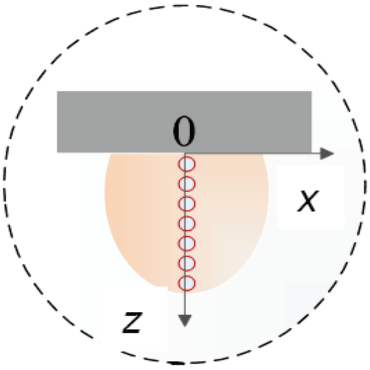

Figure 3.18 Illustration of the space-resolved detection. The position z=0 represents the surface of the target.

Additional measurement protocols for AlO molecule detection

The particularity of molecular emission detection is the large spectral width of ro-vibrational bands. Such spectral width can include several orders of the dispersion by the prism in an echelle spectrometer. This introduces discontinuities into the background of a molecular emission band. We will see later that an accurate fitting of a ro-vibrational band of a molecule needs a flat background in the spectral range of the emission band. It is why in our experiment, a Czerny-Turner spectrometer (Shamrock, Andor Technology) was used to record emission spectrum from AlO molecules. The used spectrometer was with a grating of 600 l/mm and coupled to the same ICCD camera as for the echelle spectrometer. With an entrance slit of 100 µm, the resolution of the spectrometer was determined using a mercury argon calibration source from Ocean Optics, to be $\Delta\lambda = 0.27$ nm for the full width at half maximum (FWHM).

3.3.3. Spectroscopic data treatment protocols

The typical lines used in our experiments to characterize the plasma are presented in Table 3-4.

Table 3-4 Typical lines used to characterize the plasma in the work. Lines with wavelength in red are used for the determination of the electron density, lines with wavelength in bold letters are used for the determination of the temperature using Saha-Boltzmann plots. Other lines are used for intensity profiles or/and emission images.

Species	Wavelength (nm)						
Al I	242.3	242.5	246.0	251.3	256.8	257.5	264.7
	265.2	**266.0**	305.5	305.7	306.4	306.6	308.2
	309.3	394.4	396.2				
Al II	263.8	266.9	**281.6**	**358.7**	466.3		
Si I	**243.5**	**250.7**	**251.4**	**251.6**	**251.9**	**252.4**	**252.4**
	252.9	**263.1**	**288.2**				
Fe I	248.3	**248.8**	**249.1**	**252.3**	**271.9**	**344.1**	**358.1**
	372.0	373.5	373.7	374.6	382.0	386.0	404.6
Fe II	**234.3**	**238.2**	**239.6**	**239.9**	**240.5**	**249.3**	**256.3**
	258.6	**259.8**	**259.8**	**259.9**	**260.7**	**261.4**	**261.8**
	262.6	**268.5**	**274.0**	**274.6**	**274.9**	**275.6**	
H I	**656.3**						
N I	742.4	744.2	746.8				
N II	417.6	422.8	444.7	460.7	462.1	478.8	480.3
	489.5	498.7	499.4	500.1	500.3	500.5	500.7
	501.1	501.6	502.6	504.5			
O I	777.4						
Ar II	427.8	434.8	442.6	454.5	457.9	461.0	472.7
	476.5	480.6	488.0				
Ar I	**696.5**	706.7	714.7	727.3	738.4	750.4	751.5
	763.5	772.4	772.4				

Axial profiles of emission intensity

To study the axial profiles of the emission intensity of different species in the plasma, the intensity of an emission line was extracted by fitting the line profile and by calculating the surface under the line with background subtracted. The choice of the representative line for different species in the plasma was guided by the consideration of a negligible self-absorption for the chosen line. An elementary precaution is to avoid if possible, the ground state as the lower level of the concerned transition. The selected lines to represent a plasma induced on a pure aluminum target in an argon or air ambient are listed in Table 3-5. The ensemble of these lines allowed a complete representation of the distributions of the elements evaporated from the target as well as contributed from the ambient gas in their neutral and ionized states. Except the line for neutral Al, all other lines representing respectively ionized aluminum and argon as well as neutral argon and nitrogen, have a lower level with high energy as can be seen in Table 3-5. We can thus reasonably consider that they suffer less from self-absorption. The self-absorption associated to these lines has been estimated as negligible in a similar condition in Ref. 94. For the neutral aluminum, the strong resonant line at 309.3 nm was chosen, because of the high degree of ionization in the aluminum vapor, preventing weak emission lines of neutral Al from detection with a sufficient signal-to-noise ratio, especially at short delay.

Table 3-5 Selected lines representing the 4 species of interest in the plume with their wavelength, and energy of the upper and the lower levels. Data are extracted from the NIST database [86]

Element	Species	Transition wavelength (nm)	Upper level energy (eV)	Lower level energy (eV)
Al	Ion	281.6	11.8	7.4
	Neutral	309.3	4.0	0.0
Ar	Ion	480.6	19.2	16.6
	Neutral	696.5	13.3	11.5
N	Neutral	744.2	12.0	10.3

Axial profiles of electron density and electron temperature

The axial profiles of electron density and temperature can be deduced from the axial profile of emission spectrum by using the standard plasma diagnostics method. The electronic density is determined using the Stark broadening of the Ar I 696.5 nm line when the ablation takes place in Ar and the H_α 656.3 nm line when it takes place in air as shown in Table 3-4 with wavelengths in red.

As an illustrative example, Figure 3.19 shows the evolution of the profile of H_α 656.3 nm line at different delays (Figure 3.19 a) and that of the electron density obtained by fitting the spectra (Figure 3.19 b). Note that the ablation was performed with a 50 mJ laser pulse at 1064 nm in the atmospheric air, and that for H_α 656.3 nm line, the Stark effect is linear.

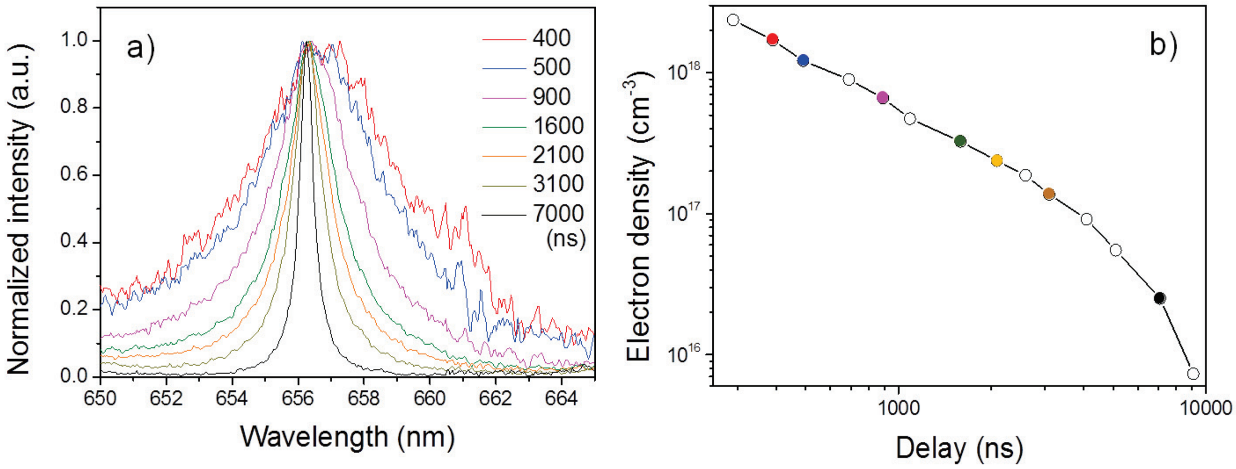

Figure 3.19 (a) Evolution of the H_α 656.3 nm line at different delay and (b) that of the electron density in the plasma induced by a 50-mJ laser pulse at 1064 nm in the atmospheric air. The same color code as in (a) is used for (b).

Similarly Figure 3.20 shows the evolution of the profile of the Ar I 656.3 nm line at different delays (Figure 3.20 a) and that of the electron density (Figure 3.20 b) in the plasma induced by a 20-mJ laser pulse at 1064 nm under Ar gas with the atmospheric pressure. For Ar I 696.5 nm, the Stark effect is quadratic and less strong than the linear broadening, and a Stark shift can be observed. At long delay such as 11 μs and 16 μs, the line broadenings are quite similar. At such delays, the electron density is quite small and the main line broadening mechanism becomes instrumental broadening. Consequently, we cannot use this method to determine an electron density smaller than 10^{16} cm^{-3}.

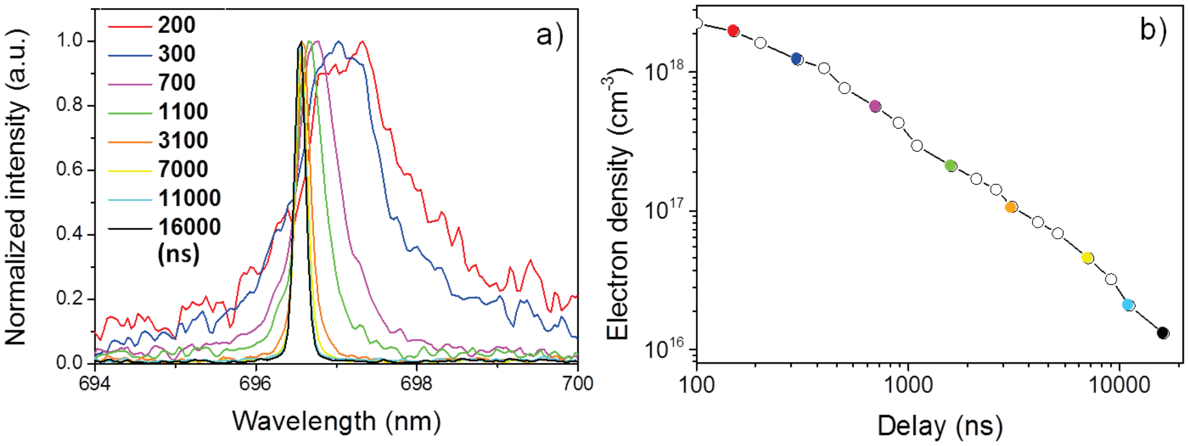

Figure 3.20 Evolution of the profile of the Ar I 696.5 nm line at different delays (a) and that of the electron density (b) in a plasma induced by a 20-mJ laser pulse at 1064 nm in Ar gas at the atmospheric pressure. The same color code as in (a) is used in (b).

As an example, Figure 3.21 shows a multi-elemental Saha-Boltzmann plot performed with emission spectra of a plasma produced by ablation with a 10 mJ laser pulse on the surface of an aluminum alloy. The detection delay is 0.5 μs. For this plot, the intensities of emission lines were extracted from a spectrum by taking their peak value. For the data shown in Figure 3.21, a determination coefficient of R^2=0.99 is obtained for a linear fit in the log-linear scale. The temperature is thus determined from the slope of the linear regression $\mathrm{T} = -1/k_B s$. For instance, a temperature of 11 500 K is extracted from the plot with an uncertainty of 3% (the uncertainty on the slope). By taking into account also the uncertainties related to the determination of the emission line intensities, we estimate the relative uncertainty of the temperature to be 5%, so that we find in this example T= (11500 $\pm$ 600) K.

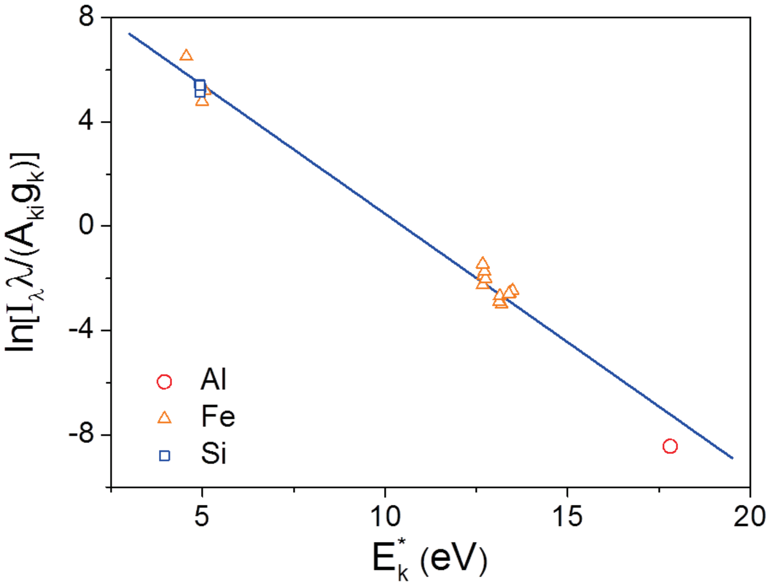

Figure 3.21. Multi-elemental Saha-Boltzmann plot applied to line emission intensities extracted from a spectrum recorded with an ablation energy of 10 mJ and a detection delay of 0.5 µs.

Determination of the temperature with Boltzmann and Saha plots or with the equivalent methods requires the plasma to be in the local thermodynamic equilibrium (LTE).[83] The discussions in the section 2.1.3 show that in the delay interval considered for the "spectroscopy" type measurement and with the experimental conditions used in the this work, LTE state is a reasonably good representation of the studied plasmas.[94, 96] Multi Saha-Boltzmann plots [74] are thus used to determine the temperature. The lines selected in this work for these plots are listed in Table 3-4 with their wavelength in bold letters. In addition, all the selected lines were inspected in our experiment, in order to check for significant self-absorption. According to the particular plasma conditions, a sub-ensemble of appropriate lines can be selected among those listed in Table 3-4. But in the most of the cases, all of these lines can be used in the plots.

3.4. Resume

In this chapter, we have presented the experimental setups used in this work for plasma generation, emission detection and diagnostics. We have discussed each part in the experimental setups in detail in view of their use for the production of the experimental results that will be presented in the following chapters of this PhD thesis manuscript. Even though there is a unique arrangement for the plasma generation, for the detection system, we used two types of setups for spectroscopy and image measurements. The specific experimental protocols for each type of measurement and the corresponding data treatment procedure associated to each type of detection system are then presented. For the image measurement, the principle of dual wavelength differential spectroscopic imaging technique has been first discussed. The choice of representative lines for the studied species is then detailed. In order to get the distribution of the emitters in the plasma, Abel inversion is applied to the differential images. Emissivity images are finally obtained. For spectroscopy measurement, a set of detection parameters is first defined to get time- and space-resolved spectra. From the experimentally recorded emission spectra, profiles are extracted for the emission intensity of investigated species, the electron density and the temperature in the plasma. The plasma diagnostics methods to determine the electron density with Stark broadening and the electron temperature with multi Saha-Boltzmann plots are further presented. The ensemble of information presented in this chapter represents the basis of understanding the experimental results which will be presented in Chapters 4, 5 and 6.

Chapter 4. Plasma properties as a function of the laser fluence and pulse duration

Starting from this chapter, we will present the main results obtained in the framework of this thesis. We will first focus on the convoluted effect of ablation laser fluence and pulse duration on the behavior of the induced plasma during its propagation into the ambient gas. The influences of the laser fluence and the pulse duration on the morphology and the internal structure of plasma are studied with ablation by infrared (IR) nanosecond (ns) laser pulse on an aluminum target immersed in argon ambient gas of one atmospheric pressure. Two types of pulse duration are used for this study with the laser B (pulse duration ~ 4ns) and the laser C (pulse duration 25 – 45 ns) as described in Section 3.1.2. Different configurations of plasma shielding are thus investigated due to the use of laser pulses with different fluences and durations. Specific plasma morphologies and internal structures will be reported for these different interaction regimes.

Plasma morphology and structure observed just after the end of the laser pulse showed characteristic features which will be used to infer the dominant mechanism of plasma shielding in terms of laser-supported absorption waves. A simple configuration of ablation with an infrared pulse of an aluminum target in argon gas of one atmosphere pressure was used in the study. As mentioned in Chapter 3, we have chosen two fluences, 65 J/cm^2 (moderate fluence regime) and 160 J/cm^2 (high fluence regime) and studied the effect of pulse duration in each of these ablation fluence regimes. The behaviors of the plasmas induced by the two types of pulse with different durations of 4 ns (short pulse) and between 25 and 45 ns (long pulse) have been especially studied and compared within the interval of delay between several tens of nanosecond and several microseconds. The delay interval between several hundred nanoseconds and several microseconds has been especially investigated because it corresponds to the typical operation range of LIBS. Time- and space-resolved emission spectroscopy [39] was employed to accede to the detailed diagnostics of the resulting plasmas.

4.1. Properties of the plasma in the moderate fluence ablation regime

4.1.1. Early stage of expansion with ablation by short pulse

Observation of morphology and structure of the plasma

The laser B described in Section 3.1.2 with a pulse duration of 4 ns has been used in the experiment with a fluence of 65 J/cm^2 on the target surface. The obtained results are shown with composite emissivity images of the 4 studied species, Al I, Al II, Ar I and Ar II (Figure 4.1). Such composite emissivity images are built by superimposing in a same image frame, the normalized emissivity images of the 4 investigated species acquired in the same experimental conditions. The images from Figure 4.1(a) to Figure 4.1(j) show the evolution of the morphology and the internal structure of the plume at different delays of 20, 60, 80, 120, 200, 280, 400, 520, 770 and 1020 ns respectively. In these pictures, we can see first that the global form of the plume, including all emitting species, aluminum as well as argon, exhibits a nearly spherical shape with a slight elongation along the axis of laser incident direction. As shown in Figure 4.1(f) recorded at the delay of 280 ns, the elongation of the plume can be measured by drawing two concentric semicircles, S_A and S_R, with the centers lying on the target surface at the middle of the plume. S_A takes into account the axial expansion of the plume by fitting its radius, R_A, to the axial extent of the plume at this delay. While S_R takes into account the radial expansion of the plume by fitting its radius, R_R, to the half of the transverse extent of the plume at the same delay. From Figure 4.1 (f), the ratio R_A/R_R is determined to be 1.44. Obviously this ratio evolves during the propagation of the plume. The measured ratio at 280 ns provides a typical value of the aspect ratio between the axial and radial expansions of the plume.

Look at now the internal structure of the plume. A layered structure can be still distinguished even though interpenetration between the different layers can be clearly observed. Starting from the target surface and go upward against the laser pulse propagation direction, we cross first an emission layer from neutral aluminum (in green). A second emission layer is observed above consisting of ionized aluminum (in red). The emission layers of the aluminum vapor are covered around the laser propagation axis by an emission layer from ionized argon (in grey). Finally an emission layer of neutral argon appears first around the top of the plume, and then later envelops the core of the plume for a delay longer than 80 ns.

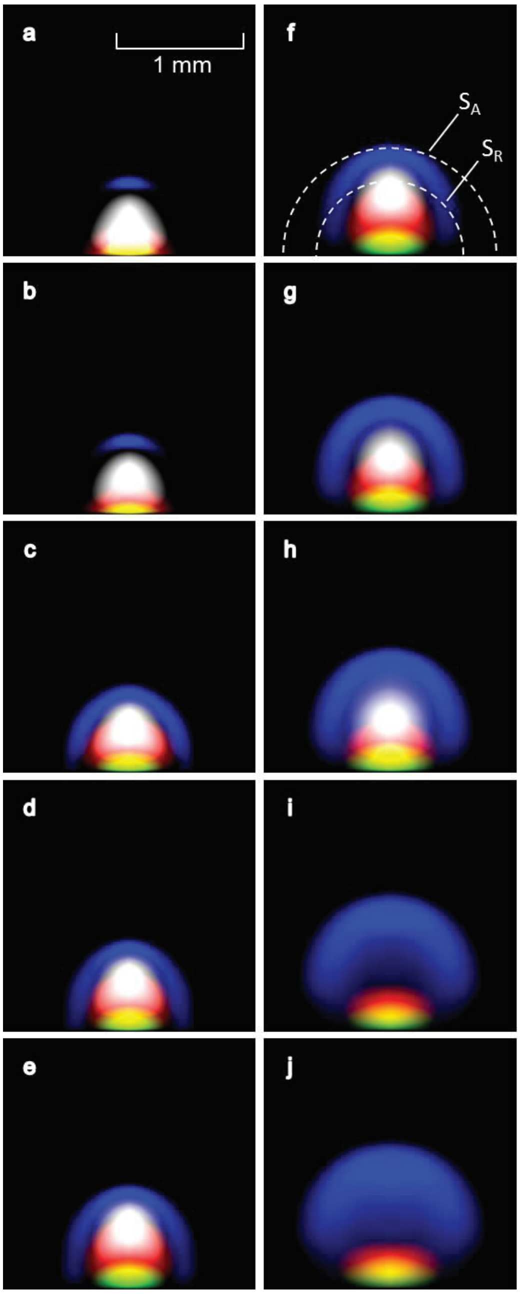

Figure 4.1 Composite emissivity images obtained in moderate fluence and short pulse duration ablation regime. Individual images correspond to detection delays of (a) 20 ns, (b) 60 ns, (c) 80 ns, (d) 120 ns, (e) 200 ns, (f) 280 ns, (g) 400 ns, (h) 520 ns, (i) 770 ns and (j) 1020 ns. The two semicircles in (f) indicate the expansion spheres according to respectively the axial and the radial expansions of the plume. The real dimension of each picture is 2 × 2 mm^2, and the bottom line of the image represents the target surface. False colors are used to represent the different species in the plume with green for neutral aluminum, red for aluminum ion, blue for neutral argon and grey for argon ion.

Discussion and interpretation

The appearance of argon ions around the axis of the laser beam may indicate the absorption of laser energy by the ionized ambient gas. However such absorption is clearly not complete here, because the aluminum vapor situated under the layer of argon ions is observed ionized. This means that during the post ablation interaction, the tailing part of the laser pulse transmits through the argon layer and continues to deposits its energy into the aluminum vapor leading to its ionization. The fact that a layer of neutral aluminum appears close to the target surface indicates the efficient attenuation of the laser pulse during its propagation in the aluminum vapor. Its energy becomes too weak near the target surface to ionize the totality of the aluminum vapor. The observed internal structure of the plume suggests therefore that for the regime of ablation studied here, the plasma shielding effect may be due to both ionized ambient gas and the ablation vapor. And due to the lower ionization potential of aluminum, the shielding by the metallic vapor should be predominant in post-ablation process. Such configuration of plasma shielding leads to an accumulation of energy during the post-ablation interaction in the middle of the aluminum vapor close to the target surface. The propagation of the plume is therefore supported by absorbed laser energy coming from the middle of the plume. This situation corresponds to laser-supported combustion (LSC) wave [97, 98].

As mentioned above, the emission layer of neutral argon is first observed around the top of the plume. With increasing delay, lateral part of the layer appears. And finally this layer, together with the target surface, completely envelops the core of the plume. The large upper level energy (13 eV) of the transition corresponding to Ar I emission line implies a very high temperature in this layer. Such high temperature layer is not due to laser radiation, because on the one hand neutral argon is initially transparent to the laser radiation, and on the other hand the lateral extent of this layer is much larger than the laser spot which was 200 μm on the target. The formation of this layer of excited argon can thus only be due to the interaction of initially cold ambient gas and the hot aluminum vapor. The mechanism of such interaction can be either radiative or thermal transfers [98]. In the first process, argon atoms are excited by the passage of shockwave and by absorption of the UV radiation emitted by the hot aluminum vapor. While in the second process, multiple collisions are the origin of the excitation of atomic argon. But the most likely, the combinations of the both mechanisms lead to an effective excitation of the layer of argon gas surrounding the plume.

As the delay increases from 20 ns (Figure 4.1 a) to 520 ns (Figure 4.1 h), the relative positions of the above identified layers do not change too much, with global expansion of all the layers. Beyond 770 ns, the emission from argon ions disappears in the noise. The corresponding population of ions transforms into neutral argon as we can see in Figure 4.1 (i) and Figure 4.1 (j). However, the structure of the plume remains similar to that observed in short delays with a nearly spherical form and distinguished layers of different species. The fact that in LSC mode of propagation, the driving force comes from the central region of the plume leads to a rather spherical expansion of the plume. At the same time, the high pressure inside of the plume with a gradient going from the middle close to the target surface to the periphery maintains its stable structure.

Evolution of the emission intensities

Besides the morphology and the internal structure, the experimentally obtained emission images are also used to study the decay of the plasma emission. For this purpose, we integrate the intensity of a raw image of a given species recorded at a given delay once the contribution of the continuum is subtracted. The integrated intensity is then divided by the corresponding detection gate width to get the mean intensity in the concerned time interval. In order to compare emission intensity decays in the different ablation configurations, the mean intensity is further corrected for the ICCD gain. The signal amplification versus the applied ICCD gain was calibrated using a continuous light source. Figure 4.2 shows integrated emission intensities of argon ion (Figure 4.2 a) and aluminum ion (Figure 4.2 b) as a function of the detection delay in the interval from 20 to 500 ns for the three investigated ablation configurations corresponding to the different combinations of fluence and pulse duration. Let us first look at the case of ablation with a 20 mJ and 4 ns pulse (low fulence and short pulse, curves α in Figure 4.2). The classical exponential intensity decay behavior [99] is observed for the both species. We remark in particular, a faster decay for the Ar II line with a time constant of 85 ns than for the Al II line with a time constant of 110 ns. This is quite normal taking into account the higher ionization potential of Ar (15.8 eV) than that of Al (6.0 eV) and the fact that the aluminum vapor is more efficiently heated during the post-ablation interaction as mentioned above.

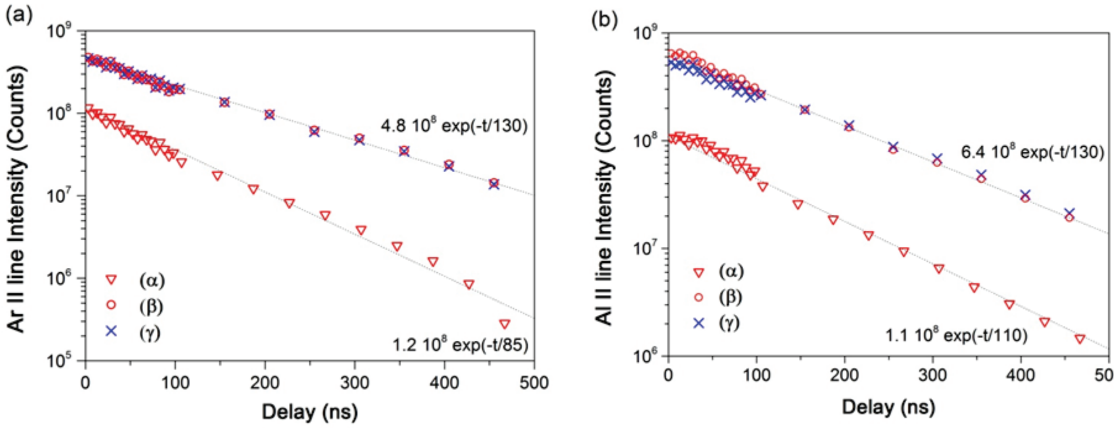

Figure 4.2 Decay of the emission intensity from ions of argon (a) and ions of aluminum (b) for a plasma induced by a pulse from: (α) laser B with 20 mJ, (β) laser B with 50 mJ, (γ) laser C with 50 mJ. The curves are fitted by exponential decay function.

4.1.2. Effect of pulse duration on the property of the plasma in the delay interval from 350 ns to 1.5 μs

Axial profiles of emission intensity

For a delay longer than several hundred of ns, the emission spectroscopy becomes efficient to characterize the plasma beyond the morphology, by including its physical parameters such as electron and temperature. In this study, we used the both laser B and C described in Section 3.1.2 at a same moderate fluence of 65 J/cm^2, which allows us observing the effect of the pulse duration in this ablation regime. Let us look at first the axial profiles of emission intensity of aluminum shown in Figure 4.3 (a) and (b). We specify that the axial position in the figure represents the distance in the plasma with respective to the target surface. The origin of the axis corresponds to the surface. The long duration pulse provided by laser C induces here a stronger emission from aluminum. The spatial extents of the emission intensity profiles are however quite similar for the plasmas induced by the two types of pulses. Concerning the emissions from the ambient gas (Figure 4.3 c and d), the difference between the intensity profiles corresponding to the two types of pulses is much reduced here as compared to that observed the aluminum vapor. We can observe a slightly higher intensity from neutral argon for the long pulse, while a slightly higher intensity from argon ion is observed for the short pulse. Overall, the emission profiles exhibit similar axial extensions for the different species in the plasma. The notable difference between the plasmas induced by the two types of pulses is a significantly more intense emission from aluminum vapor (atoms and ions) with the longer pulse.

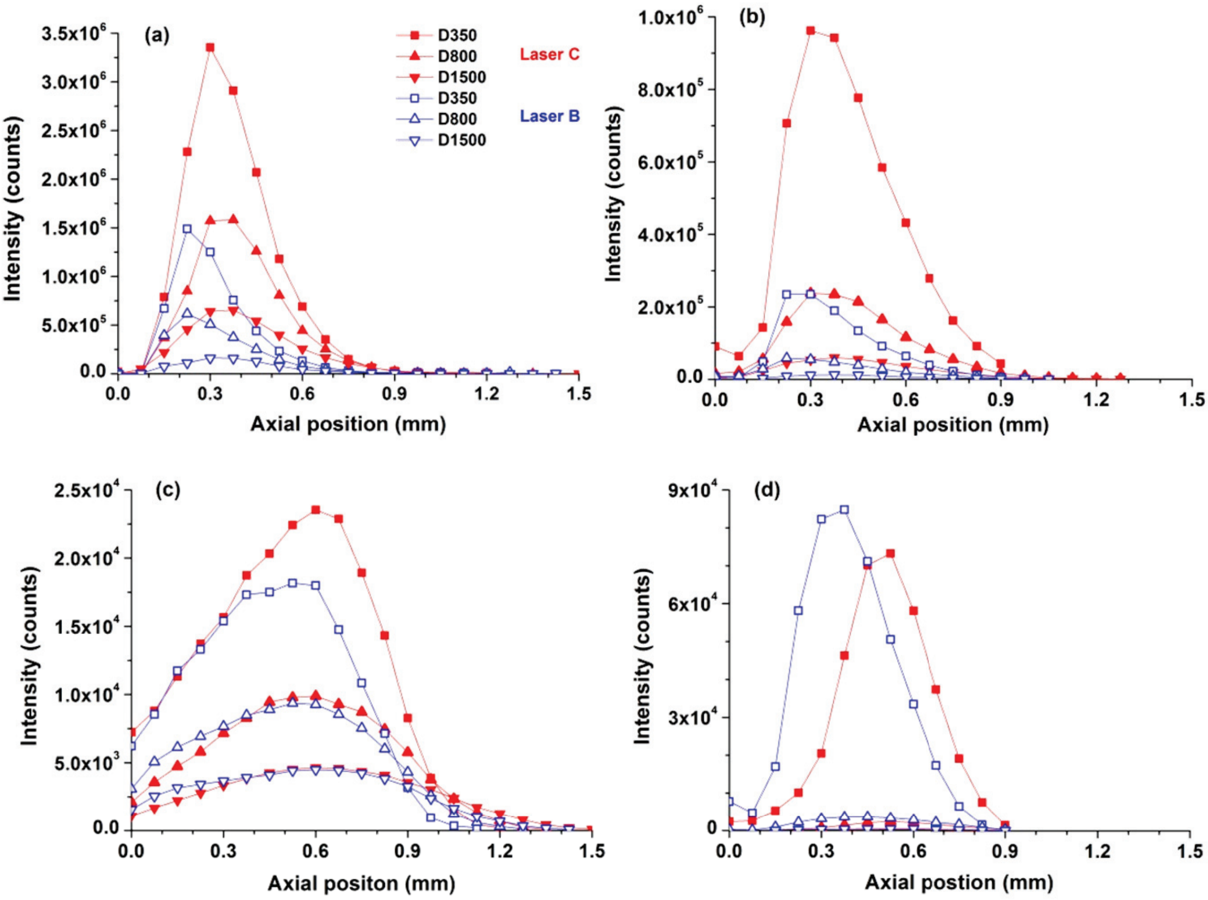

Figure 4.3 Axial emission intensity profiles of the plasmas induced by the two types of pulses: laser B of pulse duration of 4 ns and laser C with pulse duration of 45 ns. A same fluence of 65 mJ/cm² is used for the two lasers. Different species in the plasma are (a) neutral aluminum evaporated from the target, (b) corresponding ions of aluminum, (c) neutral argon contributed by the ambient gas, and (d) corresponding ions of argon.

The profiles shown in Figure 4.3 indicate therefore a similar structure for the both plasmas induced by the short and the long pulses in the delay interval of the observation. We can remark also, first, the global extent of the plume (0 mm to ~ 1.1 mm) is quite small with a thin ionized argon layer. Plasma shielding by the layer of ionized argon may thus incomplete as we mentioned above with the observation with images in the early stage of the expansion. The laser pulse can in this case, transmit through this layer and continue to deposit its energy into the aluminum vapor to further heat it. This configuration of interaction is more suitably described by laser-supported combustion (LSC) wave. The effect of the pulse duration in a regime of moderate fluence ablation where the LSC is initiated, is therefore to optimize the penetration of the pulse through the ambient gas and to increase the absorption of laser energy by the ablation vapor. In this configuration, a long pulse allows a higher efficiency to heat and to excite emission from the vapor. Higher coupling efficiencies to the target for ablation and to the ablation vapor for heating can be therefore reached with a pulse with longer duration.

Axial profiles of electron density and temperature

Axial profiles of the electron density and the temperature are shown in Figure 4.4. We specify that the axial position in the figure represents the distance in the plasma with respective to the target surface. The origin of the axis corresponds to the surface. We can see a small extent of the plasma which fits the extent of the emission intensity profiles of aluminum and argon shown in Figure 4.3 for the both plasmas induced by the short and the long pulses. We can remark also for a given delay, the plasma induced by the long pulse presents a higher temperature, which corresponds well to the fact that this pulse induces stronger emissions from aluminum and from argon. Correspondently a higher electron density is also found for the plasma induced by the long pulse.

Finally we can remark that the observations made in the delay interval between 350 and 1500 ns, and the conclusion drawn are coherent with those presented for shorter delay interval and obtained with spectroscopic images.

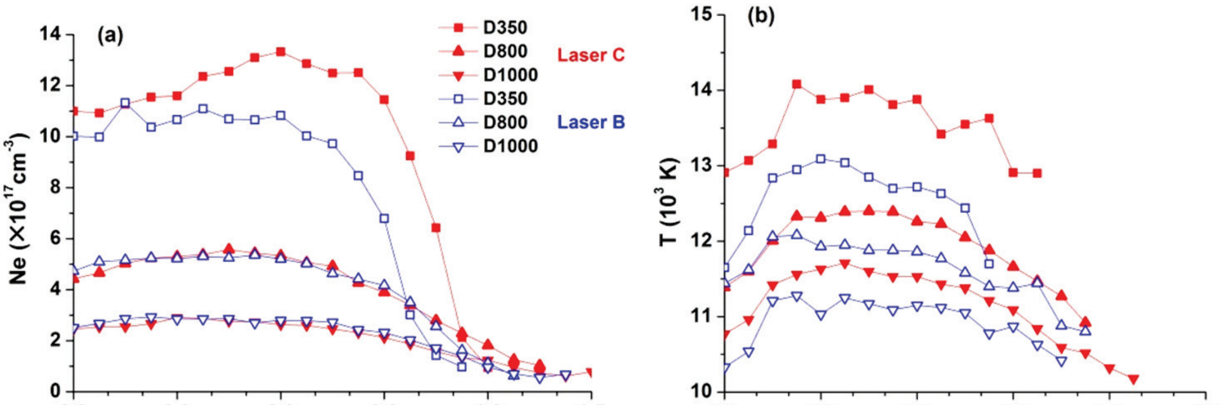

Figure 4.4 Axial profiles of electron density (a) and electron temperature (b) of the plasmas induced by the two types of laser pulses, laser B of pulse duration of 4 ns and laser C with pulse duration of 45 ns at different detection delays.

4.2. Properties of the plasma in the high fluence ablation regime

4.2.1. High fluence short pulse duration ablation regime

Morphology and structure

The laser B described in Section 3.1.2 with a pulse duration of 4 ns has been used in the experiment with a fluence of 160 J/cm^2. Composite emissivity images of the 4 studied species in this ablation regime are shown in Figure 4.5. The individual images from Figure 4.5 (a) to Figure 4.5 (j) show the morphology and the internal structure of the plume at different delays of 20 ns, 40 ns, 75 ns, 115 ns, 170 ns, 270 ns, 370 ns, 520 ns, 770 ns and 1020 ns. From these pictures, we can see first that the global form of the plume including all emitting species, aluminum as well as argon, exhibits an elongated form along the axis of laser incident direction. As shown in Figure 4.5 (f) for a delay of 270 ns, we can measure the elongation of the plume by drawing two concentric semicircles, S_A and S_R, as in Figure 4.5 (f) and in a similar way as in Figure 4.1 (f). From Figure 4.5 (f) the ratio R_A/R_R is determined to be 1.63, which is significantly larger than that we find for the plume in Figure 4.1 (f). Let us look at now the internal structure of the plume. At short delays, a plume core appears consisting of the emission zone of ions of argon and aluminum. Emission from neutral aluminum is absent (cannot be distinguished from the noise). A zone of emission from neutral argon is only observed close to the target surface and surrounding the main core of the plume. Two remarkable features of the plasma core are i) a complete mixing of ions of aluminum and argon; ii) a large axial extent of the ionized plume core of about 0.8 mm at very short delay. Such structure observed in short delay indicates a mode of propagation during the post-ablation interaction of laser-supported detonation (LSD) wave. As reported in our previous works [100], in the LSD propagation mode, strong absorption of laser energy by shocked ambient gas leads to avalanche ionization of the gas and a secondary breakdown in the shocked gas after the first one induced on the target surface. In this configuration, plasma shielding takes place at the propagation front of the plume where laser energy is deposited into the ionized shocked gas during the post ablation interaction [97, 98]. The driving force of the propagation comes from therefore the upper part of the plume and leads to an accelerated motion of the plume towards the laser pulse coming direction. It is why the plume presents an elongated form towards the laser beam. At the same time, the secondary breakdown in the shocked gas around the propagation front of the plume induced a backward flow of shocked gas [101], which may be the reason of the observed mixing between the gas and the ablation vapor in the plasma core of the plume [100].

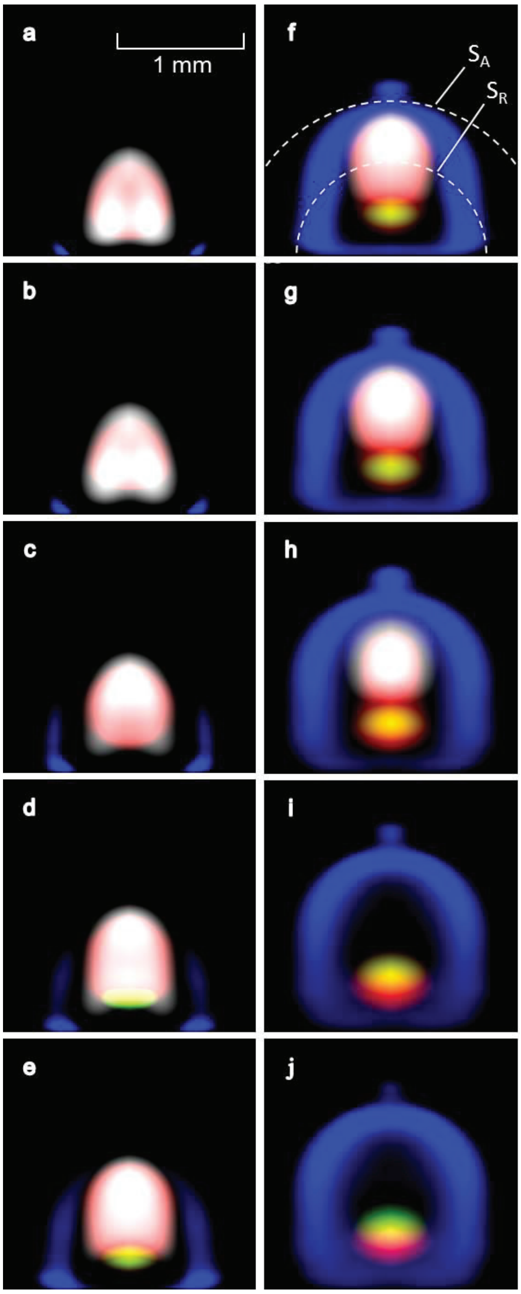

Figure 4.5 Composite emissivity images obtained in the high fluence and short pulse duration ablation regime. Individual images correspond to detection delays of (a) 20 ns, (b) 40 ns, (c) 75 ns, (d) 115 ns, (e) 170 ns, (f) 270 ns, (g) 370 ns, (h) 520 ns, (i) 770 ns and (j) 1020 ns. The two semicircles in (f) indicate the expansion spheres according to respectively the axial and the radial expansions of the plume. The real dimension of each picture is 2 × 2 mm², and its bottom line represents the target surface. False colors are used to represent the different species in the

plume with green for neutral aluminum, red for aluminum ion, blue for neutral argon and grey for argon ion.

As the delay increases, a population of neutral aluminum appears in the lower part of the plasma core close to the target surface, while the upper part remains ionized. Such configuration suggests an axial gradient of the temperature in the plume going from the upper part to the lower of the plume, which is a consequence of plasma shielding by the upper part of the plume. We can remark also the development of a layer of emission from neutral argon close to the target surface. The fact that this layer can develop between the main plasma core and the target surface indicates the existence of a low pressure zone left by the upward axial propagation of the plume. At long delay, the layer of excited argon completely encircles and envelops the plasma core. Such encirclement prevents in particular the plasma core from thermal conduction through the target surface, in such a way a layer of ionized aluminum is still observed in the lower part of the vapor at delay as long as 1020 ns.

Evolution of emission intensities

As for the moderate fluence ablation regime, the decay of the plasma emission is measured and presented in Figure 4.2 for the high fluence and sort pulse ablation regime by the curves β. The curves shows the evolution of the emission intensities from the Ar II line (Figure 4.2 a) and the Al II line (Figure 4.2 b). The classic exponential decay is again observed here. Compared to the plasma induced by a pulse with moderate fluence but with the same pulse duration, we observe first a higher emission intensities at a given delay from both the gas and the vapor. In addition, the decay rates are smaller here with a similar time constant of 130 ns for both the Ar II and the Al II lines. Even through the time constant of the Al II line is slightly increased compared to the case of moderate fluence, the increase of that for the Ar II line is much more significant with a lifetime of emission from argon ions 1.53 times longer. The difference in lifetime increases for argon ion and for aluminum ion supports furthermore the change of regime of laser-supported absorption wave from the LSC at the moderate fluence ablation regime to LSD at the high fluence ablation regime as discussed above. In the later regime, the absorption of laser energy by ionized ambient gas is a dominant process, which significantly increases the lifetime of the population of argon ions as observed in our experiment.

4.2.2. High fluence long pulse duration ablation regime

Morphology and structure

The laser C described in Section 3.1.2 with a pulse duration of 25 ns has been used in the experiment with a fluence of 160 J/cm^2. Composite emissivity images of the 4 studied species in this ablation regime are shown Figure 4.6. The individual images from Figure 4.6 (a) to Figure 4.6 (j) show the morphology and the internal structure of the plume at different delays of 20 ns, 40 ns, 75 ns, 115 ns, 170 ns, 270 ns, 370 ns, 520 ns, 770 ns and 1020 ns. From these pictures, we can see first that the global form of the plume including all emitting species, aluminum as well as argon, exhibits an elongated form along the axis of laser incident direction. As shown in Figure 4.6 (f) for a delay of 270 ns, we can measure the elongation of the plume by drawing two concentric semicircles, S_A and S_R, as in Figure 4.5 (f). From Figure 4.6 (f) the ratio R_A/R_R is determined to be 1.83, which is much larger than that we find for the plume in Figure 4.1 (f). Let us look now at the internal structure of the plume. At short delay, a similar structure is observed with a plasma core consisting of a mixture between argon ions and aluminum ions as for the case of a shorter pulse with the same fluence (Figure 4.5). The size and the form of the plasma core are also similar. Such similitude indicates that in the case of ablation with a high fluence and long duration pulse, the post-ablation regime is again better described by the LSD wave. The above remark is particularly important because it emphasizes the role of laser fluence but not irradiance in the determination of the morphology and the internal structure of the plasma, at least for that induced by nanosecond pulse. It is easy to check that the irradiance of a pulse with a fluence of 160 J/cm^2 and a duration of 25 ns, 6.4 GW/cm^2, is smaller than that of a pulse of 4 ns duration with fluence of 65 J/cm^2 of 16.2 GW/cm^2 (see also Table 3-1). A difference can however be remarked with respect to the case of the pulse with the same fluence but shorter duration concerning the distribution of neutral argon. Only a small emission zone from neutral argon is observed here in the top of the plume without lateral part. This indicates a stronger axial acceleration and a weaker radial expansion as compared to the case of the short pulse, since as mentioned above, neutral argon is most likely excited by interaction with the hot plume core.

As the delay increases, a population of neutral aluminum appears in the lower part of the plume close to the target in a way very different from what we can observe in the case of a short pulse. Such population appears first in an O-ring formed zone close to the target surface with a diameter larger than the size of the plasma core and much larger than the size of the laser beam on the target surface. The spatial disconnection of the O-ring formed population of neutral aluminum with aluminum ions observed in the middle of the plume, suggests that this population is not contributed by aluminum ions through electron capture process. The only process which can reasonably contribute to the observed O-ring formed neutral aluminum population is the delayed (or secondary) splashing ejection and evaporation from the melt phase of aluminum [102, 103]. The delayed ejection and evaporation are considered as due to the recoil momentum transfer from the primarily ejected vapor to the melted bath lying in the crater after the end of the ablation laser pulse. Such mechanism leads to ejection of material along the rim of the crater in an initial O-ring form [104]. The appearance of splashing ejection in the case of the long duration pulse indicates a plasma shielding by the layer of shocked and ionized ambient gas stronger than what happens for the shorter pulse at the same fluence. Extremely strong plasma shielding by shocked ambient gas in a LSD regime induced by a long pulse can have two consequences: i) a less efficient direct coupling of laser pulse to the target, which leads to a no-evaporated melt bath in the crater; ii) a stronger backward gas flow corresponding to a more efficient recoil momentum transfer to the melt bath. All these effects favor the formation of the delayed evaporation observed in our experiment.

For larger delays, the structure of the plume evolves differently here as compared to the case of the short pulse at the same fluence. In particular, due to the appearance of the delayed evaporation of neutral aluminum from the target, the lower pressure region close to the target surface does not exist for the case of the long pulse. This prevents ambient gas to penetrate into the regime between the plasma core and the target surface. Instead, this region is occupied by a population of neutral aluminum first evaporated due to splashing ejection and later joined by neutral aluminum contributed by electronic capture of aluminum ion in the bottom of the plasma core. So starting from a similar structure at short delay, the delayed splashing ejection leads finally to a quite different structure at long delay between the plasmas induced by the long or the short pulses.

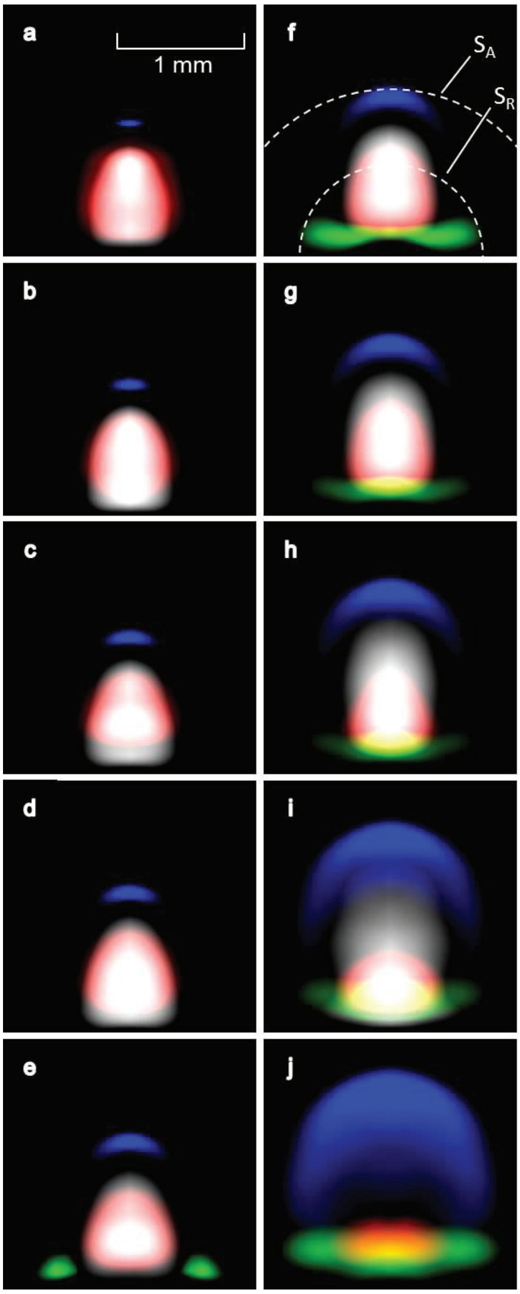

Figure 4.6 Composite emissivity images obtained in the high fluence and long pulse duration ablation regime. Individual images correspond to detection delays of (a) 20 ns, (b) 40 ns, (c) 75 ns, (d) 115 ns, (e) 170 ns, (f) 270 ns, (g) 370 ns, (h) 520 ns, (i) 770 ns and (j) 1020 ns. The two semicircles in (f) indicate the expansion spheres according to respectively the axial and the radial expansions of the plume. The real dimension of each picture is 2 × 2 mm^2, and its bottom line represents the target surface. False colors are used to represent the different species in the plume with green for neutral aluminum, red for aluminum ion, blue for neutral argon and grey for argon ion.

Evolution of emission intensities

The decay of the emission from the plasma induced by the high fluence and long duration pulse is shown in Figure 4.2 with the curve γ. We remark that the decay of the emission intensity from both Ar II and Al II behavior similarly as the plasma induced by the short duration pulse at the same fluence. This demonstrated again the importance of laser fluence, instead of laser irradiance, in the determination of the evolution of the morphology and the structure of the induced plasma.

4.2.3. Effect of pulse duration on the property of the plasma in the delay interval from 500 ns to 2 μs

Similar to the ablation regime of modest laser fluence, we study here the behavior of the plasma in a longer delay interval when emission spectroscopy becomes efficient to characterize the plasma beyond its morphology by including the electron density and the temperature. In the following, the behaviors of the plasmas induced by the short pulse and the long pulse will first be compared in detail over the delay interval between 500 ns and 2 μs. The observations show different behaviors between the plasmas produced by these two types of pulse. The observed behaviors will be thus interpreted by emphasizing the effect of the pulse duration.

Axial profiles of emission intensity

Consider now the axial profiles of emission intensities of different species in the plasma. The results are presented in Figure 4.7. Let us look at first the profiles of neutral aluminum (Figure 4.7 a). Significant difference can be observed for the plasmas induced by the two types of pulse of different durations. Laser B with 4 ns duration produces an intense emitting aluminum vapor with a large axial extent. As a function of the delay, such profile continues to propagate away from the target. Laser C with 25 ns duration on the other hand, produces a much weaker emitting aluminum vapor. In addition, the emission zone remains static in the region close to the target. The emitting zones of aluminum ions corresponding to the two types of pulse exhibit similar behaviors as the neutrals (Figure 4.7 b). Significant difference is again observed for the emission intensity profiles of neutral argon (Figure 4.7 c) between the plasmas induced by the two types of pulses. What we can see is that with laser B, the emission zone of argon overlaps quite well that of aluminum. Such distributions show the mixing between aluminum vapor and argon gas that we have already observed and reported in our previous work [39]. For laser C however, an emission zone of argon much more extended along the axial direction than that of aluminum can be observed. And we remark also the emission intensity from argon is stronger with laser C than with laser B at a given delay. The profiles of emission intensity from argon ions exhibit the same trend of a stronger and more extended emission zone observed from the plume induced by the longer pulse.

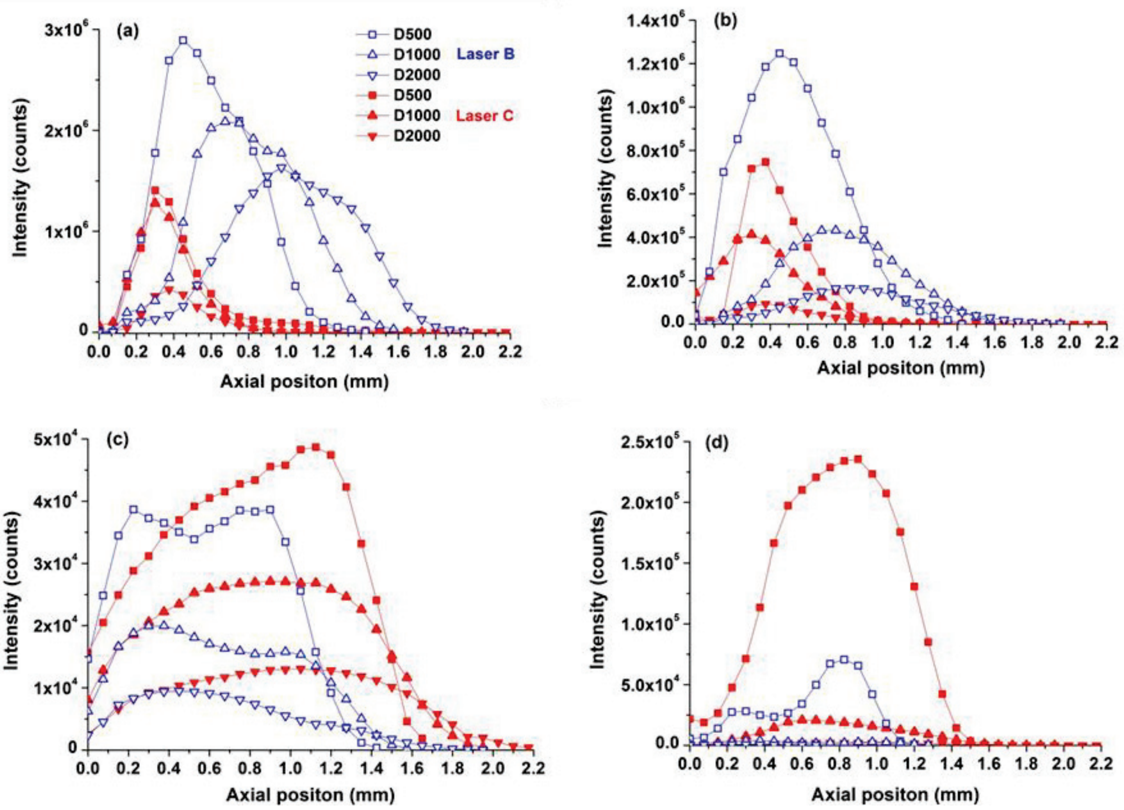

Figure 4.7 Axial emission intensity profiles of the plasmas induced by the two types of pulses: laser B of pulse duration of 4 ns and laser C with pulse duration of 25 ns. Different species in the plasma are (a) neutral aluminum evaporated from the target, (b) corresponding ions of aluminum, (c) neutral argon contributed by the shocked ambient gas, and (d) corresponding ions of argon.

By taking into account the energies of the upper levels of the detected transitions of neutral aluminum and neutral argon, the emission intensity profiles presented in Figure 4.7 can be used to indicate the distributions of different types of hot gases in an ablation plume. Different structures are therefore suggested for the plumes induced by the two different types of laser pulse over the investigated delay interval. With the short duration pulse, the plume corresponds to a mixture of hot gases of aluminum vapor and argon over the total extent of the plume (0 mm to ~ 1.8 mm). The aluminum vapor is evaporated from the target. While the hot argon gas is contributed by the layer of the ambient gas initially surrounding the vapor and ionized by absorption of laser energy during the process of laser-supported detonation (LSD) wave.

With the long duration pulse, axial extent of the hot aluminum vapor is significantly reduced and confined in a zone close to the target surface (0 mm to ~ 0.8 mm). The emission from this zone is also much less intense than with the short duration pulse. Above the zone of mixture between aluminum vapor and hot argon gas, there is a thick layer (from 0.8 mm to ~ 2 mm) of almost pure hot argon gas. Such structure is again the consequence of LSD wave which induces the ionization of argon gas in the early stage of plasma expansion. The thick layer of hot argon gas indicates here a stronger absorption of laser energy by ionized argon for the long duration pulse. In this case, more laser energy is deposited in the layer of ionized argon gas. Correspondently, less laser energy goes to the target and to the aluminum vapor leading to a reduced emission from the aluminum vapor and its confinement within a significantly smaller volume. The effect of pulse duration in high fluence regime where the LSD wave is initiated therefore corresponds to a control of plasma shielding by absorption of laser energy in the layer of excited and ionized ambient gas. A longer pulse is more shielded because the thickness of hot and ionized ambient gas increases with the pulse duration. While a short pulse penetrates better through the excited and ionized layer of the ambient gas and deposits more efficiently its energy.

Axial profiles of electron density and temperature

Measured profiles of the electron density and the temperature of the studied plasmas are shown in Figure 4.8. The electronic density is determined using the Stark broadening of the Ar I 696.5 nm line. The procedure and the used spectroscopic data are presented in Chapter 3. We estimate the relative standard deviations of the electron density and the temperature to be 15 % and 10 % respectively.

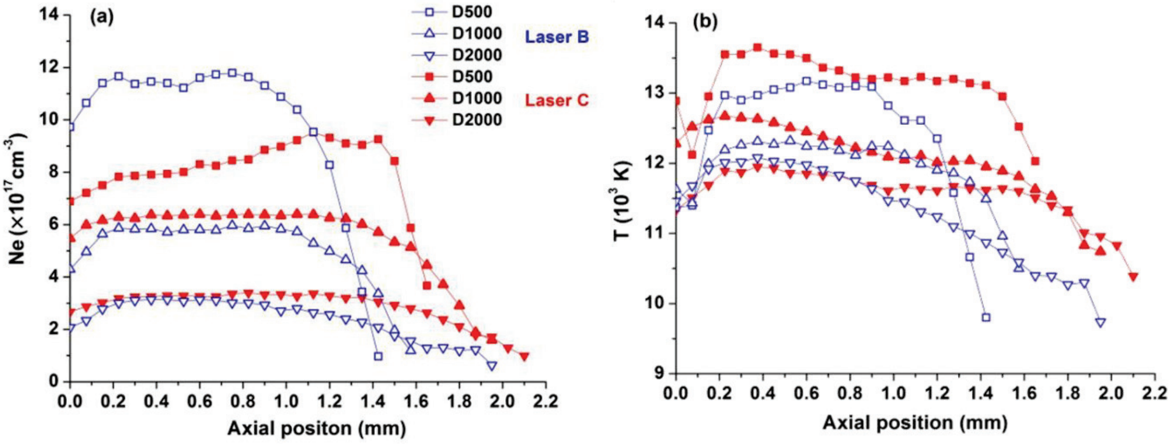

Figure 4.8 Axial profiles of the electron density (a) and the electron temperature (b) of the plasmas induced by the two types of laser pulse, laser B with pulse duration of 4 ns and laser C with pulse duration of 25 ns, at different detection delays.

We can see in Figure 4.8 (a), that the axial extent of the electron density corresponds to the zone of mixing between aluminum vapor and hot argon gas for the plume induced by the short laser pulse, from 0 mm to about ~ 1.4 mm for the delay D500. The same extent can be found for the temperature (Figure 4.8 b). Over the extent of the plasma, the profiles show a plateau of small variation in the middle of the distribution. Both parameters decrease near the target surface and near the propagation front of the plume, because of the thermal conduction in the interfaces with the target and with the cold ambient gas. Let us look at now the profiles for the plasma induced by the long pulse. The axial profiles of the electron density and the temperature are much more extended than the profile of emission intensity of aluminum. The extent of the plasma corresponds rather to that of the hot argon gas from the target surface to about 1.8 mm. Electronic population observed in the zone (from 0.8 to 1.8 mm) out of the extent of the aluminum vapor is therefore contributed by the ionization of hot argon gas. This means that in the case of ablation with the long pulse, the produced plume corresponds mainly to an argon plasma consisting of a thick excited and ionized argon layer enveloping a reduced mixing zone between aluminum and argon close to the target surface. The above observations confirm that when the LSD wave is initiated at enough high laser fluence, a longer duration pulse deposits more energy into the layer of hot gas leading to a deeper propagation of the LSD wave into the ambient gas. A long duration pulse is thus more strongly shielded than a short duration pulse and presents a smaller efficiency for ablation and for excitation of the ablated material.

The above result is quite different from what one can learn from the literature about a two-component plasma with a mixture of a metallic vapor and a monatomic gas like argon. In such plasma, the most of electrons would be contributed by the metallic vapor because of its lower ionization potential. However due to the specific internal structure of the plume that we show in this study, the situation can be different. In fact when LSD wave is initiated, the layer of shocked gas situated around the axial front of the plume is ionized by laser radiation. This layer in turn efficiently absorbs the tailing part of the laser pulse, which may have two simultaneous consequences: i) a high ionization degree of the shocked gas, and ii) a total shielding of laser pulse preventing the metallic vapor from its further interaction with laser radiation and its further ionization. In this case, electrons in the plasma can be dominantly contributed by the gas in the regions where its ionization is significant.

Let us compare now the temperatures and the electron densities of the plasmas induced by the two types of pulses. For a given delay, we find a higher temperature for the plasma induced by the long pulse (Figure 4.8 b). But at the same time, a lower electron density is found for it (Figure 4.8 a). Such comparison shows on the one hand, the efficiency of a long pulse to heat the ablation plume. On the other hand, it confirms the fact that a long pulse produces a plasma dominated by hot argon gas, while a short pulse generates a mixture between aluminum vapor and hot argon gas. The higher ionization potential of argon leads to a lower electron density for an Ar-dominant plasma than for an Al-Ar mixture plasma at the same temperature.

4.3. Resume

In this chapter we have studied the convoluted effects of laser fluence and pulse duration on the morphology and the internal structure of the plasma. In the early expansion delay interval, spectroscopic imaging technique is used to observe the morphology and the internal structure of the plasma. For longer delay, emission spectroscopy allows further characterizing the plasma with the profiles of electron density and temperature.

The ensemble of the results obtained in this study show that with a pulse of moderate fluence, the observed plasma morphology and internal structure are more likely due to laser-supported combustion (LSC) wave during the post ablation interaction. The characteristics of such interaction regime lead to a rather spherical expansion of the plume, a layered internal structure, and a fast decay of the ionized population of the ambient gas. Plasma shielding in this case is dominantly contributed by the ablation vapor, which leads to an absorption zone in the middle of the plume close to the target surface. The driving force of the plasma expansion comes in this case, from the center of the plume and it acts as a piston pushing the surrounding ambient gas away. Such mechanism of propagation leads to a rather spherical shape of the plume as we observed in our experiment. When LSC wave is initiated, the effect of pulse duration is to optimize the penetration through the layer of ionized ambient gas and to control the absorption in the ablation vapor. Our results show a better penetration through the shocked gas and a more efficient absorption by the ablation vapor for the long pulse, which leads to a more efficient excitation of the emission from the vapor.

With higher ablation fluence, the characteristics of propagation with laser-supported detonation (LSD) wave are observed. Such characteristics include a clearly elongated morphology of the plume, a dominant plasma core consisting of a mixture of aluminum ions and argon ions, and a significantly longer lifetime of argon ions. Plasma shielding in this case is dominantly contributed by the shocked and ionized ambient gas which is initially localized around the propagation front of the plume. Moreover, the effect of pulse duration leads to a stronger plasma shielding by the shocked and ionized ambient gas for a longer laser pulse. Consequently the long pulse induces a weak emission from the vapor. Such behavior is just the opposite with respect to what happens in the modest fluence ablation regime.

A delayed evaporation of neutral aluminum appears as a consequence of splashing ejection of melted aluminum bath lying in the crater. Such secondarily ejected aluminum vapor occupies the space left by the axial propagation of the plume close to the target surface, preventing from the entrance of the ambient gas in this zone.

The observed behaviors of the plasma in different ablation regimes can be summarized in Table 4-1.

Finally the qualitative explanations provided in this chapter for understanding our experimental results need to be confirmed and completed by detailed numerical simulation which represents the only way to take into account all the implications of the convoluted effects of the laser fluence and the pulse duration in a process as complex as the laser ablation and the propagation of the produced plasma into the ambient gas.

Table 4-1 Resume of the properties of the plasmas observed in different ablation conditions.

<table>
<tr><td>Fluence (J/cm^2)</td><td colspan="2">65</td><td colspan="2">160</td></tr>
<tr><td>Pulse duration (ns)</td><td>4</td><td>45</td><td>4</td><td>25</td></tr>
<tr><td rowspan="2">Plasma morphology</td><td colspan="2" rowspan="2">Spherical shape
Layered internal structure
Fast decay of the ionized population of the ambient gas</td><td colspan="2">Dominant plasma core consisting of a mixture of aluminum ions and argon ions
Significantly longer lifetime of argon ions</td></tr>
<tr><td></td><td>Secondary splash ejection of aluminum vapor</td></tr>
<tr><td>Axial profiles</td><td colspan="2">Long pulse: higher temperature and higher electron density</td><td colspan="2">Long pulse: higher temperature and lower electron density</td></tr>
<tr><td>Laser-supported absorption wave</td><td colspan="2">LSC: most absorbed by the ablation vapor</td><td colspan="2">LSD: most absorbed by the shocked gas</td></tr>
<tr><td>Emission of the ablation vapor</td><td colspan="2">More efficient with the long pulse</td><td colspan="2">More efficient with the short pulse</td></tr>
</table>

Chapter 5. Characteristics and microscopic mechanisms of laser-supported detonation wave in molecular ambient gas

After Chapter 4 where we have studied the effects of the laser parameters on the morphology and the internal structure of laser-induced plasma, we understand that the expansion behavior of the generated plasma can be greatly influenced by the laser parameters. In the present chapter, we are interested in the effects of the ambient gas on which the properties of the plasma can as well crucially depend. More specifically, the morphological information of the plume, including its size, the distribution of the species and its temporal evolution, are very important for a proper detection of the emission from the plasma. The understanding and the control of the morphology of the plasma are therefore important for the analytical performance of LIBS in terms of precision, repeatability and reproducibility.

According to the nature of the ambient gas, whether it is a monatomic gas (such as argon) or molecular gas (such as the atmospheric air), the mechanisms involved in the interactions between the vapor and the gas or the gas and the laser can be very different. Indeed, for a monatomic gas, the only microscopic processes are excitation and ionization. For the molecular gas however the situation becomes much more complicated with the contributions of other processes, such as dissociation, recombination and various chemical reactions. The microscopic energy exchange processes are thus different for these two types of gas. Consequently, the macroscopic propagation behaviors of the plasma should be different with the two different ambient gases. In addition, the influence of the nature of the ambient gas is necessarily correlated to the fluence of the laser pulse. According to the results presented in the last chapter, laser-supported absorption waves (LSAW) during the post-ablation interaction, especially the laser-supported detonation (LSD) wave, can greatly influence and modify the morphology of the plasma. Such influence is especially pronounced for IR (1064 nm) ns laser ablation at relatively high fluence (> 150 J/cm^2). However up to now, the effects of the nature of ambient gas (monatomic or molecular) as well as the microscopic mechanisms involved in LSD remain unclear. The study of this chapter has been designed to investigate the characteristics of the LSAW (particularly LSC and LSD) propagation of a metallic plasma in two types of ambient gases: argon (atomic gas) and atmospheric air (diatomic molecular gas) at moderate and high ablation fluence regimes.

5.1. Experimental investigation of the plasma expansion behaviors in different ambient gases

5.1.1. Moderate ablation laser fluence

Emission images of the plasma in the early stage of the expansion

Using an ablation energy of 20 mJ (corresponding to 65 J/cm^{-2}), and the procedure specified in Section 3.1, we first observed the expansion behaviors of the plume in the two types of ambient gas in the early stage of the expansion. Composite emissivity images obtained with the moderate ablation fluence in different ambient gases are shown in Figure 5.1. We note that the bottom line of the images represents the target surface. In these images, we can see a global layered structure of the plumes. Starting from the target surface and going upward the incidence direction of the laser pulse, we can successively meet the layer of neutral aluminum (green), the layer of ionized aluminum (red), the layer of ionized gas, argon or nitrogen (grey) and finally the layer of neutral gas, argon or nitrogen (blue).

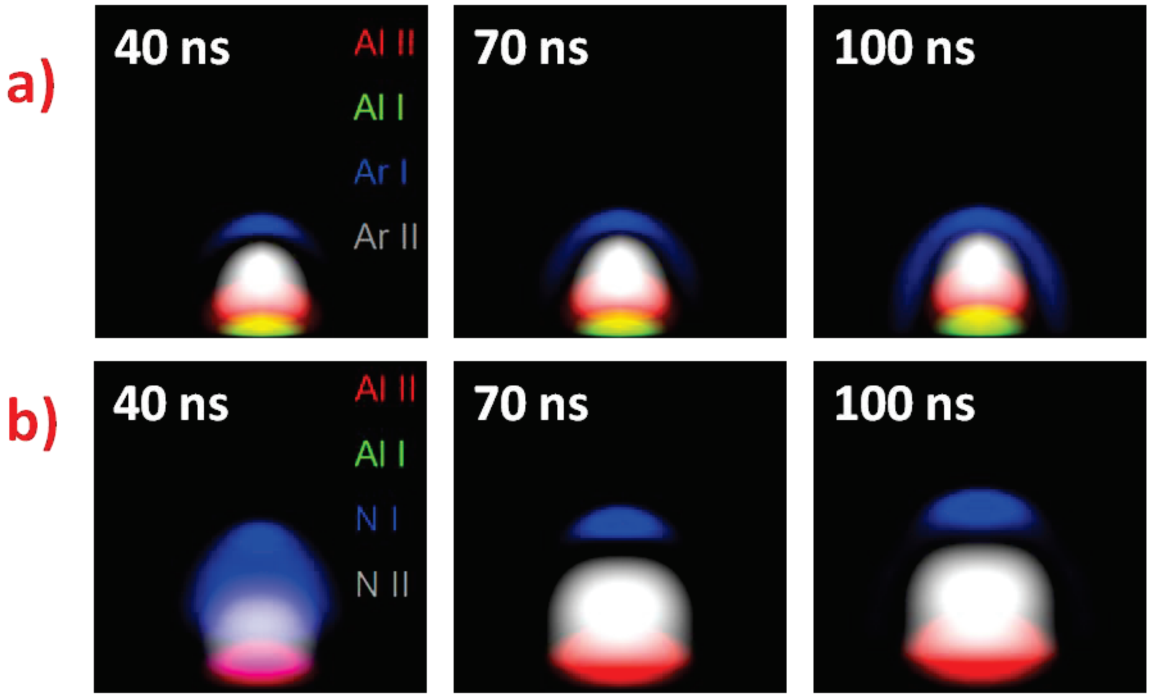

Figure 5.1 Composite emissivity images obtained with ablation with moderate laser fluence in different ambient gases (a) argon and (b) air. The delay is shown in each image. The real dimension of each picture is 1.5 × 1.5 mm^2, and the bottom line of the images represents the target surface. False colors are used to represent the different species in the plume with red for ionized aluminum, green for neutral aluminum, grey for ionized argon or ionized nitrogen and blue for neutral argon or neutral nitrogen. The intensity of each species is normalized to its own maximum.

Such arrangement of species in successive layers in a nearly spherical plasma morphology corresponds rather to the consequence of the LSC wave as we discussed in Chapter 4. In the LSC wave model, the layer of compressed ambient gas remains transparent for the laser radiation. It is why a significant tailing part of the ablation pulse transmits through the compressed gas layer and touches the ablation vapor. The propagation of the tailing part of the ablation laser pulse in the vapor leads to its ionization. Two subsequent layer structures can result from this interaction configuration.

1) If the laser pulse is enough strong after its transmission through the layer of shocked gas and/or the ablation vapor is not enough dense, then the vapor can be totally ionized. This corresponds to the case of air ambient gas (Figure 5.1 b);

2) If the laser pulse is not enough strong after its transmission through the layer of shocked gas and/or the ablation vapor is enough dense, then the vapor can only be ionized in its up part first touched by the laser pulse after its transmission through the compressed gas layer. This corresponds to the case of argon ambient gas (Figure 5.1 a).

At the same time, the fact that a significant part of ablation laser pulse transmits through the shocked ambient gas layer implies that the ionization of the ambient gas due to the ablation laser pulse is not strong in the sense that produced ions of the ambient gas is not dense and its extent limited in space. The populations of the ionized ambient gas observed in the images in Figure 5.1 may thus also contributed by the interaction with the ablation vapor heated by the tailing part of the ablation laser pulse. As we mentioned in Chapter 4, such interaction can be collisional excitation and ionization and/or absorption of UV radiation emitted by the vapor [89]. The formation of the ionized ambient gas above the ablation vapor would be thus ulterior to the transmission of the tailing part of the laser pulse through the shocked gas layer, in such way it does not contribute to the shielding of the laser pulse.

The observations made in the modest ablation fluence regime show therefore a similar morphology and structure of the plasma induced in argon or in air. More generally speaking, we can say that when the LSC wave represents the dominate mechanism of post ablation interaction, the nature of the ambient gas does not influence greatly the propagation behavior of the plasma. Qualitatively this can be easily understood since in the LSC wave propagation, the layer of compressed ambient gas, whether it is argon or the atmospheric air, remains transparent for the ablation laser pulse. The different optical properties of the ambient gases are not involved in the determination of the behavior of the plasma. The minor differences observed between the plasmas in the two kinds of ambient gas may rather relate to the hydrodynamic or thermodynamic properties of the gases. For example air is more compressible than argon ($\gamma_{air} = 1.4, \gamma_{Ar} = 1.67$). This leads to a larger plume at given delays with air than with argon as shown in Figure 5.1. This leads also to the fact that assuming the same amount of aluminum ablated from the target, in air we get a less dense ablation vapor than in argon. The last point explains why a population of neutral aluminum is obtained in argon but not in air at short delay.

In a practical point of view for LIBS application, we can say that with moderate ablation fluence, small difference exists between the plasmas induced in argon or in air. The ablation vapor is more confined in argon, leading to a stronger emission signal from the vapor for a detection system with a given collection surface. This configuration is more suitable for sensitive detection of trace elements. A denser plasma can corresponds however to a severer self-absorption effect. This means that if the sensitivity of the detection is not the main objective, ablation in air with moderate laser fluence is also a good choice for LIBS.

Axial profiles of the plasma at long delay

In order to confirm the observations performed with spectroscopic imaging presented in the above section and further investigate the physical properties of the plasma, time- and space-resolved emission spectroscopy was used to record the axial emission intensity profiles of the plasma propagating in the two kinds of ambient gas. The advantage of the emission spectroscopy is that not only the emission intensity but also the profiles of electron density and temperature can be obtained. The obtained results are shown in Figure 5.2.

Note that in Figure 5.2, the horizontal axial represents the distance from the target surface (the origin of the axis corresponds to the surface). We can remark first that Figure 5.2 (a) and (b) show similar emission intensity profiles for the both plasmas induced in Ar or in air. As mentioned in the above section, the plasma in air presents a slightly larger extent than that in argon. These results confirm well those obtained with spectroscopic images and presented above.

Axial profiles of the electron density and the temperature are shown in Figure 5.2 (c) and (d). We can see that the profile of the electron density fits the extent of the emission intensity profiles of aluminum. The both observed electron density and temperature are significantly higher in argon than those in air for a given delay. This is expected because of the lower thermal conductivity of argon than air [105]. For LIBS application, the higher temperature and electron density in argon lead to a better signal-to-noise ratio for analysis. [105] This property underlines again the advantage of the use of argon in LIBS often reported in the literature.

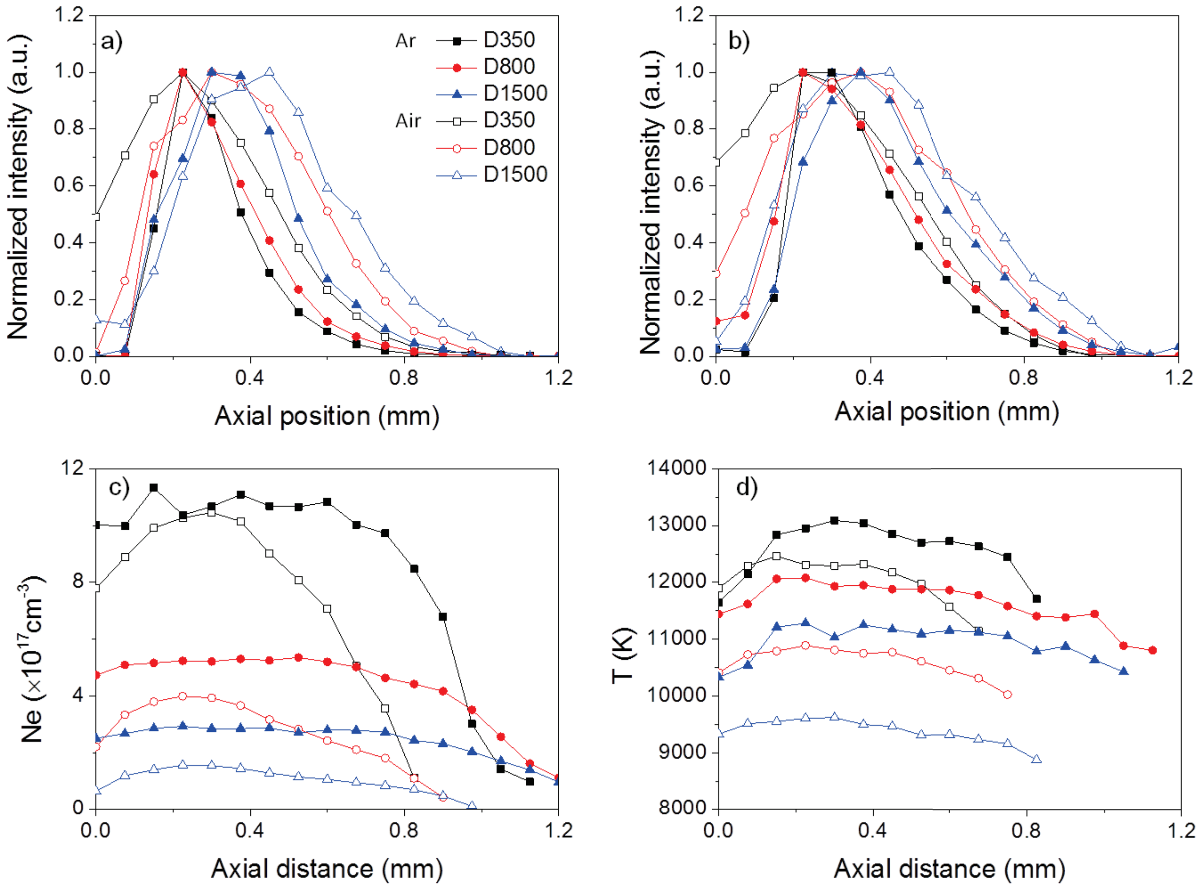

Figure 5.2 Axial emission intensity profiles of plasmas induced by 20 mJ laser pulse in Ar or in air. (a) neutral aluminum, (b) ionized aluminum, (c) electron density and (d) plasma temperature.

5.1.2. High ablation laser fluence

Emission images of the plasma in the early stage of the plasma expansion

With an ablation pulse energy of 50 mJ (corresponding to 160 J/cm^{-2}), we observed the early stage expansion of the plasma with the same procedure as in the precedent section. Composite emissivity images obtained with the high ablation laser fluence in different ambient gases are shown in Figure 5.3. For the both ambient gases, a population of ionized ambient gas can be observed with a large spatial extent which occupies almost the entire volume of the plasma. In contrast, population of neutral ambient gas is almost absent at very short delay. This situation corresponds to a complete ionization of the compressed or shocked ambient gas. As we already mentioned in Chapter 4, the ablation with the high laser fluence leads to the LSD regime in the post-ablation interaction. It is well known that in the LSD propagation, the tailing part of the ablation laser pulse is almost absorbed by the layer of shocked gas leading to its complete ionization. Our previous works [106, 107] further demonstrated that the ignition of LSD for an ablation plume propagating in an argon ambient gas leads to a mixture of ions of argon and the ablation vapor, aluminum for instance. This phenomenon is again observed in our experiment and shown in Figure 5.3 (a). At longer delays, neutral ambient gas appears first on the top of the plasma in argon and rather in the peripheral of the plasma in air.

It is very striking to remark that for the plasma in air, the above mentioned mixing between the ions of nitrogen and aluminum cannot be observed. On the contrary, the population of aluminum ions is observed confined in a small volume in the lower part of the plume near the target surface. We can also remark that the axial extent of the plume is smaller in air than in argon. This observation is just opposite of what happens in the moderate ablation fluence regime, where due to the bigger compressibility of air, the extent of the plasma is larger in air than in argon. These observations provide the evidence that in the high fluence ablation regime where the LSD wave is ignited, the behaviors of the plasma induced in air is very different from those of the plasma induced in argon.

In the practical point of view for LIBS application, a small vapor confined in a region close to the target may present a large inhomogeneity, a situation disadvantageous for a high performance analysis.

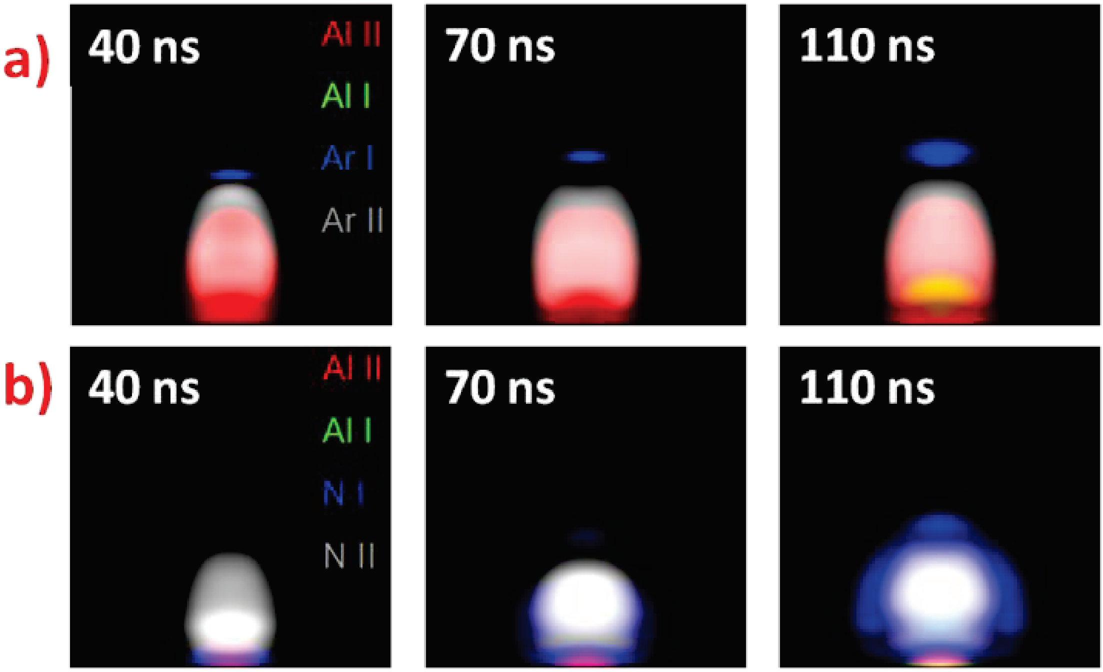

Figure 5.3 Composite emissivity images obtained with ablation with high laser fluence in different ambient gases(a) argon and (b) air. The delay is shown in each image. The real dimension of the images is 2 × 2 mm^2, and the bottom line of the images represents the target surface. False colors are used to represent the

different species in the plume with red for ionized aluminum, green for neutral aluminum, grey for ionized argon or ionized nitrogen and blue for neutral argon or neutral nitrogen. The intensity of each species is normalized by its own maximum.

Space-resolved emission spectra

In order to confirm the observations performed with the spectroscopic imaging, we further record emission spectra at different axial positions in the plasma using the "spectroscopy" type setup described in Chapter 3. In Figure 5.4, we show the recorded spectra for a detection delay of 50 ns. In Figure 5.4 (a), we can see that for the plasma induced in argon, whatever the detection position is in the plasma, there is always simultaneously aluminum ions (Al II 358.7 nm line) and argon ions (Ar II 488.0 nm line). This confirms the image observation shown in Figure 5.3 (a) for the mixing between the ions of aluminum and argon. In Figure 5.4 however, aluminum ions (Al II 358.7 nm line) and nitrogen ions (N II 500.0 nm line) can be simultaneously observed only in the lower part of the plasma. For an observation position higher than 0.45 mm, only nitrogen ions can be observed. The results from space-resolved emission spectroscopy confirm therefore the observations with spectroscopic imaging.

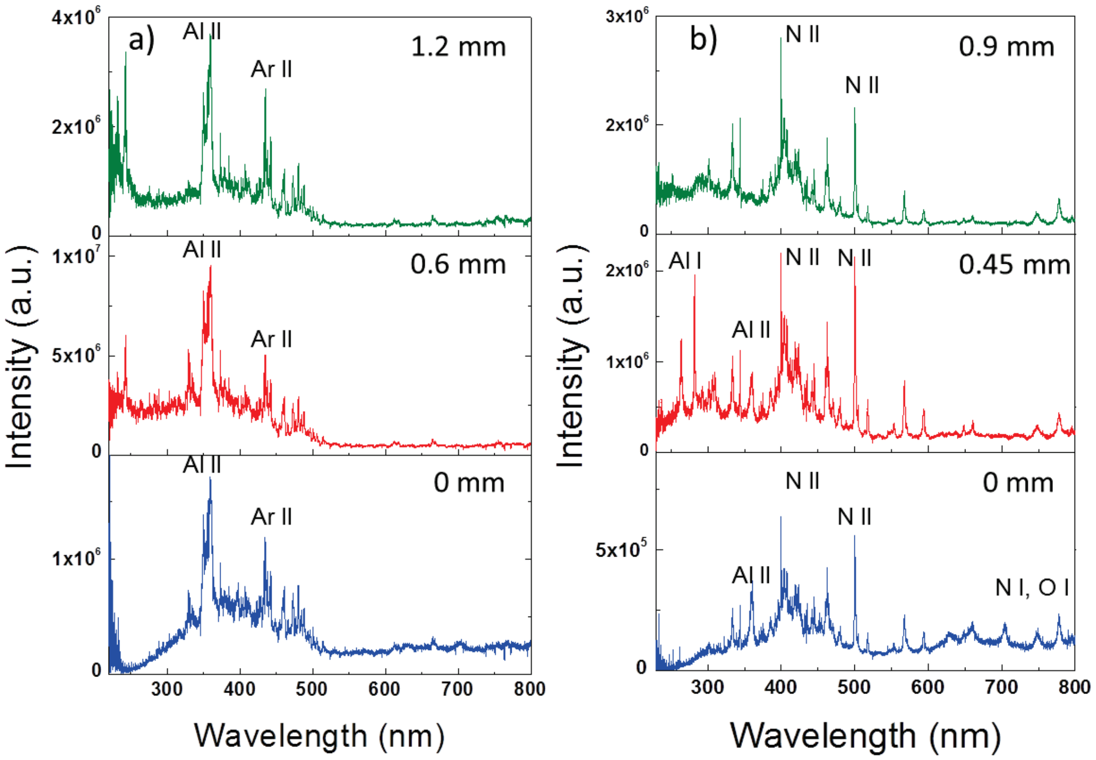

Figure 5.4 Emission spectra of the plasma at different axial positions in the ambient gas of (a) argon and (b) air recorded at a delay of 50 ns.

Axial profiles of the plasma at long delay

For longer delay, the axial profiles of emission intensity, electron density and temperature of the plasma are shown in Figure 5.5. Look at first Figure 5.5 (a) and (b). Significant differences can be observed for the plasmas induced in the two types of ambient gas. In argon, the aluminum vapor, atoms as well as ions, exhibits emission intensity profiles which propagate away from the target surface as the detection delay increases. In air on the contrary, the aluminum vapor remains static close to the target surface (0 mm to ~ 1.0 mm) without significant upward motion of the ensemble of the profiles. Look at now Figure 5.5 (c) and (d) for the axial profiles of the electron density and the temperature. Here again different behaviors can be observed between the plasmas induced in argon and air. In argon, both the profiles of the electron density and the temperature profiles exhibit an upward propagation, while in air the both profiles remain close to the target surface. Similar to the case of ablation with the modest laser fluence, higher electron density and temperature are measured for the plasma in argon than for the plasma in air.

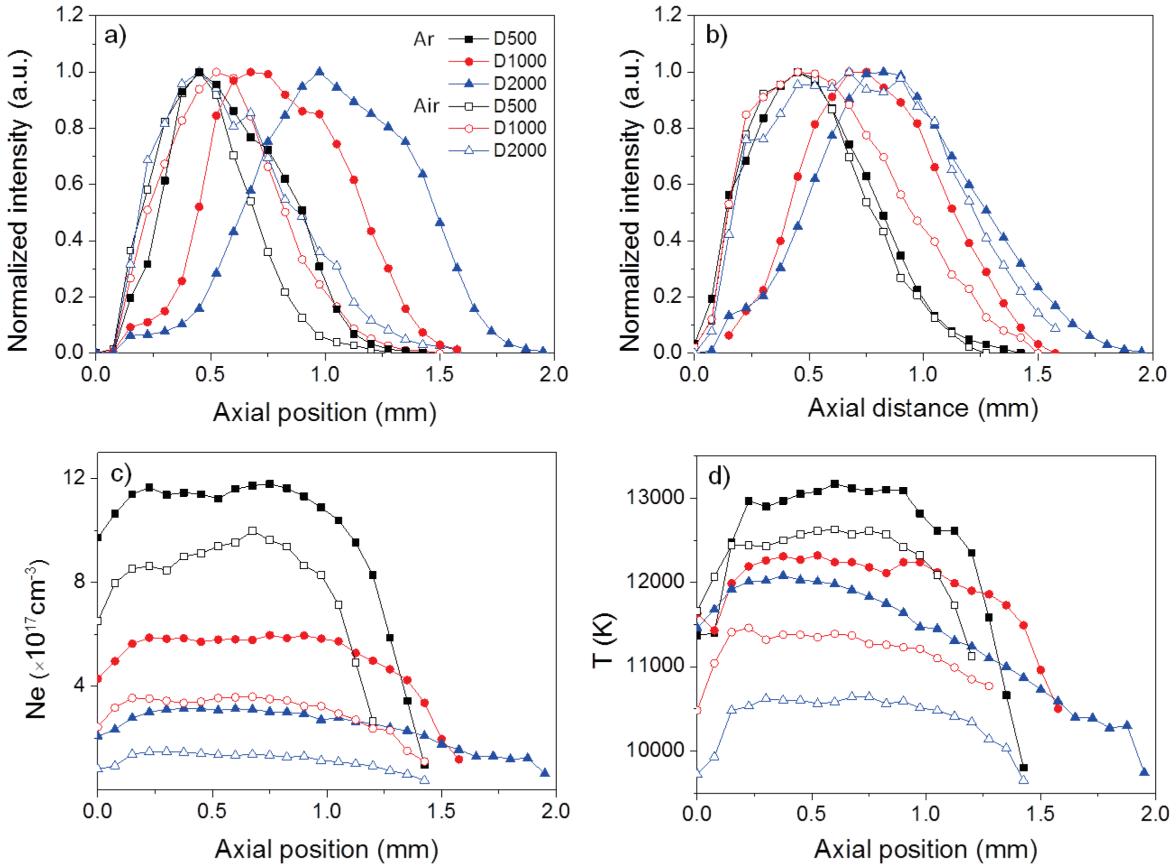

Figure 5.5 Axial profiles of the plasma induced by a 50 mJ laser pulse in Ar and air. (a) neutral aluminum emission, (b) ionized aluminum emission, (c) electron density and (d) plasma temperature

Different morphologies and structures are therefore observed for the plumes induced in the two different types of ambient gas over the investigated delay interval which is concerned by LIBS measurements. In argon at short delay, the plume corresponds to a mixture of hot and ionized gases of aluminum vapor and argon over the total extent of the plume (0 mm to ~ 1.8 mm). The aluminum vapor is evaporated from the target, while the hot argon gas is contributed by the layer of the ambient gas initially surrounding the vapor and ionized by absorption of laser energy during the process of LSD wave. Moreover, the electron density and temperature are higher in argon than in air as the case of ablation with the moderate laser fluence. On the other hand in air, the ablation vapor is confined in a region close to the target surface (0 mm to ~1 mm) and separated from the ionized ambient gas. The comparison shows therefore the advantage, in the practical point of view, to perform LIBS measurement in argon with a more uniform and extended plasma which facilitates a stable collection of the emission from the plasma, and a higher temperature which increases the intensity and the lifetime of the emission from the plasma. Such practical conclusion drawn here for the high fluence ablation regime is indeed the same as that for the moderate fluence ablation regime. In fact, the advantage to use argon as ambient gas for LIBS measurement has been demonstrated since longtime. But in our work, beyond the known empirical approach, we provide more detailed understanding of the principle. Starting with the better understood principle, we will be able to better assess the necessity to use argon ambient gas in a specific application by taking into account the practical complication related to the introduction of argon in a given experimental arrangement.

5.1.3. Craters produced in different ambient gases

To further confirm the difference observed between the behaviors of the plasmas induced in argon or in air with high fluence ablation and to observe the consequence of such difference on the craters left by ablation on the target surface, we have observed the corresponding ablation craters. Figure 5.6 shows the SEM (scanning electronic microscope) images of the ablation craters in different ablation conditions. With the moderate ablation fluence of 65 J/cm^2, the form of the craters produced in both argon and air are quite similar as shown in Figure 5.6 (a) and (b), in the sense that we can observe an effective mass removing from the crater for the both cases. This confirms our results and discussions in Section 5.1.1. By saying this however, we should mention that in this study we only intend to draw qualitative conclusion by using existing models such as LSC and LSD waves. This means that even through in the moderate fluence ablation regime the LSC is a dominant process, we cannot exclude some characteristics of LSD also being observed. In fact, our choice of ablation regime was also conditioned by experimental constraints, for example the concern of having enough large signals for detection. It is why we did not choose a very small ablation laser fluence to be sure being with a pure LSC regime. Instead, a reasonably moderate fluence was chosen for the moderate fluence ablation regime, which allowed still a good signal for detection. The above remark explains why some differences can be observed between the craters in Figure 5.6 (a) and (b) even through in our understanding, we classify the both cases into the same physical model.

For the high ablation fluence at 160 J/cm^2, in argon (Figure 5.6 (c)), a deep crater is clearly observed, showing effective mass removal. On the contrary in air (Figure 5.6 (d), the crater is only distinguishable with irregular surface modification. Such surface morphology suggests a significant material redeposit after being first removed from the surface. Such difference observed between the craters left by ablations in argon and in air corresponds well to the difference observed for the propagations of the plasmas induced in these two different ambient gases. Indeed in argon, a propagating ablation vapor facilitates the mass removal, while in air a stagnating ablation vapor near the target surface may lead to its redeposit on the crater during the re-condensation of the plume. The crater observation is therefore coherent with our image and emission spectrum observations presented in the above sections.

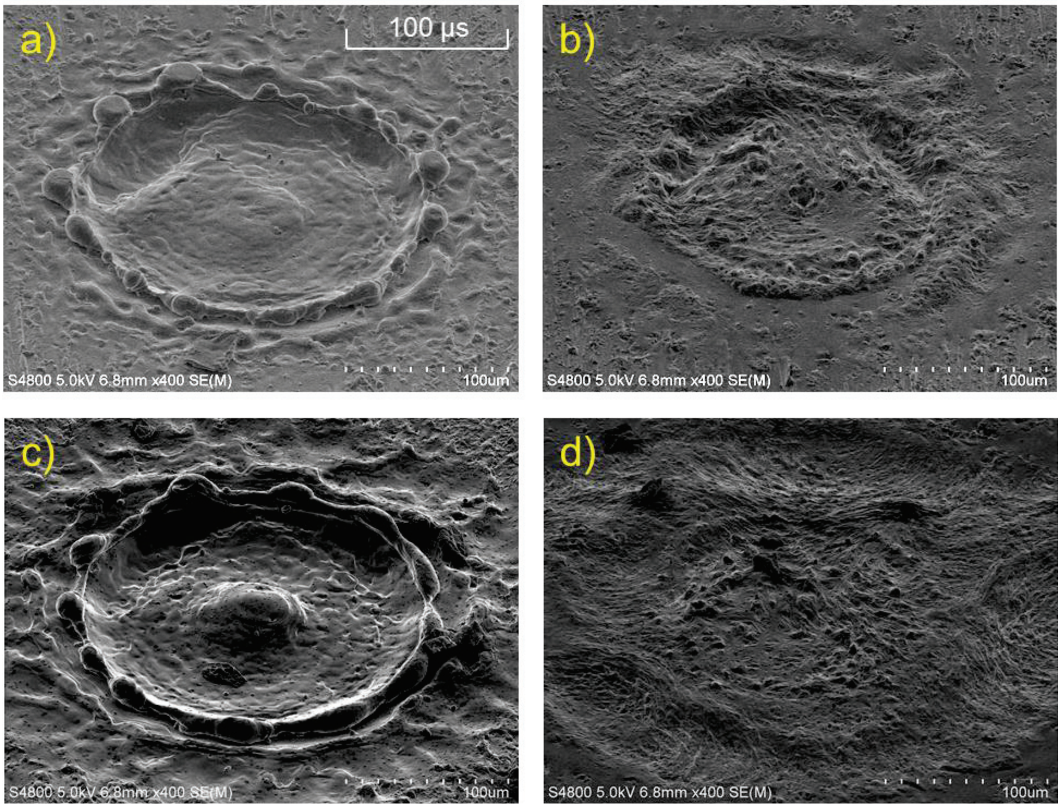

Figure 5.6 SEM images of ablation craters in different experimental conditions of ablation fluence and ambient gas. (a) 65 J/cm² in argon, (b) 65 J/cm² in air, (c) 160 J/cm² in argon and (d) 160 J/cm² in air. Each crater accumulates 10 laser shots.

5.1.4. Summary for ablations with high or moderate laser fluence and in argon or air ambient gas

We can thus resume the observed expansion behaviors of the plasma in the experimental configurations investigated in Table 5-1 :

Table 5-1 Behaviors of the plasma in different ambient gases and different ablation fluence regimes

Fluence	Moderate (65 J/cm^2)		High (160 J/cm^2)	
Ambient gas	Argon	Air	Argon	Air
Structure of the plasma at short delay	Layer structure, from the surface of the target and in the upward direction: neutral Al, ionized Al, ionized ambient gas and neutral ambient gas		Propagating Al vapor, mixing between ions of Al and Ar over the whole volume of the plume	Stagnating Al vapor close to the target surface, separation between Al vapor and shocked air ambient
Post-ablation interaction model	LSC wave		LSD wave	
Axial profiles of at long delay	Emission intensity profiles similar for the both ambient gases		Large Al vapor axial extent propagating away from the target	Small extent of Al vapor stagnating near the target surface
	Electron density and temperature higher in argon than in air			
Craters	Similar crater with effective mass removal		Deep crater with concentric rings, effective material removal	Shallow crater with irregular surface modification, material redeposit

5.2. Investigation and explanations for the different LSD wave propagations in argon and in air

We can see from the results presented in the first part of this chapter that for moderate laser fluence ablation where the LSC wave represents the dominant process in the post ablation interaction, plasmas induced under air or argon ambient exhibit quite similar behaviors in their propagation. This observation underlines in fact, the minor implication in the LSC wave of the ambient gas, since whatever the ambient gas is, air or argon, it remains essentially transparent to the ablation laser radiation. Following such argumentation, it is natural to foresee that in the high laser fluence ablation regime, the expansion behavior of the plasma changes according to the property of the ambient gas, since the ignition and the process of the LSD wave depend on the ambient gas. This is exactly what we have experimentally observed and presented in the first part of the present chapter. Accepting the principle of the different behaviors in such specific conditions does not mean that we understand the mechanisms involved in the process. And such understanding is also absent in the literature. It is why in our experiment, we specifically designed a series of complementary observations in order to go into the detailed of the understanding of the phenomenon. In the following part of this chapter, we will describe such complementary investigations and discuss the results obtained. Moreover, the knowledge and models from the literature will be used to interpret the experimental results and explain the observed difference between the plasmas induced in air or in argon at high laser fluence ablation regime. For a clear organization of our presentation, we will structure our explanations within two points of view of macroscopic and microscopic frameworks.

5.2.1. Macroscopic description with a faster LSD wave propagation in argon

Experimental determination of the propagation velocity of LSD wave in different gases

In this section, we focus on the high ablation fluence regime and perform the comparison between the plasmas induced in air or in argon. As we mentioned, in this ablation regime, the LSD wave is ignited in air as well as in argon. This situation introduces an important simplification in the sense that the laser absorption zone follows directly behind the shockwave and moves at same velocity [40]. Together with the fact that the absorption of laser radiation leads to the ionization of the shocked gas and the propagation of the LSD wave, we can understand that in this case, the LSD wave propagates as an ionization wave at the same velocity as the shockwave. Such simplification has a practical importance that the propagation of the LSD wave can be monitored with emission from the continuum over the early stage of the plasma expansion when the laser radiation is still present. This is because the continuum emission from the plasma is due to free-free transitions or free-bound transitions involving free electrons.

It is why we used the "image" type setup described in Chapter 3 together with a narrow band filter with a central wavelength of 530 nm to record plasma images with the continuum emission at different delays in argon and in air. The two obtained series of images are shown in Figure 5.7. We specify that in this spectral range, there is no emission line at the delays used for image recording.

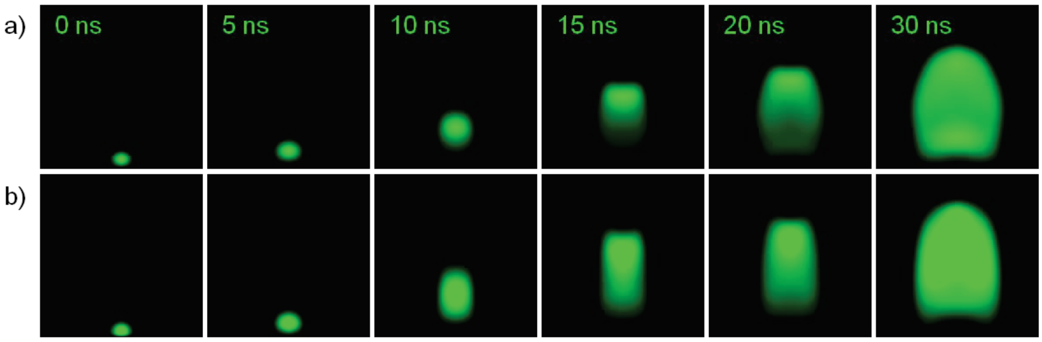

Figure 5.7 Continuum emission images at different delays with the high ablation energy (160 J/cm²) in air (a) and argon (b). The bottom line of the images corresponds to the target surface and the real dimension of the images is 1.0 ×1.0 mm².

The images in Figure 5.7 show already a higher axial propagation speed for the plasma in argon (Figure 5.7 b). From these images, we can further extract the position of the axial front of the emission zone, which corresponds to the LSD as well as the ionization wave front, as we discussed above. Such position as a function of the delay is shown in Figure 5.8 a. We specify that the origin of the time corresponds to the moment when the propagating front of the laser pulse touches the target. It is therefore reasonable to think that over ~ 20 ns the laser radiation is significantly present and interacts with the system including the target surface and the induced plume. Providing such consideration, we can see in Figure 5.8 (a) clear faster propagation of the LSD wave in argon than in air over the post ablation interaction of an interval of about 20 ns. The derivative of the data presented in Figure 5.8 (a) leads to the propagation velocity of LSD wave as shown in Figure 5.8 (b). A larger velocity is effectively measured for the plasma in argon in the interval of the post ablation interaction.

As complementary information, we plot as well the position of the transversal radius of the emission image as a function of the delay, as shown in Figure 5.8 (c). Without laser radiation, the radial expansion of the continuum emission images corresponds to the expansion of the ordinary shockwave without support from the laser. In Figure 5.8 (c) and Figure 5.8 (d) where the corresponding velocities are extracted, we can first remark similar radial velocities in the both ambient gases. We can also remark a significantly smaller shockwave propagation velocity in the radial direction than in the axial direction. This clearly shows the acceleration of the shockwave by LSD in the axial direction. A detail concerning the beginning of the radial expansion is worth to mention here: a smaller displacement is observed at very early stage of the expansion. This corresponds to the fact that at its beginning, the expansion of the plasma is essentially two dimensional with predominate axial propagation. The radial expansion becomes effective when the axial dimension of the plasma becomes comparable with its radial one.

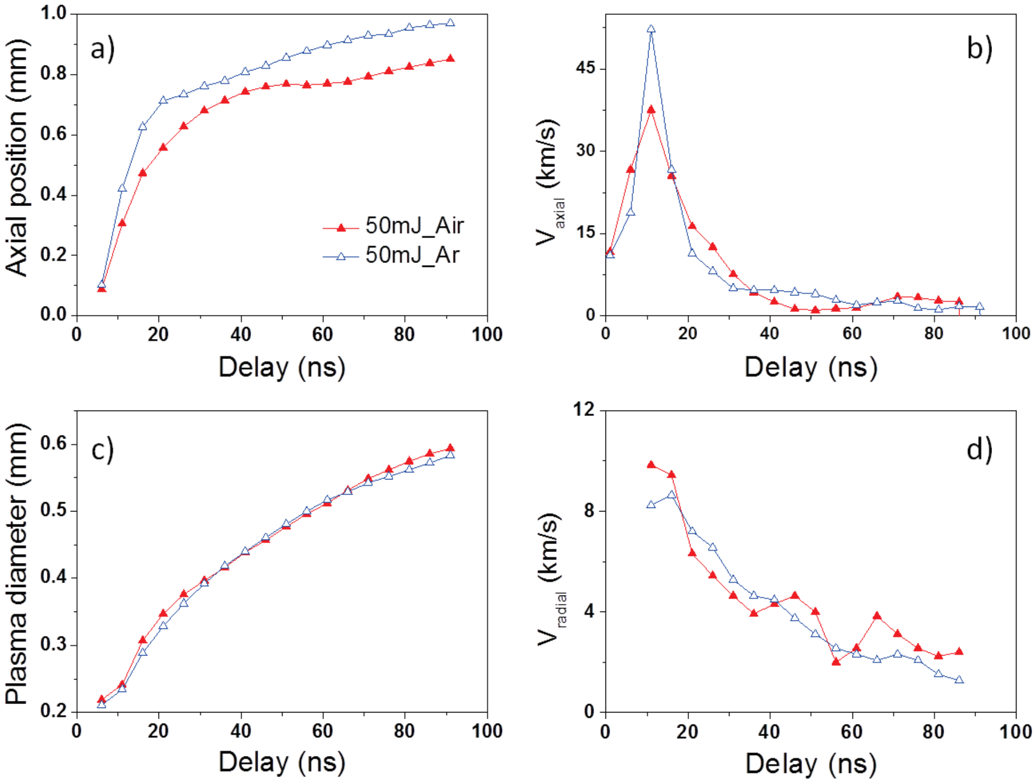

Figure 5.8 Displacement and velocity of the fronts of the continuum emission zone as a function of the delay in different ambient gases with high laser fluence ablation. (a) axial position of the front; (b) axial velocity of the front; (c) position of the lateral front at an axial position of 0.1 mm; (b) radial velocity at an axial position of 0.1 mm.

From Figure 5.8 c, experimental LSD wave velocities can be estimated as:

$$V_{LSD}^{Ar} \approx 52 \text{ km/s}$$

$$V_{LSD}^{Air} \approx 38 \text{ km/s}$$

$$V_{LSD}^{Ar}/V_{LSD}^{Air} \approx 1.37$$

Interpretation with the macroscopic hydrodynamics model

In the hydrodynamic model, by imposing the conservation of energy, momentum and mass in the zone behind the LSD wave front, where all the laser energy is absorbed, the velocity of the shockwave, which is identical to the LSD wave speed, is given by [40]:

$$V_{LSD} = \left[\frac{2(\gamma^2 - 1)I_0}{\rho_0}\right]^{\frac{1}{3}}$$

(5-1)

where V_{LSD} is the velocity of the LSD wave, ρ_0 is the density of the ambient gas, I_0 the incident laser irradiance and γ is the ratio of specific heats. For an ideal gas,

$$\gamma = \frac{f + 2}{f}$$

where f is the degrees of freedom. For a monoatomic gas as argon, with three degrees of freedom:

$$\gamma = \frac{3 + 2}{3} \approx 1.67$$

While for a diatomic gas such as the atmospheric air, with five degrees of freedom (three translational and two rotational degrees of freedom):

$$\gamma = \frac{5 + 2}{5} = 1.4$$

So γ is 1.4 for air and 1.67 for argon.

Provided that the initial conditions for argon and air are the same, so in Eq. (5-1), I_0 takes the same value. At 20 °C and 101.325 kPa, dry air has a density of 1.20 g/L and the density of argon is 1.45 g/L. Therefore we get

$$V_{LSD}^{Ar} \approx 1.2\, V_{LSD}^{Air}$$

(5-2)

So the LSD wave in argon is significantly faster than that in air, which is corresponds quite well to our experiment observation in Section 5.2.1. The consequence of a larger LSD velocity is that there is a larger difference with respect to the propagation velocity of the ablation vapor, which allows the last to propagate behind LSD wave. This corresponds to the case of the plasma in argon ambient. In this case, the fast upward propagation of the ionized argon leaves behind a low pressure zone, which by aspiration, facilitates the upward propagation of the aluminum vapor. The result is the observed mixing between the ions of aluminum and argon. In air ambient, a reduced axial propagation of the LDS wave may contribute to prevent upward motion of the aluminum vapor. However this argument is in any case not sufficient to explain the observed stagnation of the aluminum vapor close to the target surface. It is why in the following section, we will develop a second argument based on the microscopic mechanisms of the ignition of LSD wave in argon and in air, which as we will see, are different.

5.2.2. Microscopic explanation: different LSD ignition mechanisms in argon and in air

In order to develop our argument, we will first, in this section, present the results of several complementary observations. We will then deduce, with the help of the understanding elements from the literature, the different pathways leading to the LSD regime in the two different gases.

Space-resolved emission spectrum at a delay of 15 ns

This observation consisted in recording the emission spectrum of the plasma just after the termination of the laser pulse and observing its distribution over the axial extent of the plasma. Figure 5.9 shows the continuum emission at delay of 15 ns recorded at different axial positions in the plasma induced in the two different ambient gases: (a) argon and (b) air. Starting from the surface of the target (axial position = 0 mm) and going upward, two groups of continuum emission can be observed, one in the lower part of the plume and the other in its up part. If we assume that the blackbody emission is a good approximation of the continuum emission recorded, we can estimate the temperature of the plasma in the two distinguished regions by using the Wien's displacement law:

$$\lambda_{max} T = b \tag{5-3}$$

where λ_{max} is the spectrum peak wavelength, T is the absolute temperature of the black body and b is a constant of proportionality called Wien's displacement constant and equal to 2.8977721×10^{-3} m K.

So for the first group of spectrum recorded in the lower part of the plume, with a wavelength λ_{max} of about 500 nm, a temperature of 5 800 K can be extracted. For the second group of spectrum recorded in the up part of the plume, with a peak wavelength of about 240 nm, a temperature of about 12 000 K is extracted. This means that the aluminum vapor is colder than the ionized gas. This allows us to confirm that in this case, the LSD wave leads to efficient absorption of laser energy by the ionized gas. Moreover in argon, at such very early stage of the expansion, due to the faster propagation of the LSD wave, the lower part of the plume with aluminum vapor is well separated from the up part of the plume with ionized gas as indicated by Figure 5.9 (a). In air in contrast, the slower propagation the LSD wave leads to a zone of overlapping between the low temperature and the high temperature parts of the plume at 0.2 mm from the target surface as indicated by Figure 5.9 (b).

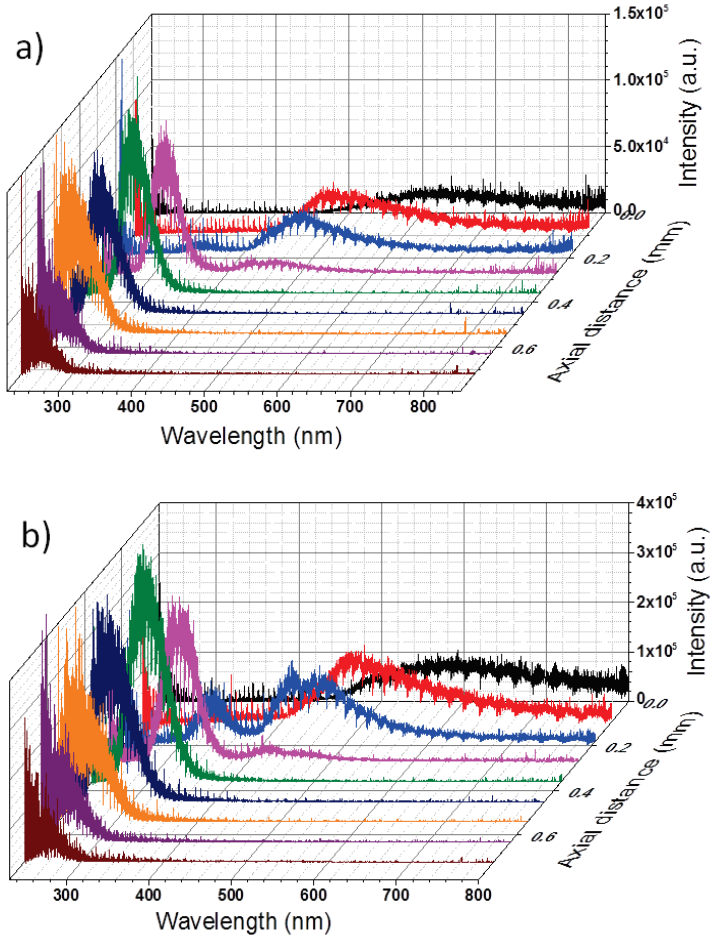

Figure 5.9 Emission spectra from the plasma at delay of 15 ns for different axial positions in the ablation plume induced in argon (a) and in air (b).

Excitation processes in the shocked gas

After the shockwave passing through the ambient gas, the ambient gas is excited. Such excited gas is called shocked gas. The results presented in the precedent section show a temperature of about 12 000 K in the shocked gas. With such high temperature, for an atomic gas such as argon the electrons are excited to upper levels, even to the continuum and getting ionized. For a molecular gas, such as the atmospheric air, dissociation can also occur besides electronic excitation processes. In order to observe the excitation state of the shocked gas and its evolution, we recorded the emission spectrum of the plasma at an axial position of 1 mm from the target surface for different detection delays. The results are shown in Figure 5.10. We can see that in argon, absorption spectrum is first observed on the continuum emission at a delay shorter than 150 ns. In Table 5-2, we list the spectroscopic parameters of the observed absorption line of Ar I in the spectral range from 690 to 780 nm. We can see that all these lines have an energy of the lower level of the transition larger than 11.5 eV. It means that the excitation by the shockwave is efficient enough to populate levels with energy higher than 11.5 eV. In other word, the excitation energy available in the shockwave is at least 11.5 eV.

Now let us think about the effect of such excitation energy for air, since a similar temperature is observed in shocked air as we discussed above (Figure 5.9 b). As we know the dissociation energy of oxygen and nitrogen molecules in the ambient temperature and pressure are respectively 5.11 eV and 9.74 eV [54], we understand easily that when the shockwave passes through the ambient air, molecules of oxygen and nitrogen are first dissociated. This explains the observation of the emission lines from atomic oxygen and nitrogen at very early stage of the plasma expansion as shown in Figure 5.10 (b). We list in Table 5-3 the spectroscopic parameter of the lines observed for atomic oxygen and nitrogen. We can see that the energies of the upper levels of the transitions observed in the spectrum are in the order of 12 eV, thus accessible with the excitation energy available in the shockwave as we discussed for the excitation of the atomic argon.

Table 5-2 Spectroscopic parameters for Al I emission lines observed in the experiment. A_{ki} is the Einstein coefficient, E_i and E_k are the energy of lower and upper levels of the corresponding transition.[110]

Wavelength (nm)	A_{ki} (s^{-1})	E_i (eV)	E_k (eV)
696.54	6.39e+06	11.55	13.33
706.72	3.80e+06	11.55	13.30
727.29	1.83e+06	11.62	13.33
738.40	8.47e+06	11.62	13.30
750.39	4.45e+07	11.83	13.48
751.47	4.02e+07	11.62	13.27
763.51	2.45e+07	11.55	13.17
772.42	1.17e+07	11.72	13.33

At longer delays, we can see in Figure 5.10 (a) that the absorption spectrum becomes emission spectrum. This means that further collisional excitations in the plume lead to significant population in higher excited states of atomic argon with energy larger than 13.5 eV. For the plasma in air, Figure 5.10 (b) shows the persistence of the emission lines from O I and N I due to a continuous population of the involved upper states by collisional excitations. The line shape becomes narrower because of the reduction of the electron density in the plasma.

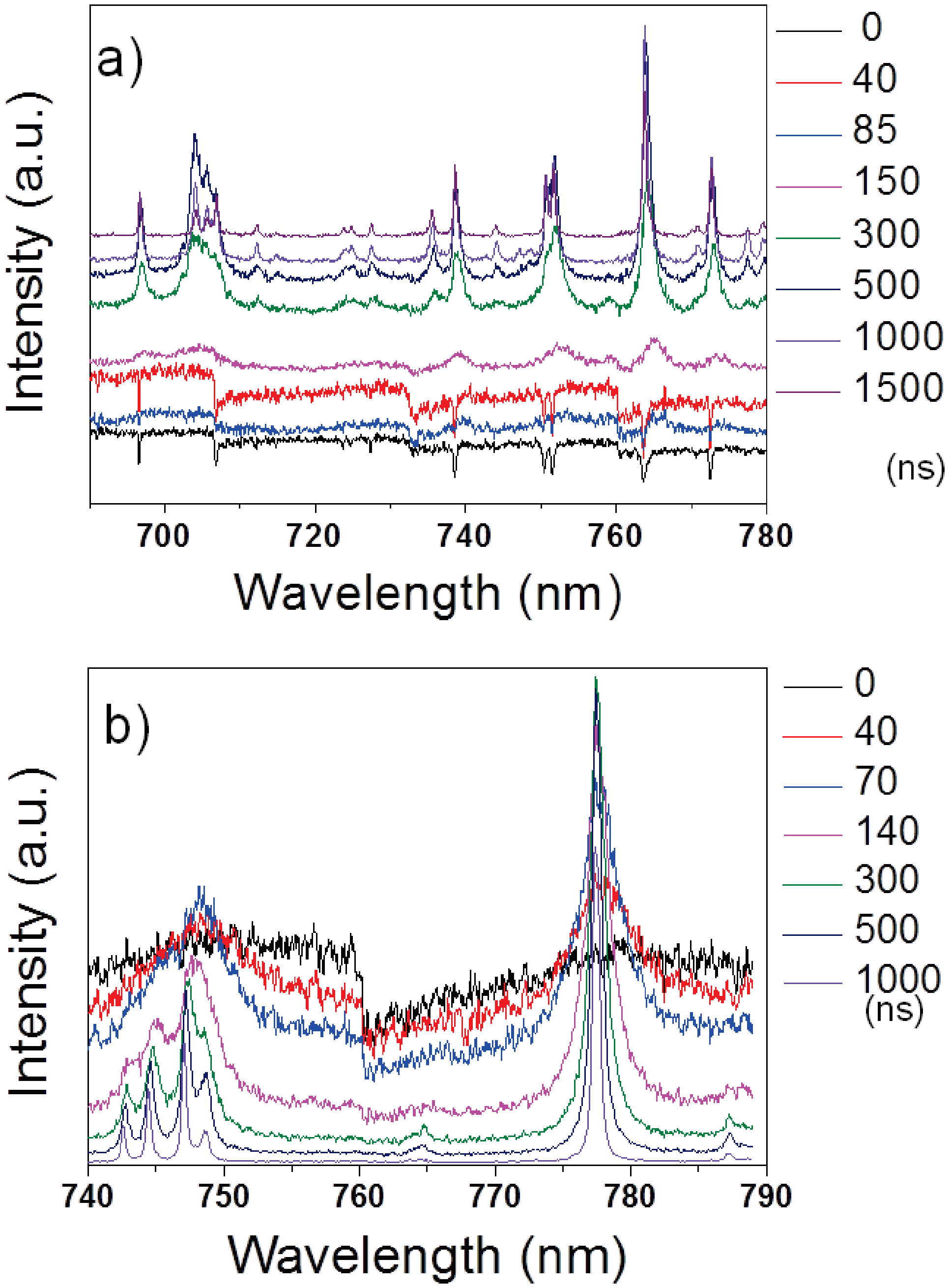

Figure 5.10 Emission spectra of the shocked gas at different delay from the plasma induced in different ambient gases and at the axial position of 0.2 mm from the target surface.

Table 5-3 Spectroscopic parameters for N I and O I emission lines observed in the experiment. A_{ki} is the Einstein coefficient, E_i and E_k are the energies of the lower and the upper levels of the corresponding transition. [110]

	Wavelength (nm)	A_{ki} (s^{-1})	E_i (eV)	E_k (eV)
N I	742.364	5.64e+06	10.33	12.00
	744.229	1.19e+07	10.33	12.00
	746.831	1.96e+07	10.34	12.00
O I	777.194	3.69e+07	9.15	10.74

Mechanism of ignition of LSD wave in argon

The detailed observations on the structure of the plasma and the excitation state of the shocked gas presented above allow us now to discuss the ignition mechanisms of LSD in argon and in air.

Let us first look at the case of argon. In argon, we know that the pathways leading to the LSD wave ignition starts with the excitation by the shockwave of atomic argon to its excited state with an energy in the order of 11.5 eV. In addition, in such shockwave velocity, about 10% of atomic argons are already ionized. [111] Taking in to account the ionization potential of atomic argon of 15.8 eV and the photon energy corresponding to the laser radiation at 1064 nm of 1.17 eV, we understand that the ablation laser radiation cannot directly ionize excited argon. However, the following reactions can lead to the further ionization of the shocked argon ambient gas:

$$h\nu(\lambda < 280\ nm) + Ar^* \rightarrow Ar^+ + e \tag{5-4}$$

$$e + Ar \rightarrow Ar^* + e \text{ then } e + Ar^* \rightarrow Ar^+ + 2e \tag{5-5}$$

The first reaction (5-4) corresponds to the photoionization of excited argon atom by the absorption of a UV photon emitted by the aluminum vapor. The second reaction (5-5) corresponds to collisional excitation and ionization by electronic impact. Once a significant amount of free electrons is available in the shocked gas, inverse bremsstrahlung absorption becomes efficient to couple the laser energy into the shocked gas. Electrons are thus getting accelerated, which leads to the further ionization of the shocked gas in an avalanche process, because the accelerated electron can more efficiently ionize neutral argon atoms. The LSD wave is thus initiated. This process can be summarized in Figure 5.11.

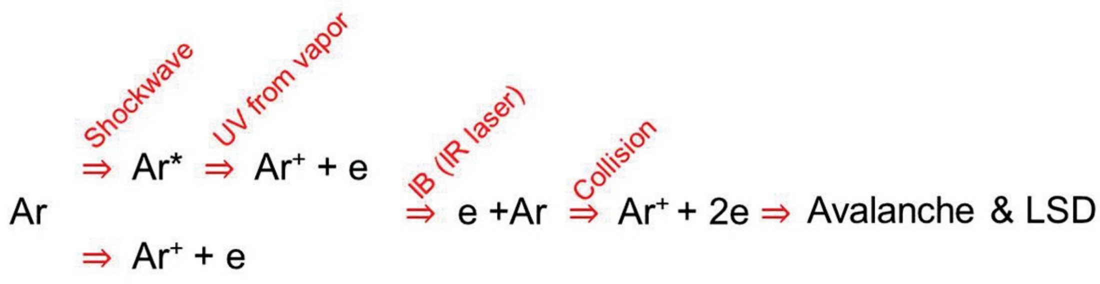

Figure 5.11 Pathways of LSD ignition in Argon

Mechanisms of ignition of LSD wave in air

Let us look at now what happens in air. Air is mainly a mixture of two diatomic gases: nitrogen and oxygen. According to the data presented in Table 5-4, for a shockwave corresponding to the velocity of about 10 km/s, the temperature in the shocked gas is about 14 000 K. Dissociation of nitrogen and oxygen molecules occur with following the chemical reactions:

$$O_2 + M = O + O + M \tag{5-6}$$

$$N_2 + M = N + N + M \tag{5-7}$$

In these reactions, *M* denotes any atom or molecule. With the compression and dissociation of nitrogen and oxygen, the pressure in the shocked gas behind the shockwave rises suddenly. According to Table 5-4, with a shockwave of about 10 km/s, the pressure rises 1000 times higher than the ambient air. According to the literature, after such strong shockwave, molecules in air are almost dissociated. [111]

Table 5-4 Hydrodynamic quantities behind a shockwave in air, with the standard condition of $p_0 = 1$ atm, $T_0 = 293$ K beyond the shock front [54]

T (K)	Velocity of shockwave (km/s)	Pressure behind the shock wave (atm)	Density ratio ρ_1/ρ_0 (ρ_1:behind, ρ_0: before)
10 000	6.97	561	11.00
14 000	9.31	1 000	11.10
20 000	11.8	1 650	10.10

However as shown by previous works [40], in the shocked air behind the shockwave, ionization as a result of atom-atom collisions or photoionization by absorption of IR radiation (1064 nm from the ablation laser) or visible one (~ 500 nm emitted by the vapor) cannot ensure the rapid formation of a large number of priming electrons to ignite the LSD wave. [40] Other ionization mechanisms should be involved to provide more electrons. Such electrons can be produced through associative ionization, in which two atoms combine into a molecule with the simultaneous release of an electron and formation of a molecular ion. [46] The reaction requiring the lowest activation energy is the following

$$O + N + 2.8\ eV = NO^{+} + e \tag{5-8}$$

Other reactions are also possible in shocked air to contribute to the production of free electron in shocked air:

$$N + N + 5.8\ eV = N_2^{+} + e \tag{5-9}$$

$$O + O + 6.5\ eV = O_2^{+} + e \tag{5-10}$$

Once enough priming electrons are produced, they get accelerated through inverse bremsstrahlung absorption of IR ablation laser radiation. The absorbed energy from laser compensates for the energy loss in the association reactions. They take place therefore at a much faster rate than the direct ionization of atoms and molecules by particle impact. Associative reactions play thus a key role in the creation of the priming electrons. As the density of free electrons increases and the inverse bremsstrahlung further accelerate them, the ionization by electron impact becomes more important and leads to avalanche ionization and the initiation of the LSD. Such process can be summarized in Figure 5.12.

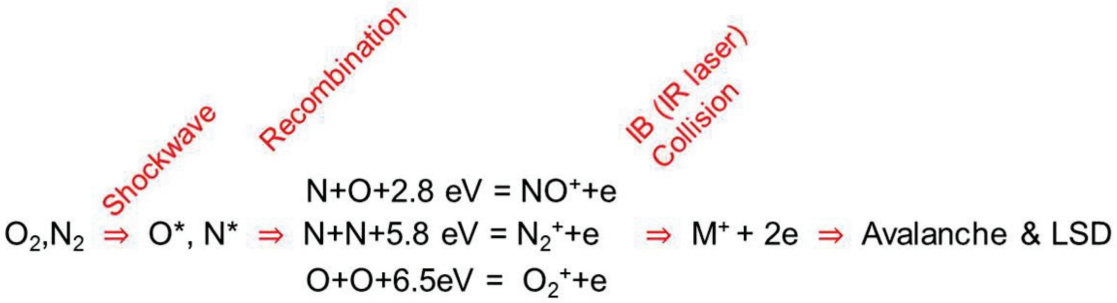

Figure 5.12 Pathway of LSD ignition in air.

With the above discussed different microscopic LSD ignition mechanisms, we understand well the faster propagation velocity of the LSD wave in argon, since it is superimposed to the ionization wave. In fact only the electronic processes are involved in the propagation of the ionization wave in argon, while in air, molecular processes (involving thus nuclei) are implied in the propagation of the ionization wave. Different time constants can be therefore expected for the two types of ambient gas.

5.3. Different plasma expansion behaviors in argon and in air

We can now summarize the different mechanisms of LSD ignition in argon and in the air. Based on these mechanisms, the observed different expansion behaviors of the plasma induced in argon or in air can be explained. Figure 5.13 illustrates the internal structures of the plasmas due to the different mechanisms of the LSD wave in argon (a) and in air (b). The initial states of the vapor are the same in the both ambient gases. The initial shockwave is generated with the same velocity. With argon ambient gas, after the passage of the shockwave in the ambient gas, due to collisions, argon atoms are excited to a high energy levels and a part of them can be ionized. With free electrons and highly excited argon atoms, laser energy can be efficiently absorbed by the shocked gas, which leads the ignition of LSD wave. The velocity of the LSD wave in argon is quite fast, so behind the LSD wave, there is a zone of low pressure above the aluminum vapor. Such low pressure zone leads to the acceleration of the upward motion of the aluminum vapor. As a result, the vapor gets a large initial velocity and propagates into the region of the shocked gas. This is why a mixing between the vapor and the gas can be observed.

In air, two phenomena lead to the observed different expansion behavior with respect to the plasma in argon. First, the speed of LSD propagation is smaller than that in argon. Second, the dissociation of air molecules suddenly raises the pressure of the shocked gas before the ignition of LSD. Thus the ignition of the LSD in air does not leave behind it a low pressure zone as in argon. On the contrary, the ignition of LSD in air imposes a high pressure zone above the aluminum vapor, and prevents the last propagating away from the target surface. Such mechanism corresponds well to our observation of the stagnating vapor closet to the target surface. We can finally summarize the relationship between the microscopic mechanisms and the macroscopic behaviors of the plasma expansion in Table 5-5.

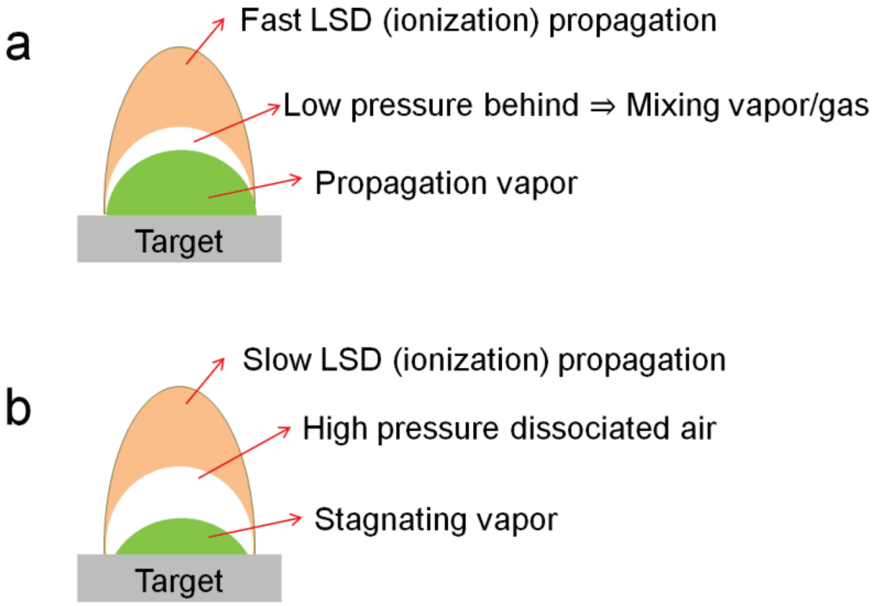

Figure 5.13 Illustration of the different structures dur to different LSD ignition mechanisms in argon (a) and in air (b)

Table 5-5 Relationship between the microscopic mechanisms and the macroscopic behaviors of the plasma expansion.

Fluence	50 mJ (160 J/cm^{-2})	
Ambient gas	Ar	Air
Microscopic mechanisms	Collisional excitation/ionization of the shocked argon, collisional/radiative ionization of excited atoms inverse bremsstrahlung absorption, electron impact ionization, avalanche ionization of the shocked air, breakdown and LSD	Collisional dissociation of the shocked air, recombination with free electron generation, inverse bremsstrahlung absorption, electron impact ionization, avalanche ionization of the shocked air, breakdown and LSD
Macroscopic behaviors	High LSD velocity	Low LSD velocity
	Low pressure rarefication zone in shocked argon behind the LSD	High pressure in the dissociated shocked air before LSD starts
	Propagation of Al vapor and mixing between ions of Al and Ar	Stagnation of Al vapor, and separation with the ionized air

5.4. Resume

In this chapter, we have investigated the expansion behaviors of the plasma in different ambient gases and at different ablation laser fluence regimes. The obtained results are presented first for the moderate ablation laser fluence (20 mJ corresponding to 65 J/cm^2). Through imaging and time- and space-resolved emission spectroscopy observations, we get the conclusion that, the plasmas induced in the two types of ambient gas exhibit quite similar propagation behaviors, with comparable propagation velocities, morphology and internal structure. The exhibited morphology and structure of the plasma suggest a post ablation interaction dominant by the LSC wave.

The results concerning a higher ablation laser fluence are then presented. The morphology and the structure of the plasmas induced in the both ambient gases show characteristics of a post ablation interaction dominantly determined by the LSD wave, which is coherent with our previous works. Moreover, a significant difference in propagation behavior is experimentally observed and confirmed between the plasmas induced in argon or in air. The most striking feature is that in argon a large zone of mixing between ions of argon and aluminum is observed, which confirms once again our previous works. But for the plasma induced in air with the same laser parameters, instead a population of aluminum confined in a zone close to the target surface and separated from the shocked gas is observed and confirmed experimentally.

We have then designed several complementary experimental observations to explain such difference due to the ambient gas in the high fluence ablation regime. Based on such observations and using considerations and models existing in the literature, we have provided the explanations in two points of view. In the macroscopic point of view, the hydrodynamic propagation of the plasma leads to a faster LSD wave in argon than in air. The fast LSD propagation in argon leaves behind it a low pressure rarefaction zone in the shocked gas, which facilitates the upward propagation of the aluminum vapor and leads to a mixing zone between ions of argon and aluminum as observed in our experiment. In the microscopic point of view, the ignition mechanisms are different in argon and in air. In argon, ionization of excited argon through photo absorption of UV radiation and electron impact represents the key mechanisms for the ignition of LSD. While in air, the key mechanism corresponds to the dissociation of air molecules by shockwave and the production of free electron in recombination reactions. This explains first a slower propagation velocity of LSD in air because of the longer time constant of the molecular process in air than that of the atomic process in argon. This leads also to the understanding that in air the dissociation of the molecules by the shockwave raises suddenly the pressure of air before the LSD starts. Such high pressure zone is placed just above the aluminum vapor. The combination of the appearance of such high pressure zone in the shocked gas before even the LSD starts and the slower propagation of the LSD wave finally results in the stagnation and confinement of the ablation vapor in a small zone close to the target surface. This is exactly what we have observed in our experiment.

Chapter 6. From plasma to molecule: monitoring of laser-induced aluminum plasma in air at long delay

In a reactive ambient gas such as the atmospheric air, a metallic plasma such as aluminum, undergoes oxidation reactions while the plasma cools down to the ambient temperature. Besides the effects observed in relative short delays after the generation of the plasma and related to a molecular ambient gas, the formation of AlO molecule in longer delay within an aluminum plasma evolving in air represents therefore an important aspect to be taken into account in our study of the properties and evolution of laser-induced plasma as a function of the ambient gas. This is precisely the purpose of the present chapter to monitoring the evolution of the plasma over the delay interval when the molecule AlO appears in the plume. Such monitoring will more specifically performed in terms of the correlation between the temperatures in the plasma and the evolution of the intensity of the molecular band observed in the emission spectrum from the plume.

In the practical point of view, measurements with LIBS usually take place in the atmospheric air. An important requirement is that a plasma is generated with the same elemental composition as the material to be analyzed within a stoichiometric ablation, and that the stoichiometry of the plasma remains constant during the interval of time when its emission spectrum is recorded. In the case of analysis of metallic elements in an air ambient, the oxidation due to the recombination with the oxygen contained in the ambient gas obviously represents a mechanism which may change the stoichiometry of the plasma. It is therefore important to avoid significant oxidation to occur in the plasma to maintain its elemental composition. Such condition is explicitly needed in the procedure of calibration-free LIBS [113]. It applies also in general because of the nontrivial relation between the concentrations of metallic elements and the oxidation rates in the plasma. Change of the stoichiometry of the plasma can thus invalidate a calibration curve.

In this chapter, we have experimentally investigated the temporal evolution and transformation of the plasma induced on an aluminum target by nanosecond infrared (1064 nm) laser pulse in the atmospheric air, in terms of its temperatures over a large interval of time from hundreds of nanosecond to tens of microsecond. Such evolution is then correlated to the temporal evolution of the emission intensity from AlO molecules in the ablation plume. In particular, for a given ablation laser pulse energy, the appearance of the molecular emission while the plume cools down, allows determining a minimal delay which corresponds to a maximal value of the temperature below which the molecular emission begins to be clearly observed and to grow as a function of the delay. Such delay or such temperature indicates thus the longest delay or the lowest temperature for laser-induced plasma to be considered suitable for a correct analysis of metallic elements without significant influence of alternation of the stoichiometry by oxidation. Beyond the practical interest for LIBS, the results shown in this chapter provide also insights to the kinetics of the AlO molecule formation in laser-induced plasma.

In the following, we will first discuss the oxidation reactions in an Al-plasma evolving in the atmospheric air. We will then present in detail the obtained experimental results. After looking at the evolution of the emission spectrum, we determine the electronic temperature of the plasma at short delays with the use of multi Saha-Boltzmann plot. This determination is first detailed for an ablation laser energy of 10 mJ. The determination of the molecular temperatures is thereafter discussed. We present in detail the obtained molecular temperatures for the same ablation laser energy. The evolution of the emission intensity from AlO molecules will then be presented. The comparison between the evolutions of the emission intensity and the plasma temperature will allow determining the values of the minimum delay and the maximum temperature for the recombination for AlO formation becoming a dominant process. By generalizing the same procedure to other ablation energies, the minimum delay and the maximum temperature will be finally determined for ablations with different laser energies. We will end this chapter with images showing the spatial distribution of the molecules obtained with time-resolved spectroscopic images and some preliminary results on the formation of nanoparticles in the plasma. The last point represents one of the perspectives opened by the present PhD thesis work.

6.1. Pathways for AlO molecule formation in an aluminum plasma evolving in the atmospheric air

In a laser-induced plasma containing aluminum vapor, $Al(g)$, and with the simultaneous presence of atomic and molecular oxygen as in general for a LIBS measurement, the main path ways of oxidation have been identified as [114]

$$Al(g) + O_2 \rightleftharpoons AlO + O \tag{6-1}$$

$$Al(g) + O + M \rightleftharpoons AlO + M \tag{6-2}$$

which are in cooperation or competition with the recombination of atomic oxygen

$$O + O + M \rightleftharpoons O_2 + M \tag{6-3}$$

In a high temperature gas, the above reactions can occur in the both ways. The dominant direction of each reaction is determined by the variation of the Gibbs free energy, ΔG, during the reaction, which is a function of the temperature of the gas.

$\Delta G < 0$: dominant forward reaction (spontaneous reaction)

$\Delta G = 0$: balanced forward and reverse reactions (equilibrium)

$\Delta G > 0$: dominant reverse reaction

Using ideal gas thermochemical table as shown in Table 6-1, the variation of the Gibbs function of the above reactions can be evaluated. In the Table 6-1, ΔG_f^0 denotes the standard Gibbs energy of formation, which is the increase in Gibbs energy associated with the reaction forming the given compound from corresponding elements with each substance in its thermodynamic standard state at the given temperature.

Table 6-1 Ideal gas thermochemical table of the standard Gibbs formation energy ΔG_f^0 of the elements involved in the reactions from (6-1) to (6-3). [115]

T (K)	ΔG_f^0 (kJ/mol)			
	AlO (g)	Al (g)	O_2	O
0	83.930	324.476	0.000	247.165
100	75.680	313.217	0.000	242.975
200	66.445	299.608	0.000	237.713

298	57.692	286.179	0.000	232.106
300	57.529	285.923	0.000	231.998
400	48.906	272.352	0.000	226.035
500	40.488	258.889	0.000	219.914
600	32.251	245.544	0.000	213.670
700	24.172	232.324	0.000	207.348
800	16.241	219.226	0.000	200.954
900	8.455	206.250	0.000	194.509
1000	1.592	194.174	0.000	188.027
1100	-4.777	182.585	0.000	181.504
1200	-11.041	171.100	0.000	174.955
1300	-17.204	159.707	0.000	168.380
1400	-23.292	148.394	0.000	161.781
1500	-29.318	137.161	0.000	155.165
1600	-35.276	126.002	0.000	148.528
1700	-41.188	114.911	0.000	141.883
1800	-47.050	103.888	0.000	135.216
1900	-52.882	92.922	0.000	128.542
2000	-58.681	82.011	0.000	121.854
2100	-64.455	71.155	0.000	115.159
2200	-70.200	60.353	0.000	108.455
2300	-75.915	49.614	0.000	101.742
2400	-81.613	38.904	0.000	95.026
2500	-87.316	28.237	0.000	88.296
2600	-92.977	17.636	0.000	81.567
2700	-98.637	7.056	0.000	74.830
2800	-100.791	0.000	0.000	68.092
2900	-95.926	0.000	0.000	61.350
3000	-91.079	0.000	0.000	54.600
3100	-86.252	0.000	0.000	47.850
3200	-81.450	0.000	0.000	41.092
3300	-76.665	0.000	0.000	34.333
3400	-71.909	0.000	0.000	27.575
3500	-67.166	0.000	0.000	20.812
3600	-62.419	0.000	0.000	14.053
3700	-57.709	0.000	0.000	7.286
3800	-53.008	0.000	0.000	0.524
3900	-48.311	0.000	0.000	-6.252
4000	-43.643	0.000	0.000	-13.018
4100	-38.984	0.000	0.000	-19.789
4200	-34.321	0.000	0.000	-26.561
4300	-29.670	0.000	0.000	-33.332
4400	-25.023	0.000	0.000	-40.111
4500	-20.397	0.000	0.000	-46.882
4600	-15.763	0.000	0.000	-53.653
4700	-11.166	0.000	0.000	-60.433

4800	-6.553	0.000	0.000	-67.212
4900	-1.936	0.000	0.000	-74.000
5000	-2.656	0.000	0.000	-80.780
5100	7.261	0.000	0.000	-87.555
5200	11.841	0.000	0.000	-94.347
5300	16.437	0.000	0.000	-101.122
5400	21.026	0.000	0.000	-107.914
5500	25.601	0.000	0.000	-114.694
5600	30.189	0.000	0.000	-121.490
5700	34.756	0.000	0.000	-128.282
5800	39.353	0.000	0.000	-135.061
5900	43.932	0.000	0.000	-141.858
6000	48.512	0.000	0.000	-148.645

Using the data of Table 6-1, we can calculate the variation of the Gibbs energy, ΔG, for the 3 reactions from Eq. (6-1) to Eq. (6-3) as a function of the plasma temperature. The results are shown in Figure 6.1. We can see that for Eq. (6-1), ΔG exhibits negative value at high temperature and it becomes slightly positive when the gas cools down. The equilibrium temperature is found to be about 600 K. For Eq. (6-2) and Eq. (6-3), an opposite behavior is observed with positive values of ΔG at high temperature and negative values at lower temperature. The equilibrium temperatures are found to be about 4300 K for Eq. (6-2) and 3800 K for Eq. (6-3). In a laser-induced plasma at an initial temperature of tens of thousands K and undergoing cooling, Eq. (6-1) is the initial process for spontaneous AlO molecule formation with negative ΔG value in the range of -100 kJ/mol at 6000 K. However, the dissociation process can dominate through Eq. (6-2) with a larger positive ΔG value in the range of +197 kJ/mol at the same temperature. . The dissociation of O_2 through Eq. (6-3) reduces also the formation of AlO in a high temperature gas through Eq. (6-1). As the plasma cools down, the situation can change, especially when the temperature approaches the equilibrium temperature of Eq. (6-2), the both Eq. (6-1) and Eq. (6-2) tend to spontaneously produce AlO molecules with exothermic reactions. Eq.(6-3) can influence the relative importance of Eq. (6-1) and Eq. (6-2), but it does not change the general tendency of more efficient AlO molecule formation. It is why in practice, the AlO $B^2\Sigma^+ - X^2\Sigma^+$emission bands appear in the emission spectrum of the ablation vapor with a delay after the laser impact on the sample when the plasma cools down into a temperature range where the recombination becomes a dominant process [116, 117]. It is thus of practical importance for LIBS analysis of metallic elements to determine such range in order to avoid significant stoichiometry change due to chemical reactions in the plasma.

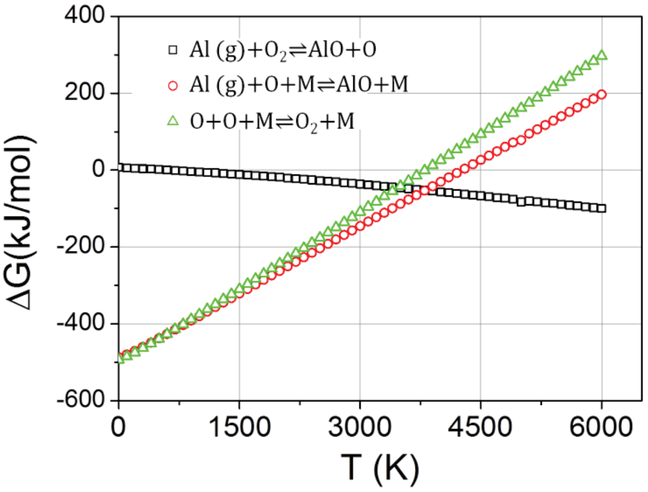

Figure 6.1 The variation of the Gibbs function for the 3 reactions of Eqs (6-1), (6-2) and (6-3). Black points correspond to the reaction Eq. (6-1), red ones to the reaction Eq. (6-2) and green ones to the reaction Eq. (6-3)

6.2. Observables in this experiment

In order to monitor the plume over a large interval of delay from hundreds of nanoseconds to tens of microseconds, and in order for such monitoring being efficient to provide useful information for a better performance of LIBS measurement, we will in the following specify a certain number of observables that we can extract from the raw spectra to characterize the plume in its evolution and transformation.

For a given ablation energy in a LIBS measurement, it is important to determine the time delay after the laser impact on the sample, notated as τ_{min}, the AlO molecule population grows significantly. Such delay corresponds automatically to a maximal value of the plasma temperature, notated as T_{max}, below which the combination processes overcome the dissociation ones. In our experiment, the temperature of the plasma is thus continuously monitored by means of emission spectroscopy. The evolution of the temperature is moreover correlated to that of the emission intensity from AlO molecules in order to determine the values of τ_{min} and T_{max}. It has to notice here that in the experiment, the emission spectrum was recorded with temporal resolution but without spatial resolution due to the fact that the signal was integrated along the line of sight in the plume. This procedure appears approximate to provide actual axial temperature distribution in the ablation plume which may exhibit an important radial gradient. Such conceptually unsatisfactory approach can however represent a great practical interest due to its ease of implementation in a LIBS experiment. For a comprehensive interpretation of the measured temperatures, the possible inhomogeneity of the plume has to therefore taken into account.

Classical techniques of plasma diagnostics are used to extract the plasma temperature. At short delays from several hundreds of ns to several μs when the plume is principally composed of electrons, ions and atoms, the plasma temperature will be extracted using Saha-Boltzmann plot [118]. Such temperature corresponds more specifically to the electronic temperature, T_e, since the LTE condition is in general fulfilled in this interval of delay [60]. At long delays beyond several μs when the emissions from the elements begin to disappear and that from AlO molecule starts to appear, the temperature will be extracted by fitting the experimental molecular spectrum with a synthetic one [84, 119]. More precisely, the rotational temperature, T_{rot}, and the vibrational temperature, T_{vib}, can be extracted by simulating the experimental spectra with a theoretical model. In a laser-induced plasma, for the $B^2\Sigma^+$ state of the AlO molecule, however, a number of authors observed a local equilibrium between the vibrational and the rotational degrees of freedom of molecule [80, 120-122]. The temperature $T_{vib} = T_{rot}$ can thus be extracted by simulating the experiment spectrum and noted as T_{mol} in the following. It should be noticed here that such temperature is not correlated to the electronic excitation temperature of the molecule, neither to its translation temperature, since at the delay when the spectrum becomes dominated by the molecular emission, the LTE condition is no longer fulfilled [60]. Here again the relevance of the extracted molecular temperature (T_{mol}) for practical use should be emphasized because it becomes the only observable to characterize the plume with emission spectroscopy for long detection delays when there is not enough elemental emission lines to perform the Saha-Boltzmann plot.

6.3. Determination of the plasma temperature for ablation with 10 mJ laser pulse

6.3.1. Temporal evolution of the emission spectrum

Space-averaged and time-resolved emission spectra were thus recorded using the spectroscopic type setup described in Chapter 3. In order to observe the evolution of the emission spectrum of the ablation plume over the investigated delays after the laser impact on the target, we present in Figure 6.2 representative spectra at 4 different delays recorded with an ablation pulse energy of 10 mJ (32 J/cm^2 or 8 GW/cm^2 in corresponding fluence or irradiance respectively) and an ehelle spectrometer. The intensities of the presented spectra are normalized to the detection gate width of 0.15 μs at a delay of 0.5 μs. In these spectra, we can see that at a short delay of 0.5 μs (Figure 6.2 a), the spectrum consists of emission lines from the elemental species evaporated from the target (Al, Si, Fe) as well as contributed by the ambient gas (N, O). The latter are due to the dissociation of the molecules O_2 (Eq.(6-3)) and N_2 in the plume. The zoom in the inset of the figure around the spectral range of the AlO emission band does not show any signal. At a delay of 5 μs, the emission lines from the elements are always observable, even though those from the N and O become very weak (remark the break used for the vertical axis of Figure 6.2 b). The zoom between 450 nm and 550 nm shows a hint of the emission band $B^2\Sigma^+ - X^2\Sigma^+$ of the AlO molecule, which indicates the presence of the molecules. The coexistence of oxygen atoms and AlO molecules confirms the fact that both the Eq. (6-1) and Eq. (6-2) mentioned above can contribute to the formation of AlO molecule in an ablation plume. For longer delays, with the further cooling of the plume, the emission lines from N and O disappear under the noise, because of their high excitation energy (~10 eV). The intensity of the molecular band continues to increase because both the Eq. (6-1) and Eq. (6-2) should contribute to the formation of AlO molecules with reduced temperature in the plume.

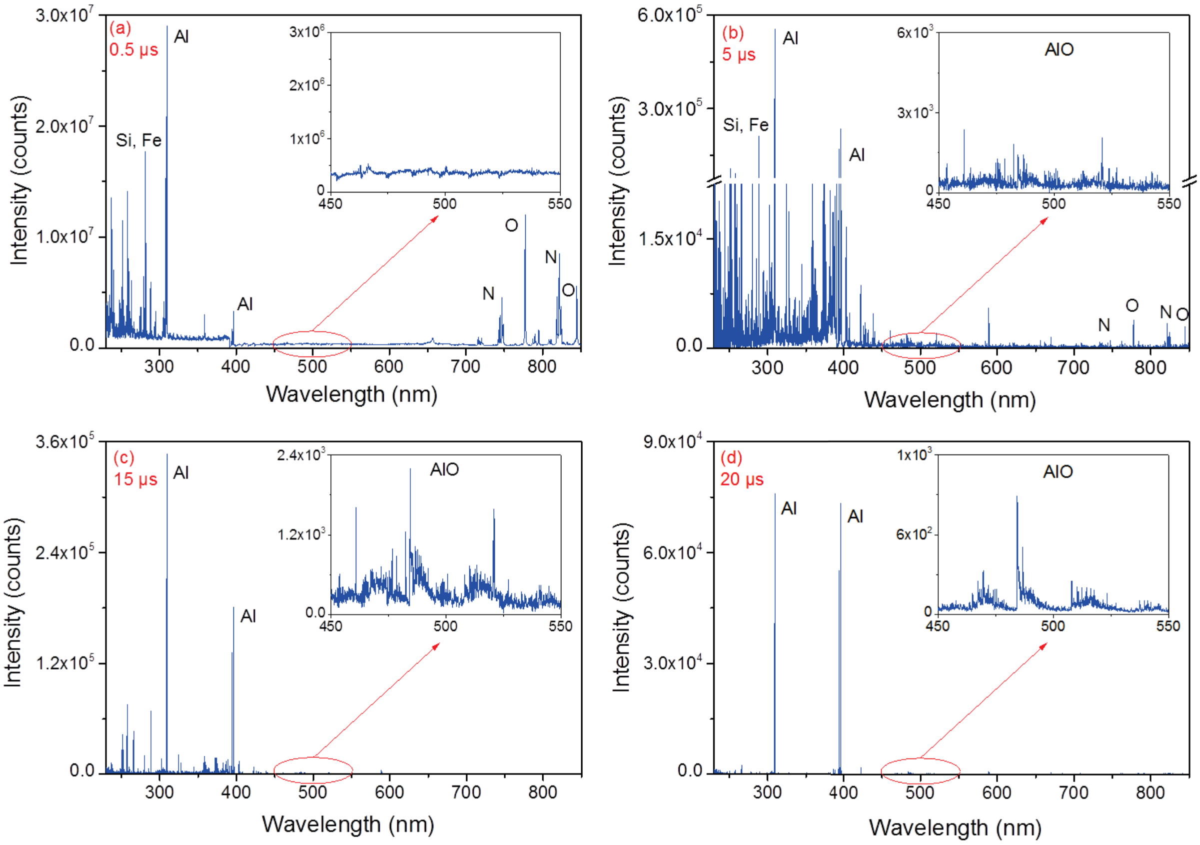

Figure 6.2 Typical emission spectra of plasma induced by 10 mJ laser pulse at delay of a) 0.5 µs, b) 5 µs, c) 10 µs and d) 15 µs with an echelle spectrometer. The intensities of the spectra are normalized to the detection gate for the delay of 500 ns.

6.3.2. Plasma temperature determination at short delays with multi-element Saha-Boltzmann plot

At short delays, typically from 0.2 to 5 µs, the plasma temperature can be extracted from the emission spectrum using multi Saha-Boltzmann plot [118], which has been also described in detail in Chapter 2. The lines selected in this experiment for the plot together with their spectroscopic parameters are listed in Table 6-2. We can remark that the majority of the lines belong to the trace elements contained in the target. Only one aluminum ion line is selected, which has a quite high energy for its lower level of the transition.

Table 6-2 Spectroscopic parameters of the lines selected for determining the electron temperature in the plasma.

Species	λ_{ki}(nm)	A_{ki}(s^{-1})	E_i (eV)	E_k(eV)	g_i	g_k
Fe II	234.3	1.70×10^8	0.000	5.295	10	8

Fe II	238.2	3.80×10^8	0.000	5.210	10	12
Fe II	240.5	1.70×10^8	0.083	5.243	6	8
Fe I	248.3	4.90×10^8	0.000	4.997	9	11
Fe I	249.1	3.80×10^8	0.087	5.070	5	7
Si I	250.7	4.66×10^7	0.010	4.960	3	5
Si I	251.4	6.10×10^7	0.000	4.935	1	3
Si I	251.9	4.56×10^7	0.010	4.935	3	3
Si I	252.4	1.81×10^8	0.010	4.926	3	1
Si I	252.9	7.70×10^7	0.028	4.935	5	3
Fe II	258.6	8.10×10^7	0.000	4.799	10	8
Fe II	259.9	2.20×10^8	0.000	4.774	10	10
Fe II	261.4	2.00×10^8	0.107	4.855	4	2
Fe II	261.8	4.40×10^7	0.083	4.824	6	6
Fe II	262.6	3.40×10^7	0.048	4.774	8	10
Fe I	271.9	1.40×10^8	0.000	4.564	9	7
Fe II	274.0	1.90×10^8	0.988	5.517	8	8
Fe II	274.6	1.90×10^8	1.078	5.596	4	6
Fe II	275.6	2.10×10^8	0.988	5.491	8	10
Al II	281.6	3.83×10^8	7.429	11.836	3	1

We can observe the evolution of the electron temperature over the time interval from hundreds nanoseconds until to 3 μs as shown in Figure 6.3. We implicitly assume that the LTE condition is satisfied by the plasma over this interval [60]. We can see in Figure 6.3 that in a logarithm scale, the decay of the electron temperature shows a quite linear behavior. In fact we can fit the experimental data with an exponential decay function in the form of

$$T(t) = T_0 exp\left(-\frac{t}{t_0}\right) \tag{6-4}$$

The fitting parameters determined with the least-square method show T_0=12 800 K, t_0 =5.7 μs and a quite good determination coefficient of R^2=0.98. Without going into the detail of the mechanisms of the electron temperature decay in a laser-induced plasma, which is a complex process and situates beyond the scope of the present work, we will use

Eq. (6-4) to describe the trend of evolution of the electron temperature in the plasma for the delays beyond those allowing an experimental determination of such temperature.

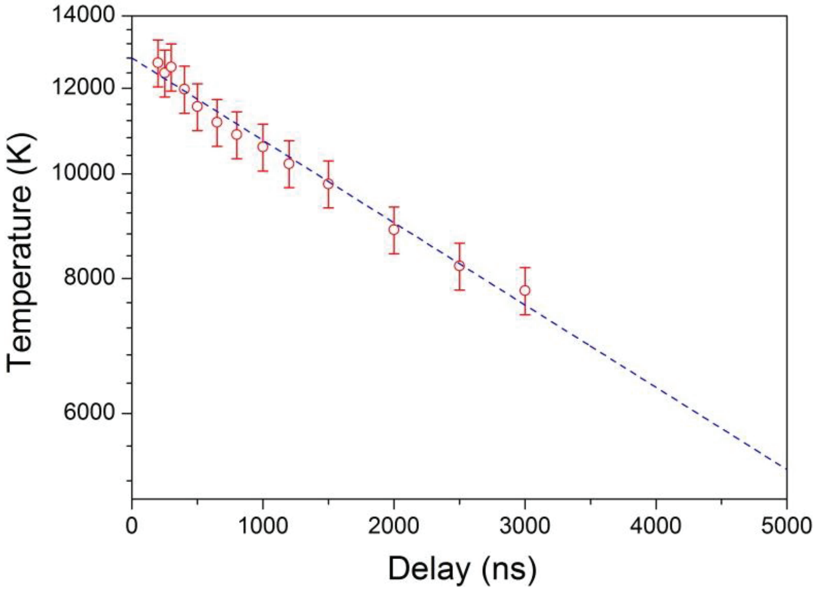

Figure 6.3 Electron temperature (open circles) in the plasma determined using the method of multi Saha-Boltzmann plot for an ablation energy of 10 mJ at different delays of detection. The decay of the temperature is fitted with an exponentially decay function (dashed line), which indicates moreover the trend of the evolution of the temperature for longer delays.

6.3.3. Detection protocols for AlO emission spectrum and emission intensity

In this experiment, two spectrometers were used. The first one was the echelle spectrometer coupled to the intensified charge-coupled device (ICCD) camera (Mechelle and iStar from Andor Technology) that we have described in Chapter 2. It was calibrated for both wavelength and spectral response using respectively a mercury argon calibration source (Ocean Optics, HG-1) and a deuterium tungsten halogen light source (Ocean Optics DH-2000). This detection configuration provided a spectral range from 200 nm to 850 nm with a resolution power of $\lambda/\Delta\lambda$=4005. Spectra recorded using the echelle spectrometer included emission lines from the elements contained in the target and contributed by the ambient gas, as well as AlO $B^2\Sigma^+ - X^2\Sigma^+$ molecular band. In order to get a better signal-to-noise ratio, a second spectrometer was used in the experiment to specifically detect the AlO molecular band with a better sensitivity. It was the Czerny-Turner spectrometer (Shamrock, Andor Technology) with a grating of 600 l/mm and coupled to the same ICCD camera as for the echelle spectrometer. This detection system is also described in Chapter 3. With an entrance slit of 100 μm, the resolution of the spectrometer was determined using the same mercury argon calibration source from Ocean Optics to be $\Delta\lambda = 0.27$ nm (FWHM) over the observed spectral range. The advantage of the Czerny-Turner spectrometer is also the absence of discontinuous variation of the background of a spectrum observed with an echelle spectrometer due to different orders of diffraction of the used prism. A flat background increases the precision of the fitting of the experimental spectrum by a synthetic one.

On the other hand, in order to observe the evolution of the emission intensity from the AlO molecules, the spectroscopic imaging system described in Chapter 3 has been used. In this configuration of imaging detection, a narrow band spectral filter was used to get the emission image of AlO molecules in the plume. The central wavelength of the filter was 488 nm and its bandwidth 10 nm, which allowed recording the emission intensity from the $B^2\Sigma^+ - X^2\Sigma^+$band of the AlO molecule. Table 6-3 shows typical detection delays and the corresponding detection gate widths used in the experiment for monitoring the plasma over a large time interval from 100 ns to 60 μs. We remark that the gate width was not identical for all the delays. This was because in the experiment for a given ablation energy, the gain applied to the ICCD was fixed and the gate width was therefore adjusted to optimize the signal. In the experiment, each spectrum or image was accumulated over 200 laser pulses distributed by burst of 10 shots, over 20 ablation sites. A displacement of 800 μm was applied between two neighboring craters. A personal computer was used to ensure the synchronization of the different events (beam shutter opening, ICCD camera triggering and target displacement) in the experiment and to manage the data recording.

Table 6-3 Delays and gate widths used for time-resolved spectroscopic and image detections

Spectroscopic detection	Delay (μs)	0.1	0.15	0.2	0.25	0.3	0.4	0.5	0.65	0.8
	Gate (μs)	0.02	0.05	0.05	0.05	0.1	0.1	0.15	0.15	0.2
	Delay (μs)	1.0	1.2	1.5	2.0	2.5	3.0	4.0	5.0	10
	Gate (μs)	0.2	0.3	0.3	0.5	0.5	1.0	1.0	5.0	5.0
	Delay (μs)	15	20	25	30	35	40	50	60	
	Gate (μs)	5.0	5.0	5.0	5.0	5.0	10	10	20	
Image detection	Delay (μs)	1.0	2.0	3.0	4.0	5.0	7.0	10	12	
	Gate (μs)	0.06	0.3	0.5	0.8	1.0	1.5	1.5	1.0	

Delay (µs)	15	17	20	25	30	35	40	50
Gate (µs)	1.0	1.0	1.0	2.0	0.3	0.5	0.8	1.0

6.3.4. Temperature determination at long delays with simulation of molecular emission spectrum

To determine the temperature of the plume at long delays beyond several microseconds, the AlO $B^2\Sigma^+ - X^2\Sigma^+$ molecular bands were simulated with a synthetic spectrum by setting $T_{vib} = T_{rot} = T_{mol}$. For the construction of the synthetic spectrum, we consider that the emission intensity associated to a rovibrational transition of a diatomic molecule [119], with the details discussed in the section 2.3.2. The fitting results of the experimental spectra by synthetic ones are presented in Figure 6.4, for the case of ablation with 10 mJ lase pulse and at detection delay of 5, 10, 15 and 20 µs. We remark that the experimental spectra were first normalized to their own maximum before being fitted by the synthetic ones.

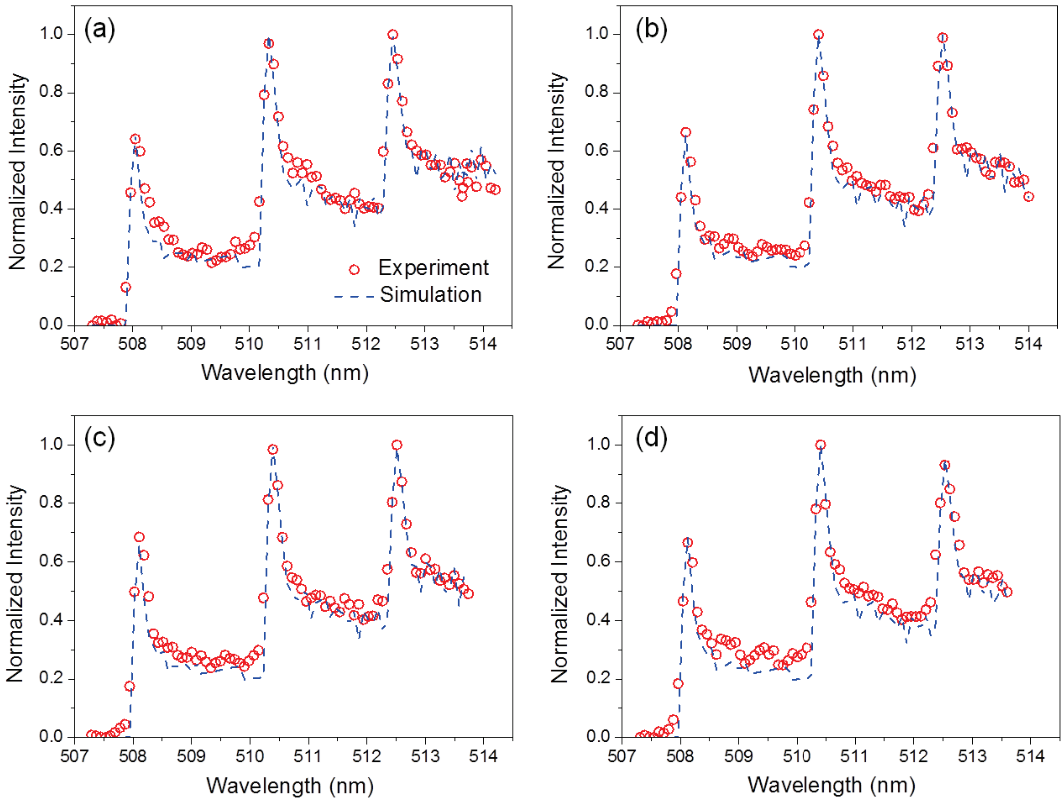

Figure 6.4 Emission band $B^2\Sigma^+ - X^2\Sigma^+$ of AlO molecules. Experimental intensities represented by red open circles, are measured at 4 delays of 5 µs (a), 10 µs (b), 15

μs (c) and 20 μs (d) for a plasma induced by a 10 mJ pulse. Experimental data are fitted with synthetic spectrum (dashed blue curve).

The fitting curves presented in Figure 6.4 show a mean determination coefficient of R^2= 0.91, and a mean root-mean-square error (RMSE) of 0.072. They allow extracting a molecular temperature for each of the concerned delay. Due to the noise, the fitting of an experimental spectrum by a synthetic one implies an uncertainty for the extracted temperature. This uncertainty is comprised between ±7% and ±9% for the 4 spectra present in Figure 6.4 . We consider that the fitting uncertainty is the main source of uncertainty of the molecule temperature determination in this experiment. The extracted molecular temperatures for all the investigated detection delays for the ablation with 10 mJ pulse are shown in Figure 6.5 with the corresponding error bars. The electron temperatures extracted with multi-Saha-Boltzmann plot at short delays (already shown in Figure 6.3 with error bars) are also displayed in Figure 6.5 to provide an overview of the evolution of the temperatures in the ablation plume from several hundred nanoseconds to 40 μs. Notice that in Figure 6.4, the positions of the experimental points with respect to the horizontal axis are actually equal to delay + the half of the detection gate in order to take into account the effect of average over the gate. We can see in the figure that at the beginning of the appearance of the molecules, their temperature is quite close to the electron temperature, since at such delay the LTE condition might be still satisfied [60]. When the delay further increases, the measured molecular temperature clearly deviated from the evolution trend of the electron temperature (indicated in Figure 6.5 by its exponential decay extrapolation). This behavior can be understood, because the electron density decreases so much that the McWhirter criterion [83] cannot be satisfied anymore. As for the electron temperature, the decay of the molecule temperature can be fitted with an exponential decay function (Eq. (6-4)) with T_0 =6590 K, t_0 =90.7 μs and a determination coefficient of R^2= 0.95.

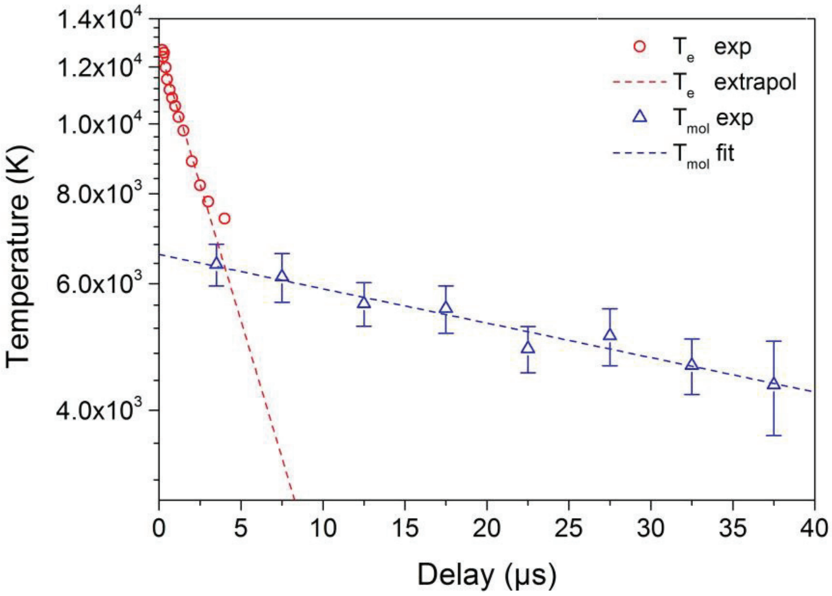

Figure 6.5 Evolution of the temperature in a plume ablated by a 10 mJ laser pulse. Open red circles: electron temperature at short delays determined with Saha-Boltzmann plot. Red dashed line: extrapolation of the electron temperature with an exponential decay function. Open blue triangles: molecule temperature at long delays determined by simulating molecular spectra. Blue dashed line: fit of the molecule temperature with an exponential decay function.

The presentation of the two temperatures in the same Figure 6.5 may however give rise of some confusion. Two facts need to be emphasized in order to get right interpretation of the results shown in Figure 6.5. First, the two temperatures do not represent the same physical quantity. The electron temperature, T_e, represents the temperature of the plasma as long as the LTE condition is fulfilled. At long delays, typically beyond 5 µs, it loses its precise physical meaning. The extrapolation in Figure 6.5 (T_e extrapol) would only indicate the tendency in which the plume cools down. On the other hand, the molecule temperature, T_{mol}, corresponds to the vibrational and the rotational temperature of the molecule AlO. As we mentioned in the section 2.3.2, this temperature is determined by assuming a local equilibrium between the vibrational and the rotational freedoms of the molecule. The LTE condition being broken at these long delays, the measured molecule temperature indicates neither the excitation temperature for atoms nor the translation one of the molecules. The second fact is that the detected emission is averaged over a certain volume of the plume. Space segregation between elements and molecules in the plume would lead to the correspondence of the above two discussed temperatures to the different places in the plume. A space-resolved detection would be more appropriate to describe the distribution of the temperatures in the plume. The motivation to present the two temperatures in the same figure as shown in Figure 6.5 corresponds rather to a practical reason: the electron temperature and the molecule temperature as determined in our experiment are the two observables that can be measured using emission spectroscopy to characterize an ablation plume over two distinguished time intervals which extend from several hundreds of nanoseconds to tens of microseconds, a very large time scale for the evolution of an ablation plume.

6.3.5. Determination of τ_{min} and T_{max} for the case of ablation with 10 mJ laser pulse

Evolution of the emission intensity of the AlO molecule

After determining the evolution of the temperatures in the plume, in this section we will correlate such evolution to that of the emission intensity from the AlO molecules in the plume. For this purpose, the molecular emission intensity was monitored as a function of delay. Such monitoring was primarily performed in our experiment with a direct imaging of plasma using ICCD camera. A filter was used to select a spectral band with a width of 10 nm around 488 nm, which allowed an efficient detection of the $\Delta\nu = 0$ sequence of the AlO $B^2\Sigma^+ - X^2\Sigma^+$ band as described in Section 2.3.2. The advantage of this method of detection is its high sensitivity thanks to the integrated intensity over the whole volume of the plume. Such high sensitivity allows high time resolution with narrow detection gates. Figure 6.6 shows the measured emission intensity as a function of the delay (taking into account of the detection gate as in Figure 6.5) for plasma induced by 10 mJ pulse (blue solid squares). The data shown in the figure are first normalized with respect to the detection gate (gain of the ICCD kept constant) and then they were normalized again in such way that the bump in the curve being equal to the unit. The disadvantage of the detection with plasma image is however the inclusion of the continuum emission and eventually interfering lines in the detected emission intensity. In order to confirm the emission from the AlO molecule, we repeated the measurement with the spectroscopic detection system. The detected spectral intensity of the AlO molecule band, with the background subtracted, is also plotted in Figure 6.6 (red open circles) after normalizing the maximum of the signal to unit.

As shown in Figure 6.6, the space-integrated intensity from the plume first decreases as a function of the delay. Such decrease corresponds to the decay of the continuum emission and the line emission from elements in spectral range covered by filter, while the plume cools down. Beyond a certain delay, 6 μs for instance, the emission intensity climbs due to, presumably, the contribution of the AlO molecules which start to emit in the plume. The contribution of the molecules is confirmed by the spectroscopic measurement which leads to the data presented in Figure 6.6 by the red open circles. We can see that the normalized spectroscopic data exhibit, with a worse time resolution because of larger detection gates used to compensate the lower sensitivity of the spectroscopic detection, the same behavior of evolution as the data obtained with the image detection. This confirms the clear appearance of AlO molecules with an increasing population in the plume after 6 μs. According to our definition given in Section 6.2, we can determine τ_{min} = 6 μs for the case of ablation with 10 mJ laser pulse.

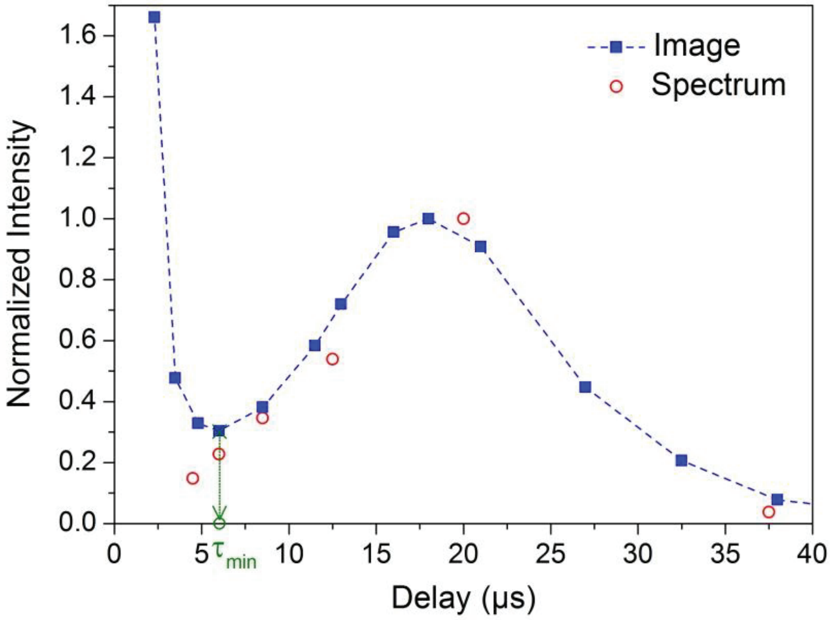

Figure 6.6 Emission intensity from the plume in the wavelength range of the AlO molecular band as a function of delay for the case of 10 mJ ablation. Blue solid squares: intensities detected with imagy detection; Red open circles: intensities detected with spectroscopic detection. τ_{min} is identified as the delay from which the emission from molecules start to clearly increase.

Correlating the plasma temperature to the molecular emission intensity

In order to determine the value of T_{max} associated to τ_{min}, we plot in the same figure the data presented in the Figure 6.5 and Figure 6.6 as shown in Figure 6.7. We can see that starting from the value of τ_{min}, we can determine the value of T_{max}. It is however possible to have two value of T_{max} as shown in Figure 6.7. The first one correspond to the molecular temperature that we call $T_{\max\_M}$. Another possible value can be obtained using the extrapolation of the electron temperature, that we call $T_{\max\_E}$. We notice the second value of $T_{\max\_E}$ has only an indicative meaning. It means that if the electron temperature continues to decreases following the exponential decay law as the short delays, then the electron temperature at the moment when molecules start to appear clearly in the plume would be given by $T_{\max\_E}$. In this way, using the data presented in Figure 6.7, we determine $T_{\max\_M} = 6300 \pm 600$ K and $T_{\max\_E} = 4500 \pm 500$ K for the case of ablation with 10 mJ. We remark that the value of $T_{\max\_E}$ is quite close to the equilibrium temperature of the reaction of (6-2), while the value of $T_{\max\_M}$ is significantly higher.

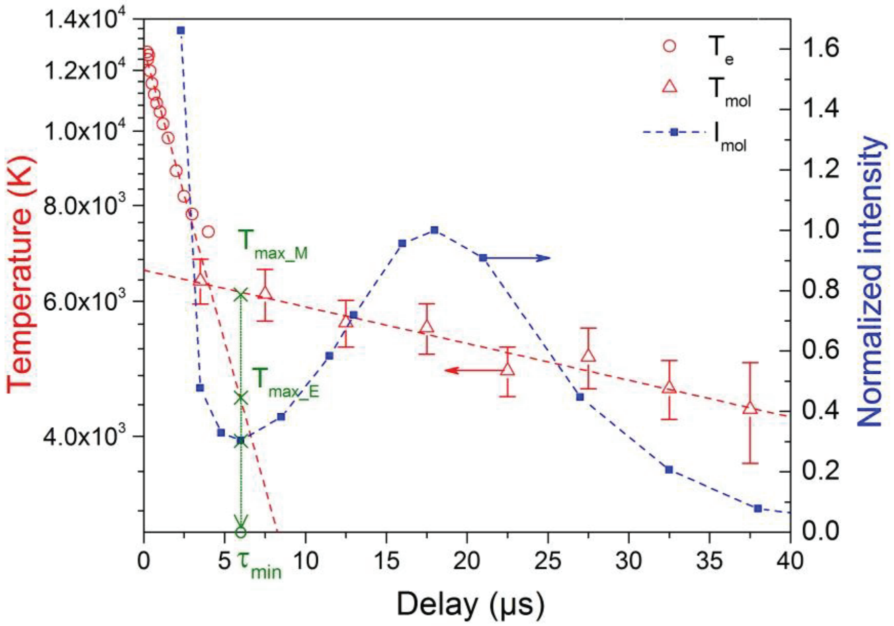

Figure 6.7 Temperature in the plume (in red) and molecular emission intensity (in blue) as a function of delay for the case of ablation with 10 mJ laser pulse and the determination of the values of T_{max}.

6.4. Determination of τ_{min} and T_{max} for other ablation energies

6.4.1. Determination of electron and molecule temperatures

We generalize now the procedure presented above for ablation with 10 mJ to other ablation laser energies of 5, 20, 30 and 50 mJ. Figure 6.8 shows electron temperatures at short delay determined with multi Saha-Boltzmann plot for the cases of ablation with these laser energies. The extrapolations of the electron temperatures to longer delay with fitting with exponentially decay law are also shown in Figure 6.8 (dashed lines). We get the electron temperatures for these energies at long delay with fitting uncertainties of 13%, 8%, 2% and 2% respectively for 5, 20, 30 and 50 mJ.

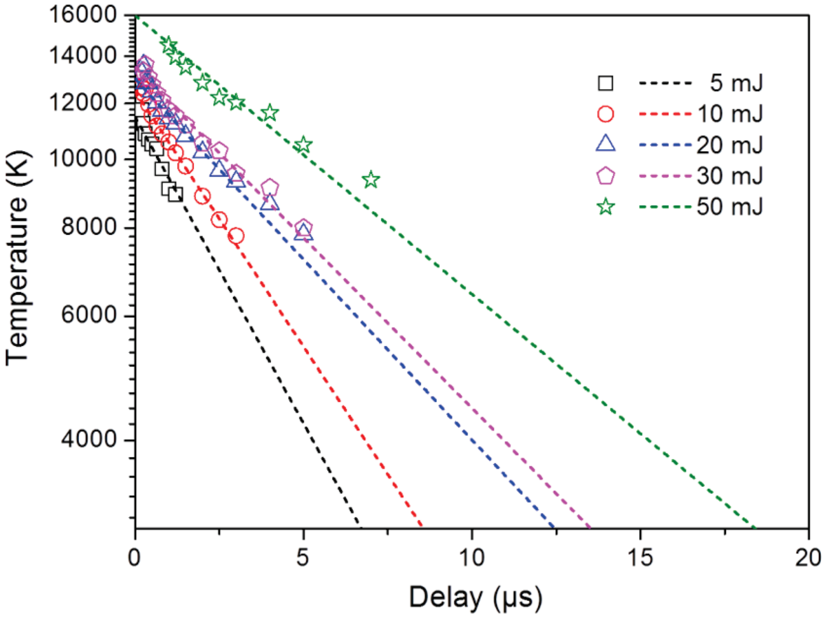

Figure 6.8 Electron temperatures in the plasmas induced with different ablation energies determined using the method of multi Saha-Boltzmann plot as a function of the detection delay. The decays of the temperatures are fitted with exponentially decay functions (dashed line), which indicate moreover the trends of evolution of the temperatures for longer delays.

In the same way as for the case of ablation with 10 mJ pulse, molecular spectra are fitted with a synthetic spectrum for the cases of ablation with 5 mJ, 20 mJ, 30 mJ and 50 mJ pulses. The results are shown in Figure 6.9 to Figure 6.12.

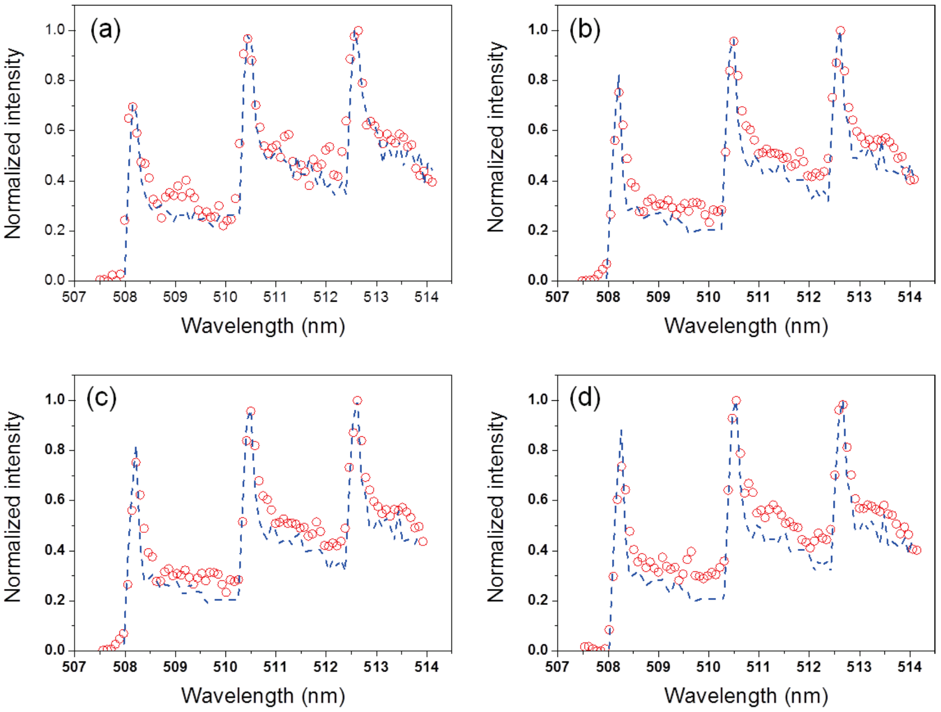

Figure 6.9 Experimental molecular emission intensities (red open circles) measured at 4 delays of 2 µs (a), 4 µs (b), 7 µs (c) and 10 µs (d) for a plasma induced by a 5 mJ pulse. Experimental data are fitted with synthetic spectrum (dashed blue curve).

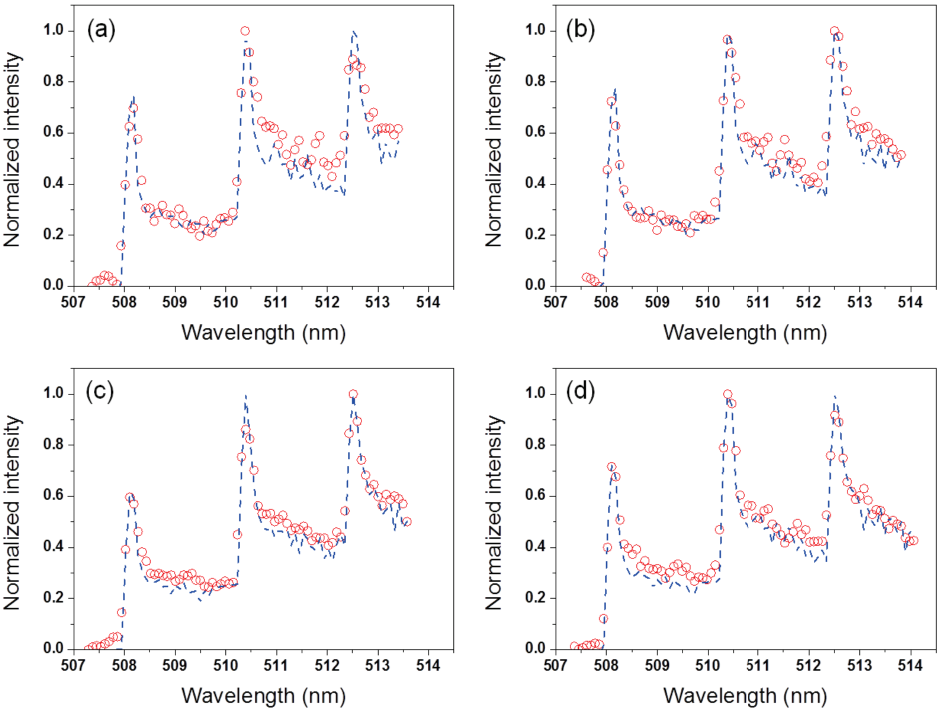

Figure 6.10 Experimental molecular emission intensities (red open circles) measured at 4 delays of 10 µs (a), 15 µs (b), 20 µs (c) and 30 µs (d) for a plasma induced by a 20 mJ pulse. Experimental data are fitted with synthetic spectrum (dashed blue curve).

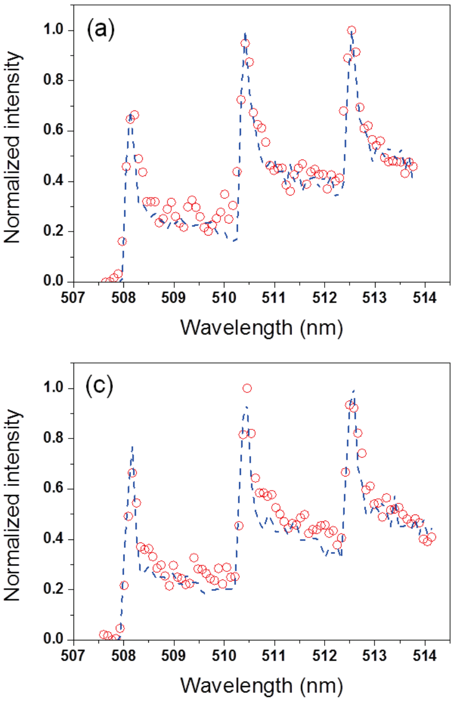

Figure 6.11 Experimental molecular emission intensities (red open circles) measured at 4 delays of 20 µs (a), 25 µs (b), 30 µs (c) and 35 µs (d) for a plasma induced by a 30 mJ pulse. Experimental data are fitted with synthetic spectrum (dashed blue curve).

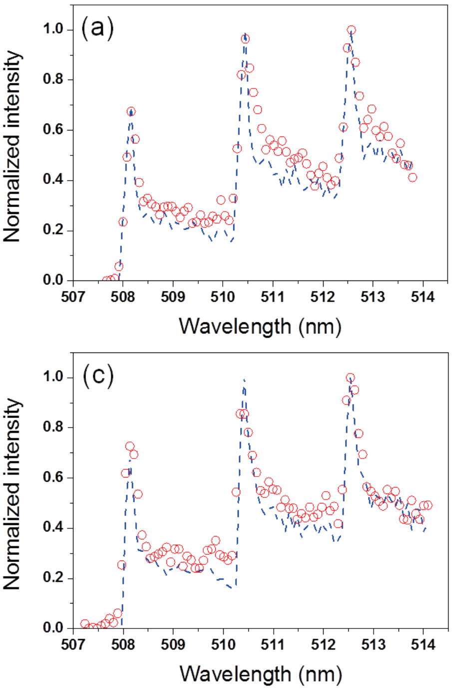

Figure 6.12 Experimental molecular emission intensities (red open circles) measured at 4 delays of 30 µs (a), 40 µs (b), 50 µs (c) and 60 µs (d) for a plasma induced by a 50 mJ pulse. Experimental data are fitted with synthetic spectrum (dashed blue curve).

6.4.2. Evolution of the temperatures for different ablation energies

From the fittings shown in Figure 6.9 to Figure 6.12, we can extract the evolution of the molecule temperature for these ablation energies. The relative errors on the temperatures related to the uncertainty of the fitting are of 10%, 8%, 10% and 11% for ablation laser energy of 5, 20, 30 and 50 mJ respectively. Figure 6.13 shows the electron as well as the molecule temperature measured for all the tested ablation energies including 10 mJ. The fitting curves are also plotted in the figure in dashed lines. We can see first that the evolution of the temperature has a similar behavior for all the ablation energies. In general, higher ablation energy corresponds to higher electron and molecule temperatures. The observation is in agreement with the previous reported results on the increase of the molecular vibrational and rotational temperatures as a function of the kinetic energies of the reactants [82]. For the molecule temperature, however, the case of 10 mJ presents a singularity, since the molecule temperature is exceptionally high. Further investigation is needed to address such singularity. We simply remark here that such inversion in the ordering of the molecule temperature versus the ablation laser pulse energy observed in our experiment for 10 mJ seems significant with respective to the precision of our temperature determination. We remark also that all the molecule temperatures decrease as a function of the delay with a rate much smaller than that of the electron temperature. And all molecule temperatures are comprised between two limit values, an upper limit around 6000 K and a low limit around 4000 K. We thus deduce that there is a temperature zone where AlO molecule can emit in laser-induced plasma, and such zone is defined by 5000 ± 1000 K. We remark that this zone is slightly higher than the equilibrium temperature of Eq. (6-2). This observation may suggest higher vibrational and rotational temperatures than the translation one for AlO molecules formed in the plume through exothermic reactions of Eq. (6-1) and Eq.(6-2). The reaction heat from the exothermic reactions may also explain the slow decay rate of the molecule temperature.

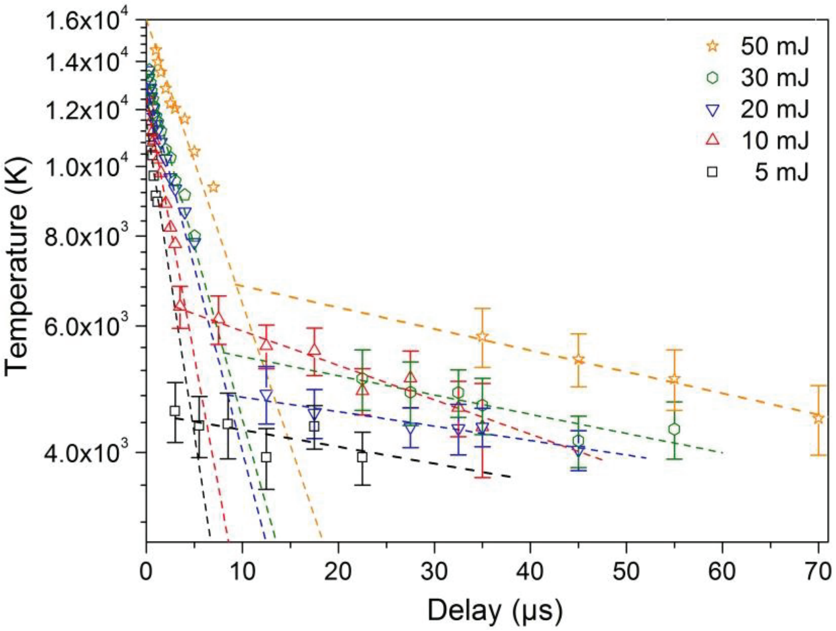

Figure 6.13 Electron as well as molecule temperatures as a function of delay for different ablation energies. The fitting curves of the decay of the temperatures are plotted in dashed lines.

Determination of the value of τ_{min} and T_{max}

As for the case of 10 mJ ablation, the evolution of the molecule emission intensity was observed and compared to the evolution of the molecule temperature. We deduce with such procedure the values of τ_{min} and T_{max} for all the tested ablation energies as shown in Figure 6.14. The obtained results are shown in Table 6-4. Only the values of $T_{\max\_M}$ are given in this table for $T_{\max}$, because $T_{\max\_E}$ determined in Section 6.3.5 has only an indicative meaning. We can see that the experimentally determined values are respectively in the range from 3 to 15 μs for τ_{min} and from 4500 K to 6600 K in terms of the molecule temperature for $T_{\max}$ for the range of ablation laser energies studied in this work.

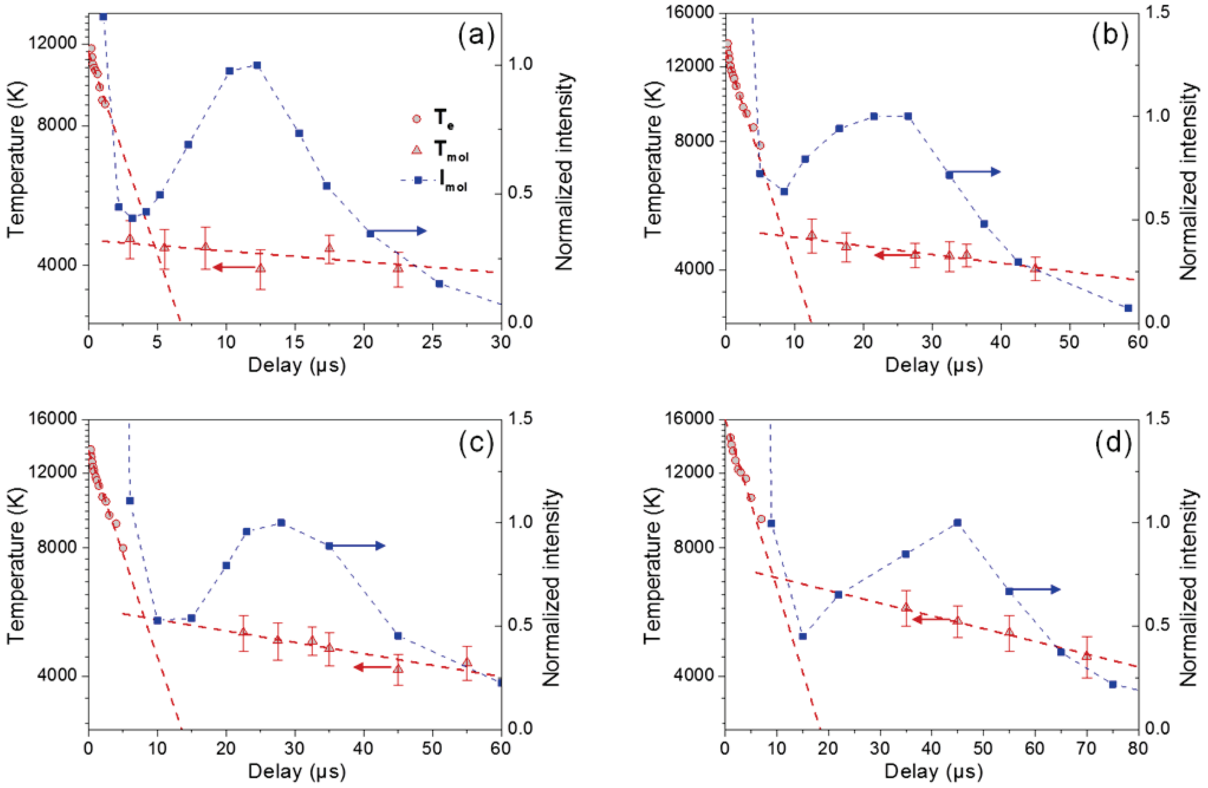

Figure 6.14 Temperatures of the plume (in red) and molecular emission intensity (in blue) as a function of delay with the ablation laser pulse energy of 5 mJ(a), 20 mJ (b), 30 mJ (c) and 50 mJ (d).

Table 6-4 Experimentally determined values for τ_{min}, $T_{\max\_M}$ for different ablation energies.

Laser energy (mJ)	τ_{min} (µs)	$T_{\max\_M}$ (K)
5	3	4500±500
10	6	6200±600
20	8	4800±500
30	10	5400±500
50	15	6600±700

6.5. Distribution of AlO molecules in the ablation plume

In this section, the space distribution of AlO molecules in ablation plume is observed with the use of spectroscopic imaging technique. The imaging detection system described in Chapter 3 is used for the observation. Three narrow band filters (10 nm bandwidth) were used to record emission images of aluminum atoms (central wavelength 400 nm), of AlO molecules (central wavelength 488 nm) and of the continuum background (central wavelength 530 nm). Figure 6.15 shows the obtained images for a plume resulting from ablation with 20 mJ laser pulse. Note that the intensities shown in this figure are normalized to the maximal value of each image. We can see in Figure 6.15 that the population of aluminum atom stays in the middle of the plume. The continuum is also emitted from the same region. As the delay increases, we can observe simultaneously the reduction of the continuum and the increase of the emission from the molecules. Such variation can be compared with the results shown in Figure 6.14 (b). We can see that from a certain delay of 7 to 8 µs, the emission from AlO molecules becomes dominant. We can see also in the Figure 6.15 that the AlO molecules were formed in the peripheral regions surrounding the hot core of the plasma, which means that the recombination of AlO needs a relative low temperature. In addition, in this peripheral region, the aluminum vapor is in contact with oxygen provided by the ambient air. For further increased delays, the molecular population appears also in the central region of the plume, due to the diffusion of the molecular population formed in the peripheral regions, and recombination in the central part of the plume with a lowered temperature. A similar result is obtained for ablation with a higher energy of 50 mJ. The images are shown in Figure 6.16.

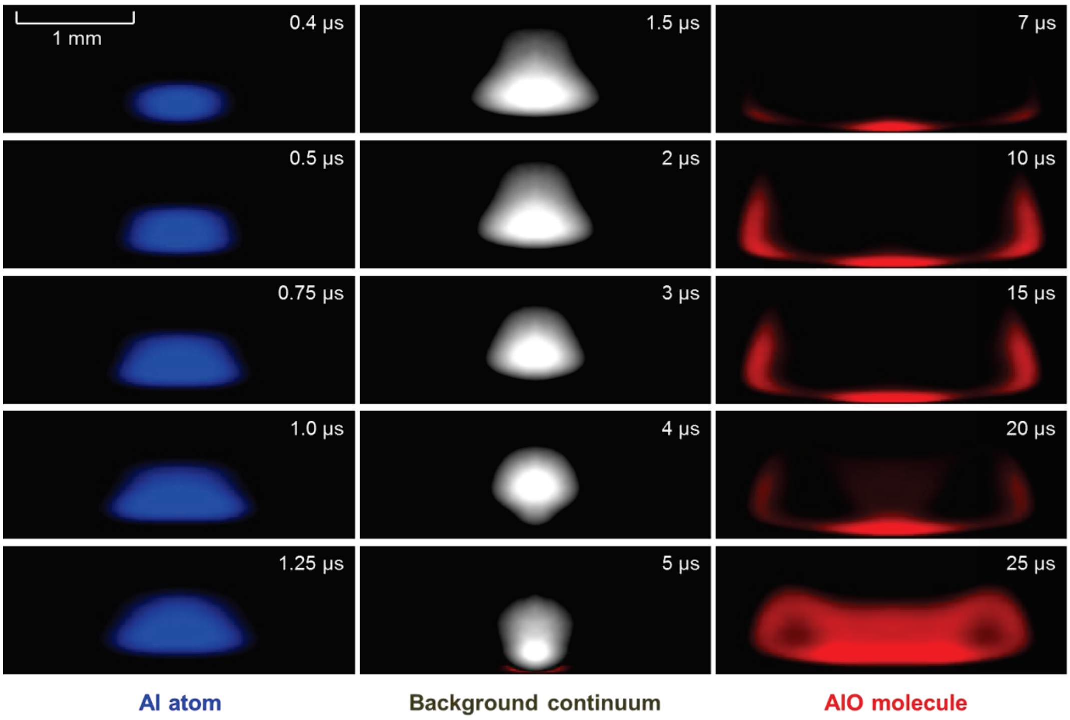

Figure 6.15 Emission images of aluminum atom (blue), continuum background (grey) and AlO molecules (red) for a plume resulting from ablation with 20 mJ

laser pulse. Individual images correspond to detection delays shown in the images. The real dimension of each picture is 1.1 × 3.0 mm², and the bottom line of the images represents the target surface.

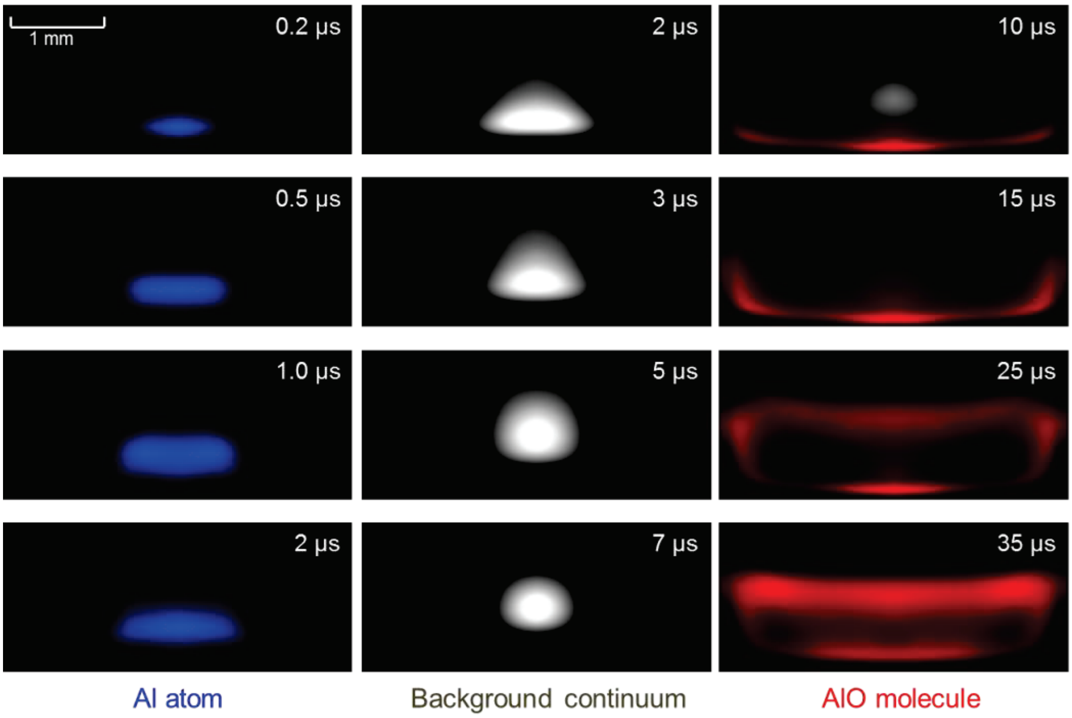

Figure 6.16 Emission images of aluminum atom (blue), continuum background (grey) and AlO molecules (red) for a plume resulting from ablation with 50 mJ laser pulse. Individual images correspond to detection delays shown in the images. The real dimension of each picture is 1.5 × 3.7 mm², and the bottom line of the images represents the target surface.

6.6. Preliminary results on the nanoparticle formation in ablation plume

As a perspective of the present PhD work, we collected the re-condensed materials with plastic plate placed at the positions where AlO population is concentrated as shown by the image study presented in the precedent section. Two plates were used in this experiment. They were respectively placed above the plume and at its lateral side as shown in Figure 6.17. Figure 6.18 shows a picture of the experimental arrangement. Typically each plate was exposed to 6000 laser ablations of an aluminum target under the atmospheric air. After particles being collected, they were observed with scanning electronic microscope (SEM). Figure 6.19 (a) shows an SEM image of a plate exposed to plumes generated with 5 mJ laser ablations. The statistics on the size of the particles shows a distribution centered around 30 nm (Figure 6.19 (b)). Further observations on the samples prepared with different ablation laser energies shows a similar size distribution of the collected nanoparticles.

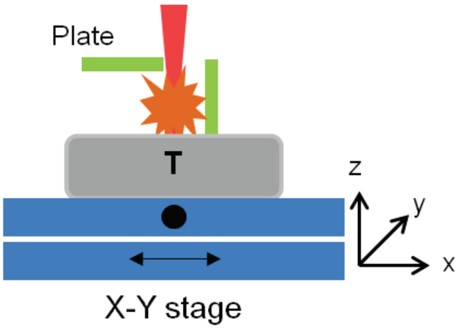

Figure 6.17 Illustration of the arrangement used to collect the re-condensed materials with two plastic plates positioned around the ablation plume.

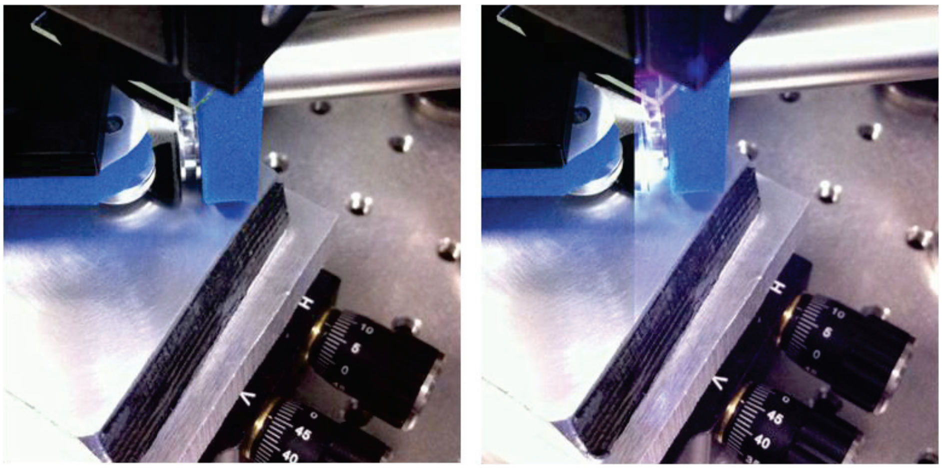

Figure 6.18 Pictures of the arrangement used to collect the re-condensed materials with two plastic plates positioned around the ablation plume.

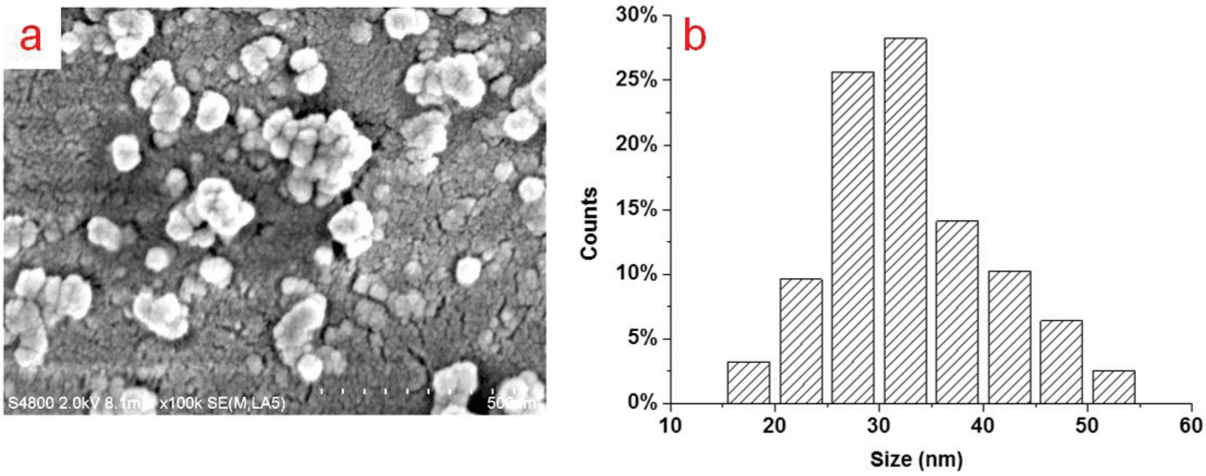

Figure 6.19 (a) SEM image of the collected nanoparticles obtained with 5-mJ ablation and (b) their size distribution (b).

6.7. Resume

In this chapter, the evolution and the transformation of the laser-induced plasma on an aluminum target in the atmospheric air has been investigated in terms of its temperatures and the emission of AlO molecules formed in the plume. The results show that it is possible by combing different plasma diagnostics techniques, multi-Saha-Boltzmann plot and molecule spectrum simulation, to monitor the temperatures in the ablation plume from hundreds of nanosecond up to tens of microsecond. This is indeed a quite large time interval in which the properties of the plasma undergo dramatic changes by involving a large number of physical and chemical processes. The evolution of the emission intensity from AlO molecules is thus observed in correlation with the decay of the electron and the molecule temperatures. More specifically, we defined two parameters which can be experimentally determined. The first one, τ_{min}, corresponds to the minimal delay for a dominant molecule recombination in the plasma. The second, T_{max} , refers to the associated maximal temperature in the plasma for a dominant molecule recombination. We have experimentally determined these two parameters for different ablation laser energies of 5, 10, 20, 30 and 50 mJ at 1064 nm. The determined values lie respectively in the range of 3 to 15 μs for τ_{min} and 4500 K to 6600 K in terms of the molecular temperature for T_{max}. These determined values indicate therefore the longest delay or the lowest temperature for laser-induced plasma to be suitable for a correct analysis of metallic elements, aluminum for instance in our experiment, in air without significant influence of the alternation of the stoichiometry by oxidation. Even though the above drawn conclusion should be applied in general for LIBS measurements, it needs however to be mentioned that the lack of space-resolution for the detection used in the experiment leads to a space-averaged characterization of the plasma. This means that for a given space-averaged temperature in the plasma, even globally the formation of AlO molecule is a dominant process, locally for example in the central part of the plume at a higher temperature, there can still be negligible molecule formation, hence suitable for LIBS measurement. Detailed spatial distribution of AlO molecules is shown in the end of this chapter. We can clearly see a predominant molecule distribution in the periphery of the plume where the temperature is a priori lower. Finally as a perspective of this PhD work, we collected re-condensed nanoparticles and examined then with SEM. Further works in this direction will be continued in our team.

General conclusion and perspectives

This thesis work is the continuation of the research works that have been started in our team with the PhD thesis of Qianli Ma. The ensemble of these works intends to study the laser-induced plasma, such as used in the most of LIBS experiments for analytical purposes. The specifications required in the design of this collection of works were a systematic, detailed and deep investigation of the spatiotemporal behaviors of the plasma generated and evolving in the typical conditions of LIBS measurements. Provided the large dispersion of the LIBS experimental configurations, required in the most of the cases by the experimental and practical constraints of the applications, a simplification procedure was guided by the “LIBS magic cube” introduced in the General introduction of the present PhD thesis manuscript. Doing this, we reduce the parametric space to explore to limited dimensions with a small number of cases to study. In our understanding, the 3 most important parameters on which the resulting properties of the plasma depend are ablation laser wavelength, ablation laser fluence and ambient gas. In a simplified and qualitative approach, we allowed for each of these parameters two variables, or more exactly two distinct domains of variation. Therefore for the ablation laser wavelength, we have UV and IR; for the ablation fluence, we have high fluence and low fluence, and for the ambient gas, we have argon (a monoatomic gas) and the atmospheric air (a diatomic gas). Such strategy leads to 8 parametric volumes to explore in our study.

In the thesis of Qianli Ma defended in December 2012, the 4 volumes with argon as ambient gas have been explored. The focus was to study the effects of the ablation laser wavelength for ablation in an atomic ambient gas. In this thesis, we continue with the effects of laser fluence and a coupled parameter of laser pulse duration. And especially we explore the 4 parametric volumes with the atmospheric air as ambient gas. The focus of the present PhD thesis work is thus to study the specificities due to the implication of a diatomic molecular gas such as the atmospheric air. Of course, the first thesis by Qianli Ma has prepared a good basis in terms of understanding of the phenomenon as well as the methods of experimental investigation. The present second thesis obviously takes the advantage of the progresses made with the first one, but contributes in its own way to the accomplishment of the investigation project in its totality.

In order to achieve the objectives of this thesis, we have continued to work with the simple model system already used in the first thesis, the ablation of an aluminum target. The initial choice of aluminum was justified by its commercial availability in analytically pure quality or with different alloys, its ease to handle in the experiments and, last but not least, its simple emission spectrum. In addition, the same experimental setups and similar experimental protocols as in the thesis of Qianli Ma have been used in this thesis. These setups and protocols allow performing classical plasma diagnostics, including time- and space-resolved emission spectroscopy and fast spectroscopic imaging, with high performance and reliability. As in the previous thesis, the data treatment methods are based on the assumption of the LTE. Such methods allow the characteristic parameters of the plasma being extracted from the experimentally recorded spectra. The most important observables in this experiment, observed and measured to characterize the plasma, include the morphology and the internal structure of the plasma, its profiles of emission intensity, of electron density and of temperature. One of the specificities of this thesis, due to the requirement of investigating the effect of a reactive molecular ambient gas, is the large time scale, from several nanoseconds to tens of microseconds, covered by the time resolved investigation. Comparative study represents also a particularity of this thesis, which allows often underlining the effect of a specific parameter.

After the above discussion on the context and the general approach of this thesis, let us now go to the synthetic presentation of the results obtained in this thesis and the conclusions drawn. These results and conclusions can be summarized into the following three aspects of our study.

1. Convoluted effects of ablation laser fluence and pulse duration on the expansion behavior of the plasma induced in argon at one atmosphere.

In this study, the morphology as well as the internal structure of the plasma has been observed closely related to plasma shielding by the different species in the plume during the post ablation interaction. Dual-wavelength differential spectroscopic imaging technique as well as time- and space-resolved emission spectroscopy have been successfully applied to reveal the detailed structure of the plume by showing two-dimensional distribution of representative species in the plasma. Time-resolved detection allows continuously monitoring the plume from 20 ns to about 1 μs. The morphology and the internal structure of the plasma have been studied for different ablation regimes characterized by laser fluence and pulse duration.

With a pulse of moderate fluence of 65 J/cm^2 and a short pulse duration of 4 ns, the observed plasma morphology and structure are more suitably described by the regime of laser-supported combustion (LSC) wave. The characteristics of such propagation regime include a rather spherical expansion of the plume, a layered internal structure, and a fast decay of the population of the ionized ambient gas. Plasma shielding in this case is dominantly contributed by the ablation vapor, which leads to an absorption zone in the middle of the plume close to the target surface. For ablation with a pulse of higher fluence of 160 J/cm^2 and the same pulse duration of 4 ns, the characteristics of propagation with laser-supported detonation (LSD) wave are observed. Such characteristics include a clearly elongated morphology of the plume, a dominant plasma core consisting of mixture of aluminum ions and argon ions, and a significantly longer lifetime of argon ions. Plasma shielding in this case is dominantly contributed by the shocked and ionized ambient gas which is initially localized around the propagation front of the plume. With a pulse of the same fluence of 160 J/cm^2 and a significantly longer pulse duration of 25 ns, similar characteristics of propagation with laser-supported detonation (LSD) wave are observed as for the high fluence short duration pulse. This demonstrates the importance of laser fluence, but not laser irradiance, for the determination of plasma morphology and internal structure. Moreover, the effect of pulse duration leads to stronger plasma shielding by the shocked and ionized ambient gas for a longer pulse. A delayed evaporation of neutral aluminum appears as a consequence of the splashing ejection of melted aluminum bath lying in the crater.

2. Comparative study of the expansion behaviors of the plasma induced under argon or air ambient gases; Investigation on the specific features of the evolution of laser-induced plasma in a molecular ambient gas; Microscopic mechanisms of laser-supported detonation waves.

In this study, we have investigated the expansion behaviors of the plasma in different ambient gases and at different ablation laser fluence regimes. In the regime of ablation with a moderate laser fluence (20 mJ corresponding to 65 J/cm^2), through imaging and time- and space-resolved emission spectroscopy observations, we get the conclusion that the plasma induced in the two types of ambient gas exhibits quite similar propagation behaviors with comparable propagation velocities, morphologies and internal structures. The exhibited morphology and structure of the plasma suggest a post ablation interaction dominant by the LSC wave. In the regime of ablation with a higher ablation laser fluence (50 mJ corresponding to 160 J/cm^2), the morphology and the structure of the plasmas induced in the both ambient gases show characteristics of a post-ablation interaction dominantly determined by the LSD wave, which is coherent with our previous works. However, a significant difference in propagation behavior is experimentally observed and confirmed between the plasmas induced in argon or in air. The most striking feature is that in argon, a large zone of mixing between ions of argon and aluminum is observed, which confirms once again our previous works. But for the plasma induced in air with the same laser parameters, instead, a population of aluminum confined in a zone close to the target surface and separated from the shocked gas is observed and confirmed experimentally. We have then designed several complementary experimental observations to explain such difference due to the ambient gas in the high laser fluence ablation regime.

Based on such observations and using considerations and models existing in the literature, we have provided the explanations in the macroscopic and the microscopic points of view for the observed phenomenon. In the macroscopic point of view, the hydrodynamic propagation of the plasma leads to a faster LSD wave in argon than in air. Such fast LSD propagation in argon leaves behind it a low pressure rarefaction zone in the shocked gas, which facilitates the upward propagation of the aluminum vapor and leads to a mixing zone between ions of argon and aluminum as observed in our experiment. In the microscopic point of view, the ignition mechanisms are different in argon and in air. In argon, ionization of excited argon atoms through photo absorption of UV radiation and electron impact represents the key mechanisms for the ignition of LSD. While in air the key mechanism corresponds to dissociation of air molecules by shockwave and the production of free electrons in recombination reactions. This explains first a slower propagation velocity of LSD in air because of the longer time constant of the involved molecular process in air than that of the atomic process in argon. This leads also to the understanding that in air, the dissociation of the molecules in the shockwave raises suddenly the pressure of the shocked air before the LSD starts. Such high pressure zone is situated just above the aluminum vapor. The combination for a plasma induced in air, of a high pressure zone in the shocked air before the LSD starts and a slower propagation of the LSD wave finally results in the stagnation and the confinement of the ablation vapor in a small zone close to the target surface as experimentally observed.

3. From plasma to molecules: monitoring of the evolution and the transformation of the plasma over a large time interval from hundreds of nanosecond up to tens of microsecond.

The stoichiometric ablation, where the elemental composition of the generated plume is identical to that of the sample to be analyzed, is a basic requirement of the LIBS technique. However even such ablation is performed with a proper choice of the ablation configuration for a stoichiometric ablation, the stoichiometry of the resulting plume can still change during the evolution of the plasma. Oxidation of metallic elements in a plasma propagating in a reactive gas such as the atmospheric air is a clear example. It is the reason why in this study, we were interested in the correlation between the molecule formation in a laser-induced metallic plasma, aluminum for instance, and its thermodynamic state. More specifically, we have used the atomic and molecular emission spectroscopies to characterize the ablation plume over a very long time interval from hundreds of nanosecond to tens of microsecond. Investigation over such long time delay is required by the observation of the molecular emission from AlO molecules. The evolution and the transformation of the plasma induced on aluminum target in the atmospheric air have been therefore investigated in terms of the temperature and the emission intensity from AlO molecules in the plasma. Our results showed that it is possible by combining different plasma diagnostics techniques, Saha-Boltzmann plot or molecule spectrum simulation, to monitor the temperature in the ablation plume from hundreds of nanosecond up to tens of microsecond. This is indeed a quite large time interval in which the properties of the plasma undergo dramatic changes by involving a large number of physical and chemical processes. The formation of the AlO molecule is thus observed in correlation with the decay of the electron and the molecule temperatures. More specifically, we have defined 2 parameters which can be experimentally determined. The first one, τ_{min}, corresponds to the minimal delay for dominant recombination leading to AlO molecule formation in the plasma. The second, T_{max}, refers to the associated maximal temperature in the plasma for dominant molecule recombination. We have thus experimentally determined these 2 parameters for different ablation laser energies in the range from 5 to 50 mJ at 1064 nm. The determined values lie respectively in the range from 3 to 15 μs for τ_{min} and from 4500 K to 6600 K in terms of the molecule temperature for T_{max}. These determined values indicate therefore the longest delay or the lowest temperature for laser-induced plasma to be suitable for a correct analysis of metallic elements in air without significant influence of the alternation of the stoichiometry by the oxidation. Beyond the practical interest for LIBS technique, our results provide also insights to the chemical kinetics for AlO molecule formation in laser-induced plasma.

Thinking about the perspectives opened by the present PhD thesis, we can already indicate three directions which will be followed in our research team with continuous efforts. The first direction would push our investigation on the effects of the experimental parameters on the properties of the generated plasma even further to their effects on the analytical performances of the LIBS technique. Our investigation would therefore focus on how to improve the figure of merit of the technique in terms of, for example, LoD, precision, accuracy, repeatability or reproducibility. Our study could also intend to reduce matrix effect, self-absorption or various saturation effects. This direction clearly engages us into further application of our basic research finds to improve LIBS instruments and to satisfy practical industrial and societal needs with suitable and dedicated LIBS solutions. A second direction that we would follow is guided by the evolution and transformation of the ablation plume beyond hundreds of microsecond. We have studied the early stage of the plasma expansion and its transformation into a molecular gas. A logical next step is necessary the investigation on the transformation of the molecular gas into re-condensed nanoparticles. Following this direction, new physics will appear and new investigation methods will be needed. A third direction would encourage us to develop more detailed theoretical models to describe and explain in a more quantitative way our experimental observations in the framework of collaboration with a theoretician team.

Collaboration is indeed the keyword in our future works in the three directions mentioned above, since the collaboration with industrial partners for LIBS applications, the multidisciplinary collaboration to favor original researches in the frontiers between spectroscopy and material science, or the collaboration with theoreticians for detailed modeling of the observed phenomena, will be certainly necessary to realize the objectives that we target.

References

1. J. L. Delcroix, A. Bers, Physique des plasmas, Paris: InterEditions/CNRS Editions 1994

2. Leon J. Radziemski, From LASER to LIBS, the path of technology development , Spectrochim. Acta B 57 (2002)1109-1113

3. J. D. Winefordner, I. B. Gornushkin, T. Correll, E. Gibb, B. W. Smith and N. Omenetto, Comparing several atomic spectrometric methods to the super stars: special emphasis on laser induced breakdown spectrometry, LIBS, a future super star, J. Anal. At. Spectrom.19 (2004)1061-1083

4. D. A. Cremers and L. J. Radziemski, Handbook of laser-induced breakdown spectroscopy, Chichester: Wiley, 2006

5. A. W. Miziolek and V. Palleschi, I. Schechter, (Eds.) Laser-induced breakdown spectroscopy: Fundamentals and applications, Cambridge: University Press, 2006

6. Jagdish P. Singh and Surya N. Thakur, Laser-Induced Breakdown Spectroscopy, Elsevier B. V., 2007

7. Reinhard Noll, Laser-induced breakdown spectroscopy: Fundamentals and applications, Berlin Heidelberg : Springer-Verlag, 2012

8. Leon J. Radziemski , Thomas R. Loree , David A. Cremers and Nelson M. Hoffman, Time-resolved laser-induced breakdown spectrometry of aerosols, Anal. Chem. 55(1983)1246-1252

9. M. Baudelet, L. Guyon, J. Yu, J. P. Wolf, T. Amodeo, E. Fréjafon, and P. Laloi, Spectral signature of native CN bonds for bacterium detection and identification using femtosecond laser-induced breakdown spectroscopy, Appl. Phys. Lett. 88 (2006) 063901

10. M. Baudelet, J. Yu, M. Bossu, J. Jovelet, J. P. Wolf, T. Amodeo, E. Fréjafon and P. Laloi, Discrimination of microbiological samples using femtosecond laser-induced breakdown spectroscopy, Appl. Phys. Lett. 89 (2006)163903

11. F. C. De Lucia Jr., R. S. Harmon, K. L. McNesby, R. J. Wonkel Jr.and A. W. Miziolek, Laser-induced breakdown spectroscopy analysis of energetic materials, Appl. Opt. 42 (2003)6148-6152

12. A. I. Whitehouse, J. Young, I. M. Botheroyd, S. Lawson, C. P. Evans and J. Wright, Remote material analysis of nuclear power station steam generator tubes by laser-induced breakdown spectroscopy, Spectrochim. Acta B 56(2001) 821-830

13. http://msl-scicorner.jpl.nasa.gov/Instruments/ChemCam/

14. J. B. Sirven, B. Sallé, P. Mauchien, J. L. Lacour, S. Maurice and G. Manhès, Feasibility study of rock identification at the surface of Mars by remote laser-induced breakdown

spectroscopy and three chemometric methods, J. Anal. At. Spectrom. 22 (2007)1471-1480

15. C. Cetinkaya, R. Vanderwood and M. Rowell, Nanoparticle removal from substrates with pulsed-laser induced plasma and shock waves, J. Adhesion Sci. Technol. 16 (2002)1201-1214
16. V. Motto-Ros, L. Sancey, X. Wang, Q. Ma, F. Lux, X. Bai, G. Panczer, O. Tillement and J. Yu, Mapping nanoparticles injected into a biological tissue using laser-induced breakdown spectroscopy, Spectrochim Acta Part B 87 (2013)168-174
17. J. Xiu, X. Bai, E. Negre, V. Motto-Ros and J. Yu, Indirect laser-induced breakdown of transparent thin gel layer for sensitive trace element detection, Appl. Phys. Lett. 102(2013)244101
18. L. Zheng, F. Cao, J. Xiu, X. Bai, V. Motto-Ros, N. Gilon, H.Zeng, J.Yu, On the performance of laser-induced breakdown spectroscopy for direct determination of trace metals in lubricating oils, Spectrochim Acta Part B 99 (2014)1-8
19. H. Lindner, K. H. Loper, D. W. Hahn and K. Niemax, The influence of laser-particle interaction in laser induced breakdown spectroscopy and laser ablation inductively coupled plasma spectrometry, Spectrochimica Acta Part B 66 (2011)179–185
20. J. Anzano, R. J. Lasheras, B. Bonilla and J. Casas, Classification of polymers by determining of C1:C2:CN:H:N:O ratios by laser-induced plasma spectroscopy (LIPS), Polymer Testing 27 (2008)705–710
21. D. Marla, U. V. Bhandarkar, and S. S. Joshi, Critical assessment of the issues in the modeling of ablation and plasma expansion processes in the pulsed laser deposition of metals, J. Appl. Phys. 109(2011) 021101
22. J. Kaiser, M. Galiová, K. Novotný, R. Červenk, L. Reale, J. Novotný, M. Liška, O. Samek, V. Kanický, A. Hrdlička, K. Stejskal, V. Adam and R. Kizek, Mapping of lead, magnesium and copper accumulation in plant tissues by laser-induced breakdown spectroscopy and laser-ablation inductively coupled plasma mass spectrometry, Spectrochim Acta Part B 64 (2009)67–73
23. C. Balas, V. Papadakis, N. Papadakis, A. Papadakis, E. Vazgiouraki and George Themelis, A novel hyper-spectral imaging apparatus for the non-destructive analysis of objects of artistic and historic value, Journal of Cultural Heritage 4 (2003) 330s–337s
24. B. C. Castle, K. Talabardon, B. W. Smith, and J. D. Winefordner, Variables Influencing the Precision of Laser-Induced Breakdown Spectroscopy Measurements, Appl. Spectrosc. 52(1998) 649-657
25. D. W. Hahn and N. Omenetto, Laser-Induced Breakdown Spectroscopy (LIBS), Part I: Review of Basic Diagnostics and Plasma–Particle Interactions: Still-Challenging Issues Within the Analytical Plasma Community, Appl. Spectrosc. 64(2010) 335A-366A
26. S.S. Mao, X. Mao, R. Greif, and R. E. Russo, Initiation of an early-stage plasma during picosecond laser ablation of solids, Appl. Phys. Lett. 77(2000) 2464
27. G. Cristoforetti, G. Lorenzetti, P. A. Benedetti, E. Tognoni, S. Legnaioli and V. Palleschi, Effect of laser parameters on plasma shielding in single and double pulse configurations during the ablation of an aluminium target, J. Phys. D: Appl. Phys. 42 (2009)225207

28. D. Bauerle, laser processing and chemistry, Springer-Verlag, Berlin, Heidelberg, 2011
29. M. Fox, Optical properties of solids, Oxford: Oxford University Press, 2010
30. N. W. Ashcrotf and N. D. Mermin, Solid State Physics, Philadelphia: CBS Publishing Asia LTD, 1976
31. C. Kittel, Introduction to Solid State Physics, John Wiley & Sons Inc, 2005
32. P. Drude, Annalen der Physik, 1900, 1: 566 and 3: 396
33. M. von Allmen and A. Baltter, Laser-Beam Interaction with Materials, Berlin Hedelberg: Springer, 1995
34. A. Bogaerts, Z.Y. Chen, R. Gijbels, A. Vertes, Laser ablation for analytical sampling: what can we learn from modeling?, Spectrochim Acta B 58(2003)1867-1893.
35. X. Xu, Phase explosion and its time lag in nanosecond laser ablation, Appl. Surface Sci. 197-198(2002) 61-62
36. V.P. Skripov, Metastable liquids, Wiley, New York, 1974
37. X. Mao and R. E. Russo, Observation of plasma shielding by measuring transmitted and reflected laser pulse temporal profiles, Appl. Phys. A 64 (1997) 1–6
38. N.M. Bulgakova, A.V. Bulgakov, Pulsed laser ablation of solids: Transition from normal vaporization to phase explosion, Appl. Phys. A 73(2001) 199–208
39. Q. Ma, Thesis: "Structure et dynamique du plasma induit par laser en propagation dans un gaz ambiant d'argon" (2012)
40. R. G. Root, Ch. 2: Modeling of Post-Breakdown Phenomena in Laser-Induced Plasmas and Applications, ed. L. J. Radziemski and D. A. Cremers, New York: Dekker, 1989
41. L. D. Landeau and E. M. Lifshitz, The classical theory of fields, Addison-Wesley, 1962
42. J. Richter, Ch. 1: Radiation of hot gases, in Plasma Diagnostics, Ed. W. Lochte-Holtgreven, Amsterdam: North-Holland Publishing Company, 1968
43. R. S. Devoto, Transport coefficients of ionized argon, Phys. Fluids 16(1973) 616-623
44. C. J. Knight, Theoretical Modeling of Rapid Surface Vaporization with Back Pressure, AIAA J. 17(1979) 519-523
45. S. Wen, X. Mao, R. Greif and R. E. Russo, Radiative cooling of laser ablated vapor plumes: Experimental and theoretical analyses, J. Appl. Phy. 100(2006) 053104
46. Ya. B. Zel'dovich and Yu. O. Raizer, Physics of Shock Waves and High-Temperature Hydrodynamic Phenomena, New York: Dover, 2002
47. D. I. Rosen, J. Mitteldorf , G. Kothandaraman, A. N. Pirri, and E. R. Pugh, Coupling of pulsed 0.35-μm laser radiation to aluminum alloys, J. Appl. Phys. 53(1982)3190
48. G. M. Weyl and D. I. Rosen, Laser-induced breakdown in argon at 0.35 μm: Theory and experiments, Phys. Rev. A 31(1985) 2300
49. D. H. Menzel and C. L. Pekeris, Absorption coefficients and hydrogen line intensities, Mon. Not. R. Astron. Soc. 96(1935) 77-96
50. L. M. Biberman and G. E. Norman, On the Calculation of Photoionization Absorption , Opt. Spectrosc. 8(1960)230

51. L. M. Biberman, G. E. Norman and K. N. Ul'yanov, On the Calculation of Photoionization Absorption in Atomic Gases, Opt. Spectrosc. 10(1961) 297

52. J. Hoffman, T. Moscicki and Z. Szymanski, The effect of laser wavelength on heating of ablated carbon plume, Appl. Phys. A 104(2011) 815-819

53. X. Mao, S. B. Wen, R. E. Russo, Time resolved laser-induced plasma dynamics, Appl. Surf. Sci. 253(2007) 6316-6321

54. Ya.B.Zel'dovichand, Yu.P. Raizer, Ch. VI: Rates of relaxation processes in gases, ed. Wallace D. Hayes and Ronald F. Probstein, New York: Dover, 2002

55. S. S. Harilal, B. O'Shay, Y. Tao and M. S. Tillack, Ambient gas effects on the dynamics of laser-produced tin plume expansion, J. Appl. Phys. 99(2006) 083303

56. G. Cristoforetti, A. De Giacomo, M. Dell'Aglio, S. Legnaioli, E. Tognoni, V. Palleschi, N. Omenetto, Local thermodynamic equilibrium in laser-induced breakdown spectroscopy: beyond the McWhirter criterion, Spectrochim. Acta Part B 65(2010) 86-95

57. J.A.M. van der Mullen, On the atomic state distribution function in inductively coupled plasmas — I. Thermodynamic equilibrium considered on the elementary level, Spectrochim. Acta Part B 44 (1989) 1067–1080

58. H.R. Griem, Plasma Spectroscopy, McGraw-Hill Inc., New York, 1964.

59. T. Fujimoto, Plasma Spectroscopy, Clarendon Press, Oxford, 2004

60. J.A.M. van der Mullen, On the atomic state distribution function in inductively coupled plasmas II. The stage of local thermal equilibriumand its validity region, Spectrochim. Acta Part B 45 (1990) 1–13

61. M. Capitelli, F. Capitelli, A. Eletskii, Non-equilibrium and equilibrium problems in laser-induced plasmas, Spectrochim. Acta Part B 55 (2000) 559–574.

62. H.W. Drawin, Validity conditions for Local Thermodynamic Equilibrium, Z. Phys. 228(1969) 99-119

63. H. R. Griem, Spectral line broadening by plasmas. Academic press New York and London, 1974

64. Siegman, AE (1986)

65. N. Konjevic, M. Ivkovic and S. Jovicevic, Spectroscopic diagnostics of laser-induced plasmas, Spectrochim. Acta Part B **65**(2010) 593-602

66. C. Aragón and J.A. Aguilera, Characterization of laser induced plasma by optical emission spectroscopy: A review of experiments and methods, Spectrochim. Acta Part B 63(2008) 893-916

67. J. COOPER, Plasma spectroscopy, Plasma Physics Group, Imperial College, London, 1966

68. W.L. Wiese, R.H. Huddlestone and S.L. Leonard, Plasma Diagnostic Techniques, Academic Press, New York, 1965

69. V. Milosavljevic and S. Djenize, Ion contribution to the prominent Ne I, Ar I and Kr I spectral line broadening, A&A 398(2003) 1179-1184

70. Gans, Section 9.3, Convolution and Cross-correlation

71. N. Konjevic H , J.R. Roberts, A critical review of the Stark widths and shifts of spectral lines from non-hydrogenic atoms, J. Phys. Chem. Ref. Data 5 (1976) 209-258

72. H.R. Griem, Principles of Plasma Spectroscopy, Cambridge University Press, Cambridge,1997

73. E. Tognoni, V. Palleschi, M. Corsi, et al., Laser-induced breakdown spectroscopy (LIBS): Fundamentals and Applications, Cambridge, University Press, 2006

74. J.A. Aguilera and C. Aragón, Multi-element Saha–Boltzmann and Boltzmann plots in laser-induced plasmas, Spectrochim. Acta Part B 6(2007) 378-385

75. H. Partidge and S. R. Langhoff, Theoretical study of the AlO Blue-Green ($B^2\Sigma^+ - X^2\Sigma^+$) band system, J. Quant. Spectrosc. Radiat. Transfer, 30 (1983) 449-162.

76. S. Behere, Oral presentation on the conference of Molecular Spectroscopy Symposium (18-22 June 2007), Columbus Ohio USA

77. G. Herzberg and K.P. Huber, Molecular spectra and molecular structure: I. Diatomic Molecules. Van Nostrand Reinhold, New York, 1950.

78. G.R. Hébert and R.W. Nicholls, Absolute band strengths for the AlO Blue-Green ($B^2\Sigma^+ - X^2\Sigma^+$) band system, J. Quant. Spectrosc. Radiat. Transfer 23 (1980) 229-235.

79. M.D. Saksena, G. S. Ghodgaonkar and M. Singh, The $B^2\Sigma^+ - X^2\Sigma^+$ system of AlO, J. Phys. B:At. Mol. Opt. Phys. 22 (1989) 1933-1996.

80. J. O. Hornkohl, C. Parigger, J.W.L. Lewis, Temperature measurements from CN spectra in a laser-induced plasma, J. Quant. Spectrosc. Radiat. Transfer 46 (1991) 405-411.

81. I. G. Dors, C. Parigger, and J. W. L. Lewis, Spectroscopic temperature determination of aluminum monoxide in laser ablation with 266-nm radiation, Opt. Lett. 23 (1998) 1778-1780.

82. O. Varenne, P. G. Fournier, J. Fournier, B. Bellaoui, A. I. Faké, J. Rostas, G. Taïeb, Internal population distribution of the B state of AlO formed by fast ion beam bombardment or laser ablation of an Al_2O_3 (Al), Nucl. Instr. And Meth. Res. B 171 (2000) 259-276.

83. J Hermann, F Coursimault, O. Motret, S Acquaviva and A Perrone, Investigation of silicon oxide emission spectra observed in a pulsed discharge and a laser-induced plasma, J. Phys. B: At. Mol. Opt. Phys. 34 (2001) 1917-1928.

84. W. Lei, V. Motto-Ros, M. Boueri, Q. L. Ma, D. Zhang, L. Zheng, H. Zeng, and J. Yu, Time-resolved characterization of laser-induced plasma from fresh vegetables, Spectrochim. Acta Part B 64 (2009) 891-898.

85. http://people.duke.edu/~hpgavin/ce281/lm.pdf ,2006

86. NIST Atomic Spectra Database: http://www.nist.gov/pml/data/asd.cfm

87. A. Sainz, A. Diaz, D. Casas, M. Pineda, F. Cubillo and M.D. Calzada, Abel inversion applied to a small set of emission data from a microwave plasma, Appl. Spectrosc. 60 (2006) 229-236.

88. C. J. Cremers and R. C. Birkebak, Appl. Opt. 5, 1057 (1966).

89. R. D. Sacks and J. P. Walters, Short-time, spatially-resolved radiation processes in a high-voltage spark discharge, Anal. Chem. 42(1) (1970) 61-84

90. O.H. Nestor and H.N Olsen., Numerical Methods for Reducing Line and Surface Probe Data, SIAM Rev. 2 (1960) 200-207

91. R. Álvarez, M.C. Quintero, A. Rodero, Radial distribution of electron density, gas temperature and air species in a torch kind helium plasma produced at atmospheric pressure, Spectrochim. Acta B 59(2004) 709-721

92. C. Aragón and J.A. Aguilera, Determination of the local electron number density in laser-induced plasmas by Stark-broadened profiles of spectral lines. Comparative results from H_α, Fe I and Si II lines, Spectrochim. Acta Part B 65 (2010)395-400

93. G. Cristoforetti, S. Legnaioli, V. Palleschi, A. Salvetti, E. Tognoni and P. Tomassini, Reconstruction of laser-induced plasma spectral emissivity in non-axisymmetric conditions, Spectrochim. Acta, Part B 60(2005) 888-896

94. Q. Ma, V. Motto-Ros, W. Lei, M. Boueri, X. Bai, L. Zheng, H. Zeng, and J. Yu, Temporal and spatial dynamics of laser-induced aluminum plasma in argon background at atmospheric pressure: Interplay with the ambient gas, Spectrochim. Acta Part B 65(2010) 896-907

95. J. A. M. Van Der Mullen, Spectrochim. Acta Part B 45, 1 (1990).

96. W.Q. Lei, V. Motto-Ros, M. Boueri, Q.L. Ma, D.C. Zhang, L.J. Zheng, H. P. Zeng, and J. Yu, Spectrochim. Acta Part B 64, 891 (2009).

97. D. Breitling, H. Schittenhelm, P. Berger, F. Dausinger, H. Hügel, Shadowgraphic and interferometric investigations on Nd:YAG laser-induced vapor/plasma plumes for different processing wavelengths, Appl. Phys. A 69 (1999) S505–S508.

98. G. R. Root in Laser-Induced Plasmas and Applications, Ed. L.J. Radziemski and D.A. Cremers, Dekker, New York (1989) 69-103.

99. V.I. Babuchok, F.C. Delucia, Jr., P. J. Dagdigian, M.J. Nusca, and A.W. Miziolek, Kinetic modelling of the laser-induced breakdown spectroscopy plume from metallic lead, Appl. Opt. 42 (2003) 5947-5962.

100. Q. Ma, V. Motto-Ros, F. Laye, J. Yu, W. Lei, X. Bai, L. Zhengand H. Zeng, Ultraviolet versus infrared: effects of ablation laser wavelength on the expansion of laser-induced plasma into one-atmosphere argon gas, J. Appl. Phys. 111 (2012) 053301.

101. P.E. Nielsen, Hydrodynamic calculations of surface response in the presence of laser-supported detonation waves, J. Appl. Phys. 46 (1975) 4501-4505.

102. A. Vogel and V. Venugopalan, Mechanisms of Pulsed Laser Ablation of Biological Tissues, Chem. Rev. 103 (2003) 577-644.

103. G. Cristoforetti, Orthogonal Double-pulse versus Single-pulse laser ablation at different air pressures: A comparison of the mass removal mechanisms, Spectrochim. Acta B 64 (2009) 26–34.

104. A.D. Zweig, A thermo-mechanical model for laser ablation, J. Appli. Phys. 70 (1991) 1684-1691

105. S. S. Harilal, C. V. Bindhu, V. P. N. Nampoori, and C. P. G. Vallabhan, Influence of ambient gas on the temperature and density of laser produced carbon plasma, Appl. Phys. Lett. 72 (2) (1998)167

106. X. Bai, Q. Ma, V. Motto-Ros and J. Yu, D. Sabourdy, L. Nguyen, and A. Jalocha. Convoluted effect of laser fluence and pulse duration on the property of a nanosecond laser-induced plasma into an argon ambient gas at the atmospheric pressure, J. Appl. Phys. 113 (2013) 013304

107. X. Bai, Q. Ma, V. Motto-Ros and J. Yu, D. Sabourdy, L. Nguyen, and A. Jalocha. Experimental study of laser-induced plasma: Influence of laser fluence and pulse duration, Spectrochim. Acta B 87 (2013) 27-35

108. A. A. Ilyin, I. G.Nagorny and O. A.Bukin, Supersonic regimes of plasma expansion during optical breakdown in air, Appl. Phys. Lett. 96(2010)171501

109. P. S. P. Wei, R. B. Hall and W. E. Maher, Study of laser –supported detonation waves by time-resolved spectroscopy, J. Chem. Phys. 59 (1973)3692-3701

110. http://physics.nist.gov/cgi-bin/ASD/ie.pl

111. J.W. Bond, Jr, Structure of a shock front in argon, Phys. Rev. 105 (1957) 1863-1894

112. V. Hohreiter, J.E. Carranza, D.W. Hahn, Temporal analysis of laser-induced plasma properties as related to laser-induced breakdown spectroscopy, Spectrochim. Acta B. 59 (2004) 327-333

113. Ciucci, M. Corsi, V. Palleschi, S. Rastelli, A. Salvetti, and E. Tognoni, New Procedure for Quantitative Elemental Analysis by Laser-Induced Plasma Spectroscopy, Appl. Spectrosc 53 (1999) 960-964.

114. S. Yuasa, Y. Zhu and S. Sogo, Ignition and Combustion of Aluminum in Oxygen / Nitrogen Mixture Streams, Combustion and Flame,108(1997) 387–390.

115. JANAF, Thermochemical Tables, 2nd ed., The Dow Chemical Company, Michigan, 1974, 1975, 1978, 1982

116. T. N. Piehler, F. C. DeLucia, Jr., C. A. Munson, B. E. Homan, A. W. Miziolek, and Kevin L. McNesby, Temporal evolution of the laser-induced breakdown spectroscopy spectrum of aluminum metal in different bath gases, Appl. Opt. 44 (2005) 3654-3660.

117. Ph. Rohwetter, J. Yu, G. Méjean, K. Stelmaszczyk, E. Salmon, J. Kasparian, J. P. Wolf, and L. Wöste, Remote LIBS with ultra-short pulses: characteristics in picosecond and femtosecond regimes, J. Anal. At. Spectrom. 19 (2004) 437-444.

118. J.A. Aguilera and C. Aragón, Multi-element Saha-Boltzmann and Boltzmann plots in laser-induced plasma, Spectrochim. Acta Part B 62 (2007) 378-385.

119. S. Acquaviva, Simulation of emission molecular spectra by a semi-automatic programme package: the case of C2 and CN diatomic molecules emitting during laser ablation of a graphite target in nitrogen environment, Spectrochim. Acta Part A 60 (2004) 2079-2086.

120. G. Parigger and J.O. Hornkohlb, Computation of AlO $\mathrm{B}^2\Sigma^+ - \mathrm{X}^2\Sigma^+$ emission spectra, Spectrochim. Acta Part A 81 (2011) 404–411.

121. G. Dors, C. Parigger, and J. W. L. Lewis, Spectroscopic temperature determination of aluminum monoxide in laser ablation with 266-nm radiation, Opt. Lett. 23 (1998) 1778-1780.

122. Varenne, P. G. Fournier, J. Fournier, B. Bellaoui, A. I. Faké, J. Rostas, G. Taïeb, Internal population distribution of the B state of AlO formed by fast ion beam bombardment or laser ablation of an Al2O3 (Al), Nucl. Instr. And Meth. Res. B 171 (2000) 259-276.

Annex

List of publications

1. Experimental Determination of the Temperature Range of AlO Molecular Emission in Laser-Induced Aluminum Plasma in Air

   X. Bai, V. Motto-Ros, L. Zheng and J. Yu, *Spectrochimica Acta Part B-atomic Spectroscopy,* 99, (2014) 193–200

2. Experimental study of laser-induced plasma: Influence of laser fluence and pulse duration

   X.Bai, Q. Ma, M. Perrier, V. Motto-Ros, D. Sabourdy, N. Luc, A. Jalocha and J. Yu, *Spectrochimica Acta Part B-atomic Spectroscopy*, 87, 27-35 (2013)

3. Convoluted effect of laser fluence and pulse duration on the property of a nanosecond laser-induced plasma into an argon ambient gas at the atmospheric pressure

   X. Bai, Q. Ma, V. Motto-Ros, J. Yu, D. Sabourdy, L. Nguyen and A. Jalocha, *Journal of Applied Physics*, 113, 013304-10 (2013)

4. Indirect laser-induced breakdown of transparent thin gel layer for sensitive trace element detection

   J. Xiu, **X. Bai**, E. Negre, V. Motto-Ros and J. Yu, *Applied Physics Letters*, 102, 244101 (2013)

5. Mapping nanoparticles injected into a biological tissue using laser-induced breakdown spectroscopy

   V. Motto-Ros, L. Sancey, X. Wang, Q. Ma, F. Lux, **X. Bai**, G. Panczer, O. Tillement and J. Yu, *Spectrochimica Acta Part B-atomic Spectroscopy*, 87, 168-174 (2013)

6. Experimental investigation of the structure and the dynamics of nanosecond laser-induced plasma in 1-atm argon ambient gas

   Q. Ma, V. Motto-Ros Vincent, **X. Bai** and J. Yu, *Applied Physics Letters*, 103, 204101 (2013)

7. Effect of ablation photon energy on the distribution of molecular species in laser-induced plasma from polymer in air

   W. Lei, Q. Ma, V. Motto-Ros, **X. Bai**, L. Zheng, H. Zeng and J. Yu, *Spectrochimica Acta Part B-atomic Spectroscopy*, 73, 7-12 (2012)

8. Ultraviolet versus infrared: Effects of ablation laser wavelength on the expansion of laser-induced plasma into one-atmosphere argon gas

   Q. Ma, V. Motto-Ros, F. Laye, J. Yu, W. Lei, **X. Bai**, L. Zheng and H. Zeng, *Journal of Applied Physics*, 111, 053301 (2012)

9. Mapping of native inorganic elements and injected nanoparticles in a biological organ with laser-induced plasma

V. Motto-Ros, L. Sancey, Q. Ma, F. Lux, **X. Bai**, X. Wang, J. Yu, G. Panczer and O. Tillement, *Applied Physics Letters*, 101, 223702 (2012)

10. Characteristics of Laser-Induced Plasma as a Spectroscopic Light Emission Source

    Q. Ma, V. Motto-Ros, W. Lei, X. Wang, M. Boueri, F. Laye, C. Zeng, M. Sausy, A. Wartelle, **X. Bai**, L. Zheng, H. Zeng, M. Baudelet and J. Yu, 17th International Conference On Atomic Processes In Plasmas (icapip), 1438, 243-248 (2012)

11. Generation and expansion of laser-induced plasma as a spectroscopic emission source

    J. Yu, Q. Ma, V. Motto-Ros, W. Lei , X. Wang and **X. Bai**, *Frontiers of Physics*, 7, 649 (2012)

12. Comparative measurements of mineral elements in milk powders with laser-induced breakdown spectroscopy and inductively coupled plasma atomic emission

    W. Lei, J. El Haddad, V. Motto-Ros, N. Gilon-Delepine, A. Stankova, Q. Ma, **X. Bai**, L. Zheng, H. Zeng and J. Yu, *Analytical and Bioanalytical Chemistry*, 400, 3303-3313 (2011)

Oral presentations

1. Morphology of Laser-Induced Plasma in Different Ambient Gases: the Microscopic Mechanisms.

   The 8th International Conference on Laser Induced Breakdown Spectroscopy, September, 2014, Beijing, China

2. Experimental Determination of the Temperature Range of AlO Molecule Emission in Laser-Induced Aluminum Plasma in Air.

   The 7th Euro-Mediterranean Symposium on Laser Induced Breakdown Spectroscopy, September, 2013, Bari, Italy

3. Convoluted effect of fluence and pulse duration on the property of a nanosecond laser-induced plasma**.**

   The 7th International Conference on Laser Induced Breakdown Spectroscopy, September, 2012, Luxor, Egypt